Doctorate Course in:

Energy and Environment Engineering Science

XXXIII cycle

Thesis Title

"Bimetallic Catalysts Prepared by Mechanical Milling for Natural Gas Vehicles Applications"

PhD candidate Andrea Mussio

Advisor Prof. Alessandro Trovarelli
Co-advisor Dr.ssa Sara Colussi

Year 2021

Index

List of abbreviations

NGV – Natural Gas fueled Vehicle

TWC – Three-Way Catalyst

M – Milling

IWI – Incipient Wetness Impregnation

BPR – Ball to Powder weight Ratio

BET – Brunauer–Emmett–Teller

TPO – Temperature programmed oxidation

TPR – Temperature programmed reduction

HRTEM – High resolution transmission electron microscopy

EDX – Energy Dispersive X-ray spettroscopy

HAADF – High-Angle Annular Dark-Field imaging

XANES – X-ray Absorption Near Edge Structure spettroscopy

XRD – X-ray Diffraction

TPC – Temperature Programmed Combustion

TOS – Time-on-stream

GHSV – Gas Hourly Space Velocity

LO – Light-off

LS – Lambda Sweep

1. Introduction

1.1 Background

The first connection between the mean temperature of the atmosphere and the presence of CO_2 was proposed by Arrhenius early in 1896. He affirmed that the mean temperature would have been lower without the presence of CO_2 in the atmosphere[1]. Apart from the scientific statement, he did not suspect any future climate change due to an excess of this gas, neither a responsibility of the mankind due to its energy and sources management. How could he? The overpopulated and connected planet known nowadays was not even imaginable. Only a hundred of years later the climate change has been globally recognized and ascribed to human activities, with some skepticism that is still present[2,3].

Despite it has a physiological oscillation, the equilibrium of the natural carbon cycle has been dramatically affected after the deep utilization of fossil fuels, and now the risk is that of an irreversible global change.

The first international report about climate change was compiled in 1990 by the International Panel on Climate Change (IPCC), established under the UNFCCC (United Nations Framework Convention for Climate Change). It followed the international treaty known as the Kyoto Protocol, committing the UN state parties to reduce greenhouse gas emissions, in line with the IPCC report[4]. Other reports from IPCC followed, the last one compiled within the Paris Agreement in 2016. Released in 2018, it is focused on how to keep the global mean temperature increase within about 1.5°C above the pre-industrial level[5]. The mean earth temperature and emissions of CO_2 increased constantly in the last decades, as reported in Figure 1-1.

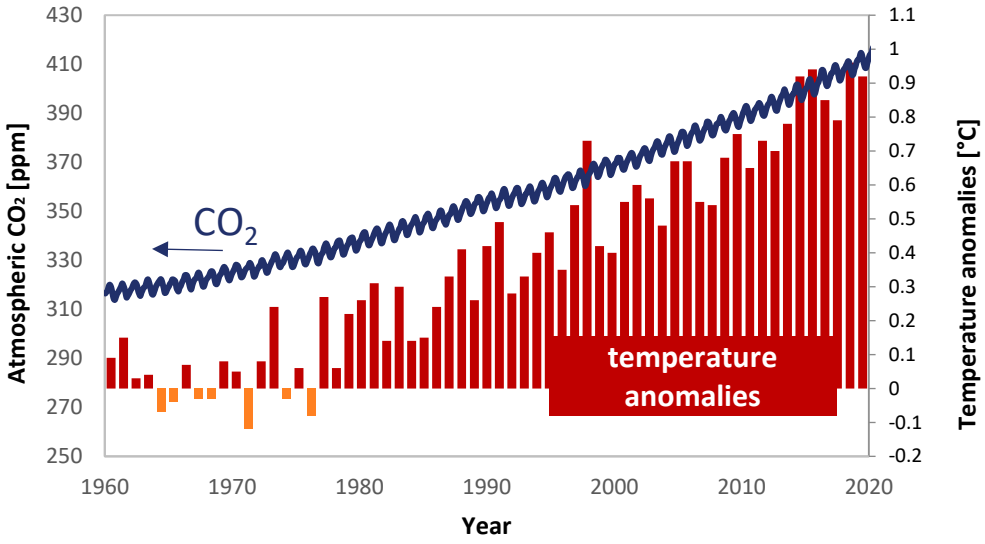

Figure 1-1: CO_2 trend (source: NASA) and temperature anomalies (source: NASA) in the period 1960-2020.

The comparison between the mean atmospheric CO_2 concentration with the earth temperature anomalies in the last 60 years clearly shows a correlation between the two. Currently, the temperature increase is around 0.9°C above the preindustrial level. It is considered that climate change will be irreversible for many natural systems if that value will increase, as summarized in Figure 1-2.

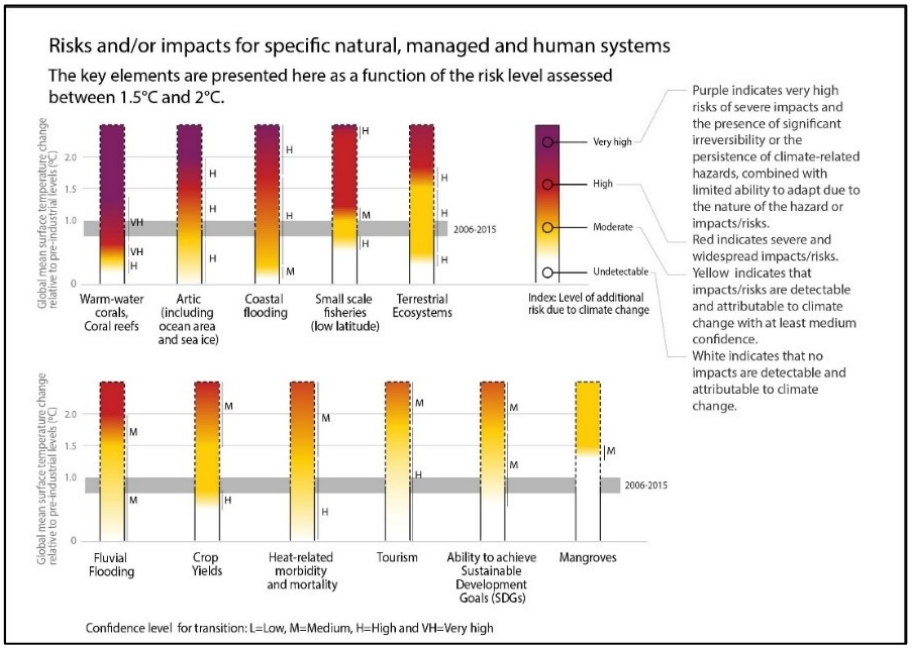

Figure 1-2: risks and impacts for specific natural, managed and human systems assessed between 1.5°C and 2°C. Reprinted from IPCC report[5].

In the meanwhile, the global population reached 7.7 billion in 2019 and it is expected to reach 9.7 billion in 2050[6]. Energy demand is consequently increased and so did the use of fossil sources and the carbon footprint. In the decade 2009-2018, 86% of total emissions were from fossil fuel use, and 14% from land use change, consisting mainly in deforestation[7]. The global energy-related CO_2 emissions accounted for the historical amount of 33Gt in 2018[8]. Global fossil CO_2 emissions have grown at a rate of 1.3 $\%yr^{-1}$ in this period. China's emissions increased by +2.2 % yr^{-1} on average dominating the global absolute trend, followed by India's emissions increase by +5.1 % yr^{-1}, while emissions decreased in EU28 by −1.4 % yr^{-1} and in the USA by −0.5 $\%yr^{-1}$.[7]

The availability and versatility of fossil hydrocarbons make them hardly substitutable. Indeed, despite the increased attention for the environment, and the increase in renewable sources, the use of fossil fuels is still receiving investments[9].

In Figure 1-3 the distribution of greenhouse gas emissions by economic sector is represented.

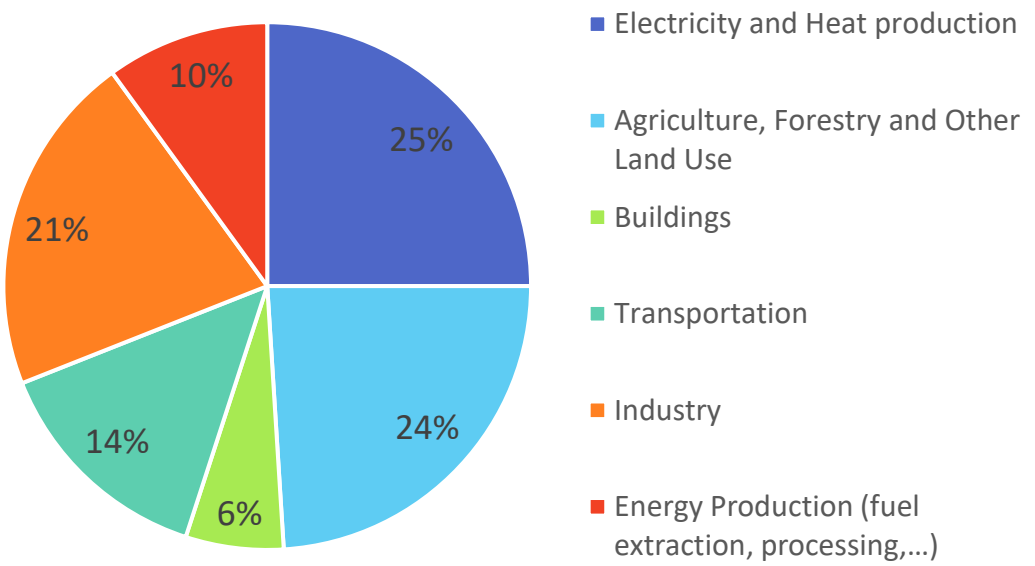

Figure 1-3: global greenhouse gas emissions by economic sector. Source: IEA.

Electricity and heat production lead the emissions balance, with a comparable weight for industry and agriculture. Transportation and buildings have a lower, but not negligible, part. However, this distribution changes a lot considering each country, so that transportation can reach almost one-third of the emissions in the most developed countries[10].

The IPCC report focused prevalently on a progressive reduction in the emissions of greenhouse gases. This relies mostly on the reduction of carbon content sources. Indeed, a realistic scenario excludes a radical change to zero emissions, but it focuses more on the *efficiency* of the transition towards a carbon-free global economy. Figure 1-4 gives an overview of what has been done in this direction for energy production.

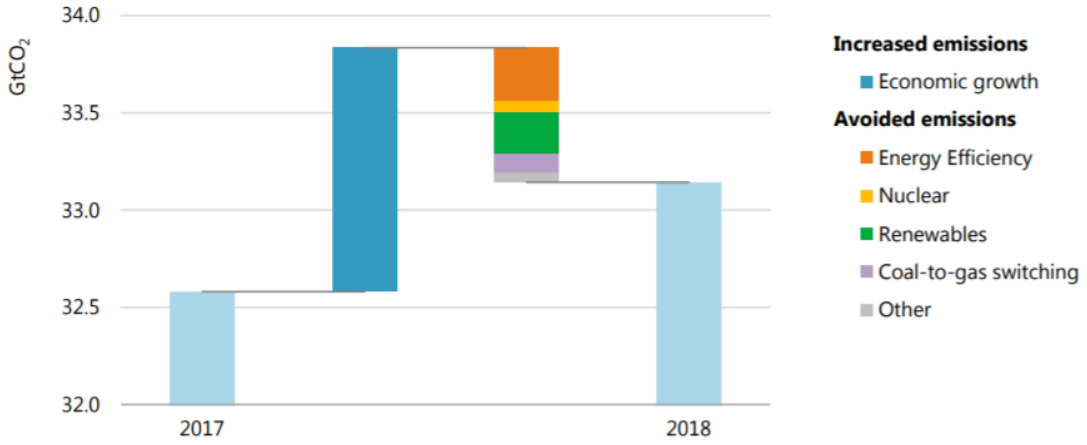

Figure 1-4: comparison between CO_2 emissions in 2017 and 2018 for energy production. Sources: IEA

It shows the comparison of the CO_2 emitted in 2017 and 2018 together with the reduction in the emissions achieved for different sectors. The economic growth would have brought to an energy consumption responsible for almost 34 Gt CO_2 in 2018. However, part of them has been avoided thanks to the improvement in energy supply (indicated by the coloured bars). The highest savings have been obtained thanks to the increased efficiency of energy conversion and to the use of renewables, followed by the switch from coal-based energy production to gas-based one. The latter is explained by the lower carbon content of natural gas compared to coal. Indeed, the main component of natural gas is methane, which has the highest hydrogen-to-carbon ratio of all hydrocarbons that turns into a lower CO_2 emitted per energy unit[11].

The use of natural gas is of great interest not only because of the possibility to switch many activities still based on coal and together increase the energy efficiency,[11] but also for the possibility to enrich the already existing natural gas feeds with biogas[12–15] or with the so-called green hydrogen, produced with renewable energies for a further reduction of CO_2 emissions[16,17]. In particular the possibility to blend natural gas with

hydrogen is not only an advantage for natural gas sustainability, but it has a key role on the insertion of the same hydrogen produced by renewable energy, prospected to become economically advantageous in the next decades.[18,19].

The substitution of fossil fuels with natural gas is interesting not only in the field of energy production, but also for transportation, which is among the major sources of greenhouse gases, as shown in Figure 1-3, and with an increasing impact from the developing economies.[20]

Since transportation is strongly linked with people's way of life, it is also one of the main discussed and controversial fields dealing with global warming. The marketing appeal of sustainability created many misunderstandings around vehicles impact, which often hides the real environmental perspectives.[21] Many alternative vehicles appeared in the market to reduce the carbon footprint in the last years. Now, the list is headed by electric vehicles. They do not directly produce emissions, being particularly good for city transportation[22]. Their indirect emissions depend on the energy mix used to charge them and so their environmental convenience must be referred to the situation explained in Figure 1-4. On the opposite, they have a considerable production footprint since they need a great amount of Li-ion batteries that, in this particular moment, can reduce their appeal compared to other alternative vehicles[23,24]. Moreover, having intrinsic problems with weight and autonomy, it is hard if not impossible to design proper solutions in the case of freight transportation at the state of art[25,26]. In a long-term vision, they surely represent a valid option, especially for city transportation, but they cannot be the only solution when thinking at the efficient transition mentioned above.

As for the case of energy conversion, the switch to natural gas usage offers a versatile solution in the direction of CO_2 reduction, for both passengers and freight transportation. They can follow the expected increase of spark ignition engines due to diesel restrictions[27,28] and take advantage of the progressive substitution with biogas and hydrogen produced by renewable sources to furtherly improve the CO_2 balance[29].

Natural gas is mainly composed of methane which is a very stable molecule that, due to his low electron affinity and high C-H bond energy activation, needs high temperatures (>1600K) or a very effective catalyst to be oxidized[30]. This means that the thermal conversion in the engine is always followed by NO_x production and uncomplete or partial conversion close to the coldest part of the engine chamber, i.e. unburned hydrocarbons, and CO[31]. In line with main thermal engines, also natural gas fueled vehicles need a proper aftertreatment, particularly effective to remove the unburned

CH_4. Indeed, besides being very stable, methane has a global warming potential 25 times higher than CO_2 in a 100-year time window[32]. For this reason, the advantage of the highest H:C ratio, which brings to lower CO_2 production, might be suppressed by methane emission in the atmosphere[33,34,35] making NGVs a promising transitional option but needing proper aftertreatment equipment.

1.2 NGV aftertreatment

The temperatures at the tailpipe of NGVs do not overcome 1000K so a very effective catalyst is needed as mentioned[30]. Despite the different typologies of engines that exploit natural gas, the most commonly used in vehicles is a spark ignited engine[36,37]. The exhaust gases pass through a honeycomb cylindric monolith coated with the catalyst. Coupled with closed-loop control, the conditions are maintained around a stoichiometric combustion window to reach the proper composition in the aftertreatment for the simultaneous oxidation of C-containing compounds and the reduction of nitrogen oxides[38]. This is possible thanks to the superimposition on the monolith of layers of oxidation and reduction catalysts. The technology is now well established and is known as three-way catalyst or TWC. The application is close to that of gasoline aftertreatment, with the additional difficulty to oxidize methane reflected in a higher amount of oxidative catalyst on the TWC (>200g ft^{-3})[36]. Moreover, the interaction of CH_4 and the other pollutants has not been studied and understood as well as in the case of unburned hydrocarbons in gasoline application. It is then fundamental to design new catalysts containing a lower amount of metal, since out of technical discussions the metal price of precious metals such as palladium and platinum is extremely high (see Figure 1-6).

Among the metallic catalysts, palladium is the most active material towards methane oxidation[39–42]. Due to the complexity of the exhaust atmosphere and the reaction mechanisms involved, the identification of the real active sites under operating conditions is not straightforward[43]. It is widely recognized that a Mars-van Krevelen mechanism is involved, with an important role of both CH_4 and O_2 surface coverage, the adsorption of CH_4 and its dissociation to CH_3 being the rate-determining step[44, 45]. It is well known that the valence of Pd is pivotal in the CH_4 dissociation to CH_3[46] and studies suggest that CH_4 is efficiently oxidized by PdO, or more specifically by a mixture of Pd oxidized species. [47–50] Some studies suggest that also the presence of metallic Pd can be beneficial for the catalysis at low temperatures[51,52]. Certainly PdO is the most active phase at high temperature, however it decomposes to metallic Pd above 973 K leading to an activity loss[53]. Another important factor when dealing with Pd-based catalysts for methane abatement in the aftertreatment of NGVs is the presence of water[54]. In stoichiometric conditions, it participates in the conversion of CH_4 through steam reforming[55,56]. In lean conditions, the fundamental exchange of oxygen species between the support and the active sites is limited by the reaction of chemisorbed

oxygen with water[57]. Hydroxyl groups are formed, which inhibits the interaction with CH_4[58]. This happens mostly at low to medium temperatures (<723K) and even if the deactivation is reversible, it can enhance Pd sintering which is not[59–61]. In Figure 1-5 it is reported the normalized rate of CH_4 conversion over time in a typical time-on-stream test in lean conditions and in presence of water. The conversion, normalized to the initial value, is visibly decreasing over time due to catalyst deactivation.

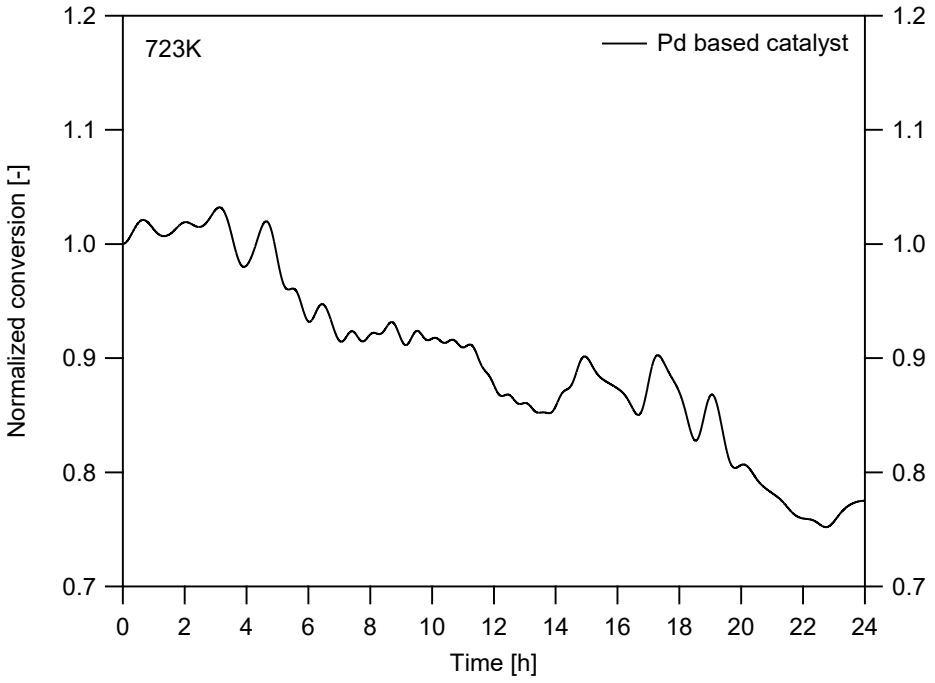

Figure 1-5: normalized conversion of methane in a time-on-stream experiment in wet atmosphere at 723K on a Pd based catalyst.

To improve the stability of Pd-based catalysts, the oxygen mobility between active sites and the support can be improved by using CeO_2 as support[62]. CeO_2 is widely used in TWC as an oxygen storage material thanks to its capability to switch between oxidized and reduced states.[63] This property has been exploited also for the stabilization of PdO at high temperature[47,64].

Another possibility investigated for increasing catalyst stability is the association of palladium with a second metal. For example, despite having a lower activity than Pd, the addition of Pt to Pd-based catalysts has been found to improve the dispersion of active sites[65], the thermal stability[66] and oxygen mobility[67]. The composition plays a major role on the characteristics of the final bimetallic catalyst[68] and the influence of several other parameters has been investigated[51,66,69]. At the same time, there is no general agreement on whether bimetallic catalysts are better than Pd single catalyst[70,71] and the possible alloy formation between the two metals and its role on methane

conversion is still debated[72–75]. Despite these discrepancies, the researchers agree on the fact that the bimetallic catalyst is more stable than the monometallic formulation, especially considering the effect of the presence of water.[66,76–79]

From a bare industrial point of view, also the price of the two metals should be considered, which is pivotal in the composition choices. In Figure 1-6 the price of Pt and Pd in the last 10 years and the relative Pt-to-Pd price ratio are reported. The horizontal line fixes the ratio at 2 below which the cost optimum is achieved only by bimetallic systems, with a different Pt content[80]. Moreover, Pt and Pd are mainly used in automotive after-treatment and their price is set by the vehicle's demand. Pt is mostly used in diesel vehicles aftertreatment while Pd in gasoline ones. Since the latter are considered to increase and substitute diesel vehicles, the same can be expected for Pd and Pt[81,82]. Thus, a stable convenience for bimetallic Pt-Pd solutions in the next years for TWC application is estimated, making them even more attractive also for NGVs applications.

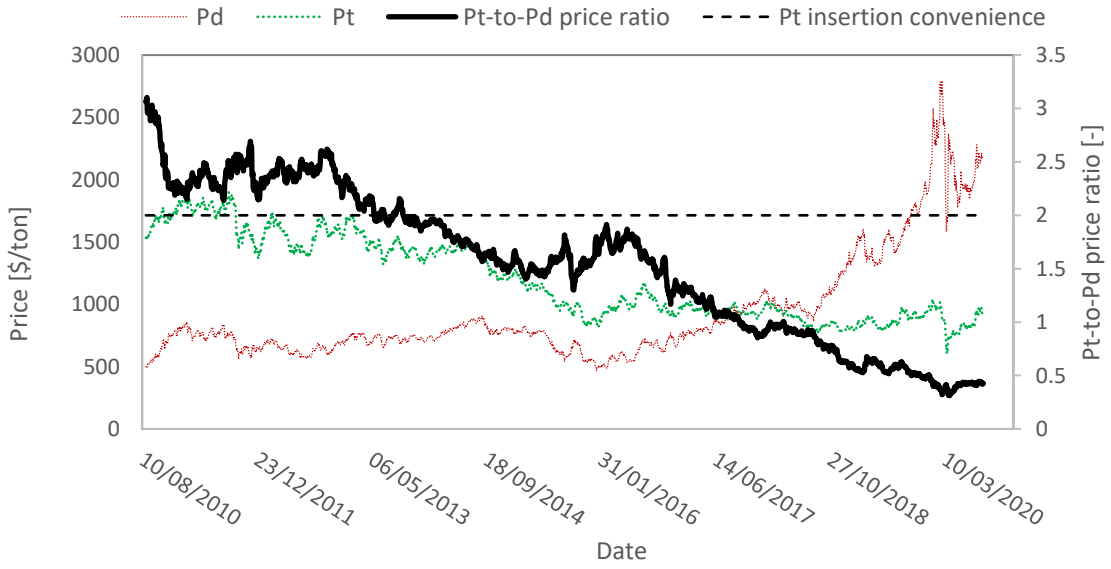

Figure 1-6: Platinum and palladium prices and their Pt-to-Pd price ratio. Sources: Umicore.

Apart from these generic predictions and considering the higher amount of PGM material requested in natural gas vehicles TWC system, the platinum substitution could not be enough to compensate for the palladium price increase. In these terms, several cheaper substitutions for bimetallic Pd-based catalysts were studied[83]. The formation of an intermetallic compound with gallium was found to be beneficial towards Pd sintering

and water stability[84]. Nickel was found to influence the surface electric environment destabilizing oxygen species turning in higher activity. Gold can reduce PdO decomposition at high temperatures[85]. Cobalt[86,87] and tin[88] are found to increase palladium dispersion and overall oxygen mobility, thus improving methane catalytic activity. The synthesis of such bimetallic systems is often complex requiring great amounts of solvents and thermal treatments. Once more, these aspects contrast the direction of the efficient transition prospected at the beginning. An organic approach should thus be developed that considers all the life of the catalyst, from production to disposal.

Keeping in mind the above mentioned issues, this work is aimed at exploring the possibility of synthesizing active and stable bimetallic catalysts containing Pd for NGVs applications. In order to meet the efficient transition requirements, i.e. a more sustainable catalyst lifecycle, the mechanochemical route has been exploited for catalyst preparation, avoiding the use of solvents and thermal treatments.

1.3 Mechanochemical synthesis

Mechanical milling is a widespread technique used in all the industries that deal with solid processing, from raw materials extraction to fine chemicals production, such as pharmaceutical ones. It is the simplest process involved in the control of particle size and mixing of solids, and the only one practicable without liquid carriers or at least with reduced amount of solvents. Mechanical energy is mainly exploited to break particles and homogenize the powder system, but despite the simple concept, it is difficult to model the mechanical dynamics involved in a mill[89–93]. It becomes even more complex when the mechanical energy is not only exploited for the breakage of particles, but also to induce particular chemical reactions between the different solid phases [94–98]. This is what is referred to as "mechanochemical synthesis", or "mechanochemistry" [99,100]. Due to its easiness and the possibility to avoid solvents, mechanochemistry is currently widely investigated for the solid synthesis of novel materials [101–110]. Figure 1-7 shows, in grey, the number of publications per year in the period 1990-2020 that include "mechanochemical synthesis" either in the title, in the abstract, or in the author keywords.

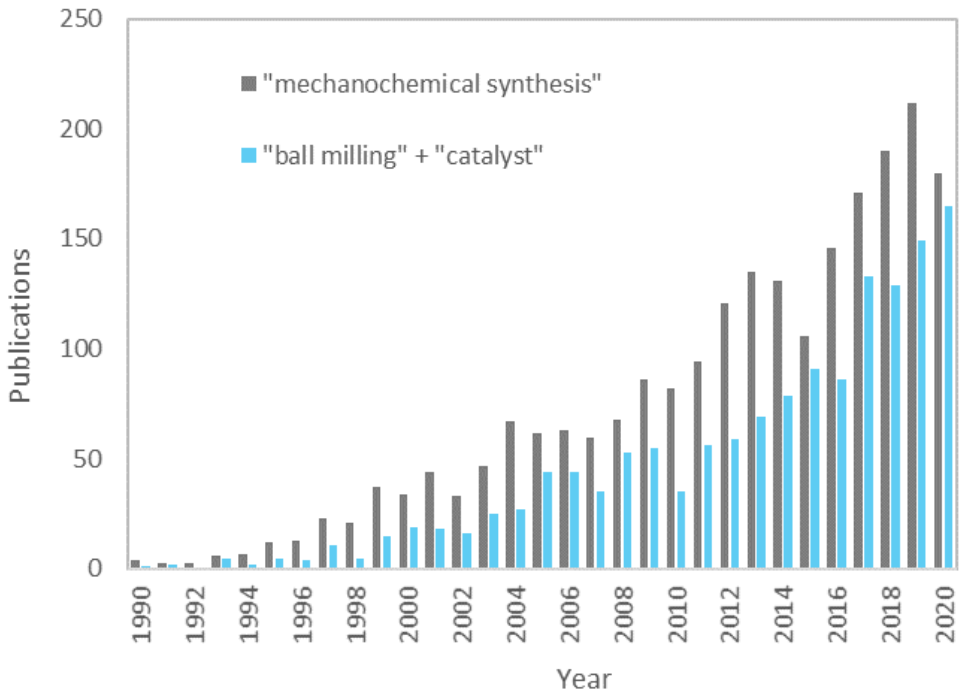

Figure 1-7: number of publications per year searching "mechanochemical synthesis" (grey) or "ball milling" and "catalyst"(light-blue) on Scopus (results on 1.10.2020).

To understand the potentiality of this synthesis, just think that for research purposes it can be carried out manually using a mortar. However, a systematic approach needs the application of reproducible parameters and thinking about microscale and nanoscale interactions ball milling is the main choice[95]. In ball milling the powder is grounded inside a jar together with grinding spheres. Both the jar and the spheres are usually made of hard materials such as zirconia, alumina, or hardened stainless steel, the choice of the material depending on the solids involved and on the final application of the resulting powder in order to avoid contamination between the jar, the balls and the product. In general, the hardness of the milling means should be higher than that of the powder involved. The mill gives the jar a controlled movement that develops a series of mechanical impacts between spheres, powder and jar walls. The direction and intensity of the impacts depend upon the type of mill. For example, rotatory mills simply rotate the jar, in vibratory mills the jar undergoes small and frequent vertical vibrations, planetary mills combine two rotation movements to exploit centrifugal forces and shakers combine linear and circular trajectories for the jar. In all these configurations, it is possible to vary the number and the size of the spheres and the amount of material to grind. These parameters are usually known as ball-to-powder ratio and, together with the type of mill, the milling frequency (rotations or vibrations per unit of time) and the milling duration, define the milling process. Overall, the amount of energy given to the powder system depends upon all these factors, and usually the processes can be classified as high energy milling or low energy milling. Again, despite the simple mechanics of the system, many parameters affect its dynamics, and the issue is even more important when dealing with chemical reactions taking place among solid phases during milling.[111–114]

The advantage of exploiting mechanical energy in chemical synthesis is to avoid thermal pathways and, possibly, the use of solvents generally employed in conventional synthesis procedures. This allows overtaking the thermodynamic equilibrium of crystalline phases and multi-component alloys, bringing to metastable phases with advantageous properties[115,116]. These aspects have been recently exploited for the successful preparation of novel metal-supported catalysts with better performances than the traditional ones [117–122]. Unfortunately, the lack of theoretical modeling of the ball milling process for chemical synthesis does not allow a systematic optimization, reducing the study to a trial-and-error approach. In the catalysis field, this is especially time consuming since each trial needs catalytic tests and an important effort on

characterization. However, the promising results of this application in catalyst preparation are pushing the research in this direction, as inferred from Figure 1-7, where the trend in the number of publications per year that contains the combination “ball milling” and “catalyst” in the title, in the abstract or the author keywords is reported.

In the end it is worth highlighting that, apart from the unquestionable advantages of a simple and effective synthesis, the possibility to avoid solvents implies the reduction of chemical waste to almost zero. This is in line with the very recently issued EU Chemicals Strategy towards a Toxic-free Environment that aims at the replacement of hazardous chemicals with eco-friendly, sustainable ones[123], and with the first principle of the so-called “Green Chemistry” which indeed promotes the reduction of chemical waste.[124] Moreover the solvents used in traditional synthesis are often hazardous ones, so that the mechanical synthesis is safer for the environment, but also for the operator who deals with it. Last, mechanical energy is exploited, the most valuable form of energy, and at the same time thermal energy is avoided, the least valuable. This turn into an important saving in the optic of industrial scale, especially in the production of catalysts. The mechanochemical synthesis reflects then all the future expectations by industry, being safer, efficient and sustainable.[125]

1.4 Scope of the work and outline

Recently, our research group developed a mechanochemical procedure to prepare Pd/CeO_2 catalysts starting from Pd and ceria powders, giving rise to particular Pd shell-CeO_2 core arrangements that are highly active for catalytic methane oxidation [126]. It was found in particular that only low energy milling was effective.[127] In fact, after a first approach in which manual grinding was carried out in an agate mortar, the synthesis was successfully implemented in a low energy vibratory mini-mill Pulverisette 23 (Fritsch). The mill, used also in this work, is shown in Figure 1-8 together with a simple scheme of its movement. In this setup it is possible to change the vibration frequency and the time of the process so ultimately the energy released in the synthesis. With this setup it is possible to produce about 1 g of material for each run.

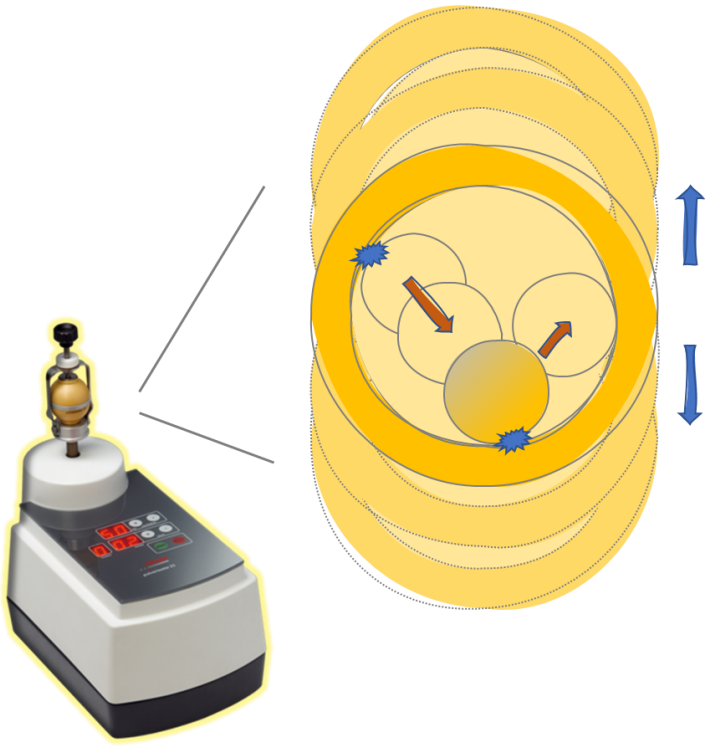

Figure 1-8: mini mill Pulverisette 23, Fritsch, and jar-ball movement scheme.

To increase the amount of catalyst prepared for each synthesis, as required for example for the preparation of structured catalysts which have also been tested in my research work, a scale-up of the synthesis has been implemented. This has been carried out with a planetary mill Pulverisette 6 (Fritsch), shown in Figure 1-9 with a schematic picture of its dynamics. The jar and its support rotate in two different directions generating variable centrifugal forces on balls and powder. For a defined set of balls (number and size), the amount of energy was controlled by the frequency of rotation and time of the process. With this mill up to 10 g of materials for each run have been prepared.

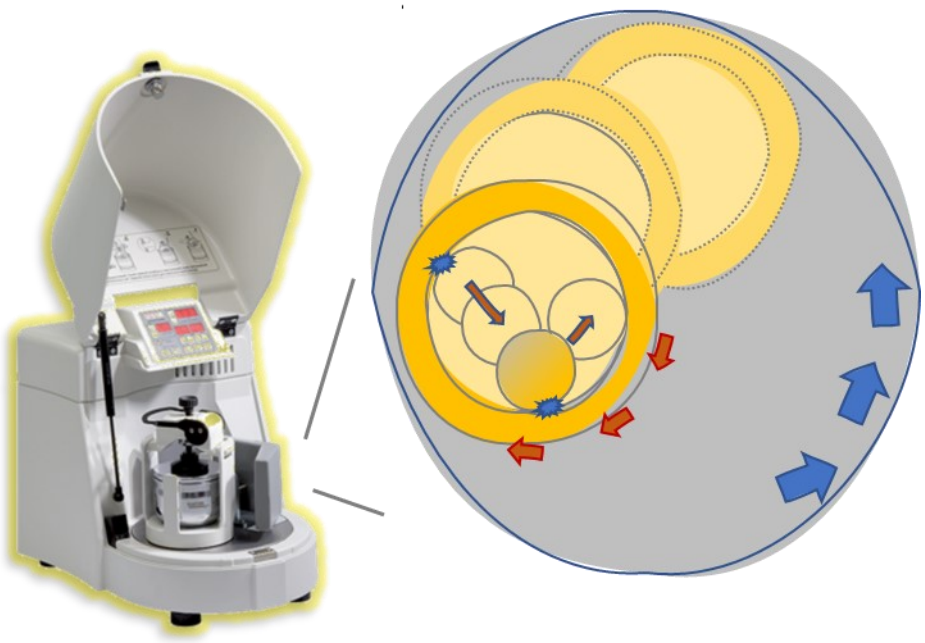

Figure 1-9: planetary mill Pulverisette 6, Fritsch, and jar-ball movement scheme.

Both Pulverisette 23 vibratory mill and Pulverisette 6 planetary mill have been used to investigate the effect of the insertion of Pt into the Ce-Pd core-shell configuration mentioned above, extending the study to a structured Pd-CZ catalyst formulation that has been tested in collaboration with Umicore Automotive Catalysts R&D Department in a close-to-real application. The bimetallic Pt-Pd catalysts have been studied for lean methane oxidation also in wet atmosphere during time-on-stream experiments, and to better understand the catalytic results, they have been characterized with the help of *in*-situ syncrothron techniques at the ALBA synchrotron beamline in Barcelona. The addition of Sn and In as substituents instead of Pt in the same Pd-Ce arrangement was also investigated. Moreover, the optimization of the milling process carried out specifically for methane oxidation led to a study of the CO oxidation reaction for the best catalysts formulated for methane oxidation.

2. Experimental

2.1 Samples preparation

The mechanical synthesis was optimized by a trial-and-error approach. Apart from the work developed with Umicore Automotive Catalysts R&D Department that required a preventive scale up study and a different approach, see Chapter 6, p.84, all the syntheses were carried out in the same vibrating ball mill Pulverisette 23 mentioned in Chapter 1 (Figure 1-8), adapting a previously reported procedure[126]. It was chosen to reduce the number of variables involved and assess the catalytic effect of small changes. The first one was the ball-to-powder ratio, fixed at 10:1. A single ball (ZrO_2, 15mm diameter, Fritsch) was used in a zirconia grinding bowl (ZrO_2, 15ml, Fritsch) and the material produced per synthesis was set to 1g. The energy transferred to the jar, and ultimately to the mixing system, depends, in vibrating mills, on the vibrating frequency and the milling duration. It was decided to fix the frequency at 15Hz for all the syntheses, with the energy released being dependent only on the milling time.

The synthesis was carried out with dry precursors, as indicated in Table 2-1, where the list of materials and support oxides involved is reported.

Another important parameter was the metal composition. It was varied and explored in the case of the preliminary Pt-Pd study reported in Chapter 3 but fixed for the others. More details will be given in each dedicated chapter.

For every metal involved a monometallic sample was prepared in a one-step milling synthesis and a bimetallic sample, in combination with Pd, in a two-step milling run. In the latter case another parameter was considered, which is the order of metal insertion during milling. It was decided to separate the metal insertion in the jar, starting from the idea of adding a second metal to the already studied one-step milled Pd/Ce sample[126]. In other words, the second metal was added with a further second milling step to an already mixed powder of Pd and Ce. This defined what was called “order of milling”, which was considered as an interesting parameter and explored preparing also samples with Pd added as last component instead of first one.

Table 2-1: list of materials prepared with corresponding Chapters.

Metal	**Metal precursor**	**Support oxide**	
Pd Pt	Pd black, Sigma Aldrich Pt black, Sigma Aldrich, ≤20µm	CeO_2, Treibacher Industrie, AG	Chapter 3,4
Pd Sn In	Pd black, Sigma Aldrich Tin(II)Acetate, Sigma Aldrich Indium III nitrate hydrate, Sigma Aldrich, 99.999%	CeO_2, Treibacher Industrie, AG	Chapter 5
Pd Pt	*details in Chapter 6		
Pd Pt	Pd black, Sigma Aldrich Pt black, Sigma Aldrich, ≤20µm	CeO_2, Umicore	Chapter 7

Apart from the different metals, two different CeO_2 supports were involved, one provided by Treibacher Industrie and he second one, used only for the studies of CO oxidation, provided by Umicore AG&Co.KG.

Starting from the addition of a second metal in the sample Pd/Ce, every further change in compositions, precursors or in the order of milling was weighted by assessing the catalytic activity and characterizing the materials. An overview of the setups involved in catalyst testing and characterization will be given in the next paragraphs.

2.2 Characterization

The adjustment and optimization of the mechanochemical synthesis to bimetallic catalyst formulation was followed with different characterization approaches in order to correlate structural, textural and redox properties to the catalytic activity. The fundamental physicochemical properties of the samples were investigated by means of surface area measurements and X-ray diffraction (XRD) analysis. The surface area was measured according to Brunauer-Emmett-Teller (BET) theory following N_2 adsorption isotherms at 77 K in a Micromeritics TriStar Porosimeter. Before nitrogen adsorption, ca. 250 mg of catalyst powder was degassed in vacuum at 423 K for 90 minutes to desorb humidity and weakly adsorbed species. Figure 2-1 shows the Micromeritics Tristar 3000 equipment together with an example of N_2 adsorption isotherm.

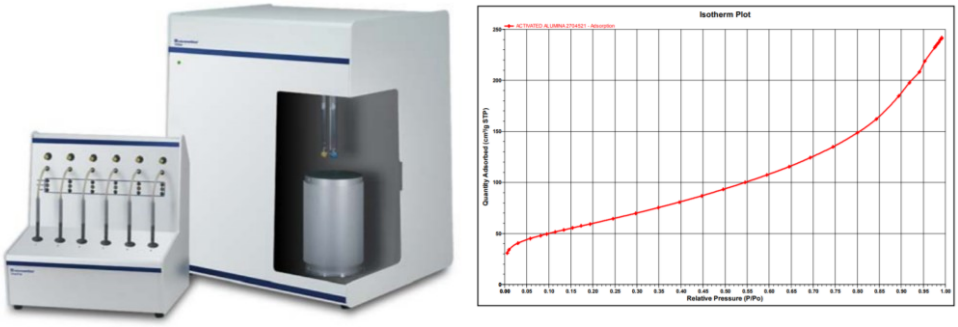

Figure 2-1: Micromeritics Tristar 3000 equipment with an example of adsorption isotherm

XRD patterns were collected in a Philips X'pert diffractometer (Figure 2-2) equipped with an X'Celerator detector using Cu-Kα radiation (λ = 1.542).

Figure 2-2: Philips X'Pert diffractometer with X'Celerator detector.

Data were generally recorded first in the 2θ range of 20-100° with a step size of 0.02° and a counting time per step of 40s. A second set of measurements was carried out in the 2θ range of 32-48° with a step size of 0.02° and a counting time per step of 320s to get more precise information on Pd species.

Redox properties of samples were studied by temperature programmed tests in reducing (Temperature Programmed Reduction, TPR) or oxidizing atmosphere (Temperature Programmed Oxidation, TPO). TPR measurements were carried out in a Micromeritics Autochem II 2920 apparatus (Figure 2-3).

Figure 2-3: Micromeritics Autochem II 2920 and Micromeritics Cryocooler

A U-shaped quartz reactor was loaded with 50 mg of catalyst on a quartz wool bed and brought from 193 K to 1173 K at a heating rate of 10 K/min. The starting temperature was reached by pumping liquid nitrogen in the furnace with a Micromeritics Cryocooler. The gas flowrate (4.5% H_2 in N_2) was set to 35 ml/min. The measurements were carried out on both as prepared and pre-treated samples. For the second option, the catalysts were treated at 623K for 1h in flowing air, then cooled to 193 K before starting the reduction. TPO experiments were carried out in the same setup used for catalytic tests by loading the reactor with 150 mg of catalyst. The gas flowrate (2% O_2 in N_2) was set at 60 ml/min. Three heating/cooling cycles were performed from room temperature up to 1273 K at a rate of 10 K/min. The oxygen uptake and release were monitored with an online ABB Magnos 106 paramagnetic analyzer.

The most interesting PtPd samples were characterized also by high-resolution transmission electron microscopy (HRTEM) thanks to the collaboration with the Institute of Energy Technologies and Department of Chemical Engineering at the Universitat Politècnica de Catalunya in Barcelona. HRTEM analysis was carried out at

200 kV with a JEOL JEM-2010F electron microscope equipped with a field emission gun. Analogous samples were also analyzed in CLÆSS beamline at the synchrotron facility of ALBA CELLS in Barcelona (Figure 2-4).

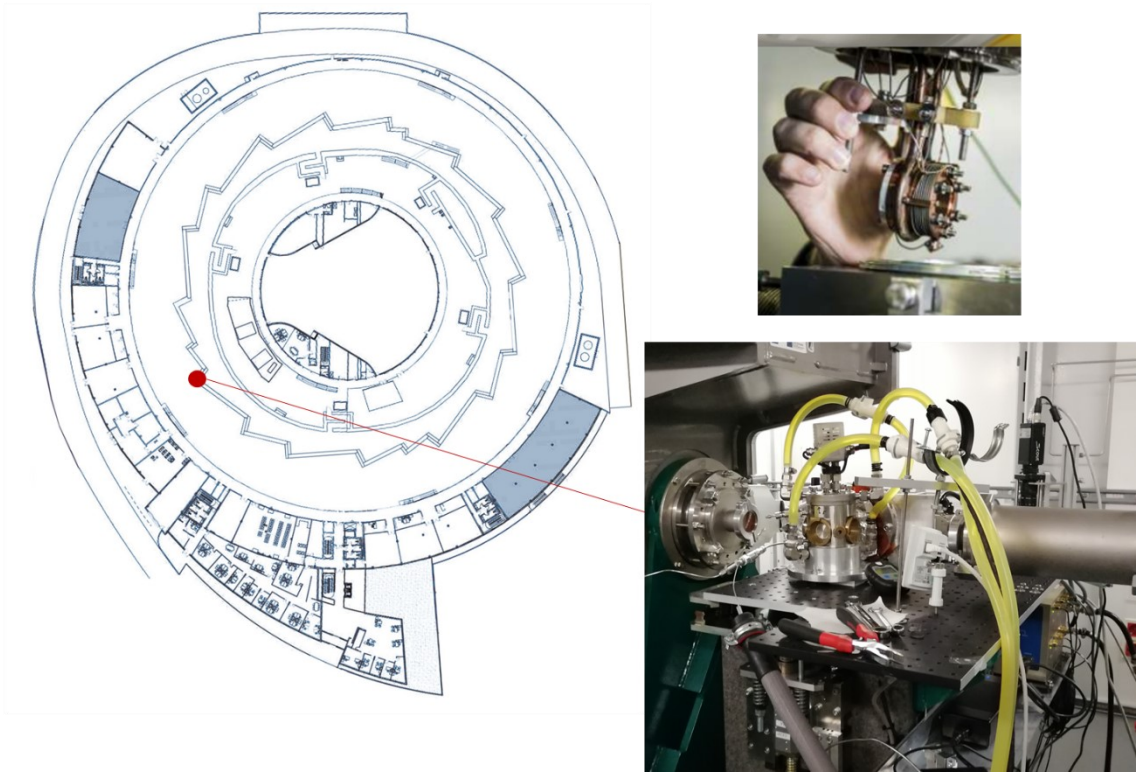

Figure 2-4: CLÆSS beamline at the synchrotron facility of ALBA CELLS in Barcelona and detail of the in-situ experimental setup

The energy range selectable by CLEAR spectrometer is 6.4-12.5 keV. The sample set-ups give access to low/high-temperature (300K-923K), low/high-energy measurements (in transmission and fluorescence mode), "in situ" solid-gas reactors. Continuous energy scanning for quick scans was available, allowed to collect X-ray absorption near edge structure.

2.3 Catalytic activity

2.3.1 Setup

The scheme of the synthetic gas bench setup for powder tests is reported in Figure 2-5. A quartz tubular reactor was placed in a temperature programmed furnace and a K-type thermocouple was inserted close to the catalyst bed.

It was possible to set, through the furnace controller, the temperature ramp rate and time dwells at fixed temperatures. A set of Brooks mass flow controllers (MFC) provided the right flow of each gas. It was possible to feed CH_4, CO, H_2, O_2 and He as balance carrier.

For the tests in wet atmosphere, an HPLC pump provided a flow of deionized water which was then evaporated by heating tapes to obtain an additional flow of steam. The outlet gas was condensed in an AGT MAK 20 sample gas cooler before entering in an online ABB gas analyzer for continuous gas composition and temperature monitoring. The analyzer is equipped with an Uras 14 infrared module to measure CH_4, CO and CO_2 concentration and a Magnos 106 paramagnetic analyzer to monitor oxygen concentration.

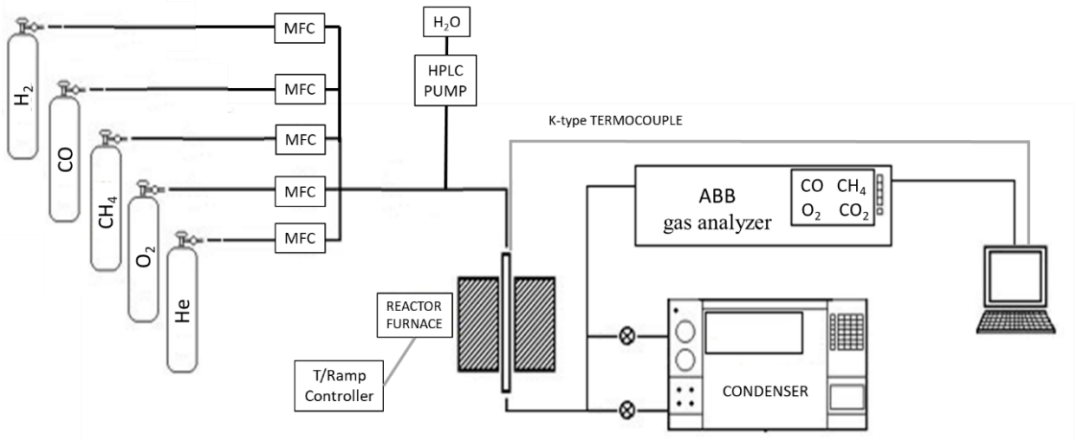

Figure 2-5: scheme of experimental setup for powder tests

2.3.2 CH_4 oxidation

Temperature programmed combustion (TPC) and time-on-stream (TOS) experiments were carried out at atmospheric pressure in a quartz tubular reactor, loaded with 120 mg of catalyst powder supported on a quartz wool bed. The total flow rate was set at 180

ml/min, corresponding to a GHSV of about 180'000 h^{-1}. The gas inlet composition was 0.5 vol% CH_4 and 2 vol% O_2 in He (dry atmosphere). For the tests in wet atmosphere, the HPLC pump provided a flow of 10 vol% of steam in the feed gas.

TPC tests in dry conditions (TPC dry) consisted of heating/cooling cycles from room temperature up to 1173K and back, with a ramp rate of 10K/min. If not otherwise specified, for TPC dry experiments the second light-off cycle is shown in the Figures, as it represents the steady state behavior of the catalyst after the first heating/cooling that can be considered a sort of activation.

For TPC experiments in wet atmosphere (TPC wet) and for the time-on-stream tests (TOS), the samples were pretreated with one dry cycle up to 1173 K. In wet TPC tests, after the dry pre-treatment 10 vol% of water was fed to the reactor and two light-off cycles were carried out up to 1173 K, followed by another cycle in dry atmosphere to check the reversibility of water deactivation. Time-on-stream experiments were carried out in dry (TOS dry) and wet atmosphere (TOS wet) by raising the temperature up to 723 K after the pretreatment and keeping it constant for 24 hours. For TOS wet experiments, the temperature was first raised up to 453 K then water was introduced in the feed.

Methane conversion was calculated as:

$$\%X_{CH_4}(T,t) = \frac{[CH_4]_{in} - [CH_4]_{out}}{[CH_4]_{in}} \times 100$$

where $[CH_4]_{in}$ and $[CH_4]_{out}$ are the inlet and outlet methane concentration, respectively. The conversion is a function of temperature during TPC tests (the temperature ramp being constant and set at 10 K/min), and function of time during TOS experiments at constant T.

In the case of TOS experiments, also a normalized conversion was calculated:

$$\mathrm{N}[\%X_{CH_4}(T = 723K, t)] = \frac{X_{CH_4}(t)}{X_{CH_4}(t=0)}$$

where t=0 is the beginning of the 24h TOS test.

2.3.3 CO oxidation

Bimetallic PtPd samples were tested also for CO oxidation chosen as a model reaction and for its implications in the abatement of the exhausts from natural gas fueled

vehicles. Light-off tests (LO) were carried out at atmospheric pressure in a quartz tubular reactor loaded with 20 mg of catalyst powder mixed with 80 mg of quartz beads (200 μm), and supported on a quartz wool bed. The mixing with inert quartz beads was used to avoid hot spots, and the ratio between catalyst and beads was selected according to the literature for CO oxidation experiments carried out in similar conditions.[128] The total flow rate was set at 100 ml/min, corresponding to a GHSV of about 600'000 h^{-1}. The gas inlet composition was 0.4 vol% CO and 10 vol% O_2 in He.

LO tests consisted in a single heating ramp from room temperature (RT) up to 523 K, the temperature ramp being constant and set at 2 K/min.

Carbon monoxide conversion was calculated as:

$$\%X_{CO}\ (T)\ =\ \frac{[CO]_{in} - [CO]_{out}}{[CO]_{in}} \times\ 100$$

where $[CO]_{in}$ and $[CO]_{out}$ are the inlet and outlet carbon monoxide concentration, respectively.

Two different reducing pretreatments were also considered: the first with CO as the reducing agent (2 vol% CO in He), and the second using hydrogen (4.5 vol% H_2 in N_2). Both treatments were carried out by increasing the temperature from RT to 523 K, with a ramp of 10 K/min, and holding for 5 minutes before cooling.

3. The effect of the addition of platinum on Pd/CeO_2 catalysts prepared by dry milling for methane oxidation in presence of water

Abstract

Pt is used as a partial substituent in Pd/Ce catalysts prepared by mechanical synthesis for the oxidation of methane in wet atmosphere. Both light-off and time-on-stream catalytic tests were carried out to evaluate the activity and stability of the catalysts. HRTEM characterization highlighted the importance of the contact between Pd and ceria in the formation of an amorphous Pd-Ce layer which has been indicated as fundamental to obtain high catalytic activity. Moreover, the formation of mushroom-like structures with a platinum head and a palladium oxide foot have also been detected after the treatment with methane and water, which were then related to the higher stability of PtPdCe milled samples.

*submitted to **ACS Applied Materials & Interfaces** as "Structural evolution of bimetallic $PtPd/CeO_2$ methane oxidation catalysts prepared by dry milling"; authors: Andrea Mussio, Maila Danielis, Núria J. Divins, Jordi Llorca, Sara Colussi, Alessandro Trovarelli.

3.1 Introduction

Pd based catalysts are known as the most active catalysts for the oxidation of methane[39,41], which is an important reaction occurring in natural gas vehicles (NGVs) aftertreatment for the reduction of hydrocarbon emissions. Many studies on this topic were performed in dry conditions to find out mechanisms, kinetics and active sites, even if the real application is a process taking place in wet atmosphere, water being present in 5 to 10 vol% in the exhaust gases of NGV engines[36]. Indeed, at the operating temperatures reached by the aftertreatment modules water affects notably the conversion of methane on Pd-based catalysts[54,36,129]. Different mechanisms have been

proposed in the literature for this deactivation, including the formation of $Pd(OH)_2$ inhibiting the interaction between CH_4 and the active sites[130,131] and the suppression of the fundamental oxygen exchange between palladium species and the support[58,132]. These two phenomena are supposed to take place at medium to low temperature (< 773 K) and are usually reversible, whereas sintering, which is found to be enhanced by water, takes place at higher temperature and is irreversible [54,132]. One of the possible strategies to improve the resistance of Pd-based catalysts in wet atmosphere is the addition of Pt[133, 65, 134, 135, 136, 137].

The significant amount of research on PtPd bimetallic systems has clearly established the beneficial role of Pt introduction on the stability of Pd-based catalysts during time-on-stream operation and against poisoning [65,137–141], whereas the effect on the transient activity during light-off experiments is still debated, with some authors observing an improvement for specific Pt:Pd ratios[142–146] and others concluding that the presence of Pt is generally detrimental for transient operation [65, 71,138,]. The discrepancies often arise from different experimental conditions and/or catalyst pretreatment before testing. The effect of support is seldom considered, high attention being paid preferentially to the mutual interplay between palladium and platinum that seems the key to tune the catalytic performances of PdPt bimetallic catalysts[65,72,74,137,147,148].

Our group recently developed a novel strategy to prepare Pd/CeO_2 catalysts by a one-step dry milling procedure.[126] An outstanding activity for methane oxidation was observed and attributed to the strong palladium-ceria interaction obtained at nanoscale during milling of Pd and CeO_2 powders[149]. The synthesis allows to obtain better catalytic performances than in the case of traditional impregnated catalysts due to a particular arrangement between metal and support at the nanoscale. This solvent-free preparation method, in fact, determines the type and distribution of palladium active species on the surface, which are substantially different from those obtained by incipient wetness impregnation.[149] The idea was then to exploit the potential of the mechanochemical route to prepare bimetallic PdPt catalysts with enhanced metal-metal interaction which could improve the stability of milled Pd/CeO_2 in presence of water.

Pt black nanopowder was mechanically supported on ceria together with palladium with different Pt:Pd ratios. The obtained catalysts were tested for lean methane oxidation in transient and in time-on-stream experiments, both in dry and wet (10 vol% H_2O) atmosphere, and characterized by x-ray diffraction (XRD) analysis, temperature programmed reduction (TPR) and oxidation (TPO) and high resolution transmission

electron microscopy (HRTEM). The results show unambiguously that a deep restructuring takes place between Pd and Pt during operation, and at the same time prove the effectiveness of the mechanical milling to prepare highly stable bimetallic PtPd/CeO_2 catalysts.

3.2 Material and methods

Pure cerium oxide (CeO_2, Treibacher Industrie, AG) previously calcined at 1173 K for 3 hours was used as support for the catalysts. Metallic palladium (Pd black, Sigma Aldrich, surface area 40-60 m^2/g) and metallic platinum (Pt black, Sigma Aldrich, ≤20μm) nanopowders were mechanically mixed with CeO_2 in a Mini-mill Pulverisette 23 (Fritsch). All the samples were prepared in two separate steps, starting by milling palladium with cerium oxide, followed by the insertion of platinum. Each step lasted 10 minutes and the oscillation frequency was set to 15Hz. The samples were named (1-X)PtXPdCe M, where X is the wt% of Pd. The name of the samples highlights the addition of platinum to an "XPdCe M" sample. Different mass ratios m^{Pd}/m^{Pt} were considered while keeping the total PGM amount constant at 1 wt%. For comparison purposes, further two bimetallic samples with $m^{Pd}/m^{Pt} = 1$ were prepared to evaluate the effect of the milling procedure. The first one was prepared by inverting the order of the metals in the mechanical synthesis, firstly preparing a 0.5% Pt Ce M and then introducing 0.5wt% of Pd (0.5Pd0.5PtCe M). The second one was prepared by conventional incipient wetness impregnation (0.5Pt0.5PdCe IWI): cerium oxide was impregnated with a Palladium nitrate solution (4.8% of Pd, Sigma Aldrich), dried overnight at 393K, then subsequently impregnated with a solution of tetramine platinum nitrate. The resulting catalyst was dried overnight and calcined in air for 3 hours at 1173K. All samples, with relative name and composition, are summarized in Table 3-1. Characterization and catalytic tests were carried out according to what previously described in Chapter 2.

Table 3-1: Composition, mass and molar ratios, and names of samples considered in this work.

Sample NAME	Nominal Pt wt%	Nominal Pd wt%	m^{Pd}/m^{Pt}	Pd/Pt molar ratio
0.8Pt0.2PdCe M	0.8	0.2	0.25	0.46
0.65Pt0.35PdCe M	0.65	0.35	0.53	0.99
0.5Pt0.5 PdCe M	0.46	0.47	1	1.83
0.2Pt0.8PdCe M	0.2	0.8	4	7.33
1PdCe M	/	1	/	/
1PtCe M	1	/	/	/
0.5Pd0.5PtCe M	0.5	0.5	1	1.83
0.5Pt0.5PdCe IWI	0.5	0.5	1	1.83

3.3 Results and discussion

3.3.1 Catalysts characterization

Specific surface area of each sample is reported in Table 3-2. CeO_2 support has a low surface area (3.0 m^2/g) due to the high temperature of calcination (1173 K). This value is only slightly affected by the addition of the metals and the mechanical mixing process, both in the case of monometallic and bimetallic samples. For all samples surface area is comprised from 3.0 to 4.0 m^2/g. The choice of a support with low surface area was carried out on the basis of our previous studies on Pd/CeO_2 monometallic catalysts, from which it resulted that the best catalytic performance was achieved on low surface area ceria when using Pd metal as precursor[149].

Table 3-2: BET surface area of all samples

Sample	BET [m^2/g]
Ce	3
0.8Pt0.2PdCe M	3.6
0.65Pt0.35PdCe M	3.6
0.5Pt0.5PdCe M	4
0.2Pt0.8PdCe M	3.2
1PdCe M	3.2
1PtCe M	3.3
0.5Pd0.5PtCe M	3.5
0.5Pt0.5PdCe IWI	3.3

The x-ray diffraction profiles of the fresh samples in the 32°-48° 2θ range are reported in Figure 3-1. Beside the characteristic peaks of cubic CeO_2, features of Pd and/or Pt

can be observed which in some cases are barely detectable due to the low metal loading. In particular, there is a visible Pt metal peak at 39.8° for the sample *1Pt*Ce M and for the sample *0.8Pt*-0.2PdCe M, together with a shoulder at 46.3° which again corresponds to metallic Pt. On *0.5Pt*-0.5PdCe IWI also a feature at 40° is detected, which might be attributed to a PtPd alloy, as this sample is the only one subjected to a thermal treatment (calcination at 1173 K). The occurrence of metallic Pd (characteristic peak at 40.1°) seems less likely since after calcination in air palladium is usually oxidized, as inferred from the broad shoulder at 33.9° on the same sample. As a general remark, the lattice constant of PtPd is smaller than that of Pt (3.924 Å) and larger than that of Pd (3.891 Å), so that a shift of the Pt peak to higher degrees of diffraction is expected when the alloy is formed[150].

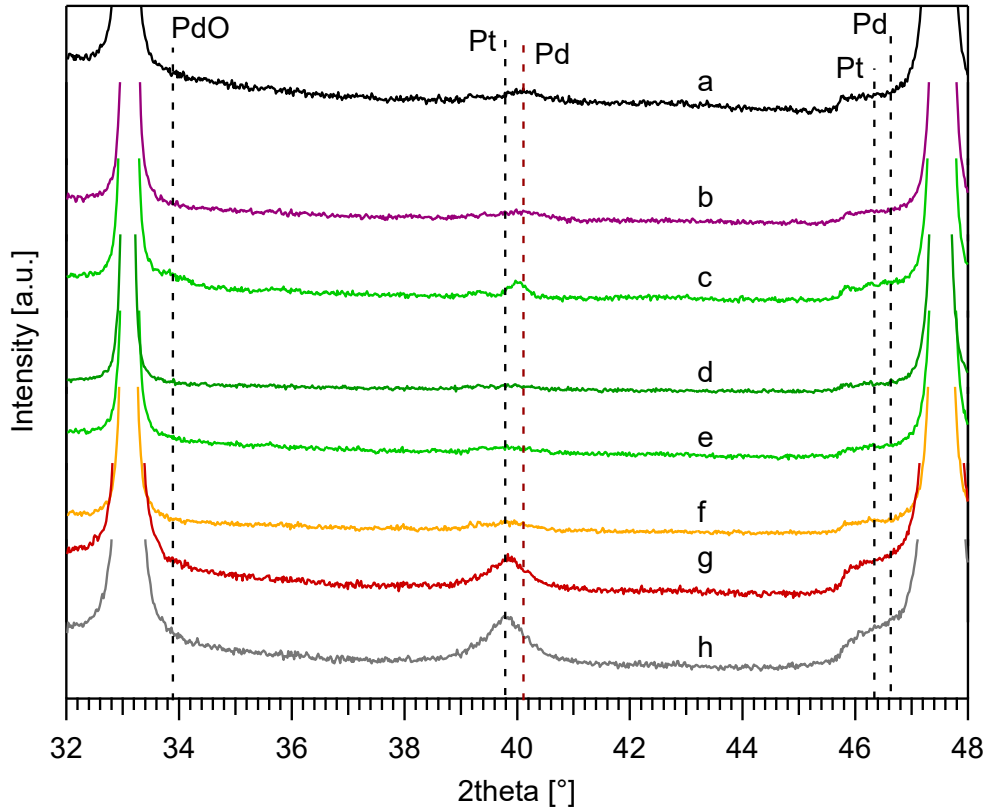

Figure 3-1: XRD profiles of fresh catalysts in the 32-48° 2ϑ range: a) 1PdCe M, b) 0.2Pt-0.8PdCe M, c) 0.5Pt-0.5PdCe IWI, d) 0.5Pd-0.5PtCe M, e) 0.5Pt-0.5PdCe M, f) 0.65Pt-0.35PdCe M, g) 0.8Pt-0.2PdCeM, h) 1PtCe M.

A hint towards the formation of a PtPd alloy in the impregnated catalyst comes also from the analysis of TPR profiles reported in Figure 3-2-A.

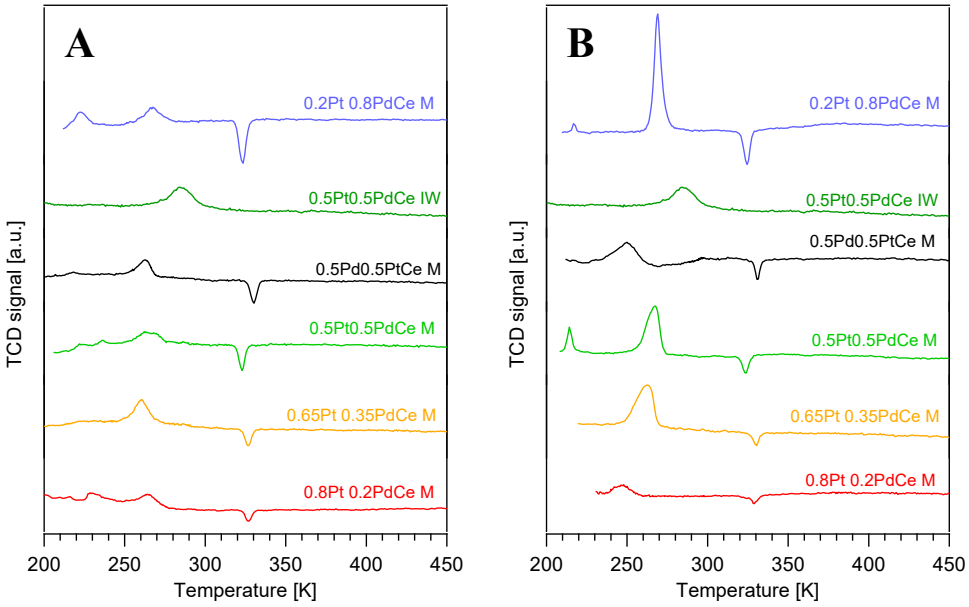

Figure 3-2: sub-ambient TPR profile of bimetallic milled samples, as prepared (A) and after pretreatment in air at 623K for 1h (B).

These profiles were obtained without any pretreatment and in the case of milled samples the hydrogen release (negative peak at about 330 K) attributed to the decomposition of Pd β-hydrides can be observed, with an increasing intensity at increasing Pd loading. This indicates the presence of free palladium on these catalysts, as the formation of hydrides occurs according to the following reactions (with x depending on temperature and H_2 partial pressure) [151]:

$$PdO + H_2 \rightarrow Pd + H_2O$$

$$Pd + x/2\ H_2 \rightarrow PdH_x$$

It is interesting to observe that this peak is not present on *0.5Pt*-0.5Pd IWI. On PtPd containing catalysts the absence of β-hydrides peak has been related to the formation of an alloy between the two metals: the alloying of Pd with Pt prevents in fact its reaction with hydrogen[152]. The peaks at lower temperature are due to the reduction of small amounts of Pt and Pd oxides, respectively, which could be present as surface layers on the metallic powders and/or might be formed during milling. The peak at lower temperature should be attributed to the reduction of PtO_x, whereas the hydrogen consumption between 260 and 270 K is due to the reduction of PdO. The attribution is made on the basis of the TPR of monometallic samples, even if in that case the peaks are not so defined, especially for Pd, Figure 3-3.

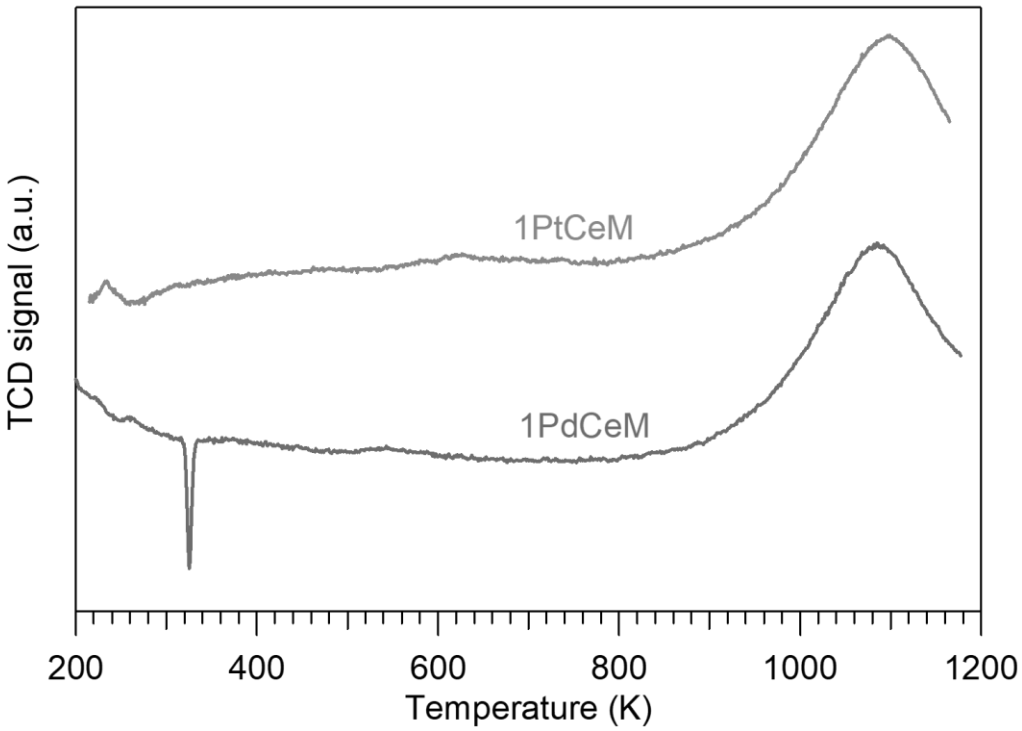

Figure 3-3: TPR profiles of fresh monometallic samples without pretreatment.

If the catalysts are treated in air at 623 K before TPR analysis (Figure 3-2-B), the β-hydride peak at 330 K becomes slightly smaller and the hydrogen consumption at lower temperature increases for samples containing > 0.2 wt% of Pd, as expected following Pd oxidation during the pretreatment. The quantitative analysis of TPR data is not straightforward, as it is known that when a metal supported on ceria is reduced it can promote the simultaneous reduction of the support at low temperature thanks to the spillover effect [153]. This, however, does not affect the amount of hydrogen released from PdH_x, which is reported in Table 3-3 as calculated fraction of Pd involved, indicating some PtPd alloying already after the treatment at 623 K (the % of PdH_x decomposing becomes slightly smaller). As a matter of fact, *0.5Pt*-0.5PdCe M shows the highest reduction in the fraction of PdH_x after the pretreatment, highlighting a higher tendency of this sample to form a PtPd alloy.

Table 3-3: Calculated fraction of PdH_x decomposed during TPR assuming x = 1 for all samples

Sample	**%PdH_x no pretreatment**	**%PdH_x pretreatment @623K**
0.8Pt-0.2PdCe M	55	41
0.65Pt-0.35PdCe M	51	42
0.5Pt-0.5PdCe M	58	36
0.2Pt-0.8PdCe M	66	56
0.5Pd-*0.5Pt*Ce M	54	56

3.3.2 Catalytic tests

Catalytic methane oxidation tests carried out in dry conditions on bimetallic samples show that the addition of platinum negatively affects the low temperature activity of Pd-based samples. Even if the presence of water can alter the results depending on the composition of the catalyst, these tests in dry atmosphere can give a first easy evaluation of the catalytic performance and thus allow to filter the worst samples. In Table 3-4 the temperatures to achieve 10% and 50% (T_{10} and T_{50}) methane conversion during the heating branch of the second light-off cycle are reported, and the corresponding light-off curves (second cycle) are shown in Figure 3-4.

Table 3-4: T_{10} and T_{50} measured during the second light-off cycle of methane oxidation in dry conditions (0.5% CH_4, 2% O_2 in He) for the samples considered in this work.

Sample	**T_{10} (K)**	**T_{50} (K)**
0.8Pt-0.2PdCe M	670	821
0.65Pt-0.35PdCe M	644	810
0.5Pt-0.5PdCe M	609	702
0.2Pt-0.8PdCe M	576	637
1PdCe M	563	631
*1Pt*Ce M	746	849
0.5Pd-*0.5Pt*Ce M	625	747
0.5Pt-0.5PdCe IWI	637	745

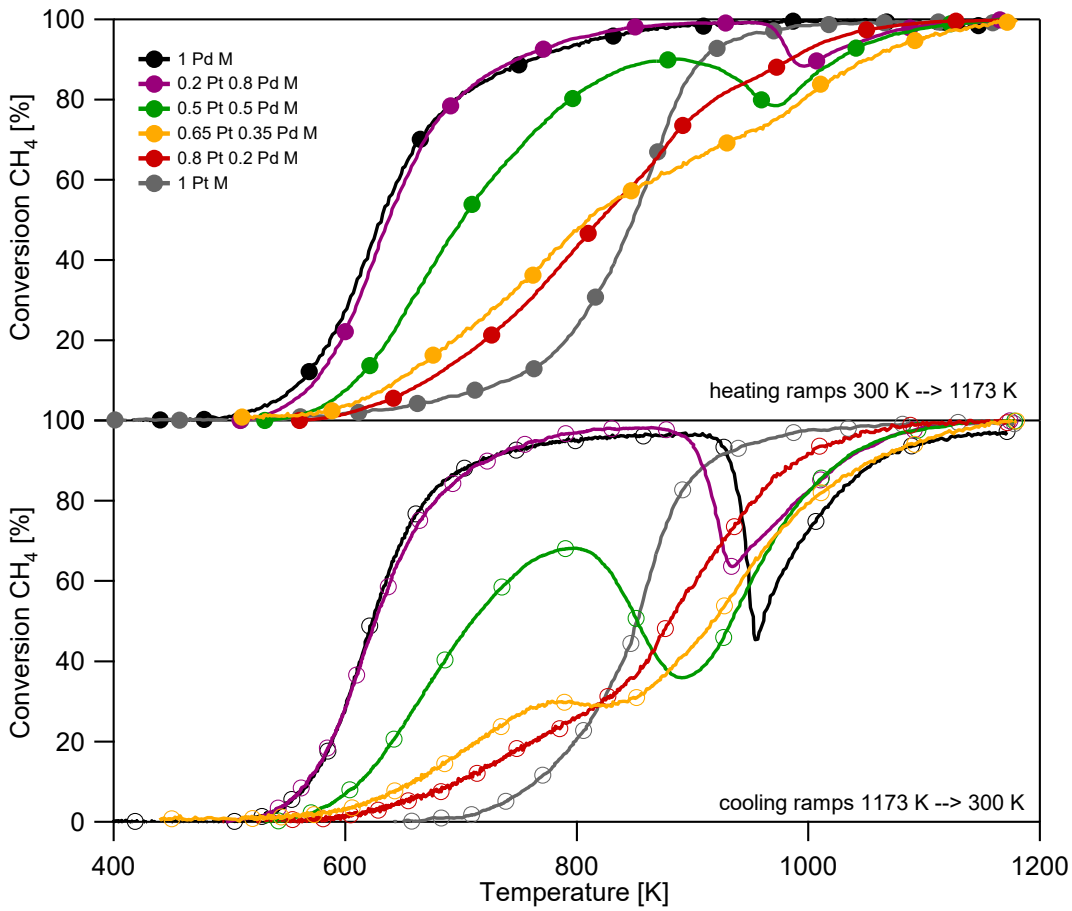

Figure 3-4: TPC-dry for bimetallic milled (M) samples compared to monometallic 1Pd M and monometallic 1Pt M; (a) heating, (b) cooling; GHSV ca.200000 h^{-1}, 0.5% CH_4, 2% O_2, He to balance.

For a better understanding, the light-off curves are divided between heating and cooling ramps. The insertion of Pt, and the simultaneous decrease of Pd to maintain the amount of metal at 1 wt%, reduces the conversion in the low temperature range. Nevertheless, also for the samples containing the same Pd amount (0.5PdCe M and 0.5Pt0.5PdCe M), the addition of Pt is detrimental. The results are in line with previous literature works carried out on conventional impregnated catalysts, which in general indicate that during light-off experiments the samples containing Pt are less active than monometallic Pd ones[65, 71, 138,156]. Looking more in detail at the light-off curves of Figure 3-4, it can be observed that at high temperature, during the heating ramp, Pt has a negative impact on the redox cycle of Pd-PdO as inferred from the decrease in methane conversion which is typically associated with the decomposition of palladium oxide.[53] This happens because the presence of Pt anticipates the PdO decomposition to metallic Pd in a range of temperature where the homogeneous methane oxidation is not yet self-sustaining (below 1100 K). During cooling it is again evident that Pt changes the process of Pd re-

oxidation, as indicated by the deep loss in methane conversion more pronounced for Pt-containing samples (with the exception of *0.2Pt*-0.8PdCe M). The effect is observable also from TPO profiles recorded for 1PdCe M and 0.5Pt-0.5PdCe M, chosen as representative ones and reported in Figure 3-5.

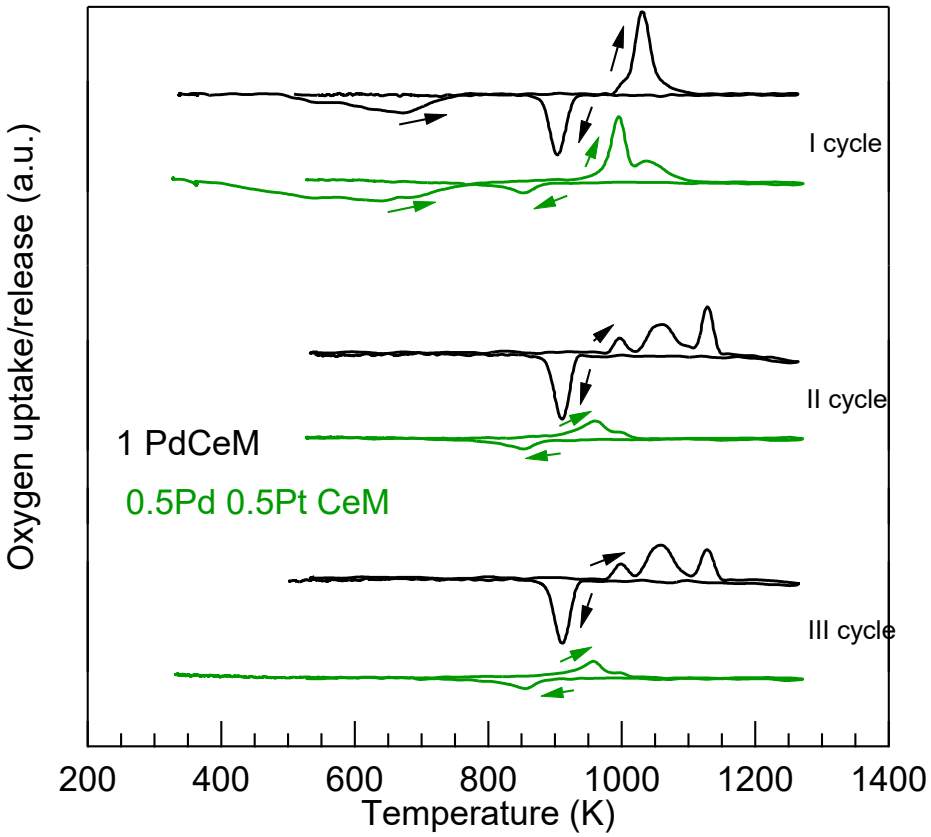

Figure 3-5: TPO profiles of three heating/cooling cycles for the samples 1PdCe M, 0.5Pt0.5PdCe M, 0.5Pd0.5PtCe M.

The role of Pt is clear: on one side it hinders the cycling of PdO-Pd-PdO (the peaks of oxygen release and uptake are barely detectable after cycle 1), on the other it anticipates PdO decomposition of about 100 K. This result was already reported in the literature, irrespective of the support [139,143,155].

The effect of platinum on catalytic activity is different when considering time-on-stream experiments. In Figure 3-6 and Figure 3-7 the conversion of CH_4 in TOS experiments in dry and wet conditions is reported, respectively. To highlight better the variations during this test also the normalized conversion N[%XCH_4(t)] is reported. The sample with 0.8%wt of Pt and the monometallic Pt sample are not reported due to their overall bad performances in these experimental conditions.

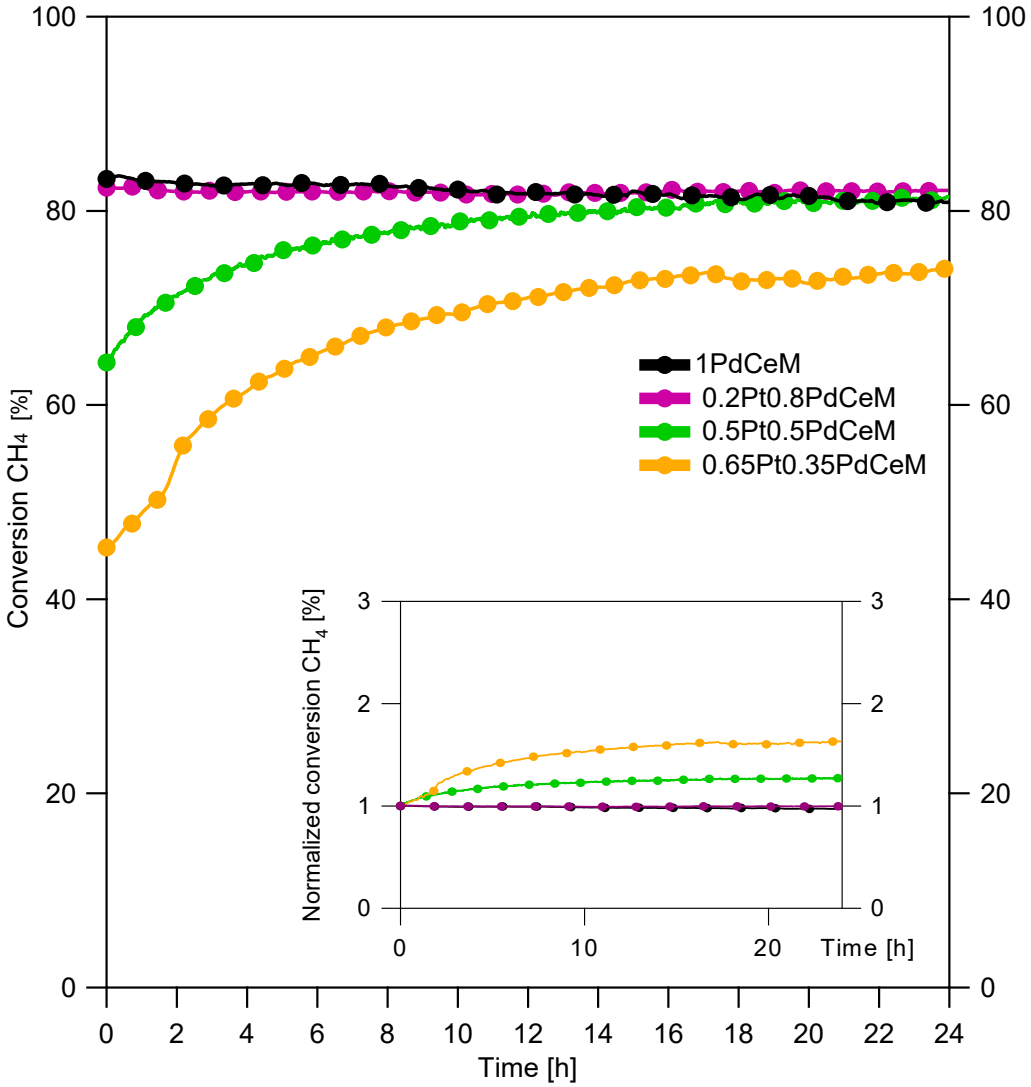

Figure 3-6: CH_4 conversion on TOS dry at 723K for bimetallic milled (M) samples compared to monometallic 1Pd M; normalized conversion in the inset; GHSV ca.200000 h-1, 0.5% CH_4, 2% O2, He to balance.

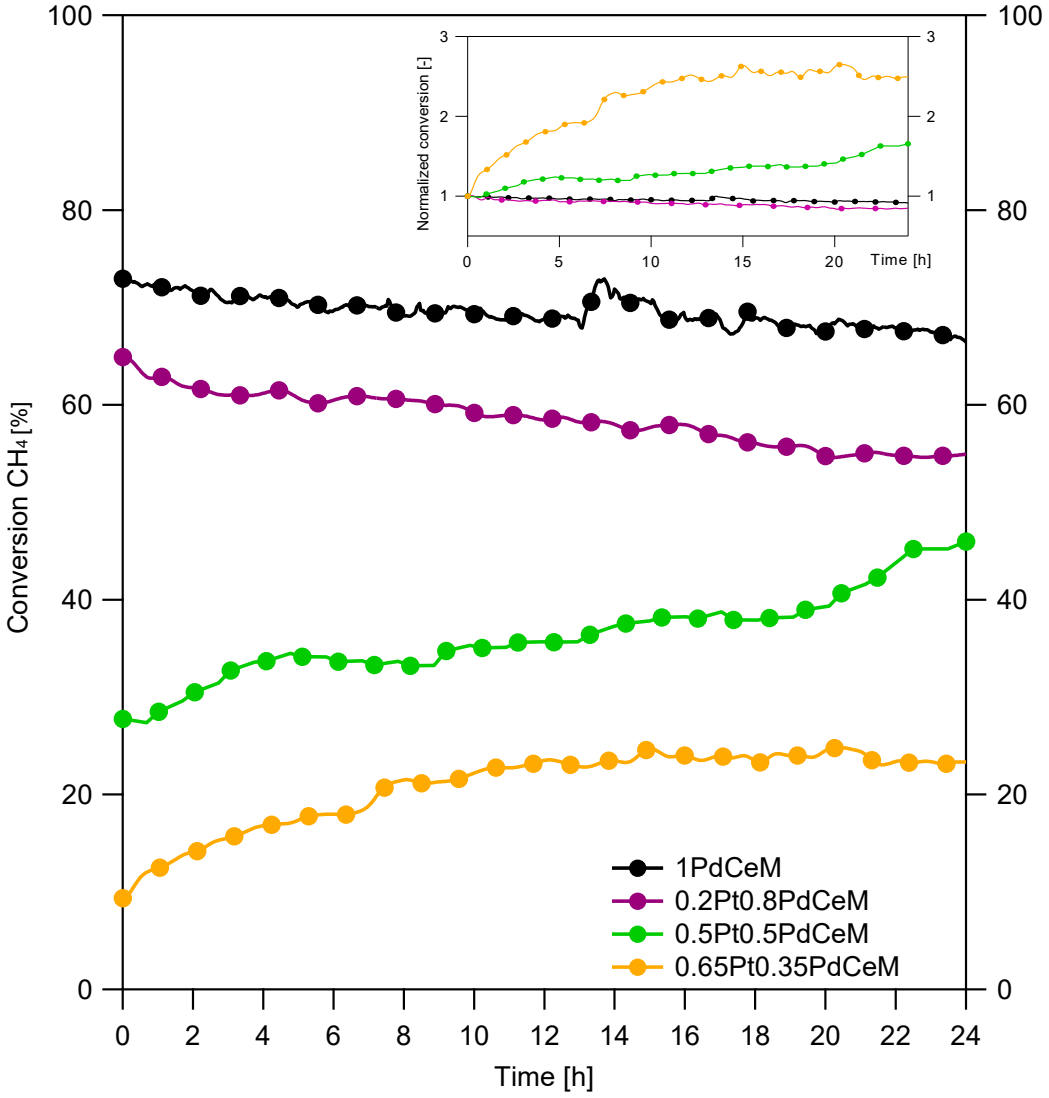

Figure 3-7: CH_4 conversion on TOS wet for bimetallic milled (M) samples compared to monometallic 1Pd M; normalized conversion in the inset; GHSV ca.200000 h-1, 0.5% CH_4, 2% O_2, 10 % H_2O, He to balance.

The bimetallic milled samples with Pt content ≥ 0.5% wt show a higher stability compared to monometallic Pd/CeO_2 catalyst, especially when the test is carried out in wet atmosphere (0.5% CH_4, 2% O_2, 10% H_2O in He). Moreover, for *0.5Pt*-0.5PdCe M and *0.65Pt*-0.35PdCe M the activity increases over time. In the literature this behavior has been tentatively ascribed to an enrichment in PdO and/or to a reconstruction of the surface during time-on-stream operation[65,74,140,154]. An activation of bimetallic PtPd/Al_2O_3 catalysts has been reported also during repeated reduction/re-oxidation cycles, which suggests a role of the mutual redox interplay between palladium and platinum[139]. This seems confirmed by the observation that after aging in air (1023 K for 10 h) only 20-30% of PdO is formed on PtPd-based samples, whereas on monometallic sample palladium is fully oxidized (100% PdO)[72]. The restructuring of PtPd nanoparticles has been observed also for supported Pd-Pt@CeO_2/Si-Al_2O_3 catalysts, with the formation of a Pt-rich core surrounded by a Pt-Pd shell under reducing conditions[156].

Among the bimetallic samples, the best performing one during TOS experiments was the one containing 0.5Pt and 0.5Pd. It is interesting to observe, Figure 3-8, that the activity of the milled sample *0.5Pt*-0.5PdCe M is much higher than the corresponding impregnated one indicating that the milling procedure, already effective for monometallic samples, can be successfully applied to the preparation of bimetallic PtPd catalysts.

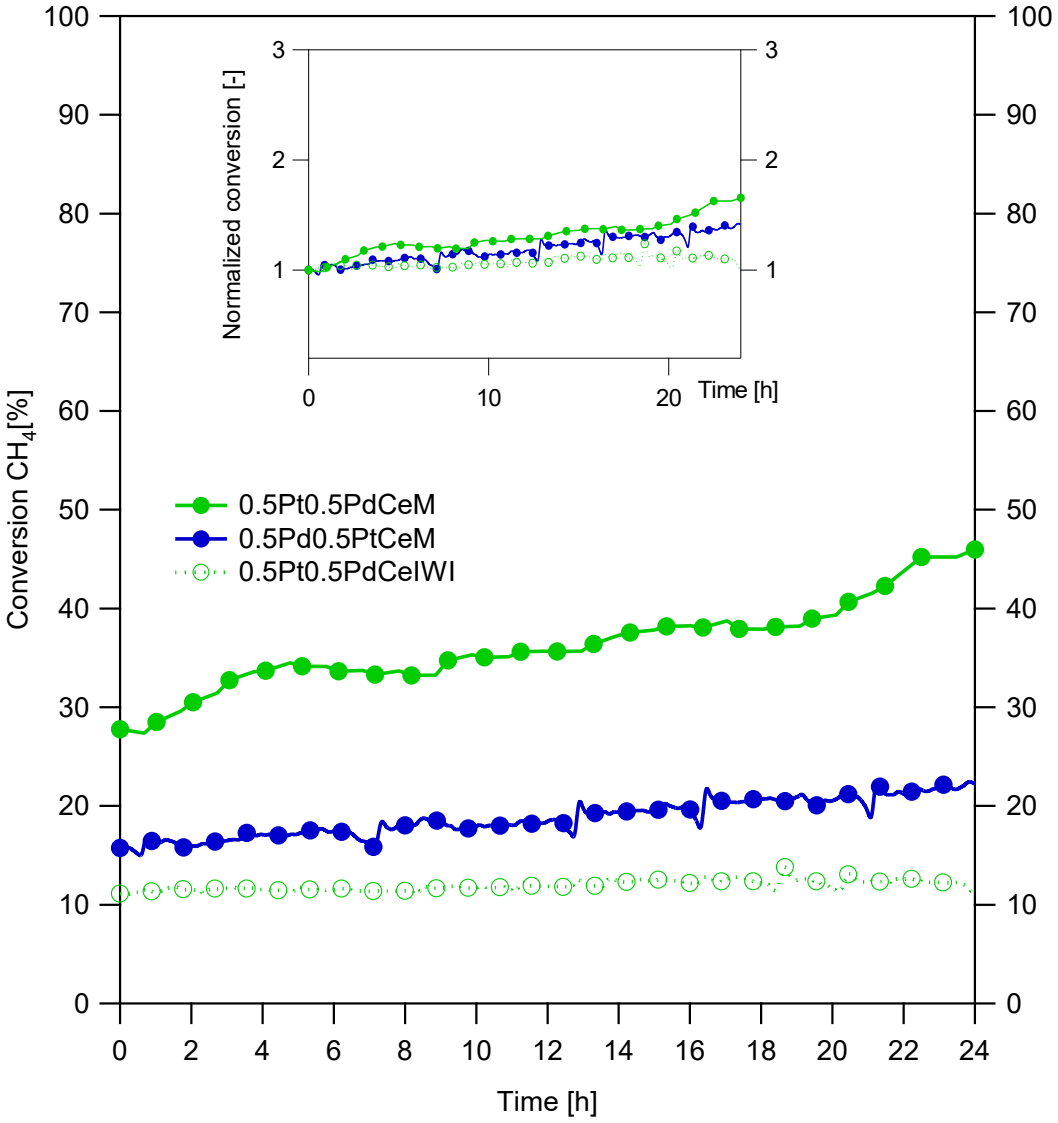

Figure 3-8: methane conversion during TOS wet for bimetallic milled (M) samples with m^{Pd}/m^{Pt} = 1; normalized conversion in the inset; GHSV ca. 200000 h^{-1}, 0.5% CH_4, 2% O_2, 10 % H_2O, He to balance.

Moreover, the order of milling is also important because better results are obtained when Pd is put directly in contact with ceria, as observed by comparing 0.5Pd-*0.5Pt*Ce M with *0.5Pt*-0.5PdCe M. This result is further corroborated by the comparison of the transient light-off experiments in dry conditions reported in Figure 3-9.

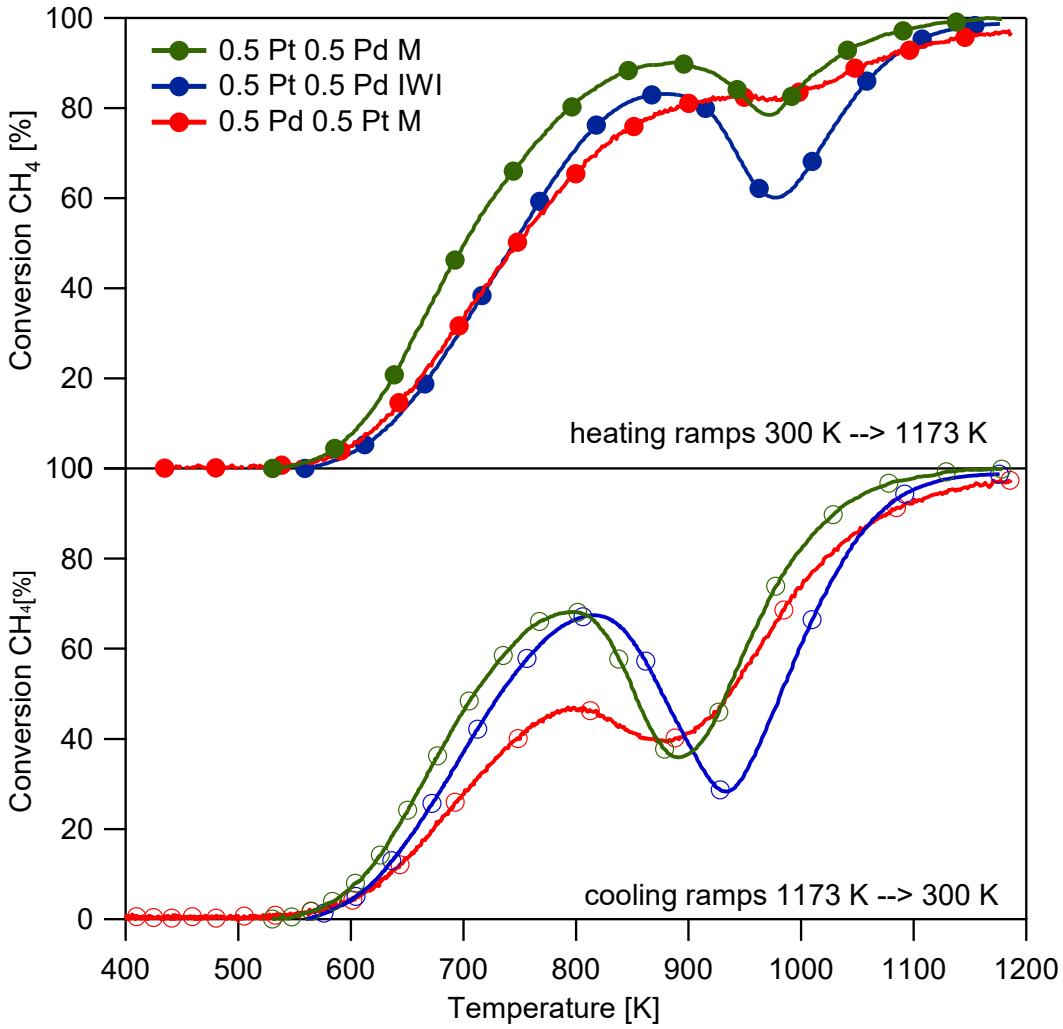

Figure 3-9: TPC-dry for bimetallic samples with $m^{Pd}/m^{Pt} = 1$; (a) heating, (b) cooling; GHSV ca.200000 h^{-1}, 0.5% CH_4, 2% O_2, He to balance.

The sample prepared by milling Pd and Ce in a first step, and secondly adding Pt, is not only better than the impregnated one but also of the other milled catalyst. This confirms the effectiveness of the milling process for catalyst synthesis, but also indicates how the order of milling can sensibly change the final result. To further analyze the effect of the prolonged exposure to the wet atmosphere, a dry TPC cycle was carried out on 0.5Pt0.5PdCe M after the TOS wet. In Figure 3-10 the conversion recorded is compared with the conversion of the fresh sample.

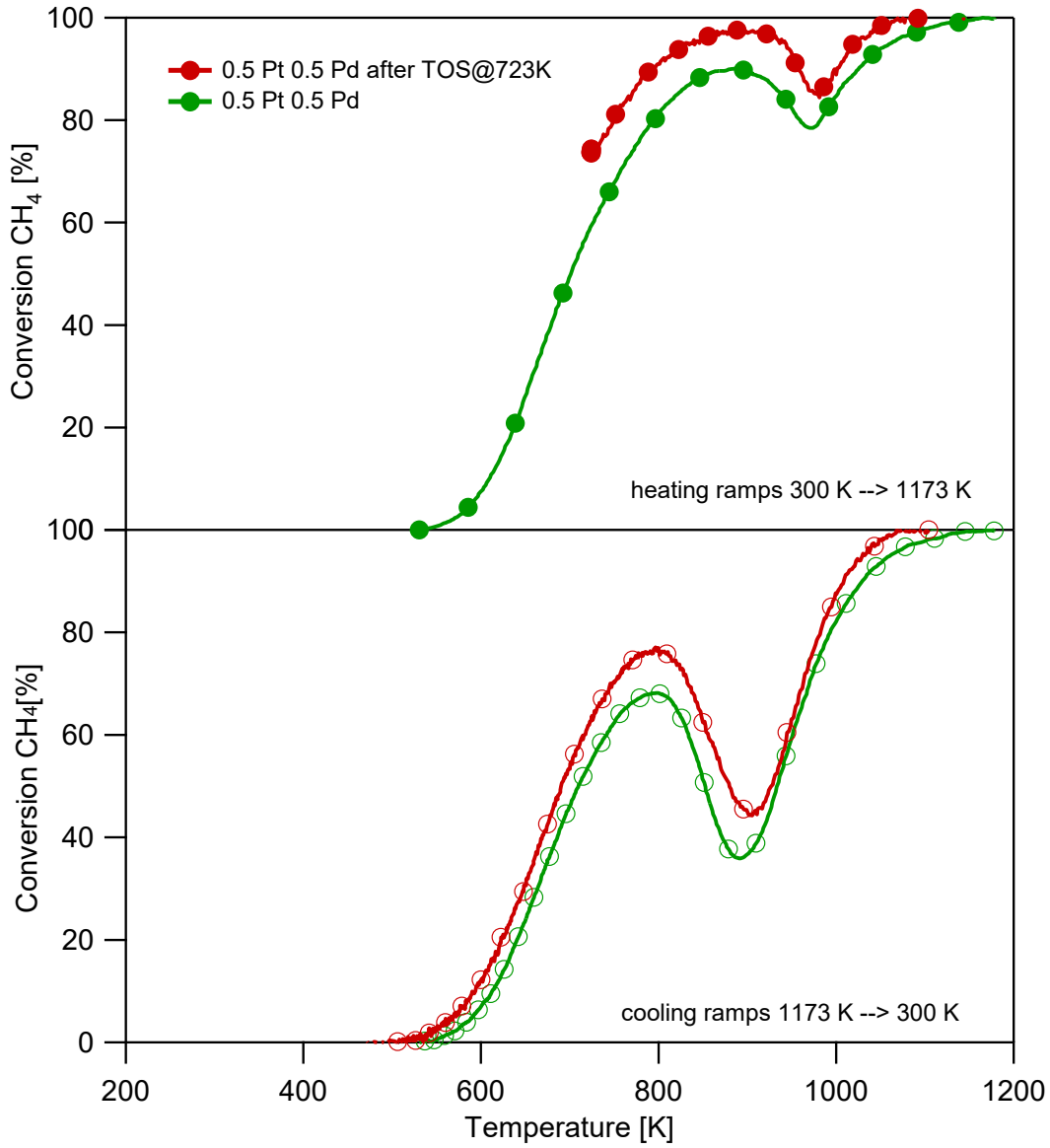

Figure 3-10: TPC-dry cycle started from 723K after TOS-wet for 0.5Pt0.5Pd M compared with TPC-dry for 0.5Pt 0.5Pd M and 0.5 Pd; GHSV ca.200000 h^{-1}, 0.5% CH_4, 2% O_2, He to balance.

The results show that the improvement in activity is maintained for this catalyst also during the cooling ramp, suggesting a permanent modification of the sample. It was decided then to characterize 0.5Pt 0.5Pd Ce M more in depth comparing it with the homologous samples obtained by impregnation and by changing the order of milling.

3.3.3 HRTEM and characterization of spent samples

Trying to better understand the reasons for the improved behavior of the milled bimetallic catalysts during time-on-stream operation in wet conditions, further characterization was carried out on spent samples after TOS experiments for most

representative ones. In particular, x-ray diffraction patterns (Figure 3-11) and TPR profiles (Figure 3-12) show that on *0.5Pt*-0.5PdCe M there is the formation of a PtPd alloy after TOS treatment in wet atmosphere. This is evidenced by the feature at 2θ=39.9°, which lays in the middle of the peaks belonging to single metals, and by the absence, in the TPR profile, of the hydrogen release peak attributed to the decomposition of Pd *β*-hydrides.

Comparing the XRD profiles of milled and impregnated catalysts, it can be observed that the TOS wet treatment has a lower impact on *0.5Pt*-0.5PdCe IWI, and that on this sample the peak is shifted to the right with respect to *0.5Pt*-0.5PtCe M indicating an alloy richer in Pd, with possibly a hint of Pd segregation.

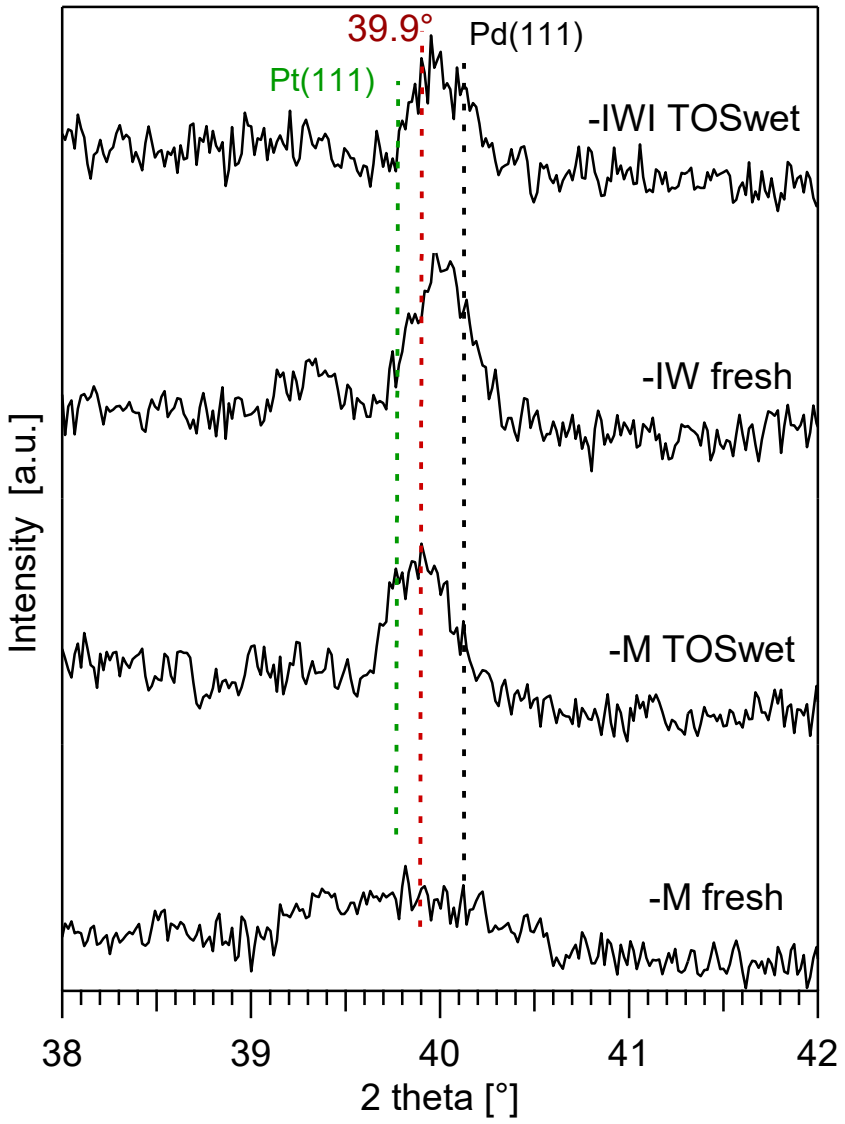

Figure 3-11: XRD profiles collected on 0.5Pt-0.5PdCe M and 0.5Pt-0.5PdCe IWI samples, as prepared (fresh) and after Time-On-Stream test in wet conditions (TOS wet). Peak positions of Pd(111) (JCPDS 00-046-1043) and Pt(111) (JCPDS 00-004-0802) are reported as reference.

The different effect of TOS wet treatment on the two samples is inferred also from the observation of TPR profiles (Figure 3-12), in which a single broad peak is detected for the impregnated catalyst, whereas for the milled one a very small peak at about 225 K (PtO_x species) and a well-defined more pronounced feature at ca. 280 K (PdO) are observed.

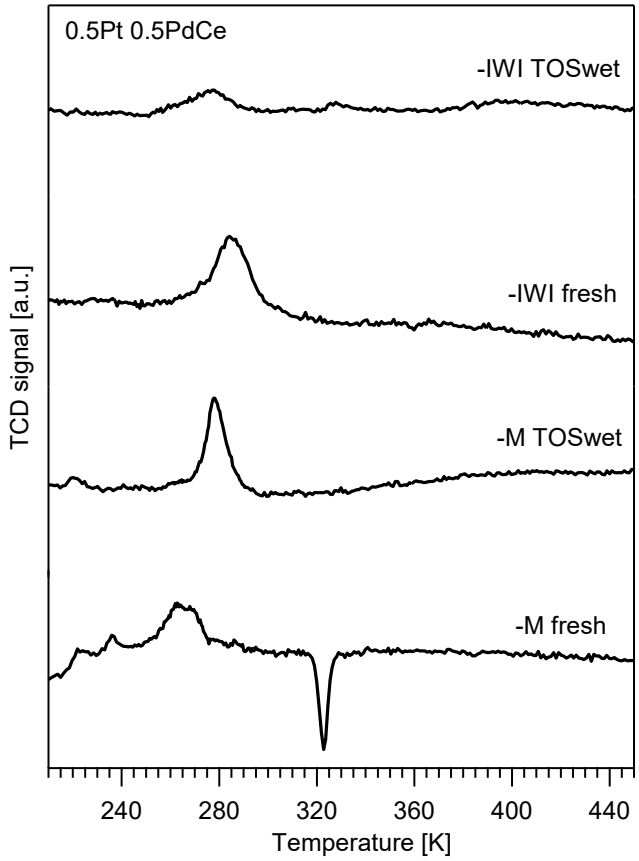

Figure 3-12: H_2-TPR profiles of 0.5Pt-0.5PdCe M and 0.5Pt-0.5PdCe IWI samples, as prepared (fresh) and after Time-On-Stream test in wet conditions (TOS wet).

The situation suggests a different interaction not only between Pd and Pt, but also between Pd and CeO_2 support. Keeping in mind that before the TOS wet treatment a TPC dry cycle is performed on the catalysts, we also investigated this aspect by characterizing *0.5Pt*-0.5PdCe M after a TPC dry by XRD, Figure 3-13, and TPR measurements, Figure 3-14.

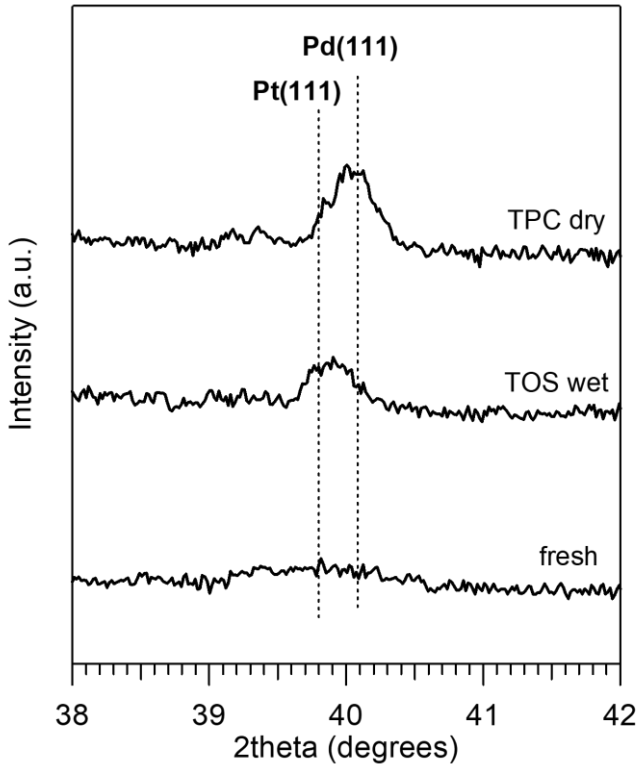

Figure 3-13: XRD profiles collected on 0.5Pt-0.5PdCe M as prepared (fresh), after dry methane oxidation experiment (TPC dry) and after Time-On-Stream test in wet conditions (TOS wet).

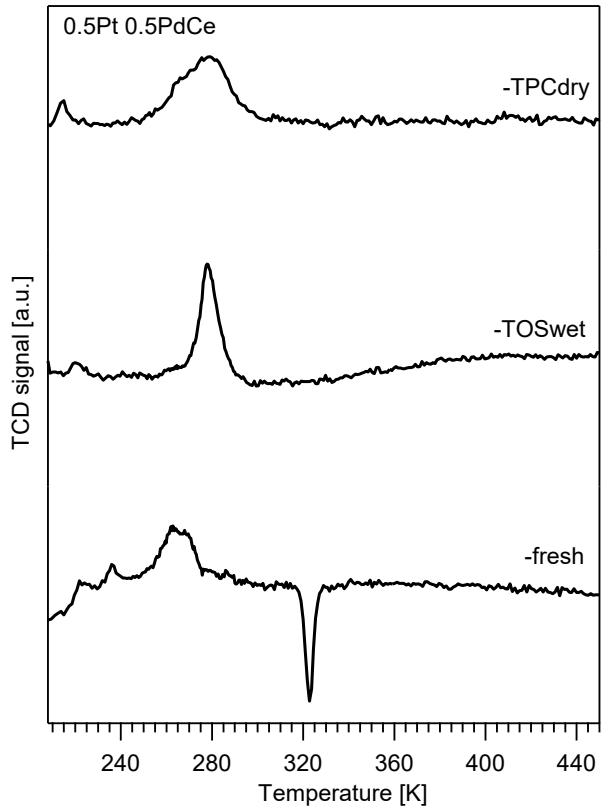

Figure 3-14: H_2-TPR profiles of 0.5Pt-0.5PdCe M as prepared (fresh), after dry methane oxidation experiment (TPC dry) and after Time-On-Stream test in wet conditions (TOS wet).

XRD patterns show that after a TPC cycle on the milled sample the Pt-Pd feature is closer to the peak of metallic Pd, and the TPR profile is similar to that recorded after TOS wet but with a broader hydrogen consumption peak related to PdO reduction. Overall, the results indicate that the restructuring of the catalyst certainly starts during the dry TPC cycle, but further modifications occur during time-on-stream experiment in presence of water. On PdPt core-shell cubes and octahedra atomic interdiffusion and alloying of the two metals has been observed starting from 773 K[157], supporting our results for samples after a dry TPC cycle.

To better evaluate the changes in the morphology that could occur during TOS wet tests, also HRTEM analysis was carried out on the fresh and spent samples. HRTEM was already applied successfully for the characterization of monometallic Pd/CeO_2 catalysts prepared by dry milling, as reported in Figure 3-15. This image reveals the presence of a unique Pd-Ce arrangement in the form of an amorphous shell covering ceria nanoparticles, capable of stabilizing highly active Pd^0/Pd^{2+} entities on catalyst surface[126,127,149]

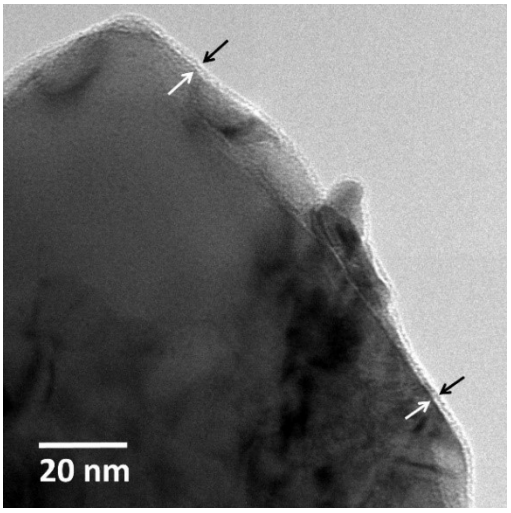

Figure 3-15: HRTEM image of the amorphous shell on a Pd/CeO_2 monometallic sample prepared by mechanical milling.

HRTEM characterization of as prepared 0.5Pt 0.5Pd Ce M, Figure 3-16, and 0.2Pt 0.8Pd Ce M, Figure 3-17, shows interestingly that the addition of Pt does not alter the presence of the homogeneous, amorphous layer already observed for Pd milled samples, indicated by white arrows in Figure 3-16. Moreover, Pt seems to penetrate the layer since it is found below it, close to ceria crystallites, in the form of clusters of 10 to 50 nm. There is no evidence of Pt mixing inside the amorphous layer.

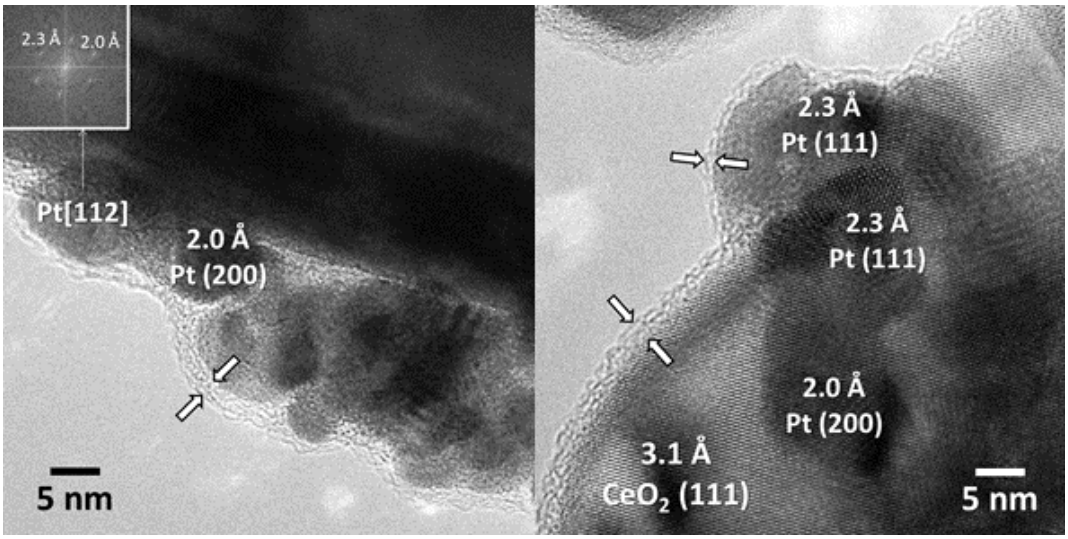

Figure 3-16: HRTEM images of sample 0.5Pt0.5PdCe M fresh.

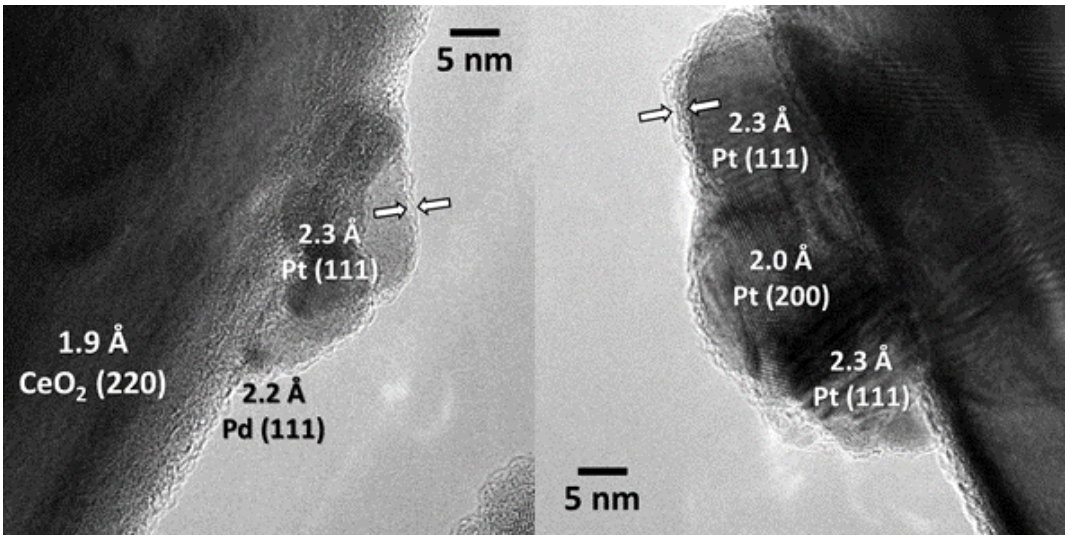

Figure 3-17: HRTEM images of sample 0.2Pt0.8PdCe M fresh.

The interaction of Pt with ceria during milling is clearly different from that of Pd, and this is inferred and supported also by the images of the milled Pt/CeO_2 catalyst, Figure 3-18, where only Pt nanoparticles on ceria are observed.

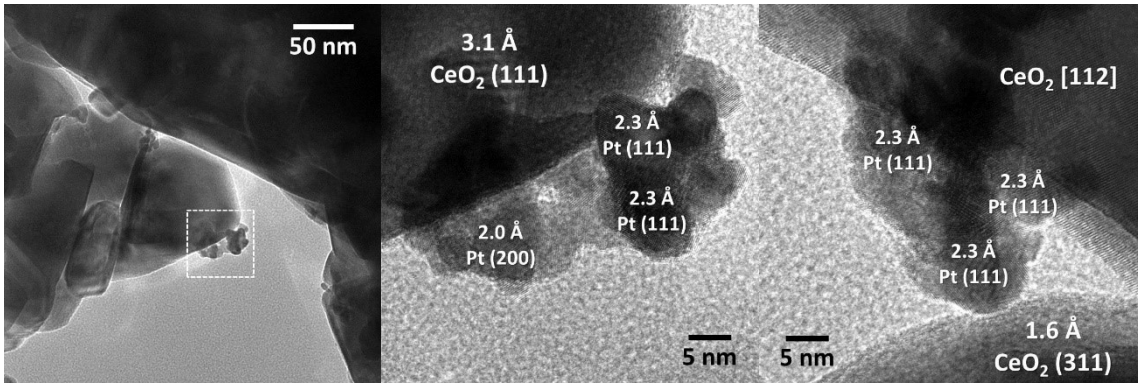

Figure 3-18: HRTEM images of milled Pt/CeO_2 sample.

This different interaction determines also the different arrangement of the sample when the order of milling is inverted (i.e. first Pt with CeO_2 followed by the milling of Pd with Pt/CeO_2). Figure 3-19 reports HAADF-STEM image together with EDX analysis for this sample. The absence of the layer for this catalyst clearly indicates the unique nature of the Pd-Ce amorphous shell, as well as the need of a physical contact between Pd and ceria to generate this particular interaction. It is interesting to observe that the occurrence of Pt clusters on ceria surface, which still should leave a fraction of bare CeO_2, is sufficient to hinder the formation of the layer. A possible explanation, that would need further investigation, is that the grinding of platinum with ceria can alter the surface properties of the latter, making it unsuitable for further interaction with Pd.

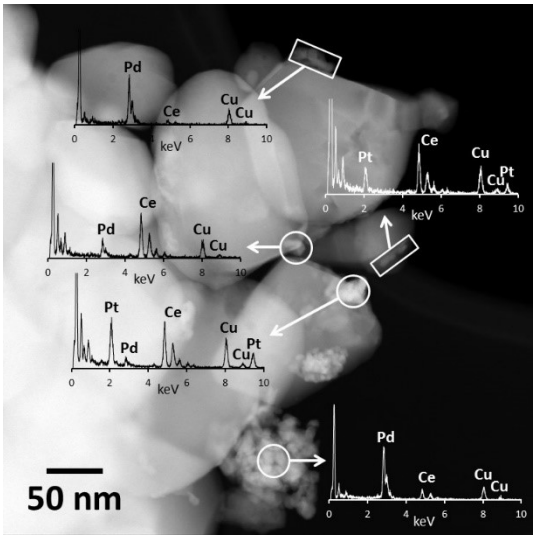

Figure 3-19: HAADF-STEM-EDX analysis of sample 0.5Pd0.5PtCe M fresh.

On the bimetallic impregnated catalyst, shown in Figure 3-20, the layer is not present and only small entities at the limit of the resolution of the microscope are visible. The absence of the layer is in agreement with what already observed for the impregnated monometallic sample[126]. It is recalled that the only impregnated sample prepared in this work is in the "equimassic" composition where Pt is added in a second step as in the milling synthesis.

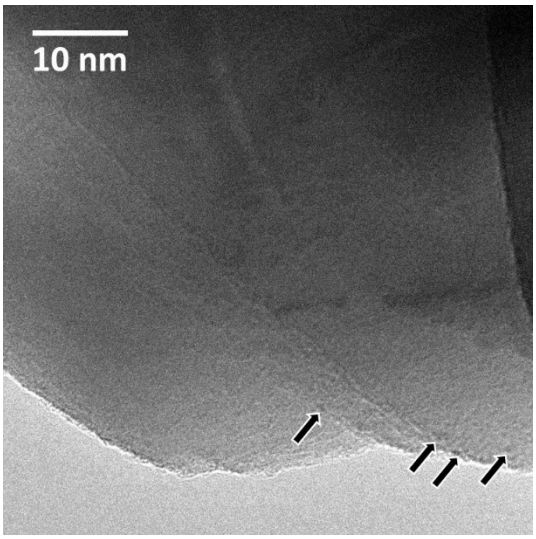

Figure 3-20: HRTEM image of sample 0.5Pt0.5PdCeIWI fresh.

The characterization of samples after TOS wet experiments at 723K reveals a significant change in the morphology for all bimetallic catalysts, as shown in Figure 3-21. Interestingly, a particular structure is visible on ceria crystallites, consisting of a PdO foot in contact with ceria covered by a Pt head more exposed to the gas phase, closely resembling a mushroom. The amorphous layer is still present, apparently not altered by the treatment, and covers also these new "mushroom-like" structures. These structures, growing on ceria surface, are present on the milled samples irrespective of the milling order (Figure 3-21 a-d). A similar arrangement is also observed on *0.5Pt*-0.5PdCe IWI, but with a less developed structure, where thinner, needle-like stems are supporting a smaller Pt head (Figure 3-21e-f), and where Pt and PdO are less clearly distinguished.

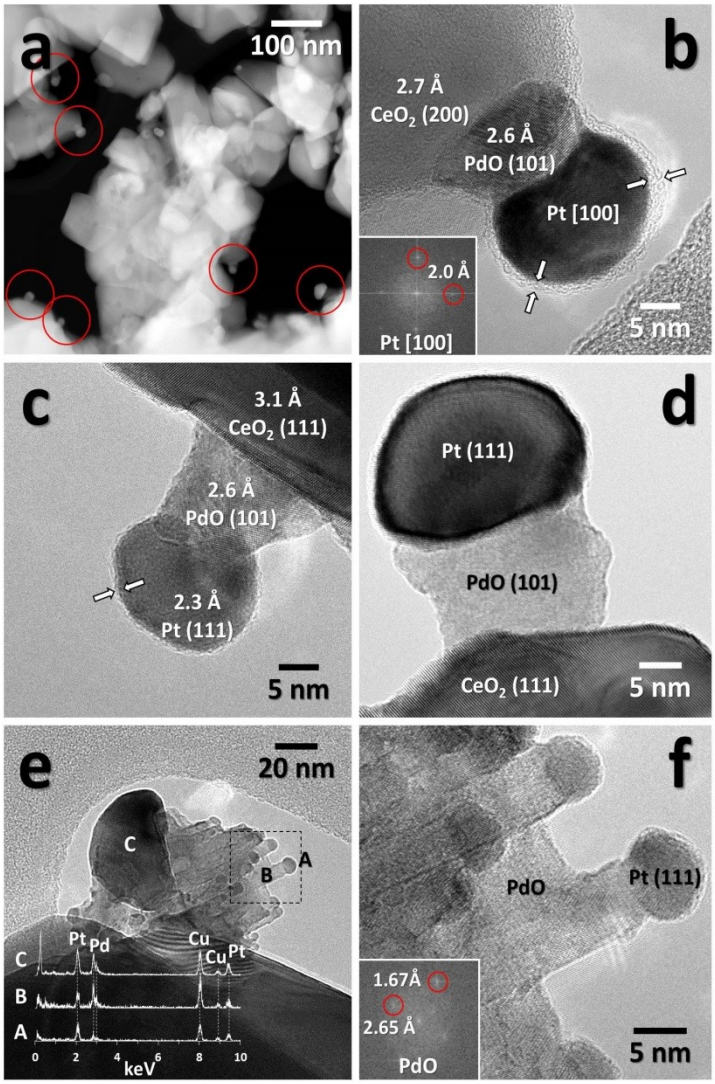

Figure 3-21: HRTEM images of samples after TOS wet experiments. (a),(b) 0.5Pt-0.5PdCe M; (c) 0.2Pt-0.8PdCe M; (d) 0.5Pd-0.5PtCe M; (e),(f) 0.5Pt-0.5PdCe IWI.

Figure 3-21a-b present a general STEM-HAADF and HRTEM images of *0.5Pt*-0.5PdCe M in which the amorphous layer characteristic of the fresh milled sample is distinctly visible (indicated by white arrows) around ceria nanoparticles and PdO-Pt mushroom-like structures (some of them enclosed in circles in Figure 3-21a). The layer is present also on *0.2Pt*-0.8PdCe M (Figure 3-21c). Figure 3-21d shows the HRTEM image of 0.5Pd-*0.5Pt*Ce M sample, in which a mushroom very similar to those observed on *0.5Pt*-0.5PdCe M is visible but without the amorphous shell, coherently with HRTEM images of the correspondent fresh catalyst. In Figure 3-21e a portion of *0.5Pt*-0.5PdCe IWI catalyst is shown, together with EDX analyses that indicate the presence of big PtPd particles that seem to evolve into needle-like structures, again with a PdO stem supporting a Pt head. In this case the PdO is supported on both the ceria surface and on the bimetallic particles. This means that on the samples prepared by mechanical

milling the interaction between Pd and Pt has a different evolution compared to *0.5Pt*-0.5PdCe IWI, where less ordered, agglomerated structures are encountered. In contrast, the formation of very homogeneous and very well distributed PdO-Pt mushroom structures identified in the bimetallic catalysts prepared by mechanochemical synthesis is unique. It seems that between Pt head and PdO body, either mushroom-like or needle-like structures, there is a mixing of the two metals that inidcates again an intermediate alloying step. In Figure 3-22 it is reported one of the mushroom-like structures evidenced in sample 0.5Pt0.5PdCeM: an EDX line-profile has been measured along the white line and the intensity of Ce, Pd, and Pt are plotted as well as the STEM-HAADF overall intensity line. The STEM-HAADF intensity profile shows a bright zone in the first 0-10 nm, which corresponds to the ceria crystal support, as evidenced also by the Ce signal. Between 10 and 30 nm, approximately, the intensity of the STEM-HAADF signal decreases sharply, and, at the same time, the Pd signal increases. This corresponds to the foot of the mushroom-type structure. Finally, from ca. 30 to 40 nm the brightness increases again, and the Pt signal appears. This corresponds to the head of the mushroom. It should be noticed, however, that the Pd signal does not vanish completely in the head of the mushroom, which indicating that some Pd-Pt alloy exists at the interface between the Pd foot and the Pt head.

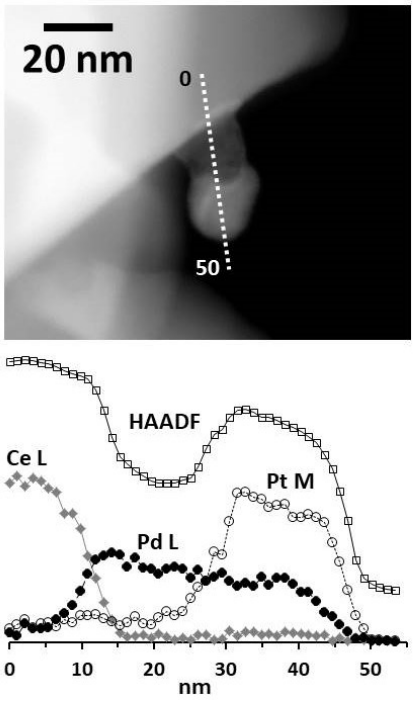

Figure 3-22: EDX line profile of a mushroom-like structure.

These structures cannot be related straightforwardly to the improvement in activity observed during TOS wet treatment, because very similar ones form also on samples which do not show any improvement (i.e. *0.2Pt*-0.8PdCe M, Figure 3.6). Moreover, similar arrangements are detected also on *0.5Pt*-0.5PdCe M after the dry methane oxidation cycle carried out up to 1173 K before TOS experiments (Figure 3-23).

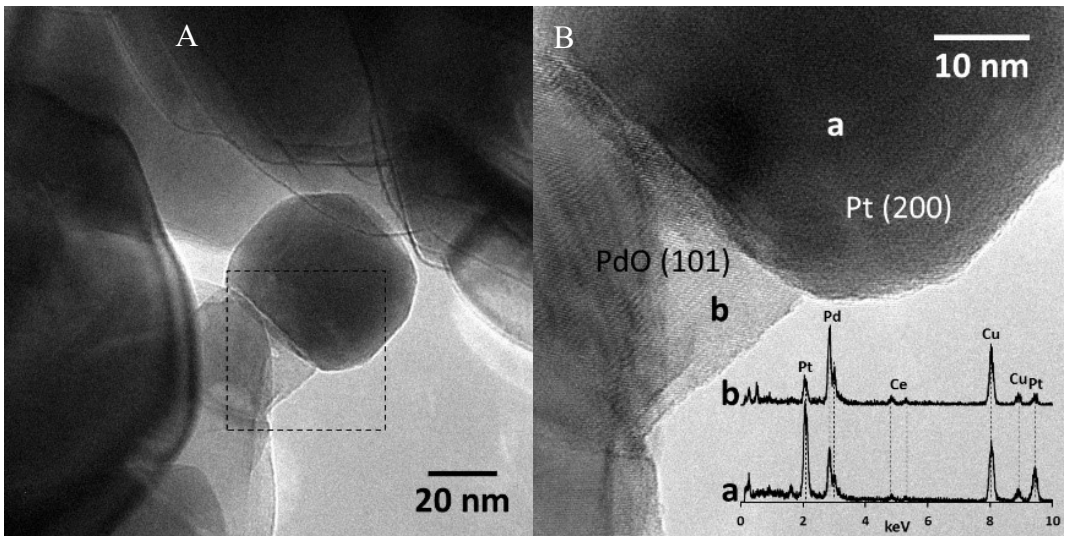

Figure 3-23: HRTEM images of 0.5Pt-0.5PdCe M after one methane oxidation cycle in dry atmosphere up to 1173 K (0.5% CH_4, 2% O_2 in He).

In this case, Figure 3-23A, Pt head shows a well-faceted morphology and overall these structures are much bigger in size then after TOS wet treatment. The coexistence of PtPd bimetallic regions is clearly observed by EDX analysis, Figure 3-23B, supporting the hypothesis of the derivation of the mushroom-like structure arrangements from PtPd alloyed clusters. This can indicate a general tendency of Pd-Pt clusters to evolve in these nanostructures where the reaction atmosphere is not a secondary parameter. Indeed, if calcined in air at the same temperature the sample 0.5Pt0.5PdCe M does not show any particular arrangement, Figure 3-24, but dispersed Pd particles similarly to what observed for the as prepared impregnated sample.

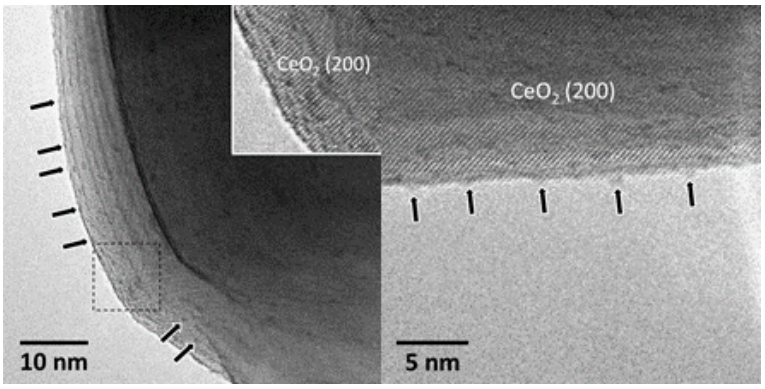

Figure 3-24: HRTEM images of 0.5Pt-0.5PdCe M after calcination at 1173K in air.

The overall picture emerging from the characterization of the spent catalysts indicates unambiguously that all samples, irrespective of the synthesis method, undergo a complex restructuring which appears to begin during the dry TPC cycle preceding the TOS wet experiment. This modification involves the formation of a PtPd alloy, as inferred from XRD and TPR profiles, and on milled catalysts further evolves in the development of mushroom-like structures detected by HRTEM in which PdO and Pt nanoparticles can be observed, being, respectively, the foot and the head of the mushrooms. This evolution seems slower on the conventional impregnated catalyst, for which big PtPd clusters are still observed after TOS wet treatment with needle-like PdO-Pt arrangements growing on them. A scheme of the proposed mechanism for the formation of the Pt-PdO arrangements is shown in Figure 3-25.

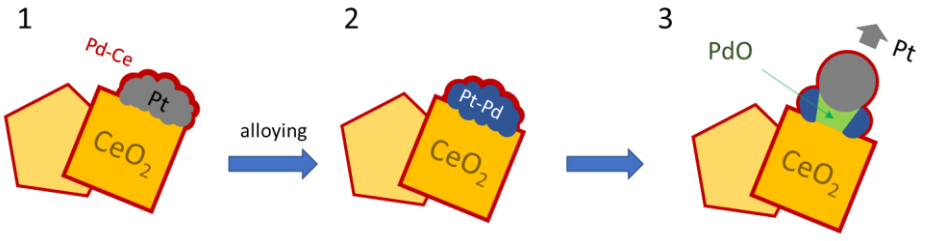

Figure 3-25: schematic mechanism of mushroom-like structures formation.

The evolution of the mushrooms could be linked to the effect of ceria support, which can favor Pd oxidation as the PdO "feet" are located on ceria surface at least for milled samples, and/or to the presence of water in the reaction atmosphere. It should be noted in fact that also during TPC dry up to 1% H_2O is formed as reaction product. The effect of water though seems less likely, since $PtPd/Al_2O_3$ catalysts treated at 1073 K in wet air do not show particular arrangements in TEM images[147]. Moreover, in some papers[145,147,148] the formation of PdO on the surface or as a layer on the outer shell of

bimetallic nanoparticles is supposed to occur, differently from what happens for the mushroom-like structures, which points again to a key role of ceria in keeping PdO anchored to its surface. Indeed, in other studies separate PdO and PtPd bimetallic phases were observed[72,74], more similarly to the impregnated catalyst, even if the occurrence of an intermetallic phase is detected also on milled samples. However, as outlined above this restructuring alone cannot explain the improvement in activity which takes place predominantly on milled samples with Pt content comprised between 0.2 and 0.65 wt%. The evidence collected in this work indicates that also the strong Pd-ceria interaction induced by the milling process, achieved only when Pd and ceria are milled first, is pivotal for both activity and stability of bimetallic PtPd-based catalysts.

3.4 Conclusions

The insertion of Pt in dry milled Pd-Ce catalysts was studied. Different compositions were considered and tested in transient and time-on-stream experiments. It was found that the addition of Pt decreased the activity of the catalyst and influenced the Pd-PdO cycling at high temperatures. However, it increased the stability of the catalyst with even an improvement in the activity during time-on-stream operation for Pd:Pt molar ratios between 1:1 and 8:1.

A key role of Pd-ceria interaction is then envisaged for bimetallic catalysts, similarly to what was reported for monometallic Pd/CeO_2 with the formation of an amorphous Pd-Ce-O layer uniformly surrounding ceria nanoparticles. The same layer is detected by HRTEM on *0.5Pt*-0.5PdCe M and *0.2Pt*-0.8PdCe M, covering also Pt clusters even if added in a second milling step. However, when the sample is prepared inverting the order of milling (first Pt and ceria, then Pd), as in the case of *0.5Pd*-0.5PtCe M, no layers are detected. A strong rearrangement occurs during the catalytic tests for all the bimetallic samples. XRD and TPR analysis pointed out the presence of an alloy for all the bimetallic samples treated at 1173K. HRTEM showed that the alloy in the bimetallic catalysts prepared by milling evolve in mushroom-like structures with a Pt head and a PdO body. With a similar mechanism, the sample prepared by incipient wetness impregnation is found rearranged in a needle-like structure with a PdO stem and a Pt head arising from big PtPd clusters not strictly interacting with ceria surface.

The catalyst obtained by milling first Pd and ceria then adding Pt (*0.5Pt*-0.5PdCe M) shows better performances with respect to its impregnated counterpart, and also with respect to the milled sample prepared inverting the order of milling.

The unique Pd-Ce interaction obtained by ball milling and the presence of the amorphous layer, unaltered after the insertion of Pt and after the TOS tests, is fundamental not only for the higher activity, but also for the development of a more defined PtPd rearrangement with high catalytic stability.

4. *In situ* XANES characterization of $PtPd/CeO_2$ catalysts prepared by mechanochemical synthesis

Abstract

Mechanically synthesized bimetallic $PtPd/CeO_2$ catalysts show an increasing activity recorded in time-on-stream experiments in presence of water, and the formation of a mushroom-like structure was observed by HRTEM on spent samples. The oxidation state of bimetallic samples is here determined during *in-situ* XANES analysis intended to mimic the time-on-stream experiment and follow the development of mushroom-like structures. A high amount of oxidized palladium is detected, which increases during the analysis, in line with the increasing catalytic performances.

4.1 Introduction

The behavior of catalysts under operating conditions is nowadays receiving more and more attention thanks to the development of *in situ* characterization techniques, which allow to unveil the chemical state of active phases following the evolution of their interaction with the support and the gas phase in conditions relevant to real applications. Looking at the interesting results obtained with $PtPd/CeO_2$ milled catalysts during wet time-on-stream experiments reported in the previous Chapter, it seemed then intriguing to investigate the modification of Pd and Pt during reaction, trying to shed some light on the possible link between the activity and the final morphology observed by HRTEM characterization.

Indeed, the chemical state of Pd is a variable which is always considered when studying Pd-based materials for lean methane oxidation[158]. For example, the support oxide is pivotal in promoting the stability of Pd or PdO, and the results achieved with some supports could not be reproduced with others.[159–162] The atmosphere of reaction is also an important variable having great influence on palladium[163–165], and even excluding too

wide compositions, the simple O_2/CH_4 ratio can change the metal oxidation state.[166] The presence or absence of water is another relevant factor affecting the state and response of Pd[78,77], as well as support morphology which modifies metal-support interaction at the nanoscale.[160,167] Our group has recently observed how, in dry milled catalysts, also the precursor has an impact on the valence of Pd.[149] It is then not surprising that the addition of a second metal can influence the chemical state of Pd, and different results are reported in the literature[159,148,79,137].

A sensitive technique for small amounts of Pd oxide is X-ray absorption spectroscopy (XAS), because it can detect dispersed oxides as well as crystallites. The x-ray absorption process is the result of the excitation of a core electron of an atom to a higher energy level by an incident photon. Different core electrons have distinct binding energies and if one plots the X-ray absorbance of a specific element as a function of incident energy, the resulting spectrum will appear similar to Figure 4-1.

As the energy of X-ray radiation is scanned through the binding energy regime of a core shell, a sudden increase of absorption appears, and such phenomenon corresponds to absorption of the X-ray photon by a specific type of core electrons. This gives rise to a so-called absorption edge in the XAS spectrum. Absorption edges are named according to the principal quantum number of the excited electrons. For example, when a 1s level electron is excited, the lowest-lying empty p-states will be occupied and the process is called K-edge-absorption. Similarly, when an electron of the 2p orbital is excited to unfilled d orbitals the absorption peak is called L-edge.

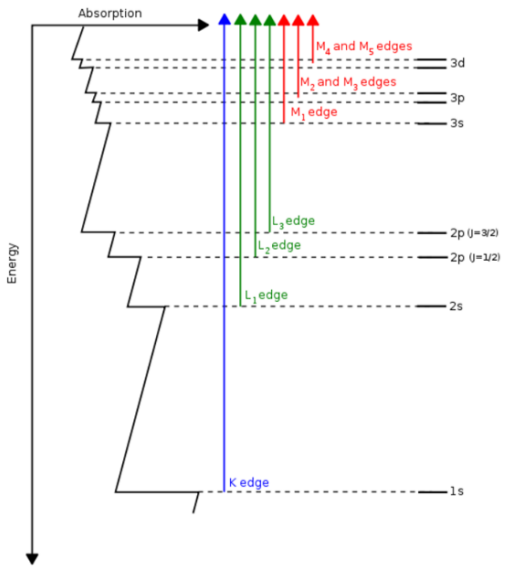

Figure 4-1: absorption edges corresponding to the excited core electrons as function of incident photon energy.

Each element has a characteristic energy level structure and therefore it can be studied separately. In a compound the empty energy levels above the Fermi level are sensitive to the nature of the chemical bond and valence. This provides a basis for valence determination through careful measurements of the position of the absorption edge, which can be useful to determine Pd oxides.

The K-edge absorption divides the spectrum into two regions, the X-ray absorption near edge structure (XANES) region, which provides electronic structure and local geometric information, and the extended X-ray absorption fine structure (EXAFS) region, which is used to obtain detailed structural information, such as bond lengths in different coordination shells, coordination numbers, and nearest neighbor atomic type.

XAS is here useful to determine the oxidation state trend of Pd by fingerprinting the spectra recorded with the standards of PdO and metallic Pd. Moreover, the linear combination analysis can return the percentage of the two species, useful to follow the complementary trend of Pd and PdO in the catalysts.

Even if it provides information that is averaged over the entire sample, it can be complemented with the results obtained by HRTEM to have a complete overview of the materials. Starting from these observations, it was decided to investigate by *in situ* x-ray absorption near edge structure spectroscopy (XANES) the activity of PtPd bimetallic milled catalysts in presence of water to check if and how the addition of Pt could alter the oxidation state of Pd, and if this was the reason for the activity improvement observed during time-on-stream experiments shown in Chapter 3, as suggested by some authors[65,74,148].

The experiments were carried out at ALBA synchrotron facility in Barcelona, in collaboration with the Institute of Energy Technologies and Department of Chemical Engineering of Universitat Politècnica de Catalunya.

4.2 Materials and methods

Samples for *in-situ* characterization were prepared by dry milling Pd, Pt, and ceria powders following the procedure described in Chapter 3.2. Three samples were prepared for the *in-situ* measurements: one bimetallic with palladium and platinum and two monometallic, one with palladium and one with platinum, as references. In this case, the amount of PGM loaded was 1.5 wt% for each metal, considered to be the minimum amount to obtain a good signal at the synchrotron beamline. A fourth sample

containing 1.5% Pd and 1.5% Pt was prepared as a reference by incipient wetness impregnation, similarly to what was reported in Chapter 3.2.

For sake of clarity, the scheme of the TOS experiment carried out in Udine is reported in Figure 4-2. (see Chapter 2 for experimental details). Three points at room temperature are highlighted which correspond to the points at which the different samples were collected for *ex-situ* XANES measurements.

The beamline cell at ALBA could not allow temperatures higher than 923K, thus it was not possible to reproduce the pretreatment in the *in-situ* experiment. It was decided to replicate thus only the isothermal part (blue line in Figure 4-2). All samples were then pretreated in lean methane oxidation (TPC) in a dry atmosphere up to 1173K (ramp rate 10 K/min) in the setup in Udine and named as "-TPCdry" as also reported in Figure 4-2 (red line). The bimetallic milled sample was also treated during the entire TOS experiment, with both pretreatment and isothermal parts, and named as "-TOSwet". This was done to compare the reproducibility of the results of the two setups, the one in Udine and the one in Barcelona. The as-prepared samples were named "-fresh" (i.e. without any treatment), thus having a reference of the materials before the experiments (see Figure 4-2, green dot).

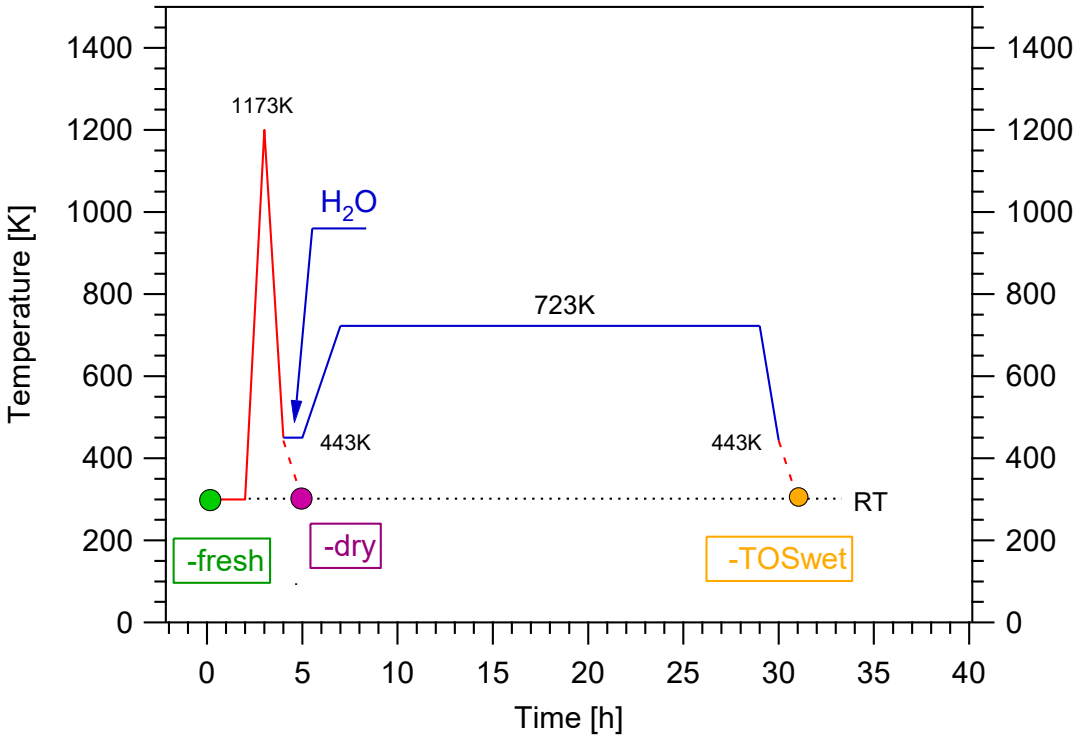

Figure 4-2: scheme of TOS wet treatment with collection points for XANES analysis. The dry pretreatment up to 1173K is reported in red, it is specified the injection of water at 443K and, in blue, the 24h isothermal step at 723K.

Table 4-1 summarizes all these samples (-fresh, -TPCdry, -TOSwet) with the nominal PGM loading and the corresponding treatment.

Table 4-1: sample list with corresponding Pd loading and treatment

Sample NAME	Nominal Pt loading wt%	Nominal Pd loading wt%	Treatment
PdCe-fresh	0	1.5	None
PtCe-fresh	1.5	0	None
PtPdCe-fresh	1.5	1.5	None
PtPdCeIW fresh	1.5	1.5	Calcined @1173K
PdCe-TPCdry	0	1.5	TPC dry up to 1173K
PtCe-TPCdry	1.5	0	TPC dry up to 1173K
PtPdCe-TPCdry	1.5	1.5	TPC dry up to 1173K
PtPdCeIW -TPCdry	1.5	1.5	TPC dry up to 1173K
PtPdCe-TOSwet	1.5	1.5	TOS wet @723K

4.2.1 *In-situ* measurements

The *in-situ* analysis was intended to simulate the TOS wet test, where the mushroom-like structures seem to form (see Chapter 3) and was carried out on samples after the TPC dry treatment. The analysis was carried out recording the Pd K-edge signals for the Pd-containing samples providing information about Pd oxidation state. The Pt L3-edge was also monitored for the Pt-containing samples. All these data were matched trying to get some insights on the mutual evolution of Pd and Pt species. This work focused on XANES data, analyzed and normalized using Athena XAS data processing software.

Before *in-situ* measurements, an *ex-situ* analysis at room temperature (RT) was carried out on foils and oxides (Pd, PdO, Pt) as references and on all samples object of this study.

The process involved is known as semiquantitative fingerprinting. The signal of the samples are compared with the references signal and thus the species are deduced. It is possible then to quantify indirectly the amount of the species by a linear combination of the signal in respect to the references.

The Pd K-edge was measured in transmission mode and the Pt L3-edge in fluorescence mode. To measure the Pt L3-edge, 23-28 mg of sample diluted with 90-96 mg of boron

nitride (BN) were used. For the Pd K-edge, 164-179 mg of catalyst diluted with 40-46 mg of BN were used. For both edges, 13 mm pellets were prepared.

The composition of the feed was kept equal to that of powder tests carried out in Udine (0.5% CH_4, 2% O_2 in He for dry conditions and the addition of 10% H_2O for wet conditions), and the flowrate was reduced based on catalyst weight to maintain the GHSV of ca. 200000 h^{-1}. The general scheme of the *in-situ* time-on-stream experiments, named TOS*, is reported in Figure 4-3. TOS* indicates the treatment carried out in *in-situ* conditions at the synchrotron beamline, to distinguish it from the TOS treatment carried out in the powder setup for sample preparation.

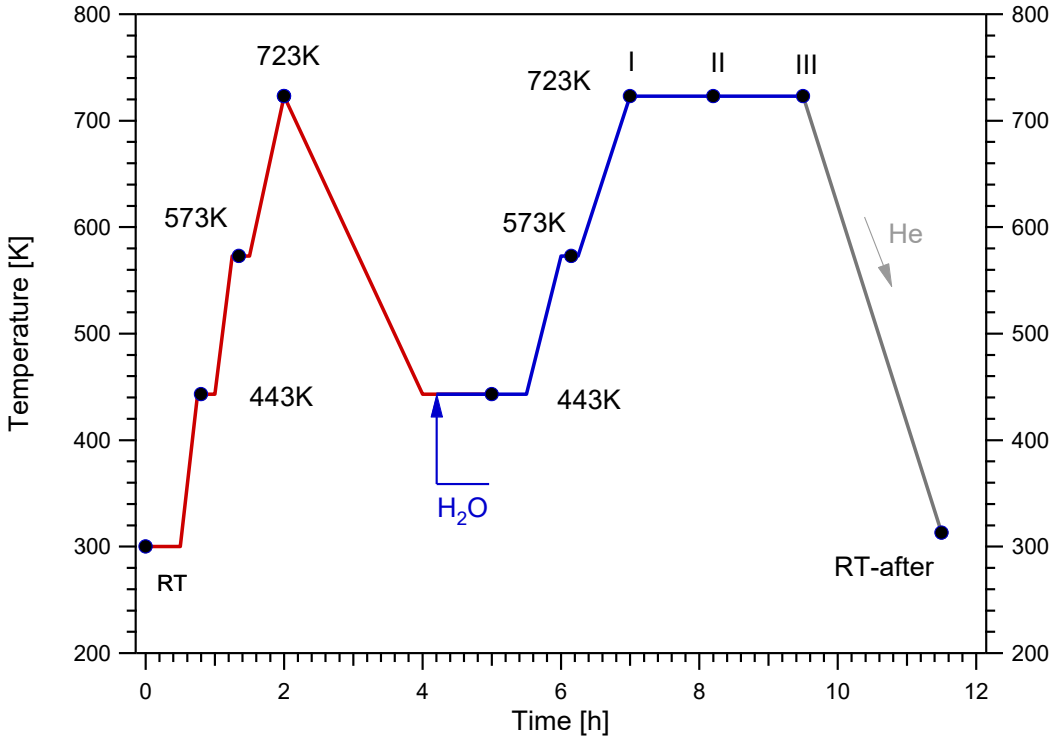

Figure 4-3: Scheme of TOS in-situ analysis.*

As shown in Figure 4-3, the samples were heated from room temperature (RT) to 723K in dry conditions and then cooled down to 443K. At this point, water was introduced and the temperature raised again at 723K for the wet isotherm. Due to lack of time at the beamline, the 24 hours of the original catalytic test could not be maintained and only three consecutive measurements were carried out (lasting about 2 hours). The sample was then cooled down to RT in He. XANES were acquired for each reported step. During both heating ramps, two intermediate acquisition steps were added, at 443K and 573K.

4.3 Results and discussion

As a preliminary step, HRTEM analysis was performed on PtPdCe-TOSwet to assess if the mushroom-like structures were formed also on the sample containing a total 3 wt% of PGM adapted for the *in-situ* XANES experiments. Figure 4-4 shows that indeed also in this case structures similar to those described in Chapter 3 are observed.

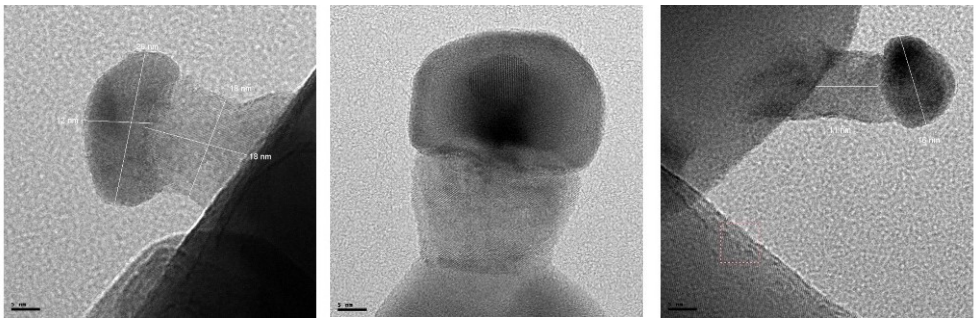

Figure 4-4: HRTEM images of sample PtPdCe-TOSwet.

4.3.1 *In-situ* measurements: Pt-L_3 edge

No changes were almost detected on Pt-L_3 edge signal during in-situ TOS* experiments. Here, in Figure 4-5, Figure 4-6, and Figure 4-7 the samples PtCe-TPCdry, PtPdCe-TPCdry, and PtPdCeIW-TPCdry are reported respectively, with only the signals recorded at RT and 723K, for an easier view (RT_after indicates the measurement at room temperature at the end of the in situ experiment).

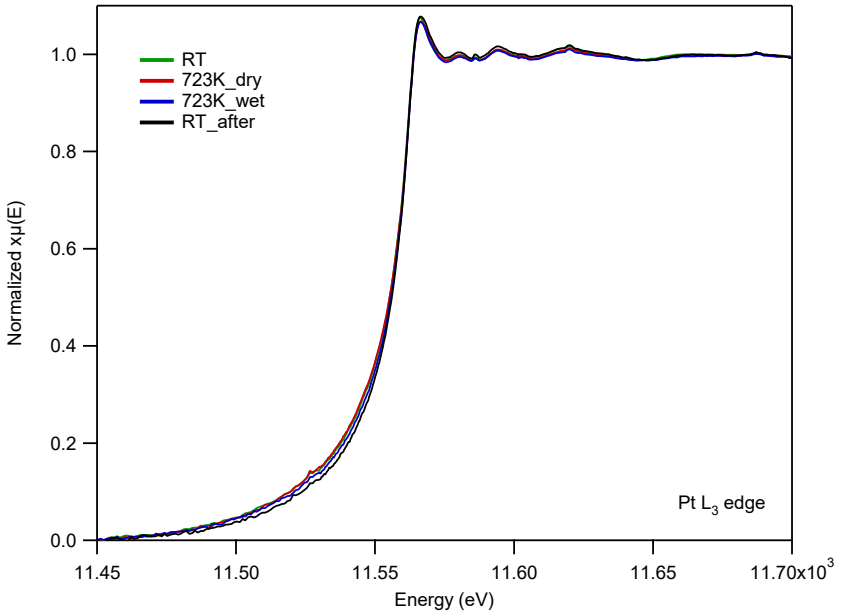

Figure 4-5: PtCe-TPCdry in-situ TOS.*

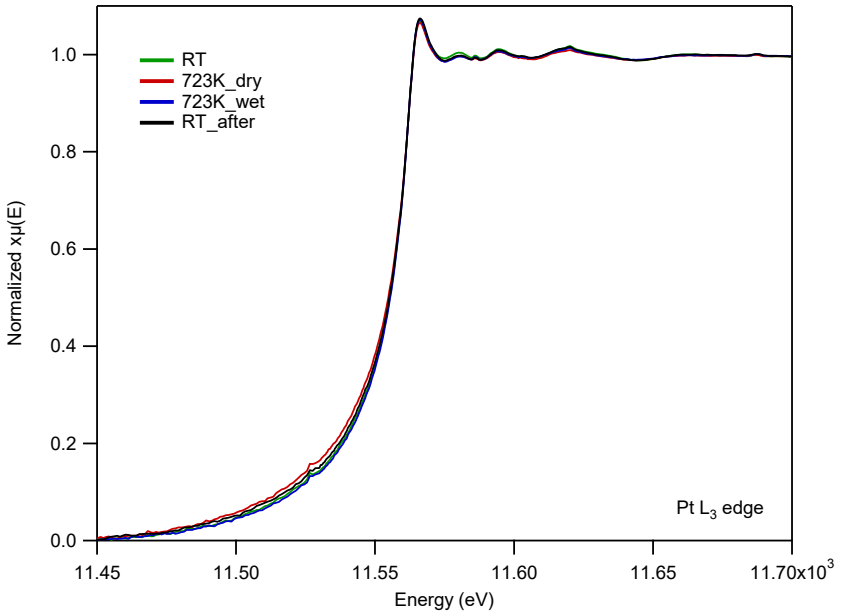

Figure 4-6: PtPdCe-TPCdry in-situ TOS.*

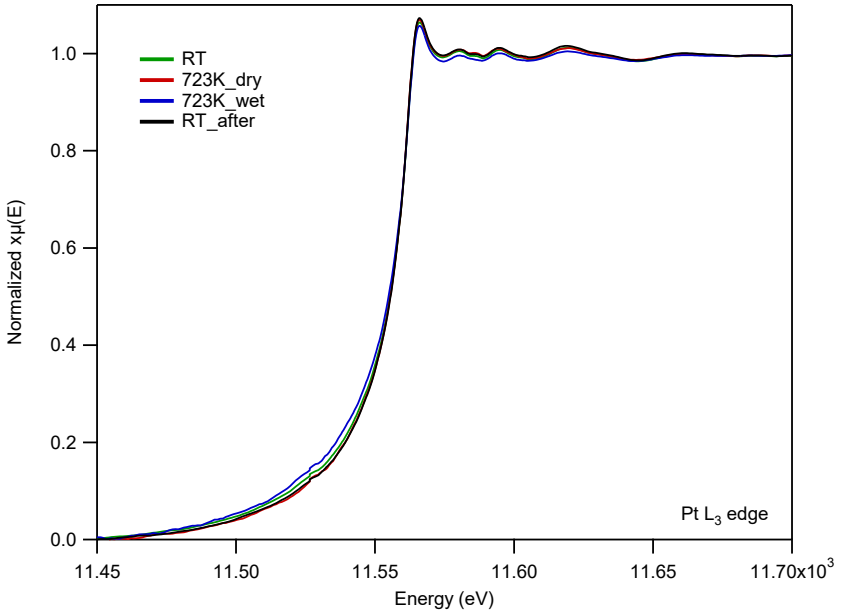

Figure 4-7: PtPdCeIW-TPCdry in-situ TOS.*

From XANES measurements it appears that no significant changes affect the Pt chemical state of the catalysts, which remain mostly metallic during *in-situ* TOS* experiments, similarly to what observed in other reports.[70]

4.3.2 *In-situ* measurements: Pd-K edge

Figure 4-8 shows the comparison between the palladium reference materials and the fresh samples (as prepared) recorded *ex-situ*. Differently from what was observed for Pt, substantial differences can be noticed for Pd K-edge.

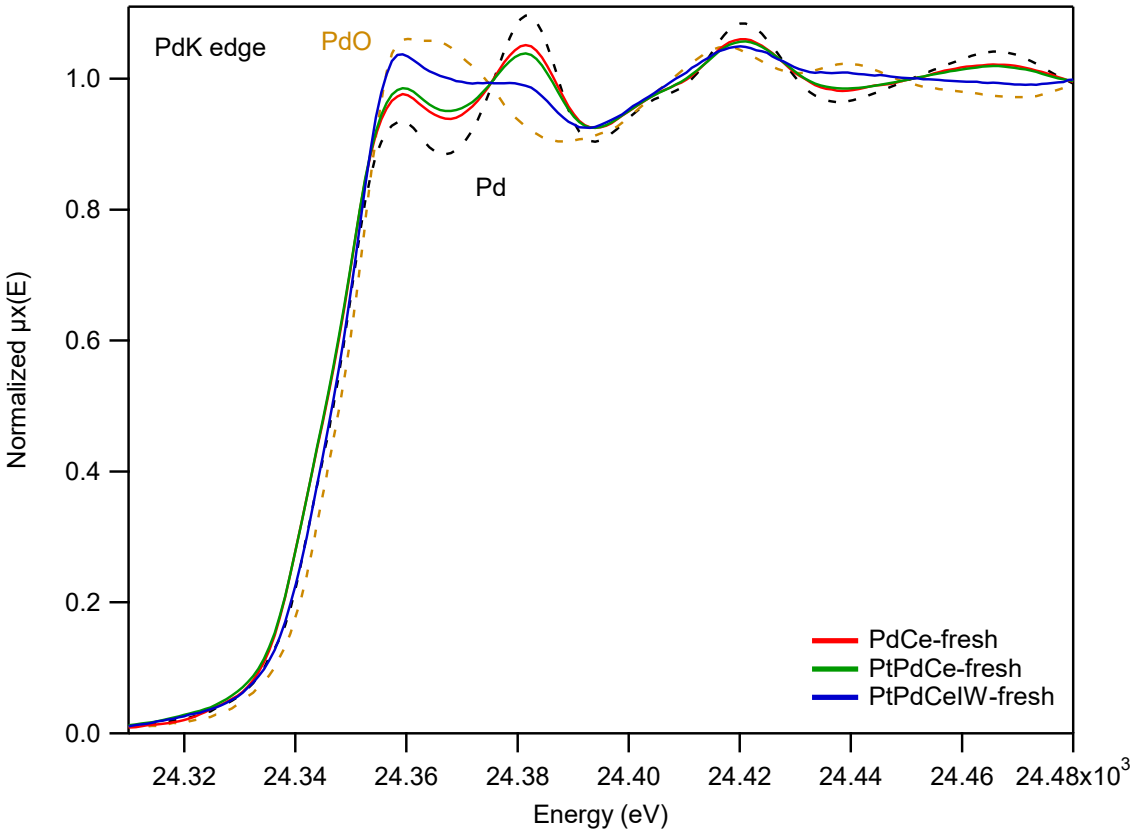

Figure 4-8: ex-situ XANES at room temperature for fresh samples, Pd foil and PdO references (dashed lines).

The sample PtPdCeIW-fresh is the most oxidized of the series, in line with what expected after the calcination treatment at 1173K. The milled samples appear to be closer to the metallic reference, and this is also in agreement with the metallic Pd precursor employed in the mechanical synthesis. In the edge position, PtPdCeIW-fresh overlays the Pd foil signal, while the milled samples are shifted to lower energies suggesting an interaction between ceria and palladium enhanced by the dry milling process (electronegativity: Ce (1.12) < Pd (2.20) < Pt (2.8)).

In Figure 4-9 the same comparison is shown for the samples after the dry TPC.

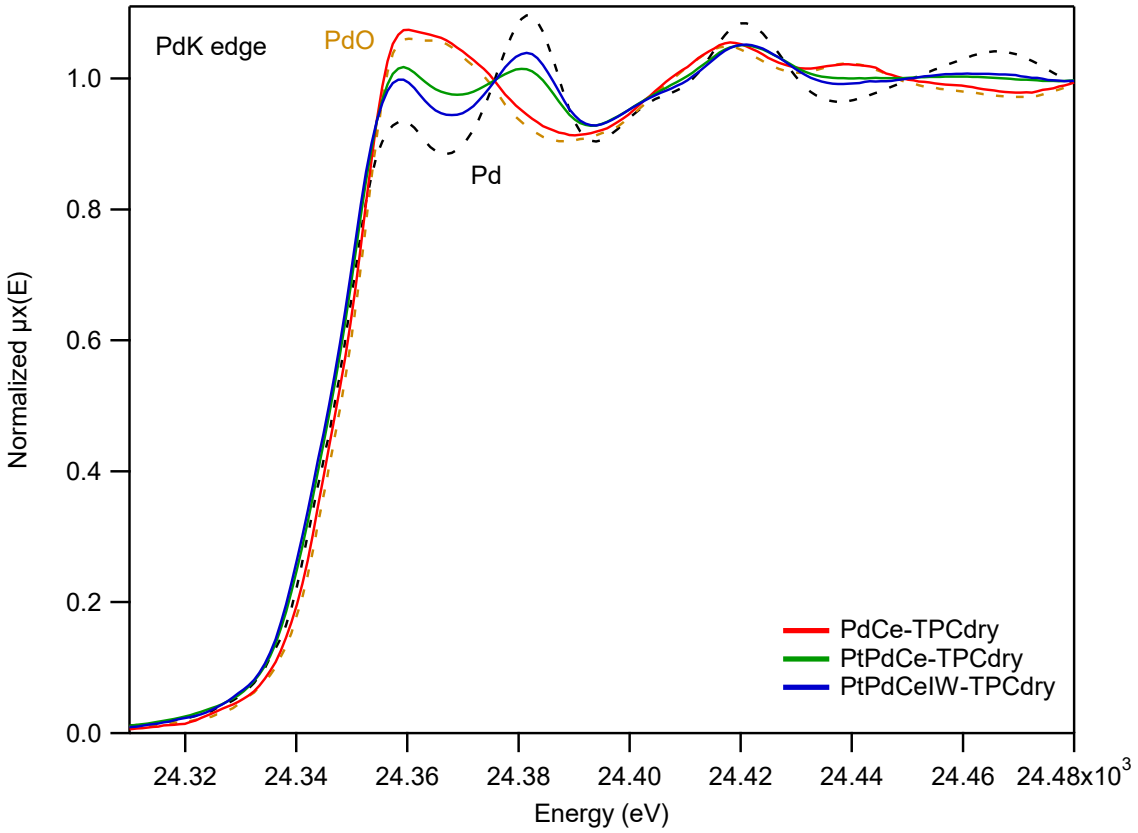

Figure 4-9: ex-situ XANES at room temperature for samples treated during TPC dry pretreatment (dashed lines: Pd foil and PdO references).

In this case, the results show a different trend, with bimetallic samples being more reduced (PtPdCeIW-TPCdry the most reduced one) and the monometallic Pd sample resembling the PdO reference. The oxidation of PdCe-TPCdry is not surprising, as the reaction takes place with an excess of oxygen that oxidizes the metallic Pd used for the preparation. In this respect, the addition of platinum inhibits Pd oxidation possibly via the formation of a PdPt alloy leading to the XANES spectra observed in Figure 4-8 which are half way between Pd foil and PdO reference. The effect of Pt on the redox cycling of Pd during the TPC dry was already discussed in Chapter 3 and it is in line with this trend.

Figure 4-10 displays the XANES spectrum of the bimetallic sample after the *in-situ* analysis, named PtPdCe-TOS*. It is compared with the spectrum recorded *ex-situ* on the catalyst after the TOS wet experiment carried out in the powder reactor, PtPdCe-TOSwet.

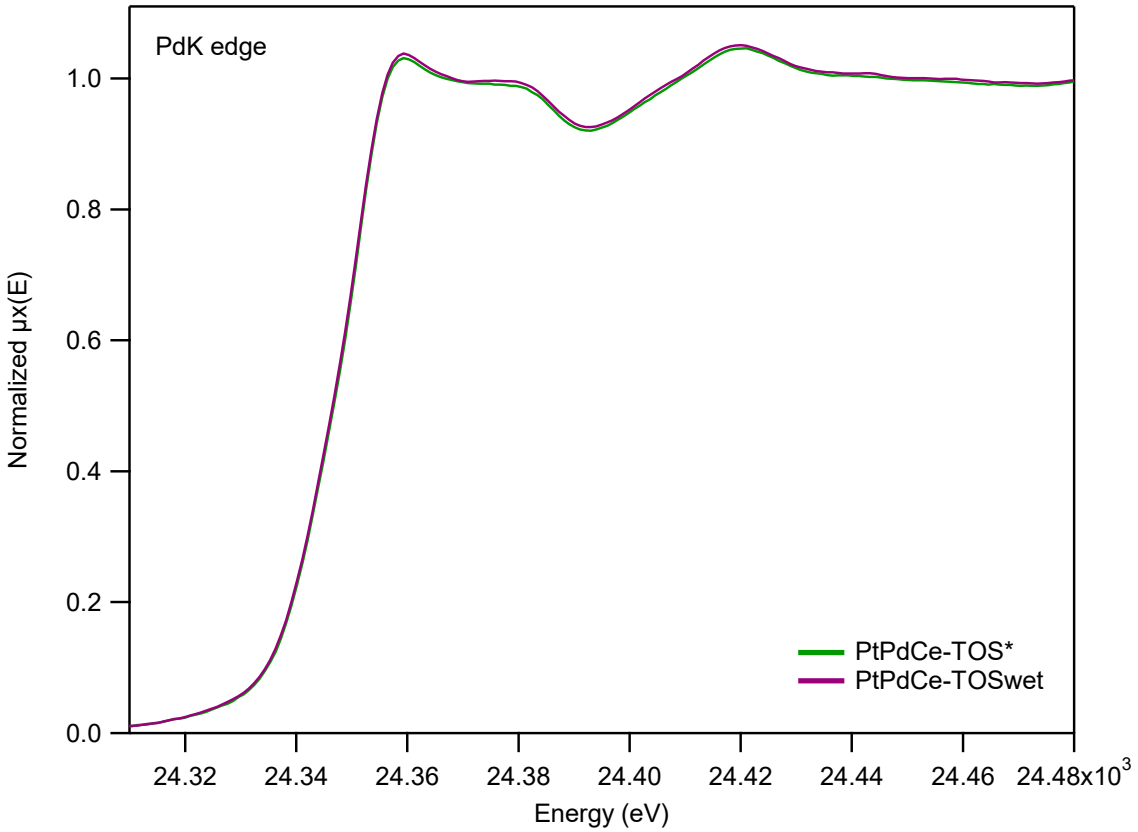

Figure 4-10: ex-situ XANES at room temperature for the sample treated during TOS wet and sample after the TOS wet in-situ analysis.*

The XANES spectrum of PtPdCe-TOSwet is superimposable to that of PtPdCe-TPCdry treated during TOS* wet *in-situ* (PtPdCe-TOS*). This confirms the consistency between experimental conditions applied in Udine and in Barcelona and allowed further *in-situ* characterization.

In Figure 4-11 a sequence of *in-situ* XANES spectra recorded for PtPdCe-TPCdry and PtPdCeIW-TPCdry is reported. For a simpler view, only the spectrum recorded at the beginning at room temperature and the three spectra recorded during the wet isotherm are shown.

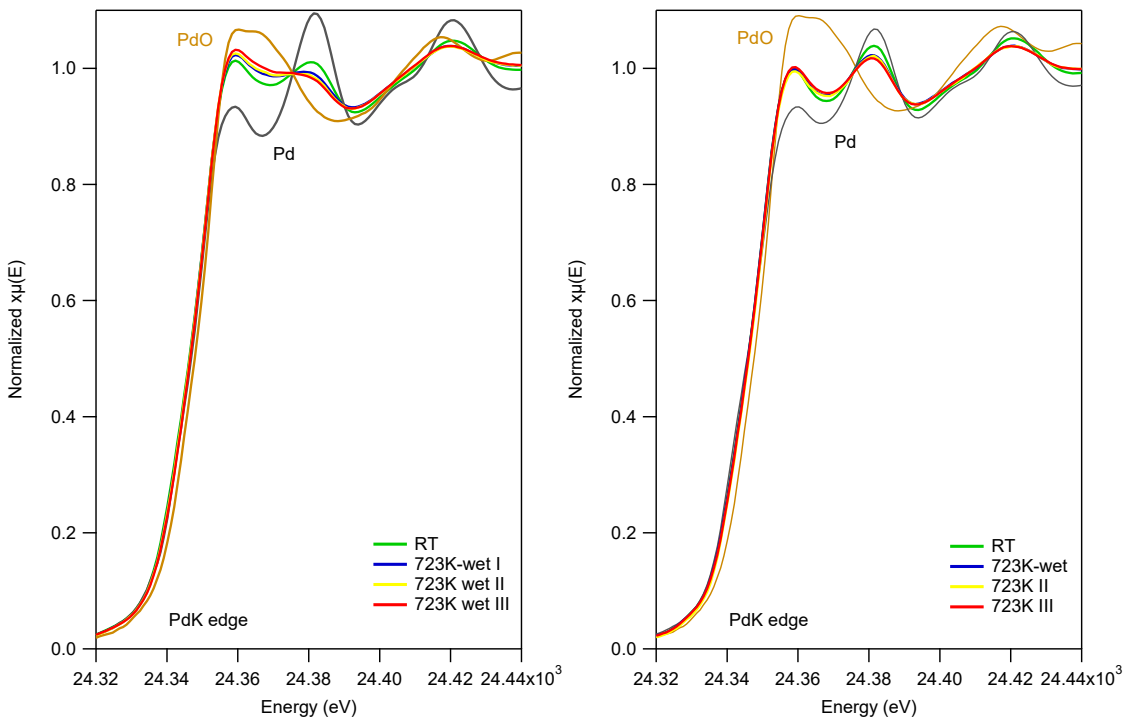

Figure 4-11: in-situ XANES for PtPdCe-TPCdry (left) and PtPdCeIW-TPCdry (right) recorded during in-situ experiments. The first spectrum recorded, at RT, and the three spectra recorded during the wet isotherm are shown.

It can be observed that, during the isothermal step, PtPdCe-TPCdry gets closer to the PdO signal, i.e. it oxidizes during time-on-stream. The bimetallic impregnated sample instead is clearly in a more reduced state which does not change significantly during the experiment.

To appreciate better this comparison, the linear combination fitting of the spectra was elaborated weighting the two spectra of the references, Pd and PdO, at the characteristic temperatures of the *in-situ* experiment. The results for the two bimetallic samples and the monometallic PdCe-TPCdry are reported in Figure 4-12 in terms of % PdO. The evolution in the Pd oxidation state during *in-situ* analysis can be clearly observed. The monometallic milled sample is the one with the highest amount of PdO, which remains substantially unchanged throughout the experiment. The bimetallic samples start both with a much lower PdO fraction (PtPdCeIW-TPCdry < PtPdCe-TPCdry), with a significant increase for the milled sample during the experiment (from 48% to 64%) which appears to be boosted by the introduction of water. Indeed, the milled catalyst goes from 54% to 64% when water is present in the feed and apparently it would have increased further if the isotherm was longer. The amount of PdO in the impregnated catalyst shows also a slight increase (from 29% to 36%), but the effect seems more

related to the temperature increase than to the wet atmosphere (from the introduction of water onwards for the whole isotherm the oxidation state does not change).

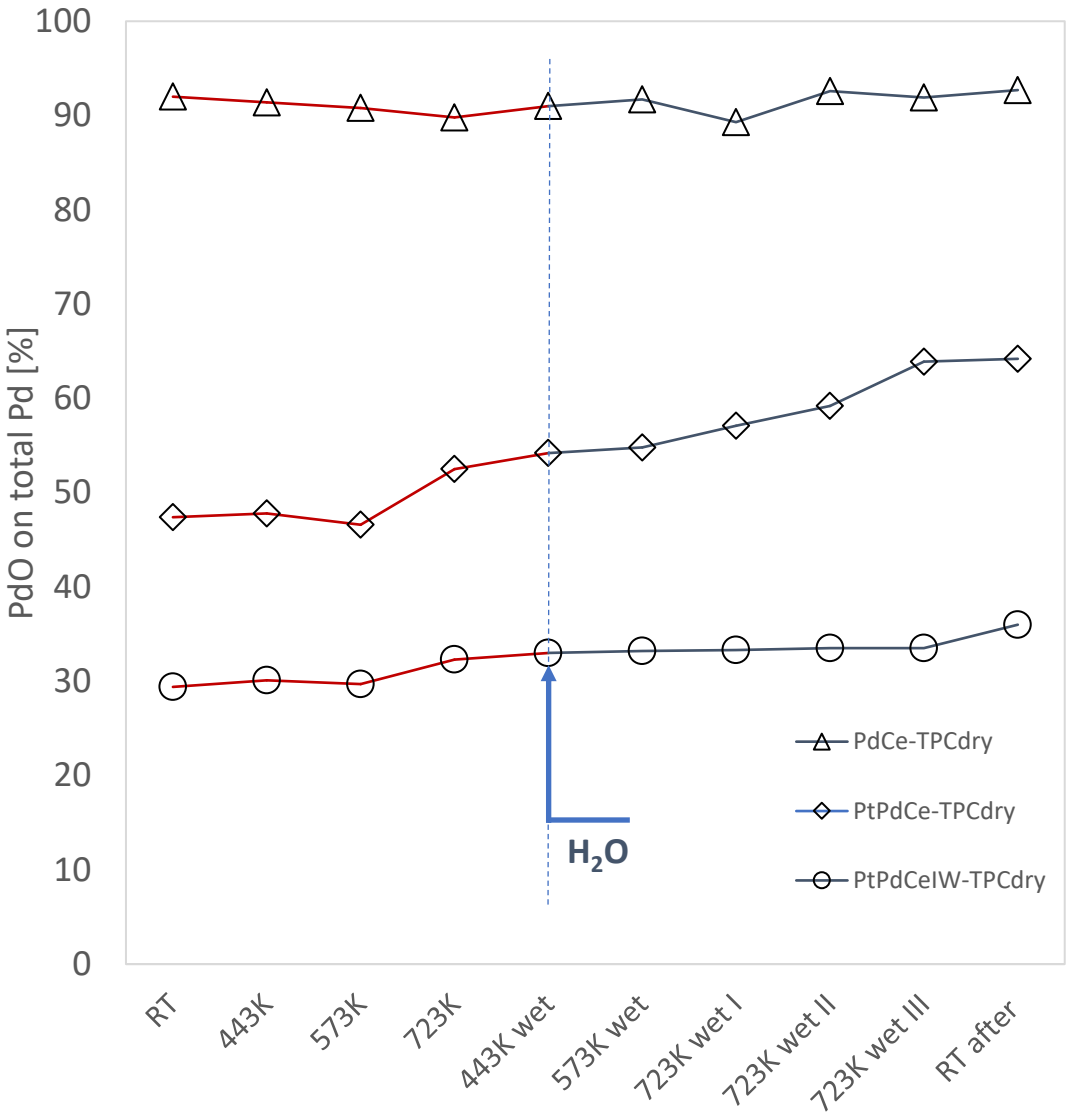

Figure 4-12: PdO content (%) obtained from linear fitting of in-situ spectra at some characteristic temperatures for PdCe-TPCdry, PtPdCe-TPCdry, and PtPdCeIW-TPCdry

The results summarized in Figure 4-12 highlight the enrichment in PdO of the bimetallic milled catalyst, which can be considered the reason of the improvement in activity observed during wet TOS experiments, as already hypothesized in the literature,[74] PdO being more active than Pt or PtPd alloy for methane oxidation. Nevertheless, the whole picture (i.e. powder TOS wet tests coupled with *in*-situ characterization) suggests that to achieve a good resistance in wet atmosphere there should be an optimum PdO/Pd ratio, as the monometallic PdCe catalyst (which has the

higher PdO fraction) is deactivated in presence of water. The simultaneous presence of Pd in different oxidation states has been indicated recently as responsible for higher catalytic activity,[149] and this also might account for the improved stability of this sample. It is likely that the coexistence of Pd in reduced and oxidized states is optimized by the introduction of Pt in the milling process. Moreover, the stabilization of PdO in PtPdCe-dry might be also physically related to the protective Pt "head" observed in the mushroom-like structures evidenced by HRTEM analysis. This, in combination with the intrinsically higher activity of milled samples and the enrichment in PdO of PtPdCe-TPCdry, can explain the good performances observed for this sample in wet atmosphere.

4.4 Conclusions

An *in-situ* XANES analysis was carried out at ALBA synchrotron facility in Barcelona on the bimetallic samples prepared by both mechanochemical synthesis and incipient wetness impregnation. The experiments were designed to study the oxidation state of the samples during time-on-stream tests in wet atmosphere, trying to find a correlation with the morphological changes observed by HRTEM analysis and reported in Chapter 3. The overall results obtained also for the monometallic PdCe milled catalyst show that the insertion of Pt sensibly changes the amount of PdO present, irrespective of the synthesis method. For the bimetallic milled sample, the extent of Pd oxidation increases significantly over time, particularly in presence of water. These evidences, coupled with the previously observed catalytic results, allow to correlate the increase in catalytic activity during TOS wet reported in Chapter 3 with the increase in the fraction of oxidized Pd for $PtPd/CeO_2$ sample prepared by dry milling. It should be recalled that the results reported in this chapter indicate that to achieve good catalyst stability in wet atmosphere, an optimum PdO/Pd ratio seems necessary.

5. Effect of Sn and In as co-metals for Pd/CeO_2 catalysts prepared by dry milling for methane oxidation

Abstract

In this Chapter a preliminary study of tin and indium as partial substituents in Pd/CeO_2 catalysts prepared by mechanical synthesis for the lean oxidation of methane is reported. Both light-off and time-on-stream catalytic tests were performed to evaluate the performances of the catalysts. The addition of Sn and In was found to have no effect on the activity of Pd/CeO_2 in transient dry experiments. The activity decreases when water is present for all samples, with a more evident trend in presence of indium and, to a lesser extent, of tin. No contribution of tin was observed in time-on-stream tests. To explain the negligible impact of the second metal on catalytic activity further studies are needed, however the effectiveness of mechanochemical synthesis is once again confirmed by comparison with a tin-based catalyst made by impregnation.

5.1 Introduction

The promotion of the stability of Pd-based catalysts by the introduction of Pt as a co-metal is well-known[54] and it has been investigated and confirmed also in this thesis for the dry milled catalysts in the previous chapters (Chapter 3 and Chapter 4).

As mentioned in the introduction, and experienced directly during the secondment period at Umicore, the price issue is at the top of the list in designing commercial catalysts. Pt will probably have an impact in these terms, given the direct role of the market prospected to change rapidly in the next years. Pt substitution, however, could be not enough to compensate for the Pd price increase. Several different co-metals for bimetallic Pd-based catalysts have been proposed and studied in literature[83–85]. From a chemical point of view, all these solutions give interesting insights for both the

formulation of new materials and for a deeper understanding of Pd based catalysts. From an engineering point of view, however, the syntheses are often complexes and a high amount of solvent is generally involved, with a strong impact on the price of production, both in economic and environmental terms. Among all the metals screened, to the best of our knowledge Pd with Co or Sn seems the easier substitution possible, requiring a simple incipient wetness impregnation method to obtain a performant catalyst[87,168]. They are found in fact to increase Pd dispersion and overall oxygen mobility, thus improving methane catalytic activity, also in the presence of water[86,88,169]. Thinking about the engineering point of view, however, Co is hardly manageable due to its high toxicity[170] and it was excluded even if interesting. Sn is largely studied as a support oxide and co-metal for Pd-based catalysts and it is specifically reported to improve stability in presence of water.[88,171,172,173] Moreover, complete methane oxidation can be achieved by doping Sn with In, in the so-called ITO (Indium-Tin-Oxide) material[174]. These two compounds are widely involved in electronic applications for CH_4 sensors[175,176] and chemical conversion of CH_4 to other products.[177,178]

Keeping in mind the above mentioned issues, we chose then to study the effect of the addition of Sn into Pd/CeO_2 catalysts by mechanochemical synthesis. At the same time, it was considered also the addition of In for the similar electronic and mechanical characteristics, even if the price is not as accessible. Indium oxide is an n-type semiconductor with wide bandwidth, which makes it of interest in catalytic applications, also for methane abatement.[179] The choice of these two co-metals has been made also on the basis of their mechanical properties, motivated by our previous experience with Pd-CeO_2 catalysts.

The high catalytic activity of Pd/CeO_2 prepared by ball milling was attributed to the intimate contact realized between Pd and CeO_2 during the milling process, and visible through the formation of an amorphous layer of Pd-Ce around CeO_2 crystallites. One of the parameters that could play a role in the formation of the layer was believed to be the reciprocal hardness of the compounds involved in the mechanical mixing. This was based on the previous observation of the formation of a carbon layer, the soft part, around CZ crystallites, the hard part, obtained by ball milling.[180] Also, in this thesis it was observed that Pt, harder than Pd[181], could not form a layer on the CeO_2 support. However, it was also observed that Pd did not form the same structure when milled with Zr[126], which is much harder than CeO_2[182,183]. The reciprocal hardness thus might explain only partially the formation of the layer. However, it is worth noting that tin has the

lowest hardness of all the compounds mentioned here, with 0.22 GPa assessed in nanoindentation tests[184]. This value is not available for indium, nevertheless it is referred to have similar hardness assessed by different procedures.[185] Sn and In then seemed promising also from this point of view, and in this Chapter are compared with a monometallic Pd sample and other Sn-containing catalysts prepared with a slightly modified procedure. A fast screening of different co-metals and formulations has been possible thanks to the versatile mechanochemical preparation, which allows very fast and cheap trials compared to other synthesis methods.

5.2 Material and methods

Pure cerium oxide (CeO_2, Treibacher Industrie, AG) previously calcined at 1173 K for 3 hours was used as support for the catalysts. Metallic palladium (Pd black, Sigma Aldrich, surface area 40-60 m^2/g), tin acetate (Tin(II)Acetate, Sigma Aldrich), or indium nitrate (Indium III nitrate hydrate, Sigma Aldrich, 99.999%) nanopowders were mechanically mixed with CeO_2 in a Mini-mill Pulverisette 23 (Fritsch) to obtain the samples defined as milled (M). A further series was obtained by calcining first tin acetate at 1173K for 1h alone in static air, obtaining SnO_2 which then was used as Sn precursor for the mechanochemical synthesis.

All samples were prepared in two separate steps, starting by milling one metal precursor with cerium dioxide, followed by the insertion of the second metal precursor. Each step lasted 10 minutes and the oscillation frequency was set to 15Hz. It was decided to fix the amount of Pd at 0.5wt% and to add an equal amount (in weight) of the second metal. The samples were named as 2°M1°M CeM, where 1°M is the first metal mixed with CeO_2 (Pd; Sn), 2°M is the second one introduced (Pd; Sn; SnO_2; In).

A monometallic 0.5 wt% Pd/CeO_2 catalyst was prepared by mechanical synthesis for comparison. Conventional incipient wetness impregnated SnPd sample (SnPd CeIW) was also prepared as reference: cerium dioxide was impregnated with a palladium nitrate solution (4.8% of Pd, Sigma Aldrich), dried overnight at 393K, then subsequently impregnated with a solution of tin acetate in ethanol (Fluka, ≥99.8%). The resulting catalyst was dried overnight and calcined in air for 3 hours at 1173K.

All samples, with relative names and composition, are summarized in Table 5-1.

Table 5-1: Composition, mass and molar ratios, and names of samples considered in this work.

Sample NAME	Nominal Sn wt%	Nominal In wt%	Nominal Pd wt%	Pd/M molar ratio
PdCe M	/	/	0.5	/
SnPd CeM	0.5	/	0.5	1.11
InPd CeM	/	0.5	0.5	1.07
PdSn CeM	0.5	/	0.5	1.11
SnO_2Pd CeM	0.5	/	0.5	1.11
SnPd CeIW	0.5	/	0.5	1.11

The physicochemical properties of the samples were investigated by BET surface area measurements and X-ray diffraction analysis (XRD). Redox properties were also studied by temperature-programmed tests in reducing atmosphere (Temperature Programmed Reduction, TPR).

5.3 Results and discussion

The BET surface areas of the as-prepared samples are reported in Table 5-2.

Table 5-2: BET surface area of catalysts and support oxide used in this study.

Sample	BET [m^2/g]
CeO_2	3.0
Pd CeM	3.1
SnPd CeM	3.6
InPd CeM	3.2
PdSn CeM	3.3
SnO_2 Pd CeM	3.2
SnPd CeIW	3.3

The values are close to that of the oxide support, around 3 m^2/g, and as already observed for bimetallic PtPd samples they do not change significantly after milling.

In Figure 5-1 the XRD patterns are reported. For sample SnPd CeM the effect of calcination was also studied (3h at 1173K in air), and it is reported as "SnPdCeM calcined". Beside the two characteristic peaks of cubic CeO_2, only three other peaks can

be observed. One is the Pd peak at 40.1° on sample PdCeM. The 33.7° peak of PdO phase is detected on SnPd CeM calcined and on SnPd CeIW, likely due to the treatment at 1173K which oxidizes palladium. The last one, very small, is the peak attributable to In_2O_3 at 35.6° on sample InPd CeM. No other peaks are detected, likely because of the low metal loading and/or a high dispersion of the metals on ceria surface.

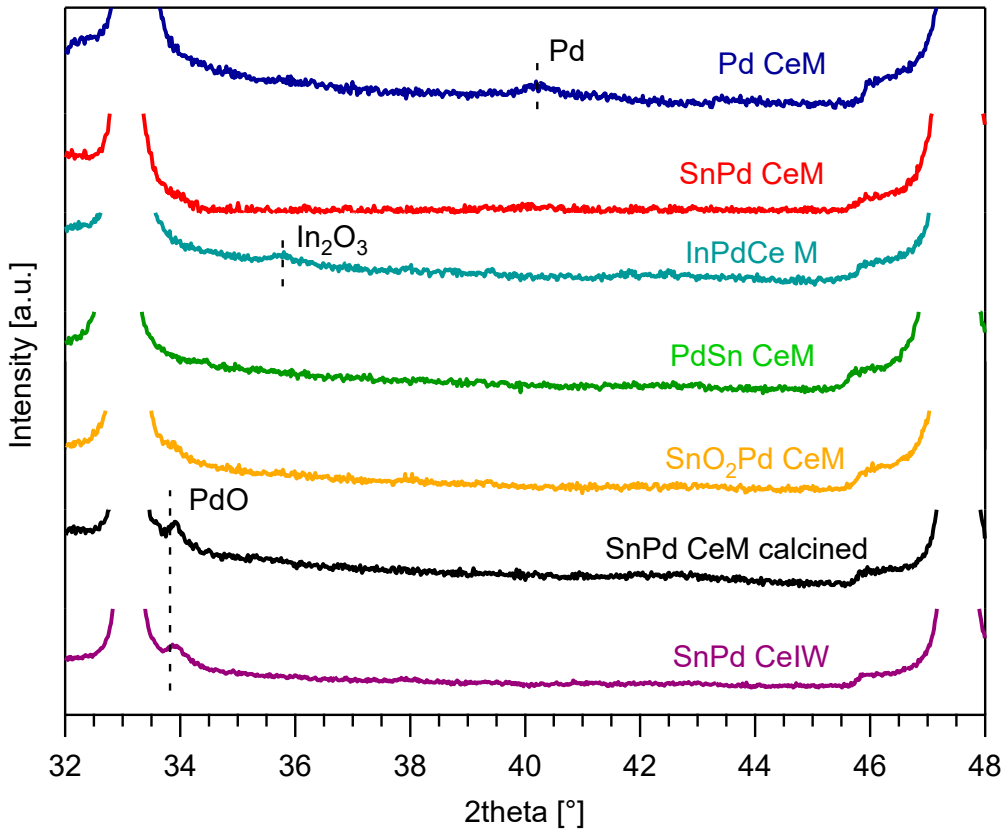

Figure 5-1: XRD spectra of fresh catalysts in the 32-48° 2θ range.

In Figure 5-2 the conversion of methane in dry lean oxidation for samples SnPdCeM, InPdCeM and PdCeM is reported.

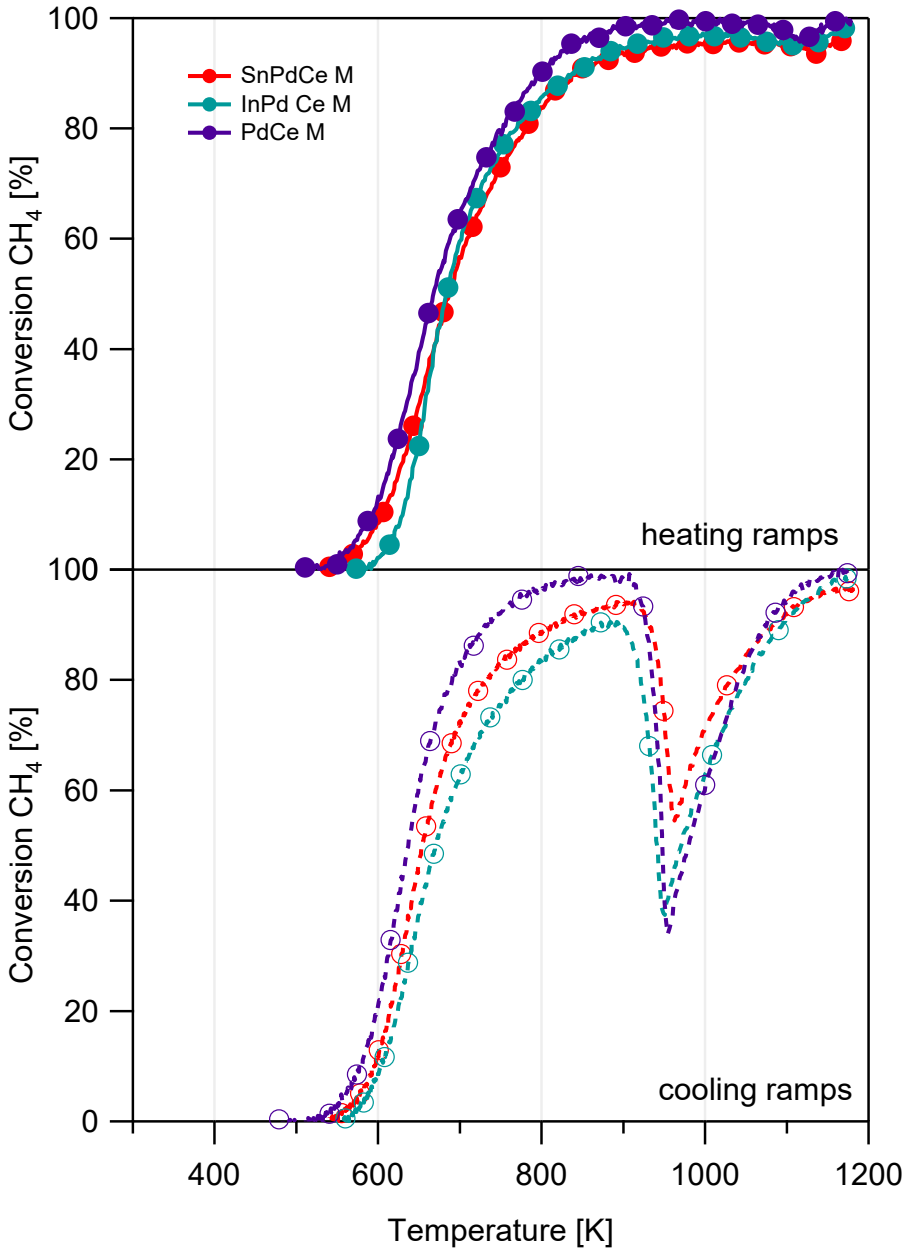

Figure 5-2: TPC-dry for bimetallic SnPdCe M and InPd CeM compared to monometallic Pd CeM; heating ramp above, cooling ramp below; GHSV ca.200000 h^{-1}, 0.5% CH_4, 2% O_2, He to balance.

The addition of the second metal to the Pd/Ce system does not alter significantly the catalytic performances. During the heating ramp, the catalytic activity almost resembles the monometallic palladium catalyst. This suggests that the Pd-Ce interaction taking place in the amorphous layer is not altered by the insertion of Sn and In, since the performances are the same. There is a slight difference in the cooling ramp with the

overall conversion following the order Pd>PdSn>PdIn. It should be observed, though, that the addition of Sn has a beneficial effect on the loss in conversion at high temperature due to the PdO-Pd-PdO transformation, indicating some interaction between Sn and Pd that helps the stabilization of palladium oxide, which is the active phase in this temperature range.

When water is added in the feed, the insertion of the second metal clearly worsens the activity of Pd/CeO_2 with a higher deactivation observed for Indium, as reported in Figure 5-3. Here the values of T_{10} and T_{50}, the temperature at which 10% and 50% methane conversion is achieved, for the I and II cycles of wet methane oxidation (TPC wet) are reported.

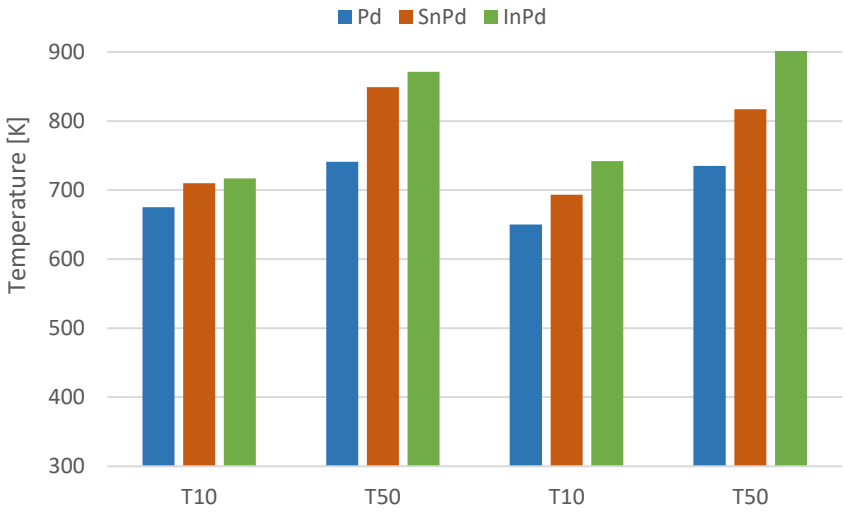

Figure 5-3: T_{10} and T_{50} for the I and II cycles of TPC wet.

Interestingly, the addition of both Sn and In has a negative effect on catalytic performances in wet atmosphere, dry TPC curves being almost superimposable to the monometallic catalyst. Indeed, it was expected to observe an improvement possibly related to higher oxygen surface exchange, at least for Sn for which a stabilization effect in wet atmosphere is reported in literature[88]. Trying to better understand the effect of Sn addition, that in the two bimetallic samples gave the best performances, further investigation was carried out.

SnPdCeM is compared, in Figure 5-4, with two homologous samples during methane oxidation in dry conditions. One is prepared by incipient wetness impregnation, SnPdCeIW, whereas the other is prepared by milling first Sn with Ce and adding Pd in a

second step, PdSnCeM. Both the two samples perform worse than SnPdCeM. As seen for the bimetallic system PtPd on CeO_2, it is then confirmed the importance of the intimate contact between Pd and CeO_2 to get good catalytic activity. Moreover, also the effectiveness of the mechanochemical synthesis is assessed by observing that the milled SnPd sample has a remarkably higher conversion with respect to its impregnated counterpart.

In the literature it is reported that Sn can cover Pd particles reducing their exposure to the gas phase if the sample is not properly calcined, and this could be the reason why we do not observe an improvement upon Sn addition[169].

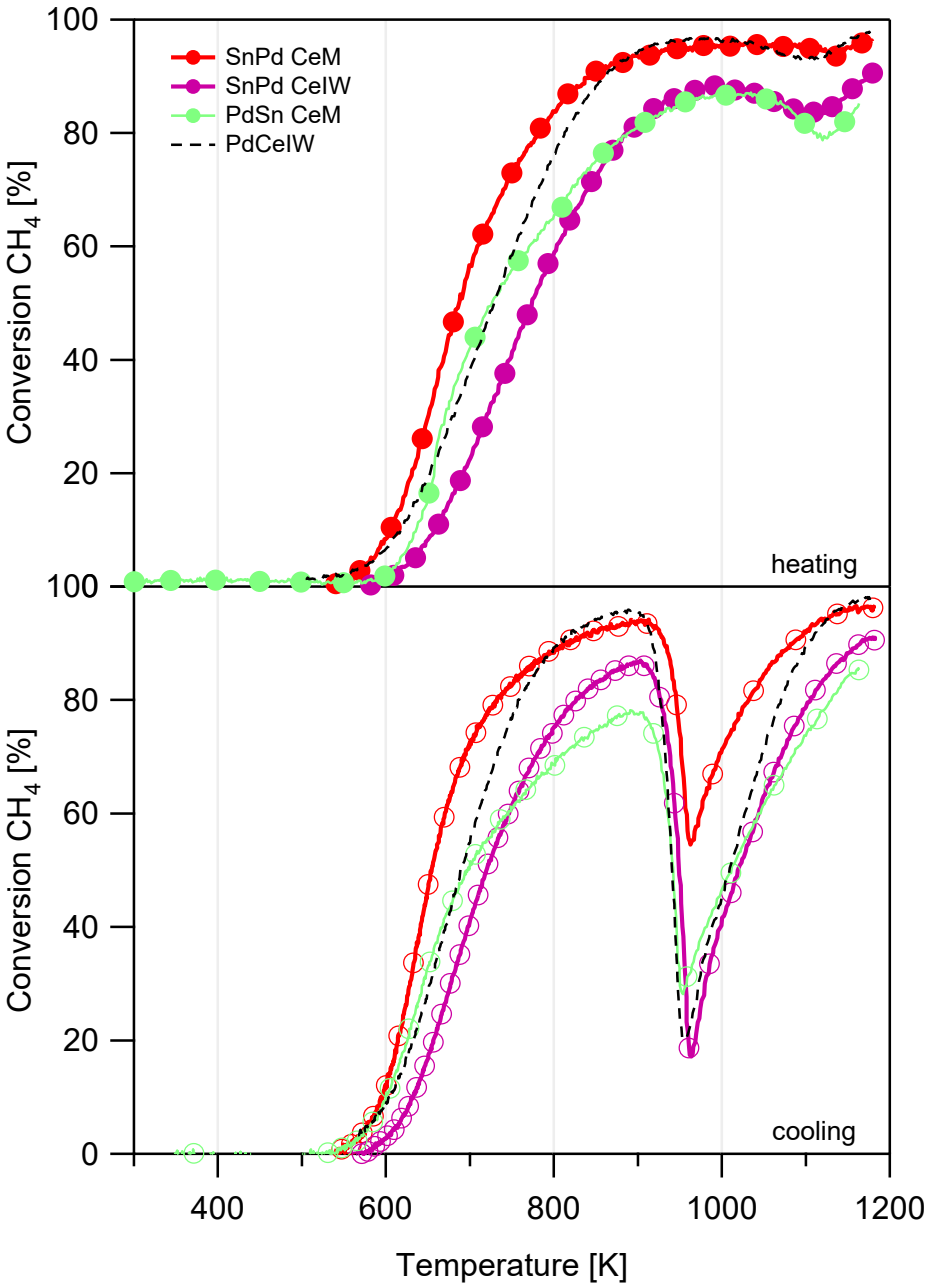

Figure 5-4: TPC-dry for bimetallic SnPdCe M compared to SnPdCeIW and PdSnCeM; heating ramps above, cooling ramps below; GHSV ca.200000 h^{-1}, 0.5% CH_4, 2% O_2, He to balance.

An attempt was then tried by calcining the milled sample, to check the effect of calcination, and also by using SnO_2 powder as tin precursor. In Figure 5-5 the conversion in TPC dry is reported for the two new samples, compared to SnPdCeM. As it can be observed, the oxidation of tin results in a serious worsening of catalytic performances. These samples where then discarded from further studies.

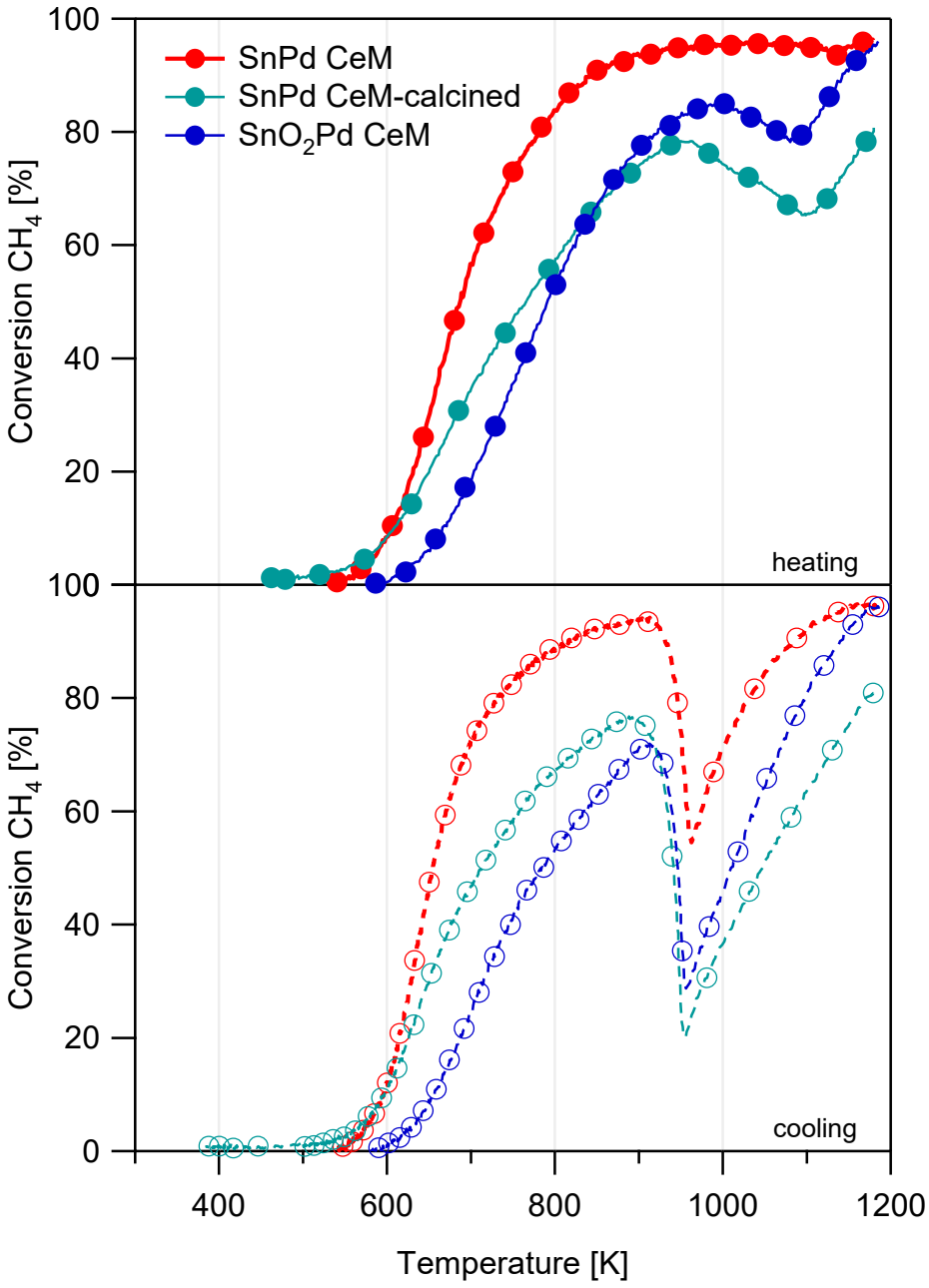

Figure 5-5: TPC-dry for bimetallic SnPdCe M compared to SnPdCeM calcined and SnO_2PdCeM; heating ramps above, cooling ramps below; GHSV ca.200000 h^{-1}, 0.5% CH_4, 2% O_2, He to balance.

The effect of tin addition was evaluated also during wet TOS experiments. In Figure 5-6 the conversion of methane of the sample SnPdCeM is reported, compared to PdCeM. The conversion at 723K is in line with the conversion recorded at the same temperature during wet-TPC, thus the overall activity of SnPd is lower. In terms of normalized conversion (see insert of Figure 5-6) the two samples show the same trend. Again, no effect of Sn on catalytic activity is observed.

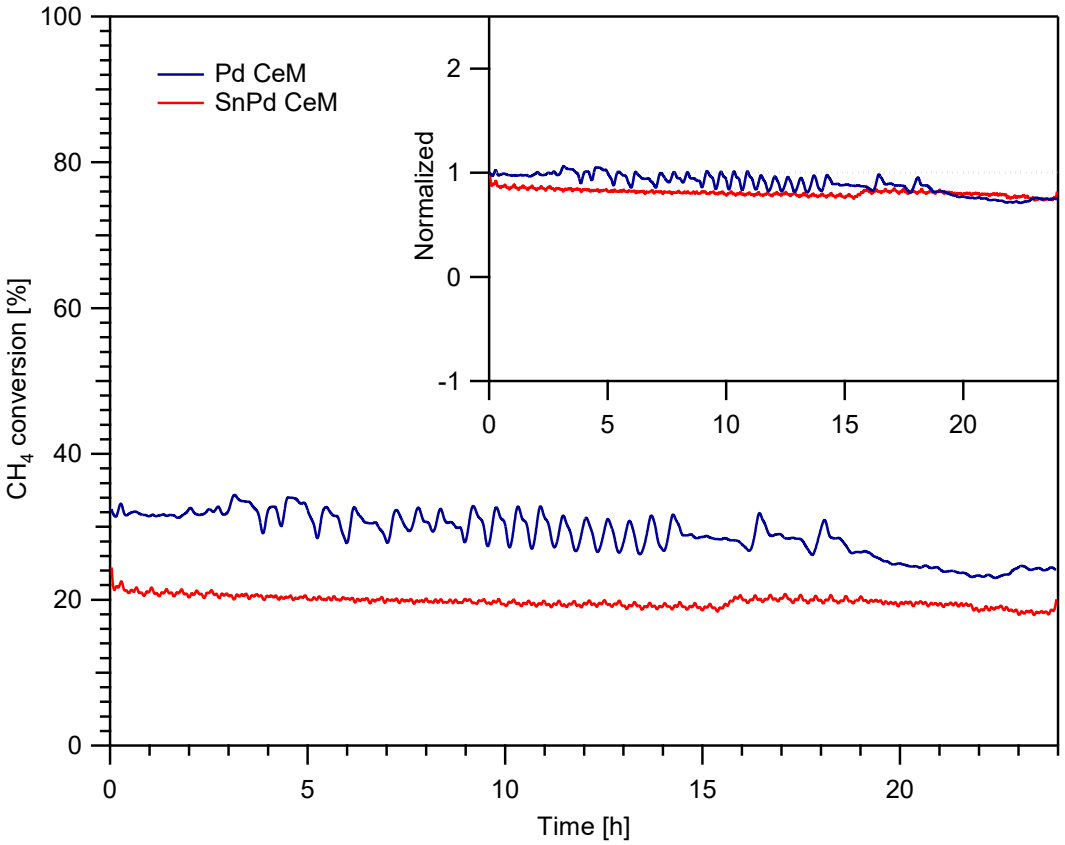

Figure 5-6: TOS-wet for bimetallic SnPdCe M compared to monometallic Pd CeM; insight: normalized CH_4 conversion; GHSV ca.200000 h^{-1}, 0.5% CH_4, 2% O_2, 10% H_2O, He to balance.

Overall, it seems that apparently tin does not affect the performance of Pd/CeO_2 milled sample, and this might be linked to the interaction between Sn and CeO_2, a strong interplay being reported in literature between Sn and Ce.[186] It is demonstrated that the deposition of Sn on CeO_2 led to the formation of a bulk Ce-Sn-O with the reduction of Ce^{4+} to Ce^{3+}.[187] This might inhibit the positive interaction between Pd and Ce and/or cancel the effect of tin on methane oxidation in the case of milled catalysts. Moreover, if Pd is deposited onto such a mixed oxide structure, it is found to interact weakly with Ce but strongly with Sn reducing simultaneously the extent of Ce^{3+}.[188]

To check the occurrence of these interactions, TPR experiments have been carried out and Figure 5-7 shows the TPR profiles of samples SnPdCeM and PdCeM.

For both samples, there are two H_2 uptake below 300K, ascribed to the reduction of PdO and part of CeO_2 due to spillover effect,[189] and a hydrogen release due to the decomposition of Pd-hydride (PdH_x) at about 320K. The sample SnPdCeM is reduced at lower temperatures and to a slightly higher extent, while the PdH_x peak is smaller. This might indicate that some alloying occurs between the two metals, but the difference is not so significant to draw definitive conclusions.

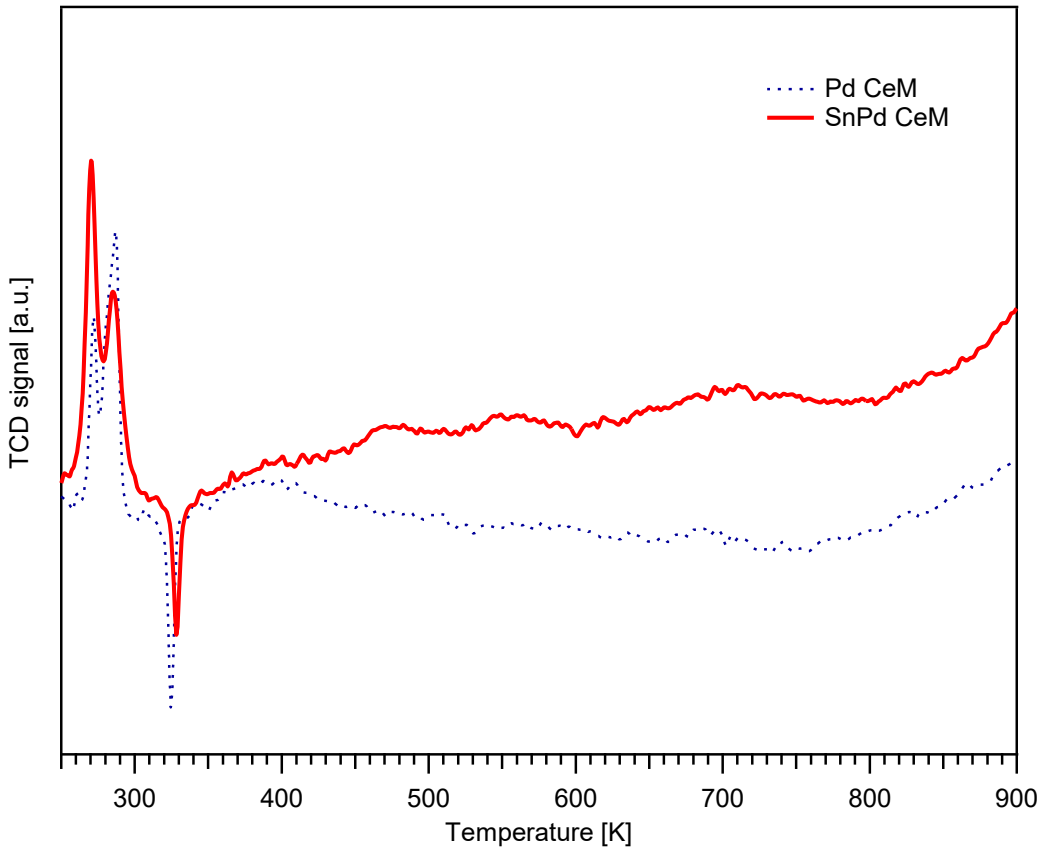

Figure 5-7: TPR-H_2 of the samples PdCeM and SnPdCeM.

The two profiles are much different starting from ca. 400 K. For the system Sn/CeO_2 three peaks have been observed in the range of 450-770K and referred to the reduction of dissociatively adsorbed oxygen on SnO_2[88]. Three not well defined and broad peaks are indeed visible in the sample SnPdCeM, making the identification of the contribution by SnO_2 somehow complicated. The fact that they are broad and merged might indicate that there is an effect of CeO_2 in the H_2 uptake in this range, and this could confirm a

strong interaction between Sn and ceria that could prevent tin from an active participation in methane oxidation reaction.

5.4 Conclusions

A preliminary analysis of the insertion of Sn and In in Pd/CeO_2 catalysts by dry ball milling was carried out. The results obtained in dry and wet methane oxidation, also during time-on-stream operation, show that the effect of the addition of the co-metals is negligible (dry conditions) or even negative (wet atmosphere), with indium being worse than tin. In the case of tin, based also on literature studies, it is hypothesized that a strong interaction with ceria support could inhibit its catalytic action, but further studies are needed to clarify this point. Nevertheless, by comparison with an impregnated $SnPd/CeO_2$ sample and with a milled sample obtained by changing the order of milling (PdSn CeM) it is once again confirmed the effectiveness of the mechanical synthesis to obtain active Pd-based catalysts and the importance of the direct contact between Pd and CeO_2.

6. Structured catalysts for stoichiometric oxidation of methane

Abstract

In this part of the work, carried out in collaboration with Umicore Automotive Catalysts R&D Department, the mechanochemical synthesis was applied to prepare structured catalysts and to study the stoichiometric oxidation of methane in close-to-real conditions. A bimetallic Pt/Pd sample and a monometallic Pd sample were mechanically prepared by a solvent-free milling procedure and used in a coating process developed by Umicore. Light-off tests up to 873K and isothermal lambda sweep tests at 723K and 773K were carried out to gain a better comprehension of the main reactions occurring in the variable conditions of stoichiometric oxidation and to assess the performances of the catalysts. The relevance of steam reforming and the inhibiting effect of CO on the conversion of methane are part of the outcome in the working conditions considered and track the possible future developments. The stability of the catalysts was evaluated through two different aging treatments, and the results show that the structured bimetallic sample improves its activity after a wet treatment as in the reported case of lean methane oxidation when used in powder form. Moreover, both monometallic and bimetallic catalysts show a superior stability for NO reduction and CO oxidation compared to the standard reference provided by Umicore.

6.1 Introduction

This work has been carried out in collaboration with the Gasoline Research & Development Department of Umicore Automotive Catalysts in Hanau, Germany, during a six months secondment. Umicore is specialized in technologies related to applications of precious metals with a particular attitude for environmental sustainability, using a high level of innovation on materials engineering to sell sustainable technology and

propose a cleaner industry[190]. For these reasons it looked promising for us to collaborate on the improvement and testing of the powder catalysts obtained by dry mechanical milling and described in the previous chapters. In this context, the collaboration allowed to test the materials under more realistic conditions to better understand their behavior and suitability for real application.

Stoichiometric and lean burn oxidation systems are commonly used in natural gas vehicles (NGV)[37,191]. The lean burn technology exploits an excess of oxygen to guarantee an efficient fuel use, but it requires complex aftertreatment systems. Instead, the aftertreatment systems of exhausts from stoichiometric engines are simpler, relying on three-way catalysts (TWCs) technology adapted from gasoline applications to oxidize the very stable unburned CH_4, the main component of natural gas[36,192].

TWC system consists of a single catalyst coupled with an electronic control of the emissions realized through the precise injection of fuel and air in the engine, to ensure a composition of the exhaust around stoichiometry[193,194]. In these conditions both the oxidation of C-containing compounds and the reduction of NO_x are optimized[195,196]. Noble metals are employed in TWCs as active components: usually a monolith is coated with a Pd/Pt layer overlapped by a Rh layer, both dispersed in an alumina matrix. Ce-Zr solid solutions are also used in light of their oxygen storage capacity, helping the catalyst to operate in the stoichiometric range[197, 198]. The solution is extremely simple and fits with NGV application, but it needs a higher amount of noble metals due to the higher stability of unburned CH_4, that turns into a higher price for the catalyst. In this respect, the mechanochemical synthesized catalysts prepared in our group for the oxidation of CH_4 can play a role, as better performances result in a lower use of material and a cheaper technology which is essential in the three-way catalysts for NGVs.

Although many papers have been focused on TWCs systems for gasoline applications[193], only few studies have been devoted to TWC for NGV and most of them are based on commercial catalysts without taking into account the preparation methods[55,199,200]. There are several differences in the mechanism of oxidation of methane compared to gasoline due to its stability, to the temperatures involved and to the interaction with the complex exhaust composition of the TWC[31] that influences also the conversion of NO and CO. For example, the so called CO-NO crossover point, the condition around which all the pollutants are efficiently converted, does not exactly correspond to stoichiometric conditions, but it is slightly shifted to the richer side[201]. Moreover, the high conversion window around this point is considerably narrower than

in the gasoline case. CH_4 appears to be converted more efficiently in rich conditions through steam reforming with water[56,200], while the temperatures seem too low for the dry reforming with CO_2 in this application[202,55]. Under lean conditions, O_2 is consumed mainly to oxidize CO resulting in an inhibiting effect on CH_4 oxidation, which is reported to be then preferentially oxidized by NO[203]. There is no evidence of NO reacting with CO, as it happens in the case of gasoline TWC. Another point to be considered carefully when dealing with TWC technology for the aftertreatment of NGVs exhausts is the large amount of water produced by the oxidation of CH_4, which deactivates the Pd active sites on the catalyst leading to a lower conversion of methane.

It is well known from the literature that the oxidation state of palladium plays a major role on CH_4 oxidation activity of Pd based catalysts, and many studies were carried out investigating methane oxidation in lean static conditions. In the case of stoichiometric conditions, the oscillations experienced by the feed may influence the oxidation state of Pd [46,204,205]. A deeper understanding of the phenomena taking place in TWC for stoichiometric methane oxidation is then necessary to improve the efficiency and the economy of all the components of NGVs aftertreatment in order to improve their performances.

This work is thus aimed at (i) verifying the feasibility of the application of powder milled catalysts as precursors for structured TWC for natural gas fueled vehicles under close-to-real conditions and (ii) exploiting their higher stability and activity showed for methane oxidation in lean conditions[126] for the application under stoichiometric oxidation. In collaboration with Umicore Gasoline Research & Development Department a method for the implementation of mechanochemically prepared catalysts in the production of structured catalyst was developed. These materials were then tested in close to real conditions with a full composition gas feed and using monolith configuration. Due to the complexity of this approach, different kind of tests were carried out starting from the light off and lambda sweep model tests which belong to the protocol usually carried out at Umicore. Two series of catalysts were prepared, a bimetallic Pt-Pd series and a monometallic Pd series, to evaluate not only the performances of the dry milled catalysts, but also the insertion of Pt in the Pd-based catalyst in line with the previous studies of this thesis work.

6.2 Material and methods

6.2.1 Structured catalysts preparation

Structured catalysts were prepared in order to be tested in a bench scale setup simulating real NGV operation. The preparation by dry mechanical milling of PtPd catalysts studied in the first part of this thesis was adapted and optimized for the preparation of samples to be tested in structured form. A reference structured catalyst was prepared following a procedure provided by Umicore to prepare coated monoliths; in this method all catalyst components (support, binder, active phase) were combined simultaneously in water. Figure 6-1 reports a flowsheet showing the general steps of the method.

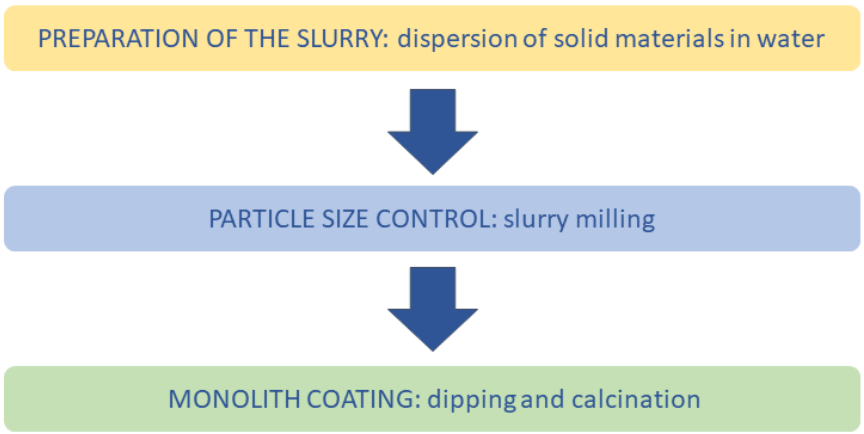

Figure 6-1: flowsheet of the structured catalysts preparation procedure.

A second procedure was developed to coat onto cordierite monoliths the powders prepared by dry milling. In this case, the active phase containing the noble metals was prepared separately in a dry milling step. The only difference consists in how the metals of the platinum group (PGM) are introduced during the *preparation of the slurry*.

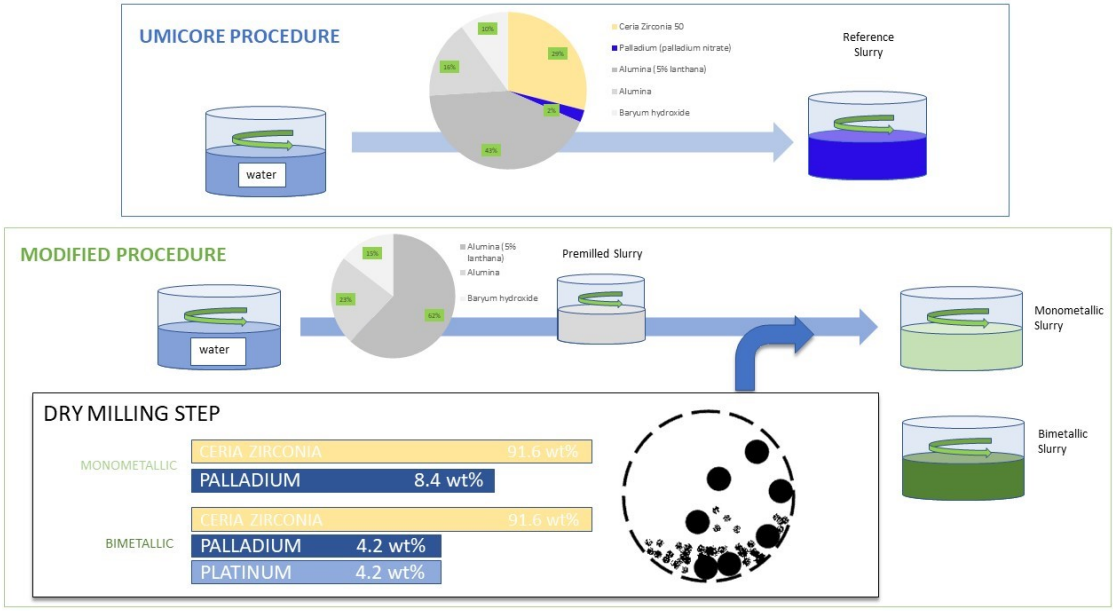

Figure 6-2: detail of the Umicore procedure for the preparation of the reference slurry and of the one containing the two mechanochemically prepared catalysts (monometallic with 8.4%wt of Pd and bimetallic with 4.2% of Pd and 4.2% of Pt).

In the Umicore method, cordierite cores were coated with a water-based slurry containing 30%-40% of solid powders. The solid fraction weight composition was: 42.5% Alumina Puralox SCFa140 L3 (97% Al_2O_3, 3% La_2O_3), 16.12% Alumina Puralox SCFa 140, 9.67% barium oxide ex barium hydroxide ($Ba(OH)_2 \cdot 8H_2O$ Umicore, 47.387%), 29.03% ceria zirconia solid solution (Umicore, CZ50: 50% ceria-50% zirconia; 62m^2/g) and 2.66% palladium (Umicore, Pd nitrate solution, 21.4%).

The preparation of the slurry proceeded as follows. Deionized water was put in a beaker with a stirrer and all the dry powders were poured in sequence, starting from barium hydroxide, then the two aluminas followed by CZ50, creating a homogeneous slurry with pH=13. A flow of 4g/min of Pd nitrate was then injected with a pump inside the slurry and the pH was decreased to 7 with the addition of nitric acid. The slurry so obtained was put in a linear mill DYNO-MILL KDL (600ml) with a flow rate of 25 l/min and recirculated until the particle size reached the desired value (3.5-4.5µm for the D_{50} value, <10µm for the D_{90} value). The particle size was measured on a CILAS 1064 laser particle size analyzer. As a last step, the slurry was passed linearly through the mill, without recirculation. The milling steps were carried out to obtain a selected particle size, functional to optimize the coating process.

Before the coating, the slurry was checked for weight loss by thermogravimetric analysis and its viscosity was measured indirectly on a Bostwick consistometer. A 7.8% of weight loss between 623K and 1273K was measured. For consistency measurement,

100 ml of slurry were let instantaneously falling on the inclined plane of the consistometer and the slurry was considered suitable for the coating if it stopped in the range between 10 and 20 cm. Otherwise, a change in the pH or more simply in the water content could be used to adjust this parameter.
The physical parameters of the reference slurry are summarized in Table 6-1.

Table 6-1: physical parameters of the reference slurry.

	D_{50} [µm]	D_{90} [µm]	Consistency [cm]	Starting solid material [%]	TGA loss 623K-1000K [%]
Reference slurry	3.56	10.02	14	30.4	7.8

Cylindric cores with a diameter of 25mm and a length of 75mm were obtained by drilling cordierite supports (NGK, 600cpsi/4mil), thus having monoliths with a volume of 0.039L. The washcoat load was fixed at 155g/L, so that each monolith had to be coated with 6.84 g of powder, considering also the TGA loss. At the beginning of the coating session, 10mg of slurry were evaporated at 393K, assessing the water content and thus the solid percentage. From these values also the wet loading was established, i.e. the amount of slurry for each core. These parameters are summarized in Table 6-2.

Table 6-2: loading parameters for cores coating.

Core volume [l]	Load [g/l]	Load per core [g]	Starting wet load [g]
0.039	155	6.84	22.495

The coating process was carried out by dipping: the cordierite core was dipped for 2/3 of the length in a beaker filled with the slurry, then turned upside down to let the slurry flow down. In this way all the channels were filled by the slurry. Compressed air was then blown in the same direction till all the channels were open. The monolith was now weighted, and the actual wet loading was checked. If the amount was higher than the one expected, further air was blown. Otherwise the entire process was repeated. Once reached the right loading, the monolith was dried in an oven with flowing air at 393K.
It was possible to weight again the core to know the water evaporated and so to update the value of the slurry solid content, since water could evaporate while the cores were coated (the entire coating process took several days). Eventually, the wet loading was

adjusted for the following coatings. Otherwise the core was let in the oven and the temperature raised till the monolith reached the temperature of 623K. It was weighted again and the final load was checked. If it differed more than ±5% of the desired load, the core was discarded. Since with this procedure a decreasing layer is formed along the channels, to compensate this gradient the coating process was divided in two steps: 60% of the slurry was coated following one direction of the core and then calcined, then 40% was coated in a second step inverting the direction.

To coat the monoliths with the powders prepared by dry milling, two different catalysts supported on ceria-zirconia provided by Umicore (CZ50) were prepared, one containing Pd only (reference, to be compared with the Umicore one) and one containing both Pd and Pt. First, the same amount of metal was adopted: 8.4% counting the only weight of the metal and the ceria-zirconia support on Umicore procedure (see Figure 6-2). This amount was divided exactly in a 4.2% of Pd and 4.2% of Pt for the bimetallic sample.

The standard procedure used for Pt-Pd samples (Chapter 3) had to be adapted in order to obtain a suitable amount of material for the preparation of the slurry. In fact, Pulverisette 23 (Fritsch) allows to prepare no more than 2 grams per synthesis, while for the preparation of the slurry almost 50 gr were needed. To avoid multiple preparation steps, a scale up was carried out in a Pulverisette 6 planetary mill (Fritsch) equipped with a zirconia jar of 250 ml. Trying to reproduce the conditions of the smaller mill, a single zirconia ball with a diameter of 40mm or two smaller zirconia balls with a diameter of 20 mm were used. The dynamics of the planetary mill is totally different from that of the Pulverisette 23 (planetary vs vibratory), but since modeling the mechanics of the milling process was out of the scope of this thesis work a trial and error approach was used.

Firstly, two reference catalysts (8.4 Pd(ac) CZ50 m and 4.2Pt4.2Pd CZ50 m) were prepared with Pulverisette 23 following the procedure reported in Chapter 3 for Pt-Pd samples, and tested on lean methane oxidation with the standard conditions (120mg of sample, two heating/cooling cycles from T_{room} to 1173K at 10K/min, 0.5% CH_4, 2% O_2 in He, see also Chapter 2.3.2). The same test was performed on the scaled up catalysts prepared in the Pulverisette 6, so that the comparison of the light-off curves was used as the method to ascertain the reproducibility of the preparation. The catalysts prepared in the Pulverisette 6 were named 8.4 Pd(ac) CZ50 M_i and 4.2Pt4.2Pd CZ50 M_i, with i being the number of the trial. For each synthesis 10 grams of sample were produced.

The samples prepared together with the milling parameters used are reported in Table 6-3.

Table 6-3: dry milling parameters for each trial.

	Steps #	Time per step [min]	Milling speed	Balls #
8.4 Pd(ac) CZ50 m	1	20	15 Hz	1
8.4 Pd(ac) CZ50 M_1	1	10	100 rpm	2
4.2Pt4.2Pd CZ50 m	2	10	15 Hz	1
4.2Pt4.2Pd CZ50 M_1	2	5	100 rpm	2
4.2Pt4.2Pd CZ50 M_2	2	10	100 rpm	2
4.2Pt4.2Pd CZ50 M_3	2	15	150 rpm	1

Regarding the monometallic sample, the first attempt in the bigger mill, 8.4Pd(ac) CZ50 M_1, gave a result comparable to that of the catalyst prepared in the smaller one, as it can be inferred from the comparison of the light-off curves reported in Figure 6-3.

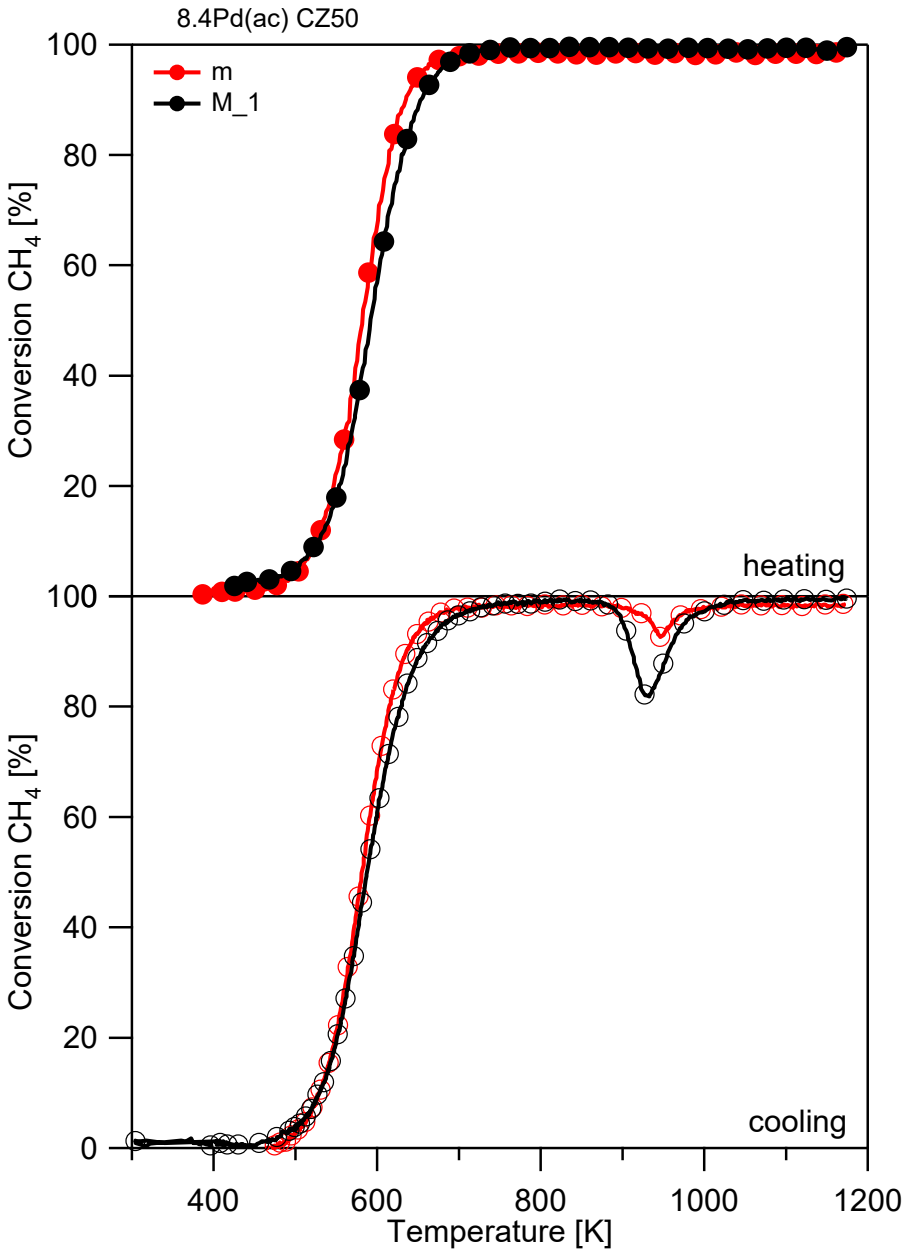

Figure 6-3: second light-off cycle on the samples prepared by dry milling in the standard (8.4Pd(ac) CZ50 m) and scaled up (8.4Pd(ac) CZ50 M_1) procedure.

Differently from the monometallic case, three attempts were needed for the bimetallic sample to reach acceptable results as it can be observed by looking at Figure 6-4.

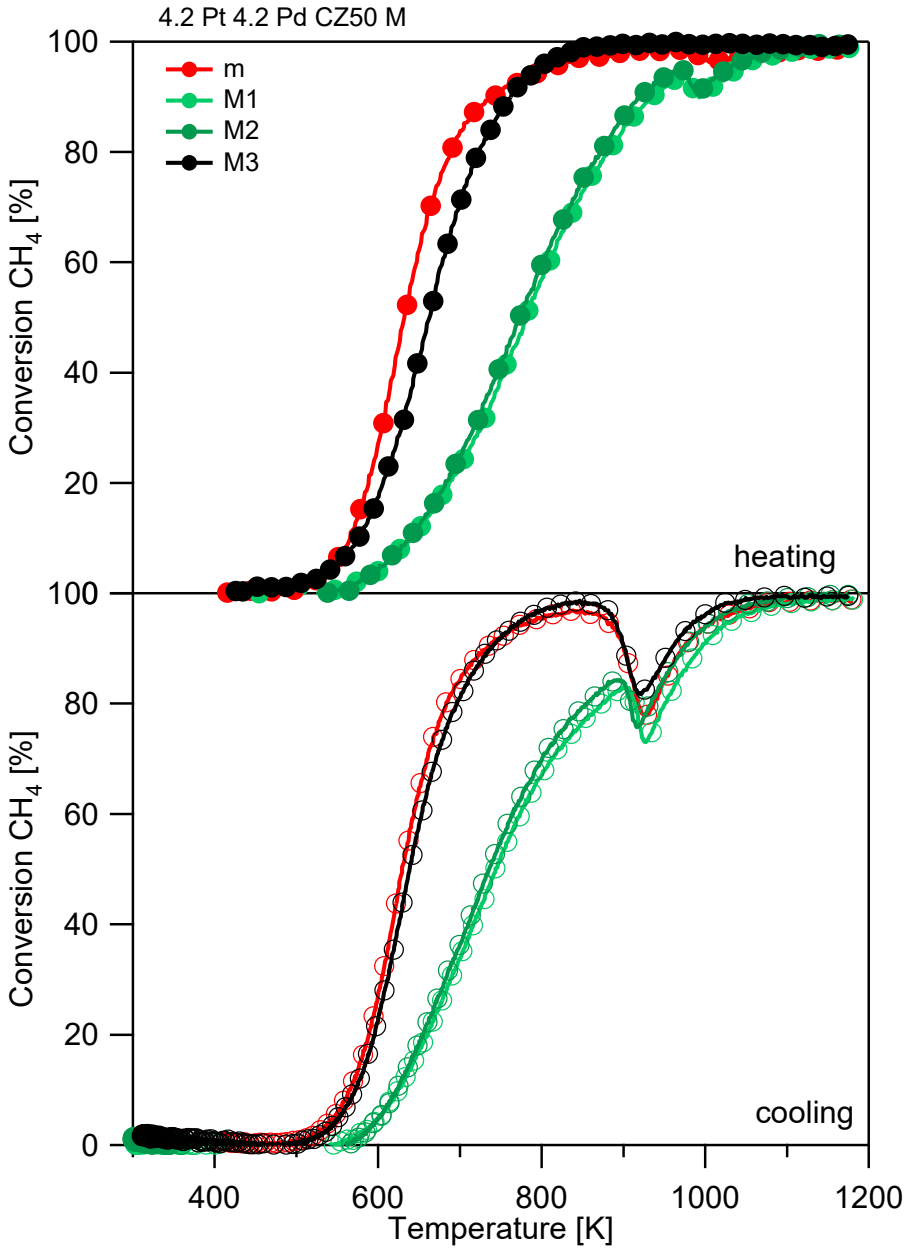

Figure 6-4: second light-off cycle on the bimetallic samples prepared by dry milling in the standard (4.2 Pt 4.2 Pd CZ50 m) and scaled up (4.2 Pt 4.2 Pd CZ50 M_1, 4.2 Pt 4.2 Pd CZ50 M_2, 4.2 Pt 4.2 Pd CZ50 M_3) procedure.

Once the catalysts were available in a suitable amount, a slurry, named pre-milled slurry (see Figure 6-2), was prepared with all the components and same composition used in the method provided by Umicore for the reference, except for the active phase (metal precursors + CZ50). The pre-milled slurry and the powders prepared by dry milling were mixed together in a second step, to avoid an excess of milling for the PGM containing phase as it is known from our previous experience that a prolonged milling deteriorates the catalytic performances [127].

The pre-milled slurry was prepared similarly to the Umicore reference. Briefly, deionized water was put in a beaker with a stirrer and barium hydroxide was poured in it and the two aluminas were added. The measured pH was 13.4 at this point and nitric acid was added to bring it to 7. This slurry was milled in the same conditions of flow and particle size restrictions of the reference. The physical parameters of the premilled slurry are summarized in table Table 6-4.

Table 6-4: physical parameters of the premilled slurry.

Slurry	D_{50} [µm]	D_{90} [µm]	Consistency [cm]	Solid content [%]	TGA loss 623K-1000K [%]
Pre-milled slurry	3.77	8.86	13	30.0	4.68

To avoid any detrimental interaction of the palladium acetate precursor of the monometallic catalyst with the water slurry, 8.4Pd(ac) CZ50 M catalyst powder was calcined at 623K for 30 minutes in air (8.4Pd(ac) CZ50 M) or in nitrogen atmosphere (8.4Pd(ac) CZ50 M-N_2). Overall, three different coating materials were prepared by mixing the precise amount of dry milled catalyst with the pre-milled slurry giving the final composition of the Umicore reference (PGM loading of 2.66%). They were named as the dry milled powders introduced: 8.4Pd(ac) CZ50 M, 8.4Pd(ac) CZ50 M-N_2, 4.2Pt4.2Pd CZ50 M.

To check if the milling of the slurry could affect the catalyst, it was also chosen to prepare a homologous set of slurries with linear milling (8.4Pd(ac) CZ50 M-LM, 8.4Pd(ac) CZ50 M-N_2-LM, 4.2Pt4.2Pd CZ50 M-LM), i.e. passing the slurries linearly through the DYNO-MILL, without recirculation. The six materials and the respective physical parameters are reported in Table 6-5.

Table 6-5: slurries from milled powder and physical parameters

Slurry name	D_{50} [µm]	D_{90} [µm]	Consistency [cm]	Starting solid content [%]	TGA loss 623K-1000K [%]
8.4Pd(ac) CZ50 M	3.15	8.13	15	37.30	2.74
8.4Pd(ac) CZ50 M N_2	3.11	8.02	15	37	2.92
4.2Pt4.2Pd CZ50 M	3.32	8.28	14.5	40.05	2.79
8.4Pd(ac) CZ50 M-LM	3.04	7.87	14	36	2.74
8.4Pd(ac) CZ50 M N_2 -LM	3.06	7.90	13.5	39.5	2.92
4.2Pt4.2Pd CZ50 M-LM	3.16	8.14	14	35.2	2.79

The coating process was the same used for the reference, using the same cordierite cores with 0.039l volume and the same load of 155 g/l. After the measurement of the TGA loss for each slurry it was possible to know the loading parameters, reported in Table 6-6.

Table 6-6: loading parameters for cores coating.

Slurry name	Load per core [g]	Starting wet load [g]
8.4Pd(ac) CZ50 M	6.403	17.166
8.4Pd(ac) CZ50 M N_2	6.529	17.645
4.2Pt4.2Pd CZ50 M	6.521	16.282
8.4Pd(ac) CZ50 M-LM	6.403	17.473
8.4Pd(ac) CZ50 M N_2 -LM	6.529	16.529
4.2Pt4.2Pd CZ50 M-LM	6.521	18.525

At the end of the entire coating procedure several cores were produced for each catalyst material, in order to have enough samples to perform different kind of catalytic tests.

6.2.2 Catalytic activity tests

The catalytic tests of the prepared materials were carried out in a gas bench specifically set up for testing monoliths. The set up can be divided into three main parts:

1. Dosing section
2. Reactor section
3. Analyzing section

The dosing section scheme is shown in Figure 6-5.

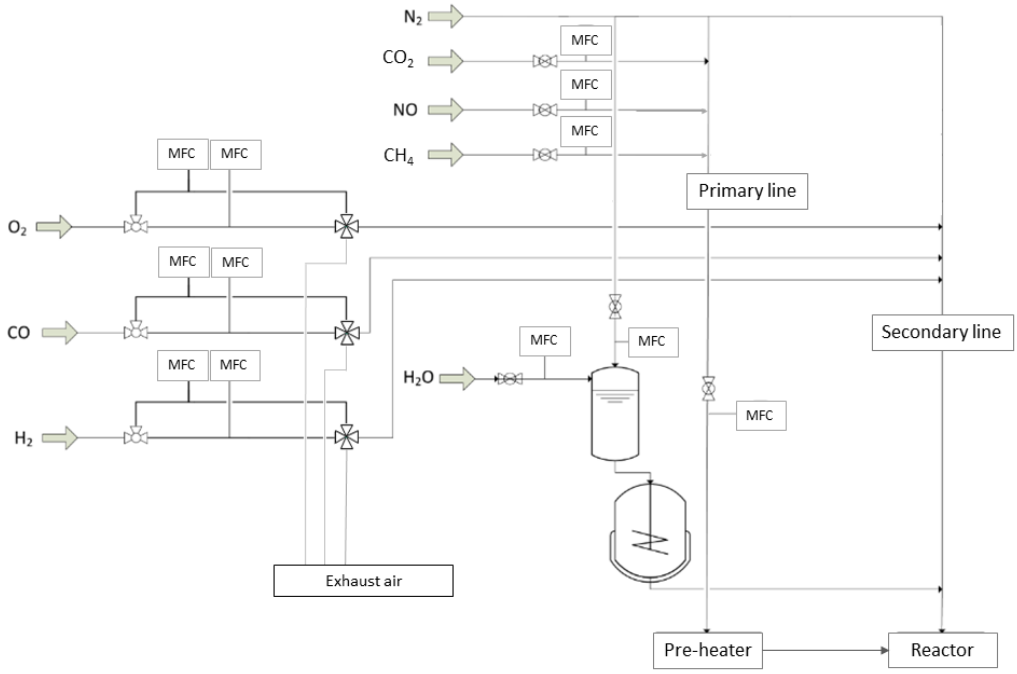

Figure 6-5: dosing section scheme.

In the setup it was possible to dose N_2 (99.999%, Praxair), CO_2 (99.995%, Praxair), NO (10%±2% in N_2 bal., Praxair), O_2 (99.995%, Praxair), CO (99.97%, Praxair), H_2 (99.999%, Praxair) and CH_4 (10%±2% in N_2 bal., Praxair). All the gas flow rates were controlled by Bronkhorst EL-flow mass flow controllers. Deionized water was fed by a Bronkhorst Liqui-flow mass flow controller and passed through an evaporation unit CEM Bronkhorst High-Tec that saturated a flow of N_2 used as carrier.

The dosing section was divided in a primary (CO_2, NO and CH_4 in N_2) and a secondary line (H_2, CO and O_2 in N_2). The primary line, with fixed flowrates, was fed to the reactor through a pre-heater. The secondary line was used to switch between rich and lean atmosphere, and for this purpose it was equipped also with a by-pass line and two mass flow controllers for each gas. Two flows were set and, with an external control unit (Sara Electronic), it was possible to pass from one to the other with the desired frequency that could vary between 0.5Hz and 1Hz. This line was directly fed to the reactor together with water, without passing through the pre-heater to avoid anticipated reactions.

The reacting section scheme is represented in Figure 6-6. An isolated stainless-steel cylinder working as an air-to-air heat exchanger formed the reactor section. Room air was heated and blown into the cylinder allowing to vary the system temperature from

313K up to 973K. The primary line entered from the bottom of the cylinder into a coil, whereas the actual reactor was positioned in the upper part of the cylinder. The monoliths were wrapped into a quartz wool mate and positioned in the reactor. The primary and secondary line were mixed together just before entering into the reactor. The temperature was measured by two K-type thermocouples placed before and after the reactor. Similarly, one jump probe lambda sensor was placed before the reactor and one broadband lambda sensor was placed after the reactor in order to check the value of lambda.

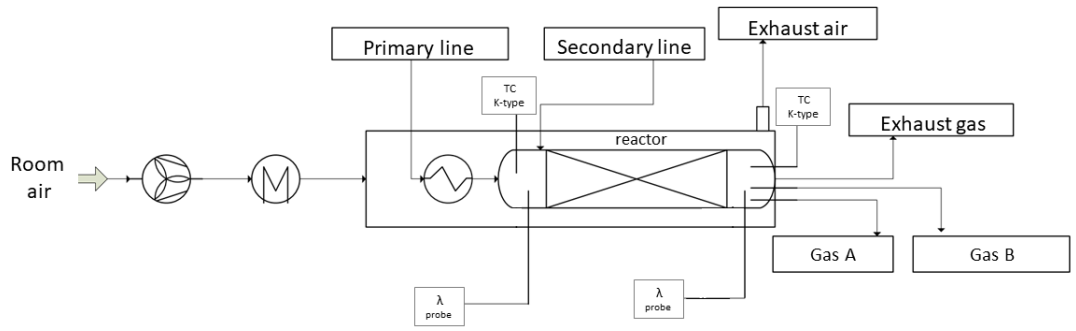

Figure 6-6: reaction section scheme.

Two separate lines, Gas A and Gas B, departed from the reactor and reached the analytical section. The Gas A line passed through a condenser and was then directed to a mass spectrometer (H sense, MS4) for the analysis of hydrogen. The other line, Gas B, was analyzed by an FTIR module (TERMO FISCHER SCIENTIFIC, Antaris ICGs Gas Analyzer to analyze CH_4, NO_x, N_2O, NH_3, CO and H_2O), a CLD detector (CLD 700RE ht, Eco Phisics for the specific evaluation of NO_x) and an FID (NGA TFID, Emerson for the specific evaluation of CH_4). The line eventually passed through a condenser, then through an NDIR (NGA 2000 MLT 4, NDIR, Emerson) for the quantification of CO_2 and a paramagnetic detector for the oxygen content (NGA 2000 MLT4 PO_2, Emerson).

The analytical section scheme is represented in Figure 6-7.

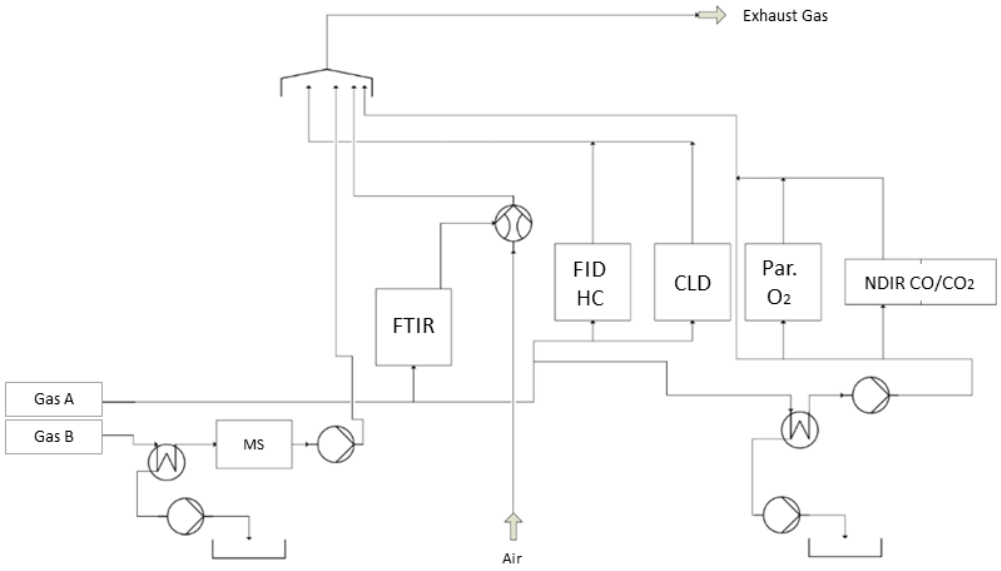

Figure 6-7: analytical section scheme.

In the lab scale bench setup two kind of tests were carried out:

- light off tests
- lambda sweep tests

The light off tests consisted in heating ramps from 473K to 873K with a space velocity of 100000 h^{-1} at 20K/min. Seven light off tests differing in gas composition were performed and named LOi, with i = 1,…,7. The compositions of each test are summarized in Table 6-7, together with the values of λ calculated according the equation (1)[201]:

$$\lambda = \frac{X_{O_2} + X_{CO} + X_{NO} + 2X_{CO_2} + X_{H_2O}}{X_{CH_4} + 2X_{CO} + X_{H_2} + 2X_{CO_2} + X_{H_2O}}$$

Table 6-7: light-off compositions.

	Primary line			Secondary line					
	CH_4 [ppm]	NO [ppm]	CO_2 [%vol]	H_2O [%vol]	O_2 [ppm]	H_2 [ppm]	CO [ppm]	$\lambda_{average}$ [-]	λ [-]
LO1	1000	\	\	10	\	\	\	0.9615	
LO2	1000	\	\	10	6300	3767	11300	0.95	
LO3	1000	\	\	10	[6300-8400]	3767	11300	0.9665	[0.9504-0.9826]
LO4	1000	1000	13	10	4850	6833	20500	0.95	
LO5	1000	1000	13	10	5800	2333	7000	0.9981	
LO6	1000	1000	13	10	[5800-11900]	[2333-5400]	[7000- 16200]	0.998	[0.9504-0.9826]
LO7	1000	1000	13	10	[5800-18500]	[2333-8700]	[7000-26100]	0.9981	[0.9383-1.0649]

As mentioned, the primary line had a static flow while the secondary line could operate in a dynamic mode and was used to vary the lambda value by changing O_2, CO and H_2 concentration (LO3, LO6 and LO7). LO1 had only 1000 ppm of CH_4 and 10%vol of H_2O. The flow was static and λ was 0.9615. All the other six light offs had the same amount of CH_4 and H_2O as LO1. In Figure 6-8 it is briefly summarized which gases are present for each light-off test.

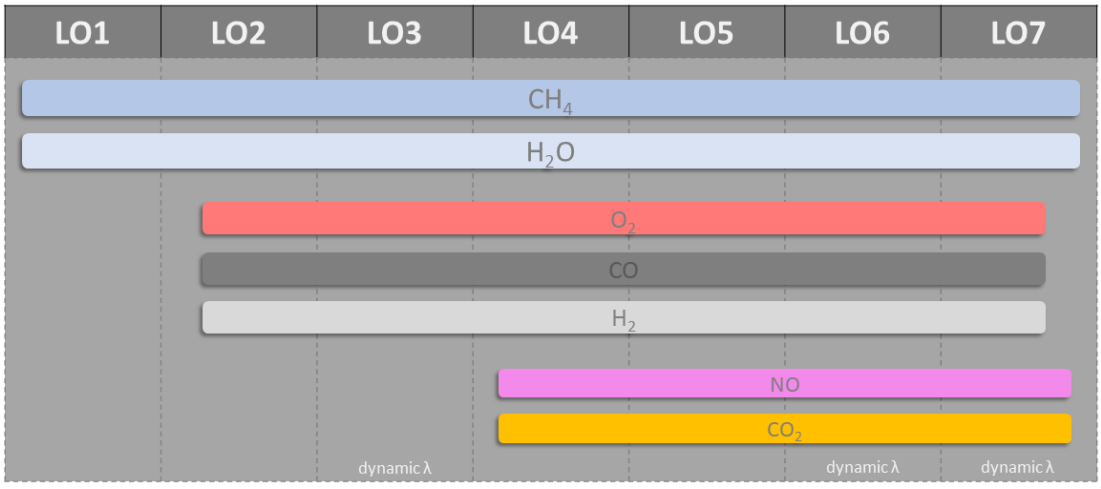

Figure 6-8: distribution of the gases into the different light-off tests.

Differently from the light-off tests where the temperature was ramped, the lambda sweep tests were carried out at constant temperature (723K or 773K) and consisted in a variation of the average λ value around the stoichiometry, from the rich value of 0.975 to the lean one of 1.025 and vice versa as represented in Figure 6-9.

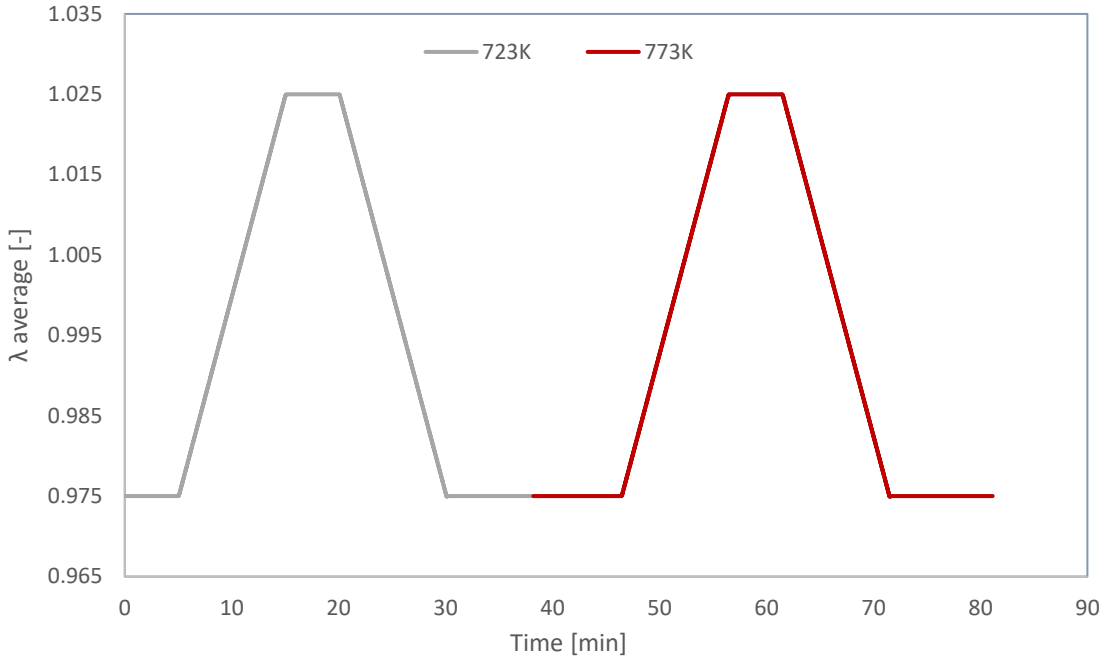

Figure 6-9: λ trend over time during the two isotherms 723K (grey) and 773 (red).

Three lambda sweep tests were carried out and named LSi, with i = 1,…,3. In the first one O_2 was constantly increased from 1420 ppm to 10930 ppm and back to 1420 ppm. In the second and third lambda sweep test the average value of O_2, and consequently of lambda, was the same as for the LS1. However, the lambda value oscillated to have a variation of ±0.034 and ±0.068 for LS2 and LS3, respectively, around the average value with a frequency of 1Hz in both LS2 and LS3 (see Figure 6-10).

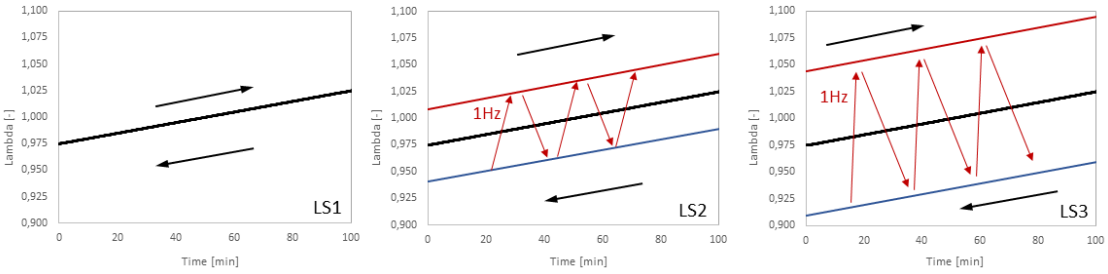

Figure 6-10: lambda sweep dynamic scheme of LS1, LS2 and LS3; the oxygen amount was modulated so that lambda follows the black line in LS1 and it switched from the blue to the red lines in LS2 and LS3 (determined by amplitudes ±0.034 and ±0.068 respectively) with a frequency of 1Hz.

All these tests were carried out on as prepared monoliths to evaluate the performances of the catalysts and the effect of the different compositions on the stoichiometric oxidation of methane. An ageing effect was also considered to assess the stability of the systems. Two ageing processes were considered. The first one was an ageing treatment in water and so referred as *wet ageing*: the monoliths were left in a static flow with 10%vol of water and 21% O_2 in N_2 balance for 8 hours at 1173K. The second one was a dynamic treatment and referred as *pulsed-ageing*: monoliths were left for 16 hours in a flow which was switched between 10% CO and 10% O_2 in N_2 with a frequency of 1Hz at 1173K. The aged monoliths were again tested with the most representative light-off experiment (LO6).

6.3 Results and discussion

At Umicore, the light off test LO6 and the lambda sweep test LS2 at 773K are the main references to assess the catalysts performances. Both the tests have a fully formulated feed and the lambda value is oscillated by ±0.034 around an average point at 1Hz frequency. This is to reproduce the real exhaust working conditions. All the other tests mentioned in the previous paragraph were carried out to gain a deeper understanding of the reactions that occur during the stoichiometric oxidation on mechanochemically prepared catalysts.

In this paragraph, firstly the results of the investigation of the best way to implement the milled catalysts in the coating process considered will be reported. The best performing material for each composition will be then chosen to examine the conversions of the main species for each light off test and lambda sweep test. The best bimetallic sample will be compared with the best monometallic one. Finally, the dry milled catalysts will be compared with the reference provided by Umicore, both in the fresh version and after the two ageing processes.

6.3.1 Implementation of the dry milled catalysts in the Umicore coating process

Methane conversion was chosen to compare the performance during the light-off LO6 test. The main aspect considered was the effect of linear milling on the slurries; for the monometallic sample also the effect of the calcination atmosphere, air rather than N_2,

was evaluated. In Figure 6-11 the methane conversion for all the cores prepared starting from the monometallic dry milled catalysts is reported.

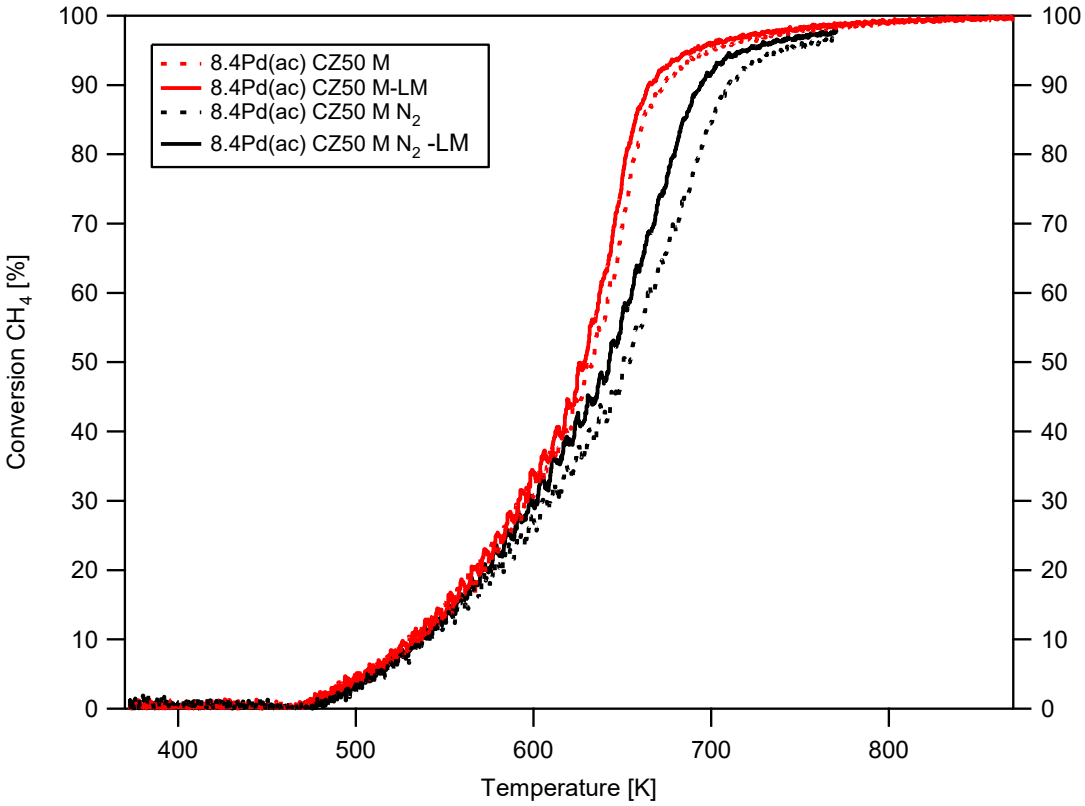

Figure 6-11: methane conversion in light-off LO6 for the monometallic samples.

All samples display similar conversions at low temperatures, while at high temperature the linearly milled samples show a slightly better conversion. Moreover, the monometallic catalyst calcined in air is better than the one calcined in N_2. This can be explained by looking at the x-ray diffractograms reported in Figure 6-12, which shows a comparison between the X-rays diffraction (XRD) patterns recorded on the two dried slurries of the respective samples.

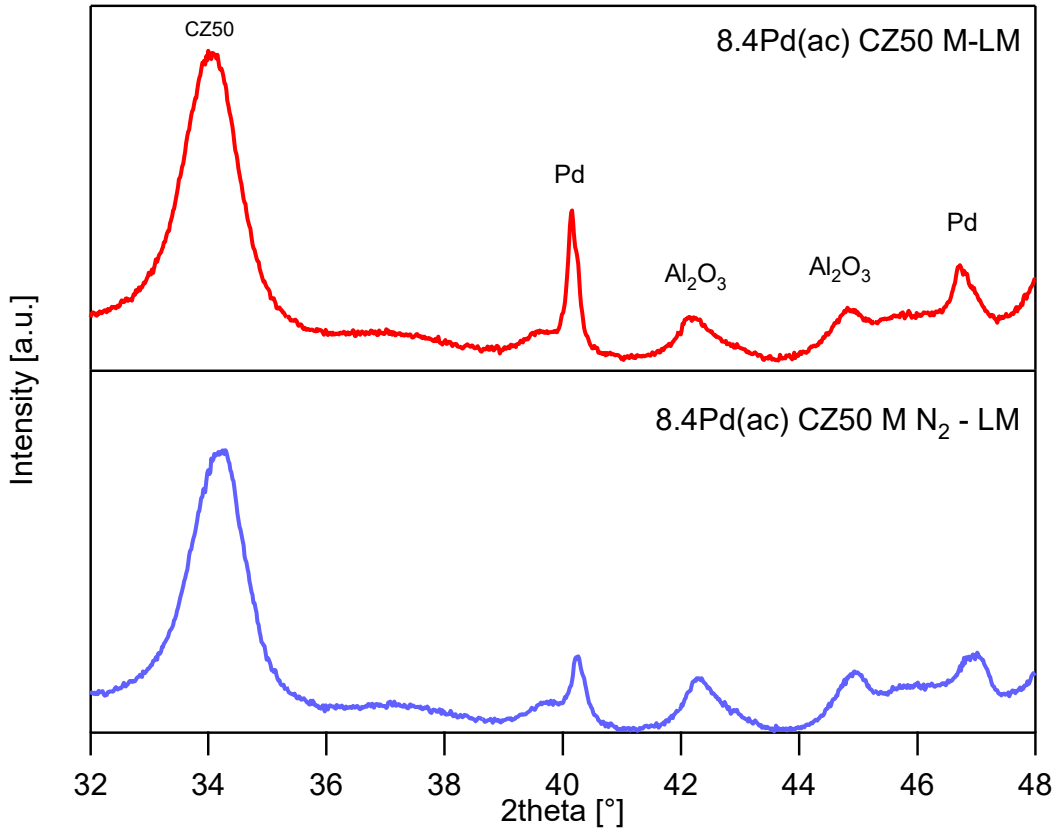

Figure 6-12: XRD diffractograms of 8.4Pd(ac) CZ50 M-LM dried slurry (above) and 8.4Pd(ac) CZ50 M N_2-LM (below).

Beside the features of CZ50 and alumina, a sharp peak at 40°, which corresponds to metallic Pd, is visible for both the samples. This peak has two shoulders, which can be referred again to alumina, but most important it is higher and sharper for the sample calcined in air. It is reported that the decomposition in air of the acetate precursor favors the formation of the metallic Pd phase due to a complex series of exothermic oxidation reactions[206,207]. Likely, this pathway is not followed in N_2 atmosphere resulting in a less developed crystalline metallic Pd phase. This in turn could be the cause of the different catalytic activity. So, from here onwards the sample 8.4Pd(ac) CZ50 M-LM will be considered as a reference for comparison.

In Figure 6-13 the methane conversion for the dry milled bimetallic catalysts is represented.

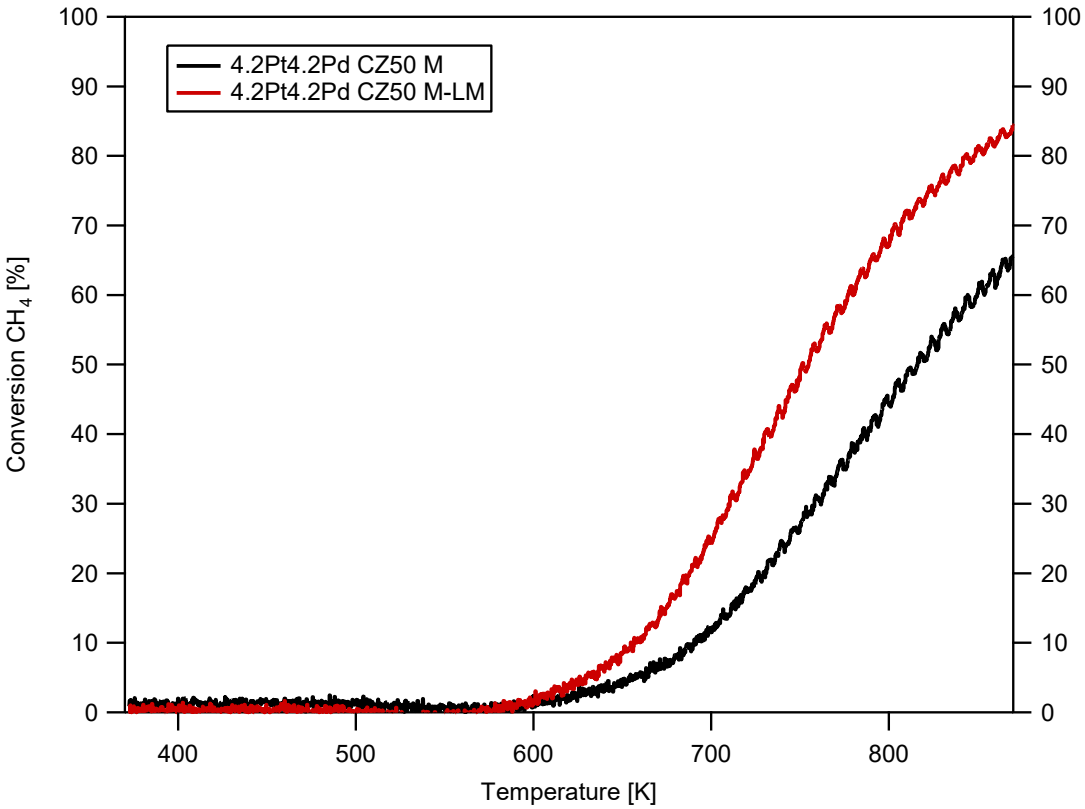

Figure 6-13: methane conversion in light-off LO6 for the bimetallic samples

In this case, the difference between the bimetallic samples with and without linear milling is more relevant than for the monometallic catalyst, with 4.2Pt4.2Pd CZ50M-LM giving the best results. This is probably due to the fact that the bimetallic sample prepared with the dry milling method in the bigger setup was not optimized and required longer milling times or higher milling intensity to improve its performances.

To check this hypothesis, the sample used as reference in the optimization process of the bimetallic catalyst (4.2Pt4.2PdCZ50m) was further milled for 5 minutes at 15Hz in the minimill Pulverisette 23 and tested on lean methane oxidation as explained in the previous paragraph. The results are reported in Figure 6-14.

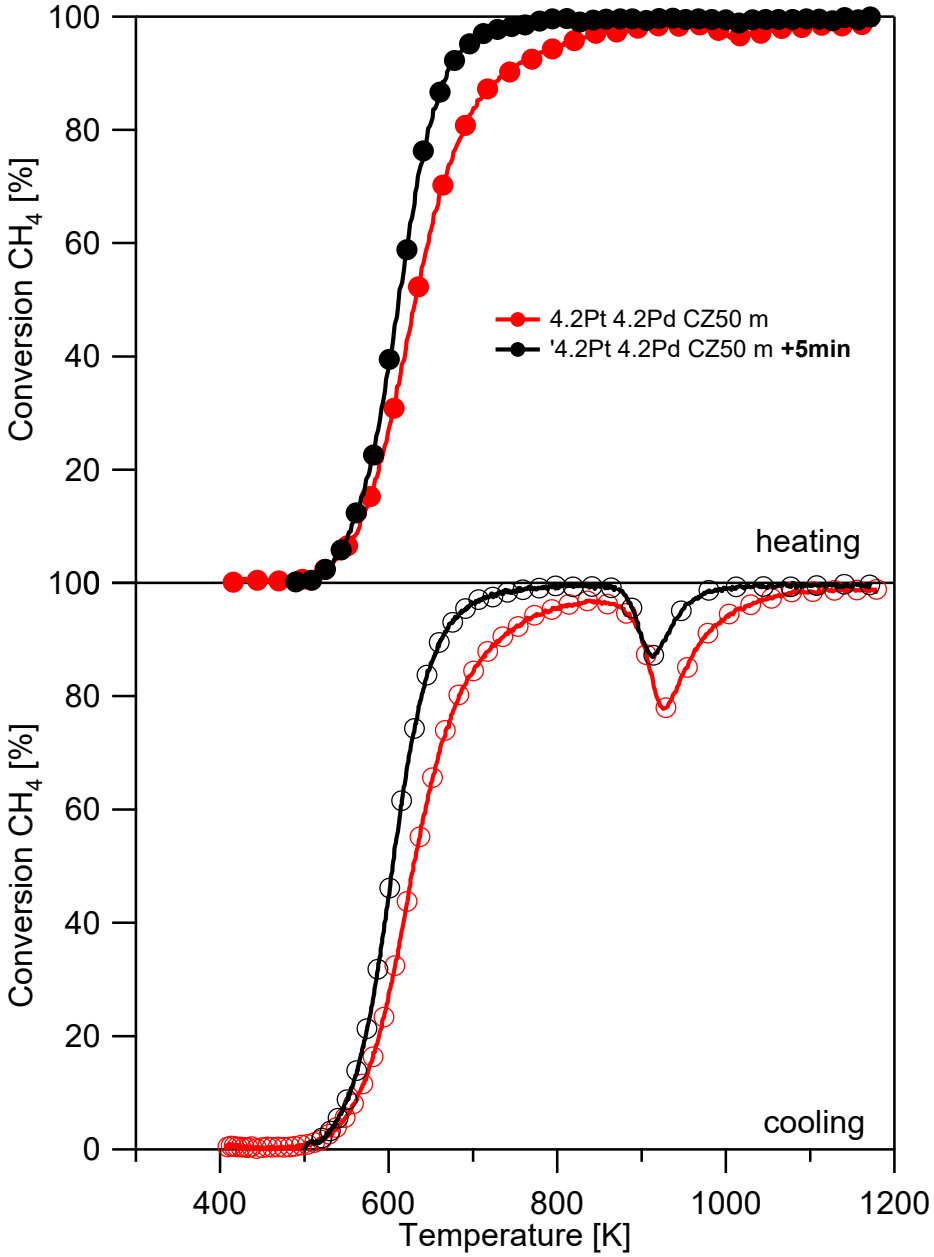

Figure 6-14: lean methane oxidation, second light off cycle; comparison between the sample taken as reference for the optimization of the bimetallic catalyst "4.2Pt 4.2 Pd CZ50 m" and the same sample further milled for 5 minutes at 15Hz "4.2Pt 4.2 Pd CZ50 m ***+5min".***

The better conversion achieved by further milling the sample 4.2Pt4.2Pd CZ50 m is a clear evidence that the method was not properly optimized. Unfortunately, this check was performed only after all the tests were carried out at Umicore, after the secondment period and further testing in the facilities has not been possible in the timeframe of this thesis work. However, the sample 4.2Pt4.2Pd CZ50 m presented anyway better performances than the homologous prepared by incipient wetness impregnation as

shown in Figure 6-15, so it can still be considered representative to understand the role of the mechanochemical synthesis under more realistic testing conditions.

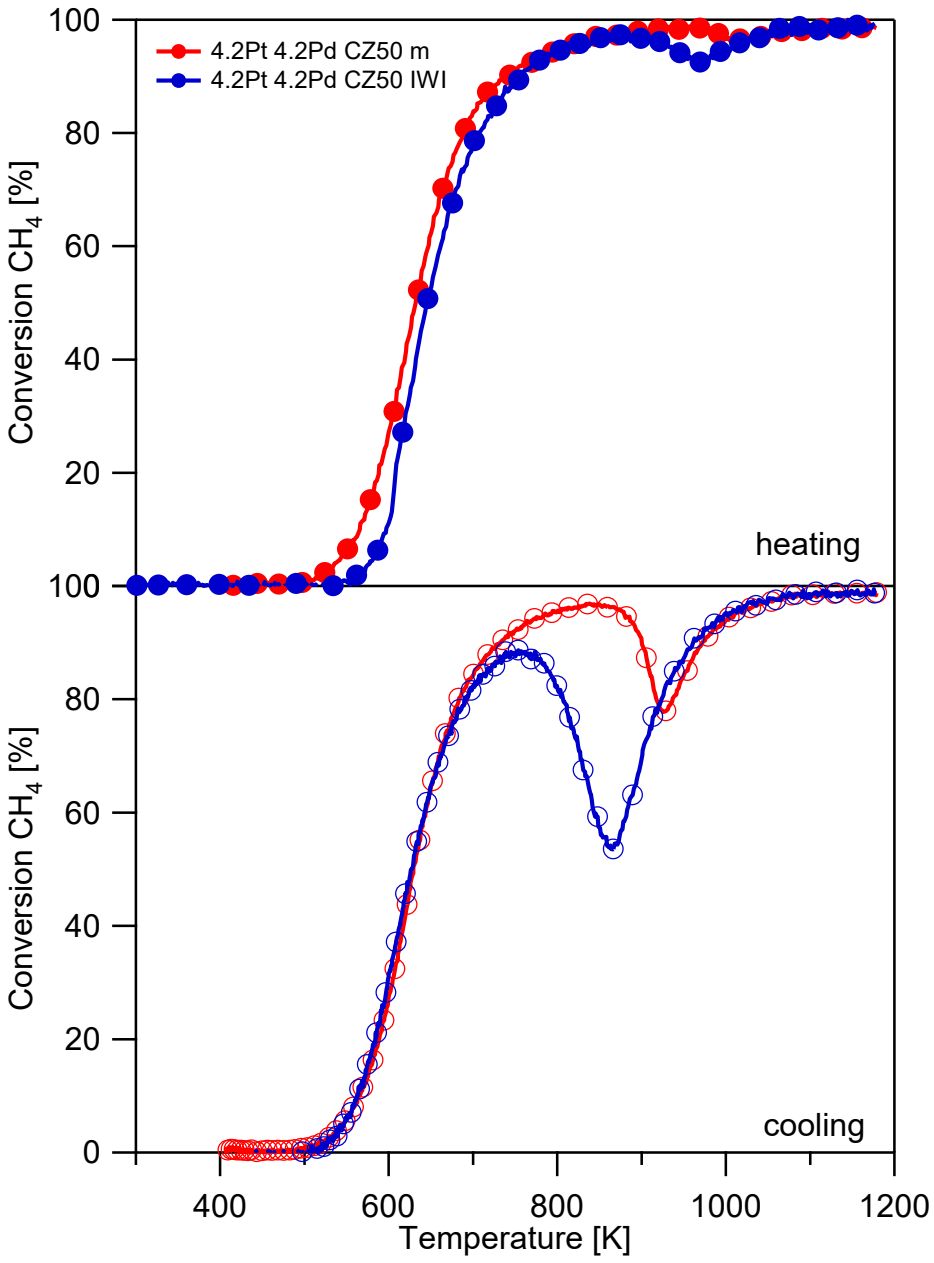

Figure 6-15: lean methane oxidation, second light off cycle; comparison between the sample taken as reference for the optimization of the bimetallic catalyst "4.2Pt 4.2 Pd CZ50 m" and the homologous prepared by incipient wetness impregnation "4.2Pt 4.2 Pd CZ50 IWI".

6.3.2 Light Off Tests

6.3.2.1 Dry milled catalysts

In the first light-off (LO1) the feed consisted of only water and methane. Steam reforming reaction (SR) between CH_4 and water (1), is an important pathway for the reduction of methane in the TWC technology under net reducing conditions[56].

$$CH_4 + H_2O \rightarrow CO + 3H_2 \quad (1)$$

The main products are H_2 and CO. CO can be converted to CO_2 through water gas shift (WGS) reaction and additional H_2 is produced (2).

$$CO + H_2O \rightarrow CO_2 + H_2 \quad (2)$$

The concentrations of the reactants and products from the LO1 tests for 8.4 Pd(ac) CZ50 M-LM and 4.2Pt4.2Pd CZ50 M-LM are reported in Figure 6-16.

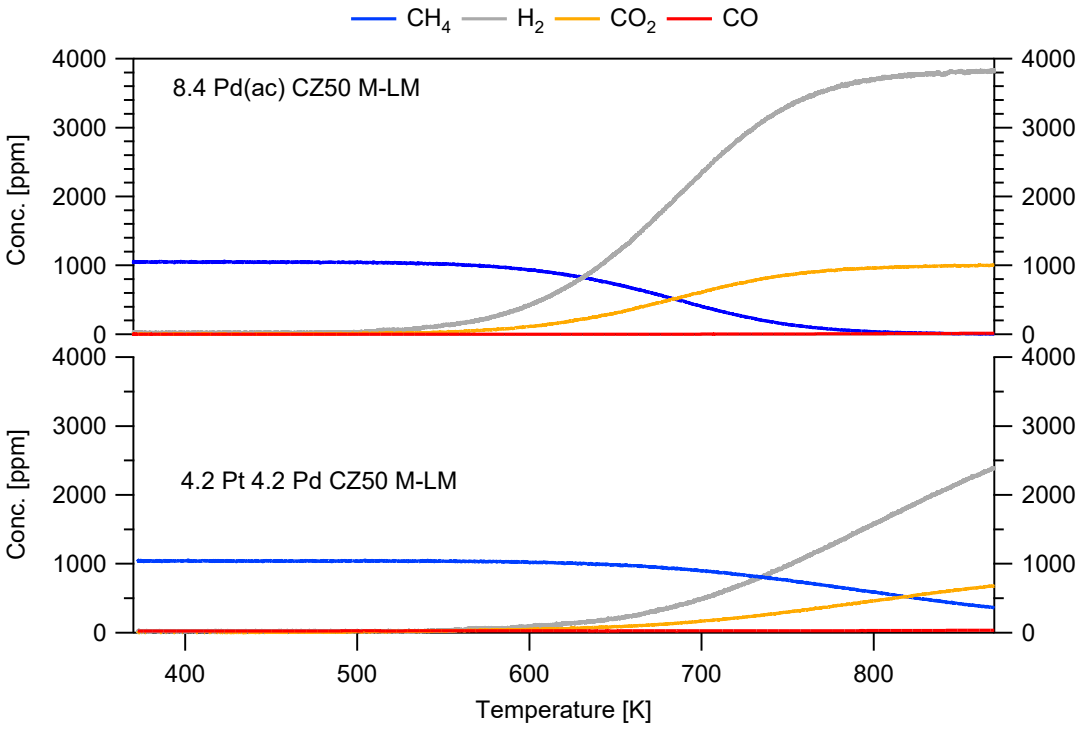

Figure 6-16: concentration of reactants and products during the heating ramp of LO1 ($\lambda_{average}$=0.9615).

The monometallic sample starts to convert methane at about 550K and it seems that WGS follows rapidly the SR reaction as it can be seen by the absence of CO and the simultaneous increase of H_2 and CO_2. The concentrations detected agree with reactions

(1) and (2). Methane is fully converted at 800K. On the contrary, the bimetallic sample is less active and methane is not entirely converted at the end of the test. The behavior is the same as for the monometallic sample, with no detection of CO.

The subsequent light-off experiments, LO2 and LO3, had the same amount of water and methane, but also hydrogen, carbon monoxide and oxygen were introduced. LO2 was carried out in static mode, while during LO3 oxygen pulses were introduced (see Figure 6-8).

In light off LO2 the conditions are net reducing, the λ value being 0.95. The outlet concentration of gases from the reactor is reported in Figure 6-17 for the monometallic and bimetallic samples.

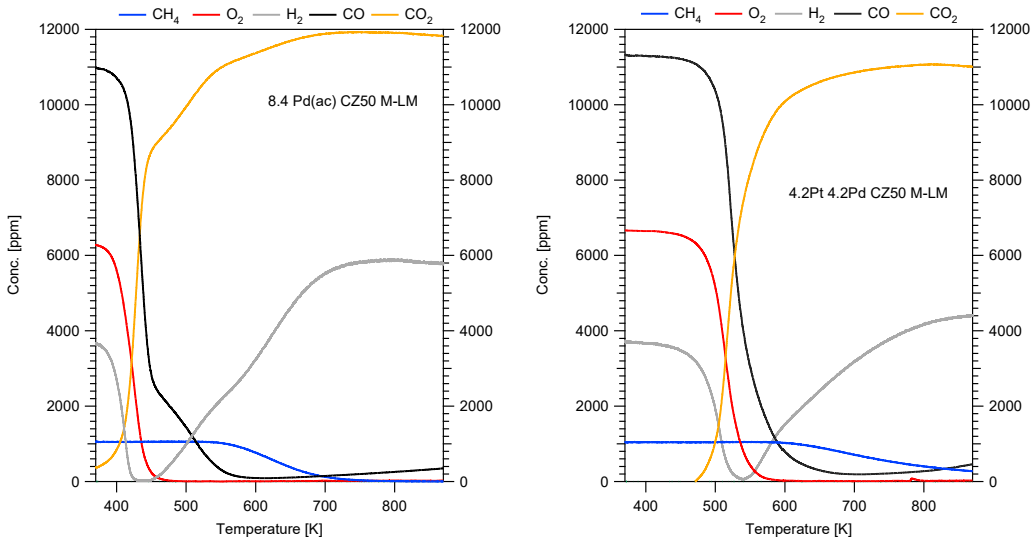

Figure 6-17: concentration of the reactants and products during the heating ramp of LO2 ($\lambda_{average}$=0.95).

O_2 is completely consumed below 450K in the monometallic case and 550K in the bimetallic case, to fully oxidize hydrogen and partially CO, which is present in higher amount. In the case of the monometallic sample, the rest of CO is oxidized by water through WGS reaction above 450K as it can be seen by the simultaneous increase of the H_2 amount followed by CO_2 with the same trend. The conversion of CO is slower through this pathway, as indicated by the different slope of the CO concentration. Above 550K CO is fully oxidized and methane starts to convert. The WGS reaction proceeds (H_2 and CO_2 keep increasing) up to ca. 700K when also methane is totally oxidized. Again, the oxygen deficiency pushes the conversion of methane through SR reaction consuming water, so that also CO starts to increase again after it reached its

minimum. By observing this trend, it seems that there is competition between the conversion of CO and CH_4. It is already reported that CO can inhibit the CH_4 conversion in TWC system[202,204] when the conditions are not oxidizing. While PdO is generally considered as the most active site for CH_4 conversion, the role of metallic Pd in CH_4 conversion can be important especially under net reducing conditions[46]. It is as well reported that CO seems preferentially oxidized by reduced metals, in this case metallic Pd[208]. Furthermore, in rich atmosphere, reduction of PdO by H_2, CO and CH_4 can take place, according to the following reactions [200]:

$$PdO + H_2 \rightarrow Pd + H_2O \quad (3)$$

$$PdO + CO \rightarrow Pd + CO_2 \quad (4)$$

$$4PdO + CH_4 \rightarrow 4Pd + CO_2 + H_2O \quad (5)$$

In LO2 the atmosphere is net reducing and, according to the above reactions, even in the presence of an oxygen storage material like ceria-zirconia, the majority of palladium is likely in the metallic form. CO can be adsorbed on the metal more efficiently than CH_4, which may have to wait the complete removal of CO to access the Pd-based active sites. The bimetallic catalyst acts in a similar way. However, all the reactions are shifted to higher temperatures and the decrease in CO concentration proceeds with a similar rate (no change in the slope as observed for 8.4Pd(ac)CZ50 M-LM) indicating a similar kinetics between oxidation and WGS.

Light off LO3 is carried out similarly to LO2, but with O_2 pulses. The reactants and products composition at the reactor outlet is represented in Figure 6-18.

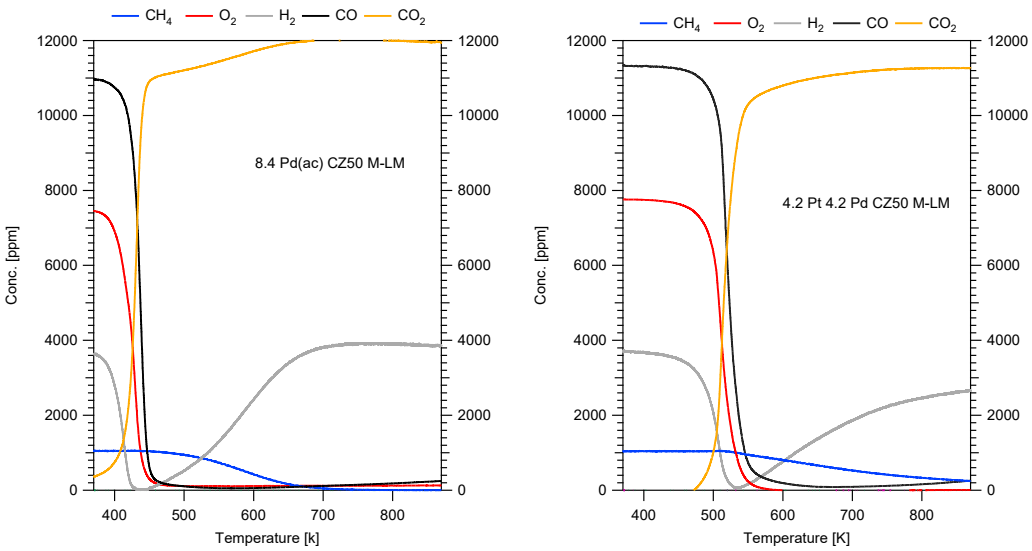

Figure 6-18: concentration of reactants and products during the heating ramp of LO3 ($\lambda_{average}$=0.9665); 8.4Pd(ac) CZ50M-LM on the left; 4.2Pt 4.2Pd CZ50 M-LM on the right.

The results are very similar to LO2, because even if the O_2 pulses increase periodically the λ value, the conditions remain predominantly reducing. The main effect is that the minimum of CO concentration is reached at lower temperatures and the contribution of WGS reaction at higher temperatures seems less important, as it can be inferred by the lower amount of hydrogen produced. Again, methane conversion starts when CO concentration reaches almost zero. This is clearer in Figure 6-19, where the conversions of CO and CH_4 for LO2 and LO3 are reported and compared for the two catalysts, showing that in presence of oxygen pulses both components are converted more efficiently.

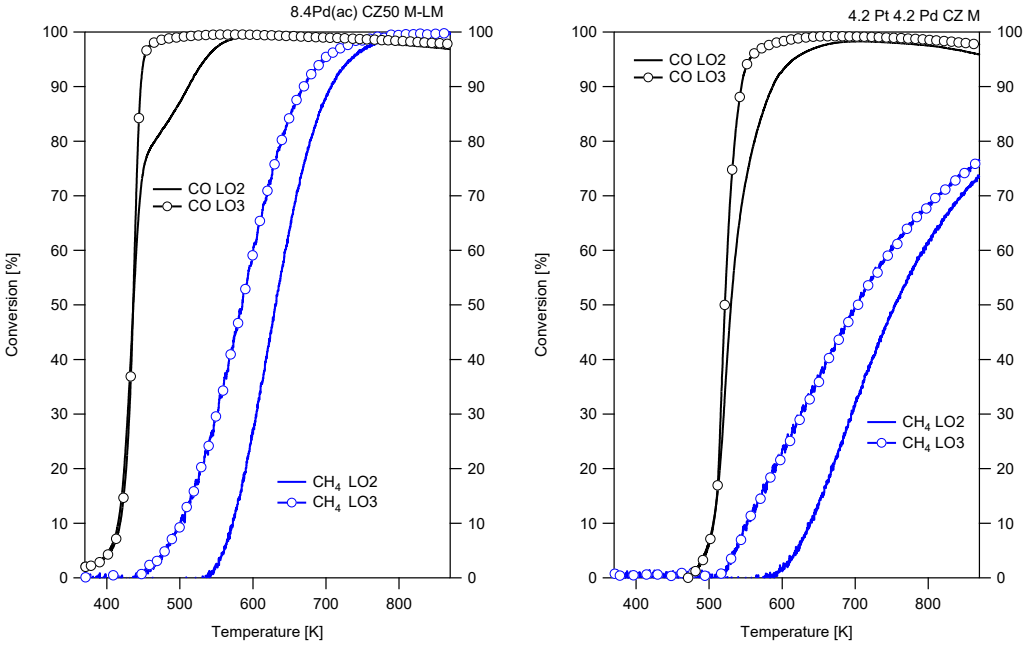

Figure 6-19: CH_4-CO conversion for LO2 ($\lambda_{average}$=0.95) and LO3 ($\lambda_{average}$=0.9665); 8.4Pd(ac) CZ50M-LM on the left; 4.2Pt 4.2Pd CZ50 M-LM on the right.

Light off LO4 is carried out with the fully formulated feed. The λ value is kept constant at 0.95 in static conditions like in LO2, but in this experiment NO and CO_2 are also present making it possible to assess their effect. The results are reported in Figure 6-20. The components are divided due to their high number and their different concentration to better observe the respective trends. For CO_2 and H_2O, due to the higher amount in the feed, it was chosen to display the difference between inlet and outlet concentration and not their evolution.

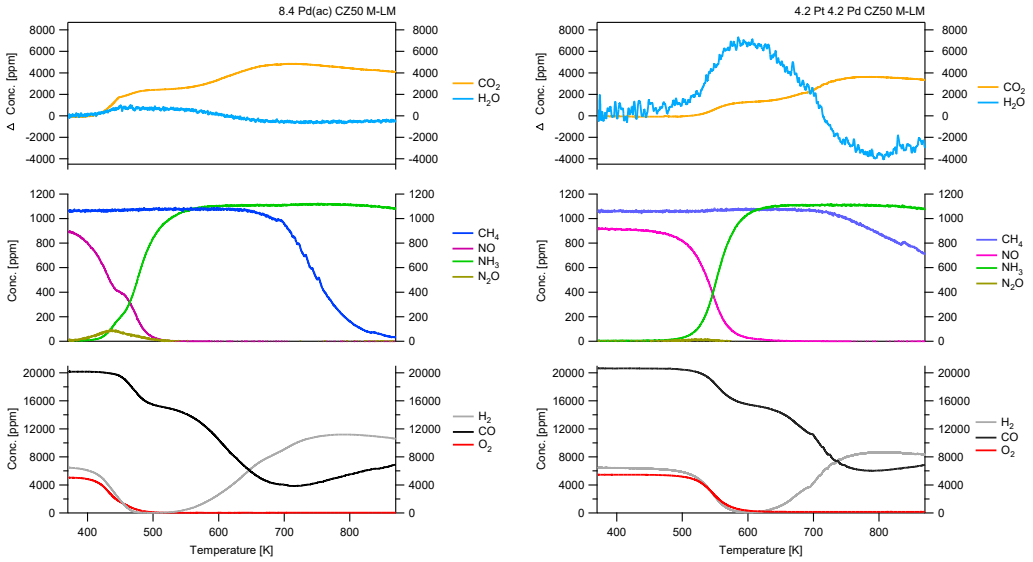

Figure 6-20: reactants and products during the heating ramp of LO4 ($\lambda_{average}$=0.95); 8.4Pd(ac) CZ50M-LM on the left; 4.2Pt 4.2Pd CZ50 M-LM on the right.

In LO4 the amount of CO and H_2 is increased to compensate the addition of NO, with a consequent lack of oxygen for the oxidation of the two species at low temperatures. However, O_2 consumption is shifted to higher temperatures compared to the previous light off tests, likely because in these conditions H_2 reacts first with NO to produce NH_3 and N_2O for both monometallic and bimetallic catalysts. Alternatively, it can be reduced to N_2.

The reactions that may occur are[200]:

$$NO + \frac{5}{2}H_2 \rightarrow NH_3 + H_2O \quad (6)$$

$$2NO + H_2 \rightarrow N_2O + H_2O \quad (7)$$

$$NO + H_2 \rightarrow \frac{1}{2}N_2 + H_2O \quad (8)$$

According to the stoichiometry of reaction (6) and to the composition of the feed, 1000 ppm of NO should produce 1000 ppm of NH_3 while consuming 2500 ppm of H_2. The residual H_2 (4333 ppm) should consume 2166 ppm of O_2, while the remaining oxygen (2684 ppm) can oxidize about 5368 ppm of CO. These amounts are coherent with what is reported in Figure 6-20, at temperatures below 550K for the monometallic sample, below 600K for the bimetallic one. Based on these observations, the interaction between CO and NO is excluded.

Hydrogen starts again to increase above these temperatures proportionally to the decrease of CO, presumably due to WGS reaction. For both samples, this reaction

seems not effective at high temperature (above 700K) where CO starts to increase again. At this point methane conversion is initiated. Again, a competition for the active sites between CO and methane can be observed. The variations in the concentration of water and CO_2 reflect the trend of hydrogen and CO, respectively, and confirm that at high temperature CH_4 is converted more efficiently by steam reforming. There is no evidence of dry reforming between CO_2 and CH_4.

In light-off LO5 the feed is still complete and static, but the amount of oxygen, hydrogen and carbon monoxide is changed to have a λ value of 0.99. The results are reported in Figure 6-21.

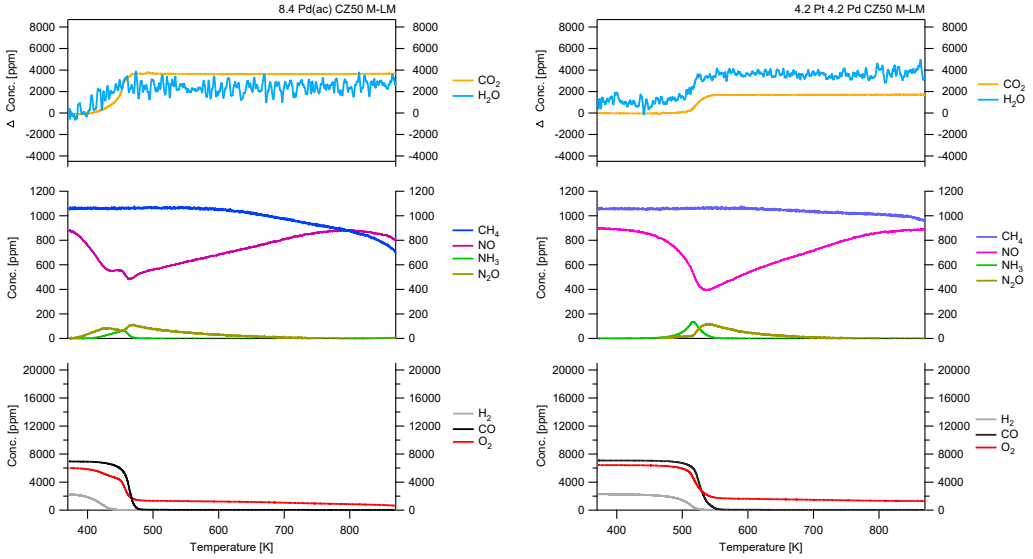

Figure 6-21: reactants and products during the heating ramp of LO5 ($\lambda_{average}$=0.9981); 8.4Pd(ac) CZ50M-LM on the left; 4.2Pt 4.2Pd CZ50 M-LM on the right; in the upper part it is reported the difference between the amount of H_2O and CO_2.

At low temperature NO is again reduced to produce NH_3 and N_2O, according to reactions (6) and (7). What is clear here is that, for both samples, the NH_3 produced is lower than in LO4 and there is a slightly higher amount of N_2O. This results in a lower conversion of NO till a certain temperature, whereas H_2 seems preferentially oxidized, as it can be inferred also from the water trend. Also, in LO6 there is a small amount of oxygen that remains unreacted after the complete consumption of CO and H_2.

Methane shows the worst conversion for all the light-off tests of this study. Here the onset of methane conversion does not correspond to the temperature at which CO is oxidized and water does not decrease as in the previous cases.

It should be observed that in the case of monometallic catalyst NO starts to decrease again above 800K, along with a slight change in the concentration of CH_4. The effect is present also for the bimetallic catalyst, but much less evident and at higher temperature. This leads to a further speculation that a reaction between CH_4 and NO may happen at higher temperatures:[55]

$$4\,NO + CH_4 \rightarrow 2\,N_2 + CO_2 + 2\,H_2O \quad (9)$$

However, there are no visible changes in CO_2 concentration, but neither in the other gases analyzed due to low conversion.

Light off LO6 is the first of the series that has a fully formulated feed and a dynamic mode. λ is kept averagely around 0.99, oscillating with a fixed amplitude of about ±0.034 going from net oxidizing conditions to net reducing ones. The flow composition at reactor outlet is reported in Figure 6-22.

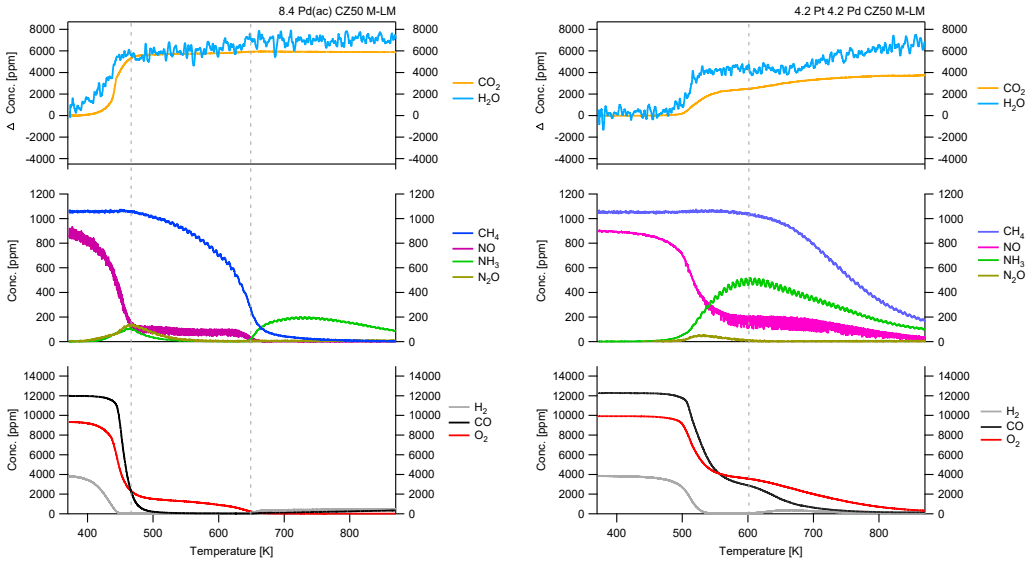

Figure 6-22: reactants and products during the heating ramp of LO6 ($\lambda_{average}$=0.998); 8.4Pd(ac) CZ50M-LM on the left; 4.2Pt 4.2Pd CZ50 M-LM on the right; in the upper part it is reported the difference between the amount of H_2O and CO_2.

In all the previous experiments, the difference between monometallic and bimetallic catalyst was essentially due to a shift of the overall reactant conversion to higher temperature in the bimetallic case. For LO6 instead, we can observe an important increase in ammonia production for the bimetallic catalyst, which can be due to a different response towards the higher amount of H_2. What is valid for both samples is that even if the average λ is the same as in LO5, the conversion of methane is shifted very efficiently to lower temperature by the oscillating dynamic. As seen for the first light-off tests it is likely that the incursion on the rich side emphasizes the conversion as it might also be inferred from the low conversion of O_2 and the occurrence of steam reforming. Indeed, steam reforming seems still the preferential path for methane conversion at high temperature, as it can be observed by the slight increase in H_2 concentration at 600K. The composition of the outlet gases can be related to the temperature, highlighting three intervals in the monometallic sample and two on the bimetallic sample as the vertical lines in Figure 6-22 are expected to do. It is evident a relation between the species in each interval, whit only a not better defined behavior of NO, that between 500K and 600K shows a plateau. In the end, the interaction between CH_4 and the other two main pollutants, NO and CO, is again confirmed also in the oscillating mode.

Light off LO7, reported in Figure 6-23, is very similar to LO6 having changed only the amplitude of the oscillations.

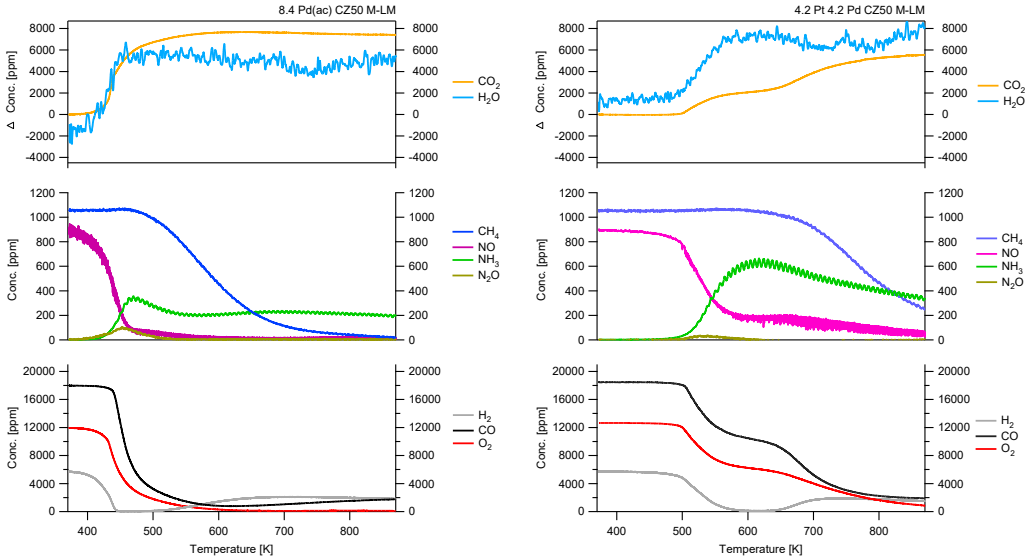

Figure 6-23: reactants and products concentration during the heating ramp of LO7 ($\lambda_{average}$=0.9981); 8.4Pd(ac) CZ50M-LM on the left; 4.2Pt 4.2Pd CZ50 M-LM on the right; in the upper part it is reported the difference between the amount of H_2O and CO_2.

The most evident differences are in the NO-NH_3 behavior of the monometallic catalyst: the higher amplitude seems to increase the production of NH_3 and the NO barely forms a plateau. This could be referred to a poor effect of OSC material, which is less important in the case of a large amplitude[199], or to a deeper shift to rich conditions and an averagely higher amount of H_2 produced by steam reforming. The production of H_2 here is indeed more appreciable at higher temperatures and it is again visible the increase of CO like in LO4, corresponding to a larger effect of steam reforming. It should be observed that overall the different amplitude of the oscillation of lambda seems to affect less the bimetallic sample. This might be related to the stabilization of Pd species when interacting with Pt forming an alloy, as reported in Chapter 3, which can be then less prone to take part in redox cycles under oscillating atmosphere.

6.3.2.2 Comparison with Umicore reference sample (fresh)

Figure 6-24, Figure 6-25 and Figure 6-26 display the conversions of CH_4, CO and NO respectively, for the samples 8.4Pd(ac) CZ50 M-LM, 4.2Pt 4.2Pd CZ50 M-LM and Umicore REF on the LO6 test. This test is the one taken as model for the TWC real conditions.

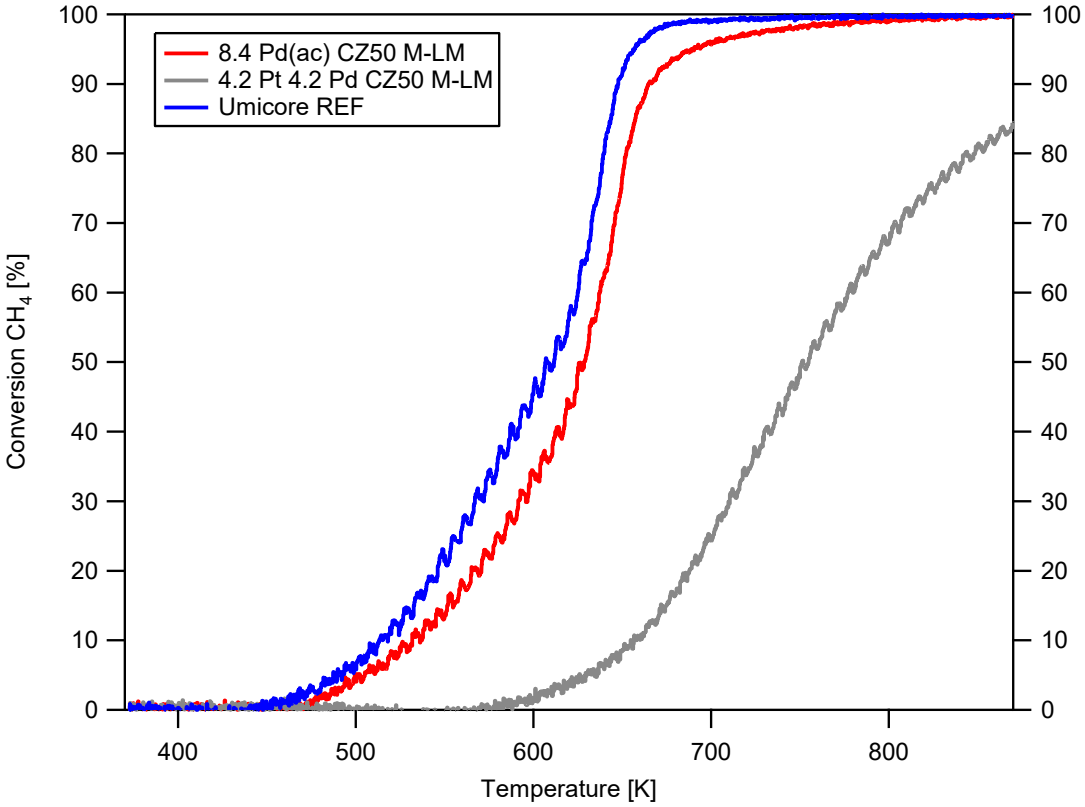

Figure 6-24: comparison of CH_4 conversion in LO6 for 8.4Pd(ac) CZ50 M-LM, 4.2Pt 4.2Pd CZ50 M-LM and Umicore REF.

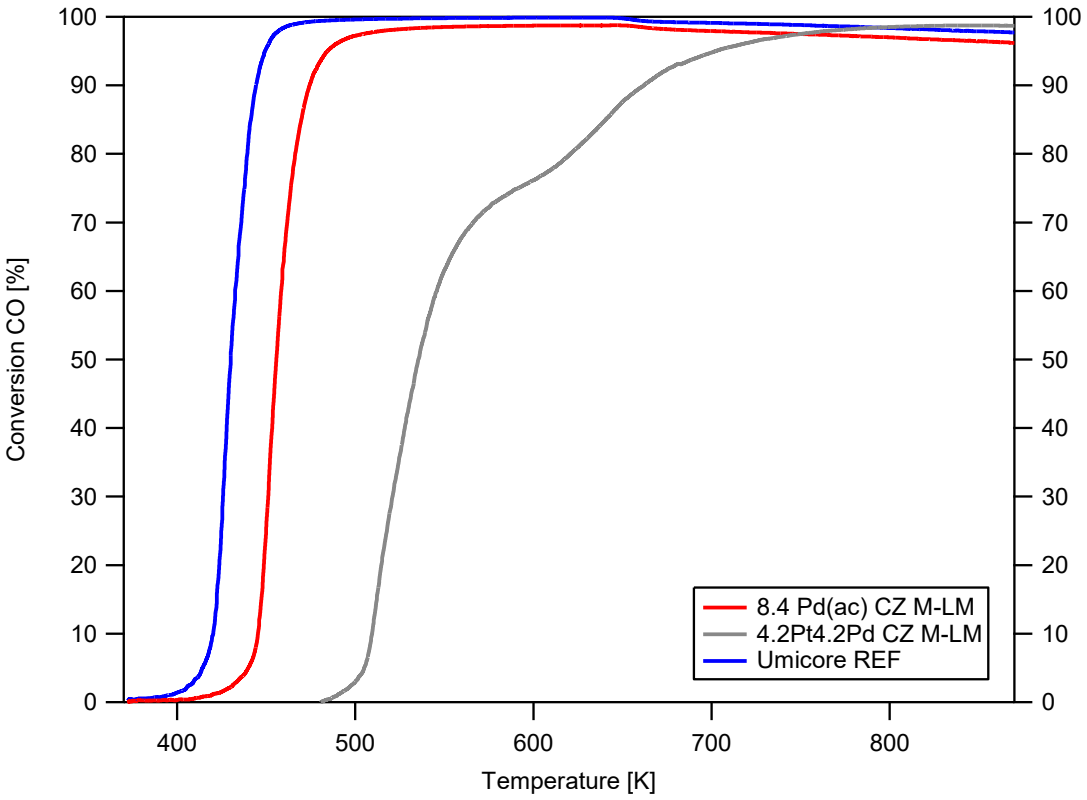

Figure 6-25: comparison of CO conversion in LO6 for 8.4Pd(ac) CZ50 M-LM, 4.2Pt 4.2Pd CZ50 M-LM and Umicore REF.

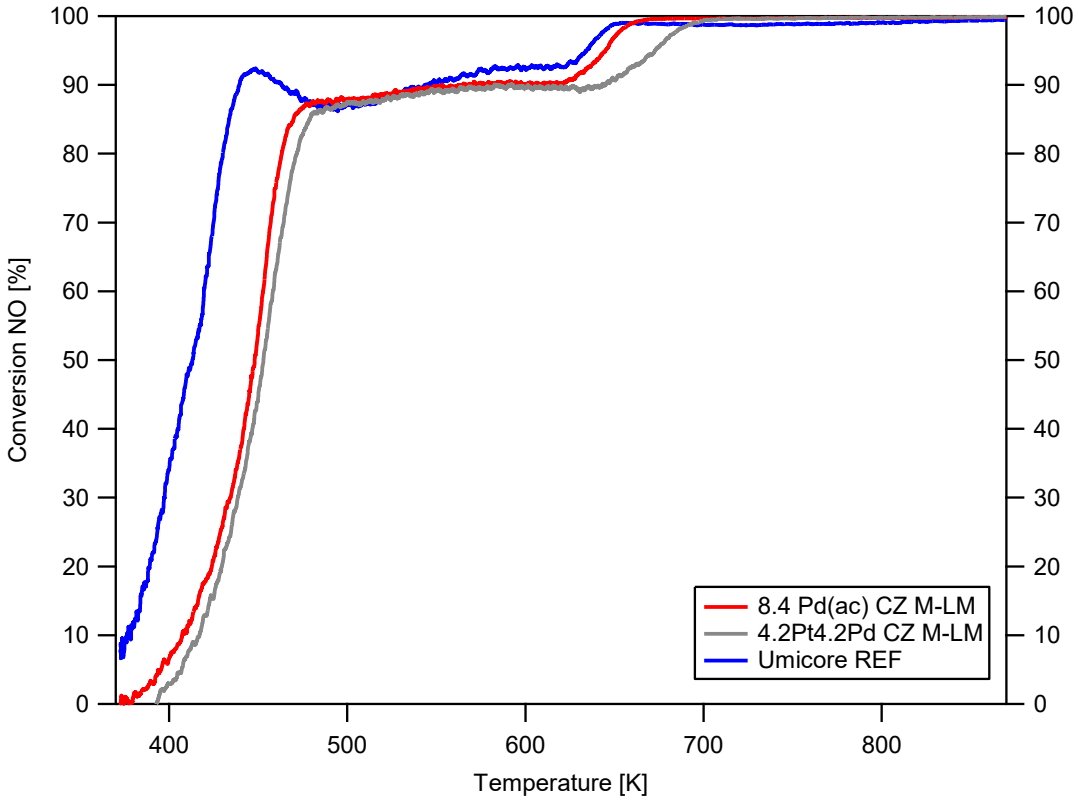

Figure 6-26: comparison of NO conversion in LO6 for 8.4Pd(ac) CZ50 M-LM, 4.2Pt 4.2Pd CZ50 M-LM and Umicore REF.

The Umicore REF shows generally the best performances. For C-containing pollutants this can be ascribed to the better activity towards CO oxidation, which is reflected then to CH_4 conversion for all the samples. In the case of NO, the conversion is comparable for all the samples and the highest activity for the Umicore REF at low temperature should be referred to the higher production of N_2O which has to be considered a pollutant as well (see Figure 6-27).

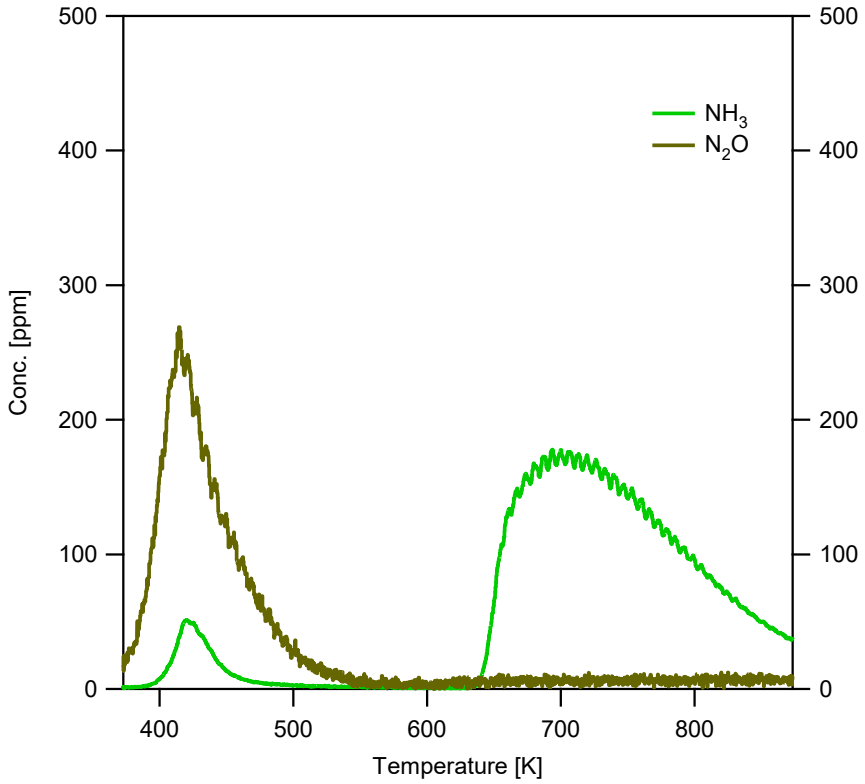

Figure 6-27: NH_3 and N_2O composition for the Umicore REF catalyst in LO6.

The results of this comparison are quite encouraging in light of future possible real applications of the milled catalysts, especially for the monometallic sample which presents conversions similar to the reference material. It should be noticed in fact that the samples are not fully formulated (they do not contain Rhodium) while the milled samples have not been systematically optimized for the coating process.

6.3.3 Lambda Sweep Tests

6.3.3.1 Dry milled catalysts

In Figure 6-28 and Figure 6-29 it is reported the conversion of CH_4, CO and NO for the samples 8.4Pd(ac) CZ50M-LM and 4.2Pt 4.2Pd CZ50M-LM respectively, on the lambda sweep test LS1 at 773K. The arrows indicate the direction of lambda sweep (from 0.975 to 1.025 or vice versa).

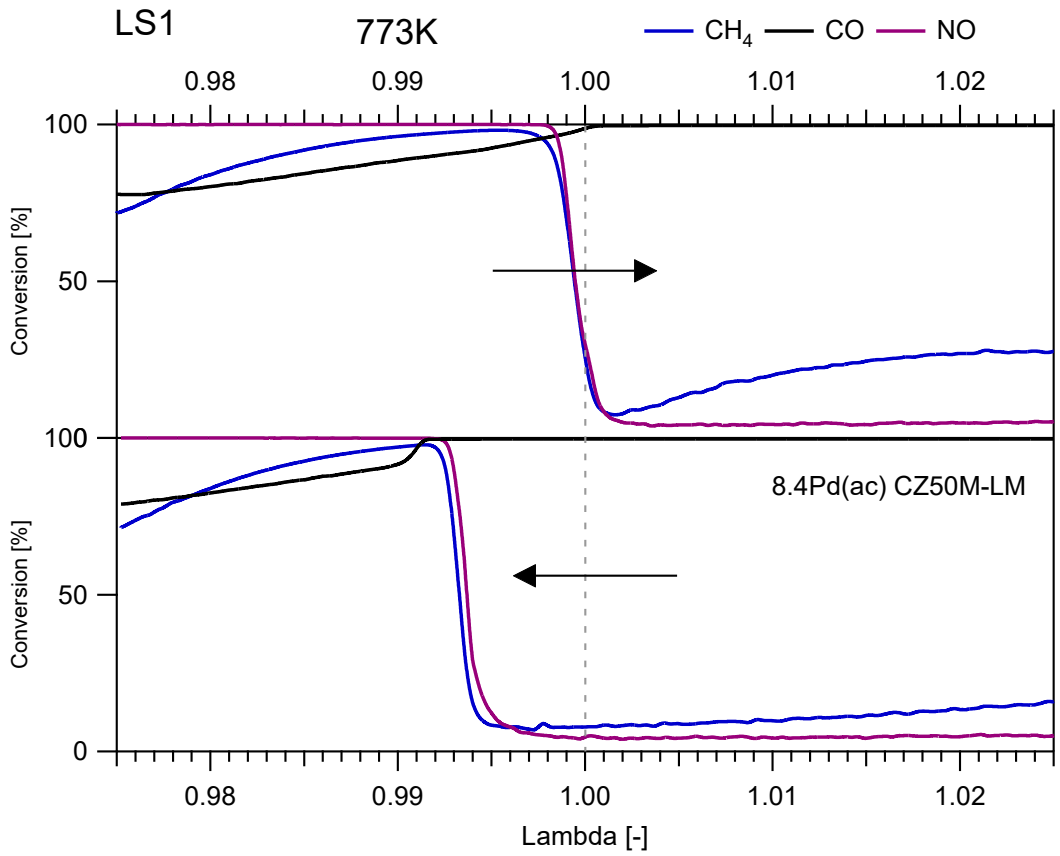

Figure 6-28: lambda sweep test LS1 for the sample 8.4Pd(ac) CZ50M-LM.

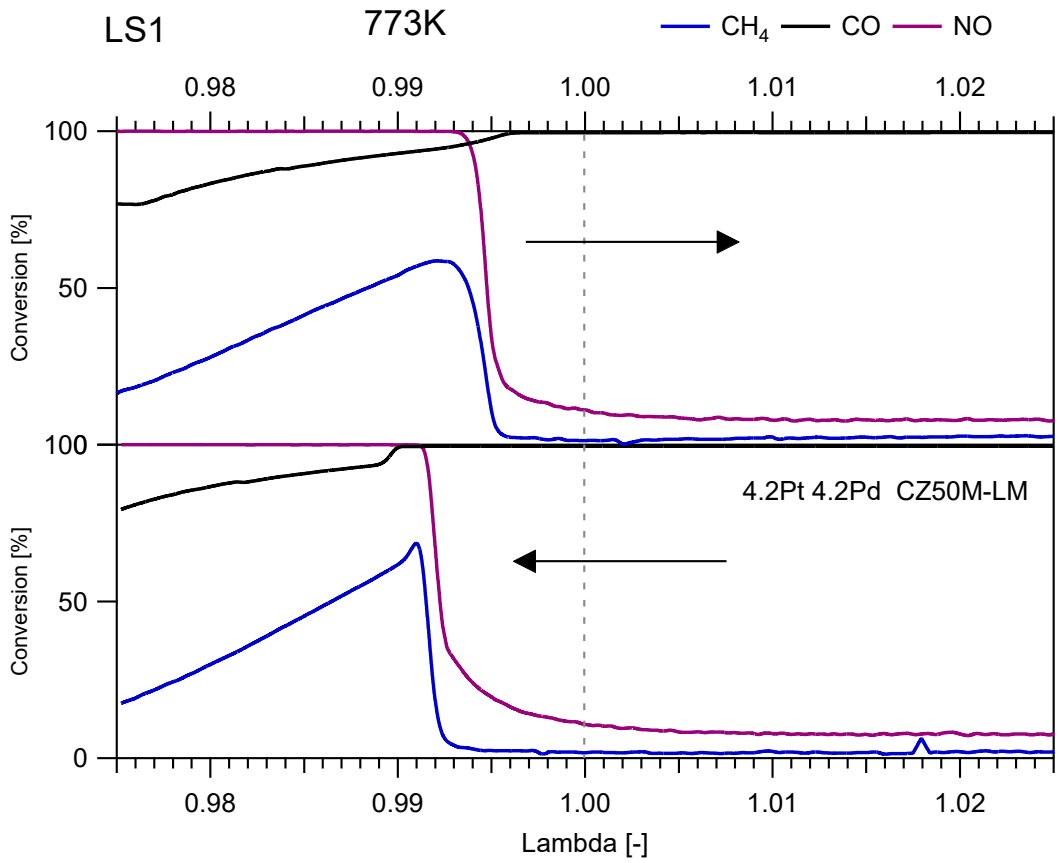

Figure 6-29: lambda sweep test LS1 for the sample 4.2Pt4.2Pd CZ50M-LM.

It is reported that for NGVs the so-called CO-NO crossover point, at which all the pollutants are efficiently converted, takes place in net rich conditions rather than at stoichiometry as in the case of gasoline TWC aftertreatment[202]. In the LS1 tests this is clearly appreciable: both the samples display the crossover point in rich conditions. Interestingly, this point is shifted in the direction of the test: it is closer to 1 if the test is moving from rich to lean conditions, it is closer to 0.99 in the opposite case and this is much more appreciable for the monometallic sample. As mentioned before, it is likely that the interaction taking place between Pd and Pt on the bimetallic catalyst hinders the sensitivity of Pd species towards lean or rich atmosphere, making the catalyst more stable during the variations between lean and rich conditions.

It should be observed also the different conversion of CH_4 on the sides of the crossover points. As already observed on light off tests, rich conditions are essential for the abatement of methane and at the same time lean ones are much less efficient. It must be noticed however that there is a maximum on the trend and too rich conditions are not favorable as well. According to the previous outcomes, the decreasing conversion on the rich side should be attributed to the unconverted CO that inhibits the reaction of CH_4. The decreasing of the conversion on the lean side for sample 4.2Pt4.2Pd CZ50M-LM

should be attributed instead to a less effective steam reforming, and the trend of NO that follows CH_4 reflects the missing H_2 from that reaction. Interestingly, in the monometallic case the conversion of methane increases again in lean conditions after the crossover point independently from NO, likely because the system switches to CH_4 oxidation path.

In Figure 6-30 the set of LS2 and LS3 lambda sweep tests carried out at 773K on the monometallic catalyst are reported. The LS2 test at 773K is the reference test for the stoichiometric oxidation of methane, and it is recalled that LS2 and LS3 are carried out with oscillating lambda at different amplitude (see Figure 6-10).

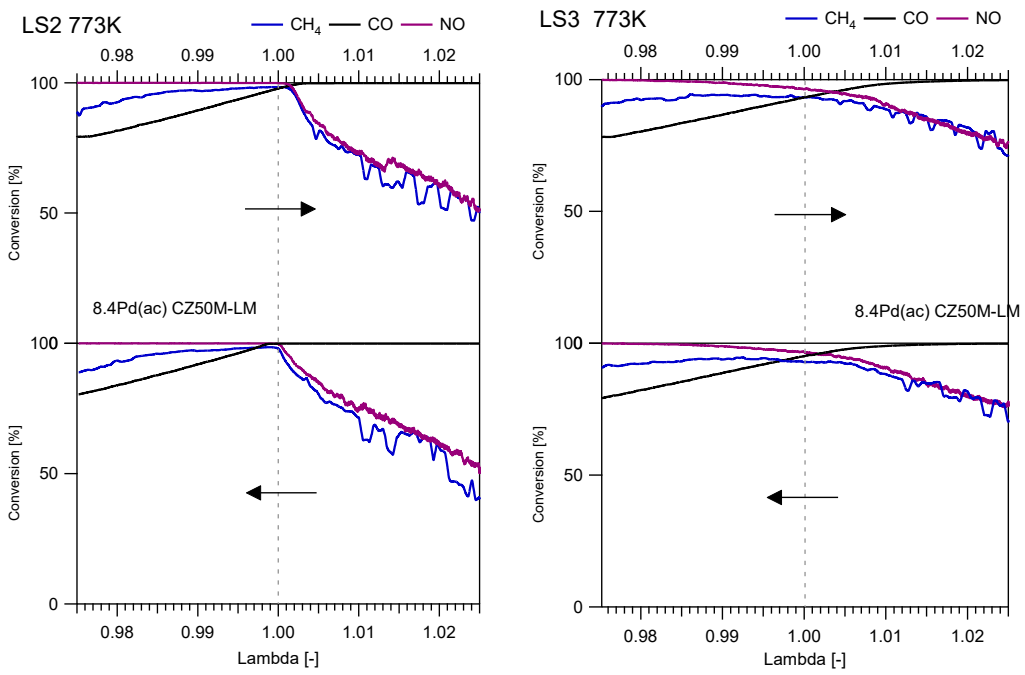

Figure 6-30: lambda sweep test LS2 and LS3 for the sample 8.4Pd(ac) CZ50M-LM.

Interestingly the CO-NO crossover point is not at rich conditions, but more close to stoichiometry if not on net lean conditions. Again, the direction of the test influences the position of the crossover point. It must be noticed that in LS3 the crossover point between CO and NO does not correspond to the maximum conversion of CH_4. It seems also that the high amplitude adopted has a sort of smoothing effect on the CH_4 trend that turns into a flatter line. It is recalled that the lambda reported in the graph is the average one.

The conversion on rich conditions is comparable for all the lambda sweep tests carried out, while the dynamic mode appears fundamental for a good conversion on lean conditions, as already observed. Differently from the LS1, NO follows the trend of CH_4

even at the leanest values. Again, this is referred to the incursions on rich conditions and the presence of H_2 from steam reforming.

In Figure 6-31 the set of LS2 and LS3 lambda sweep tests carried out at 773K for the bimetallic catalyst is reported.

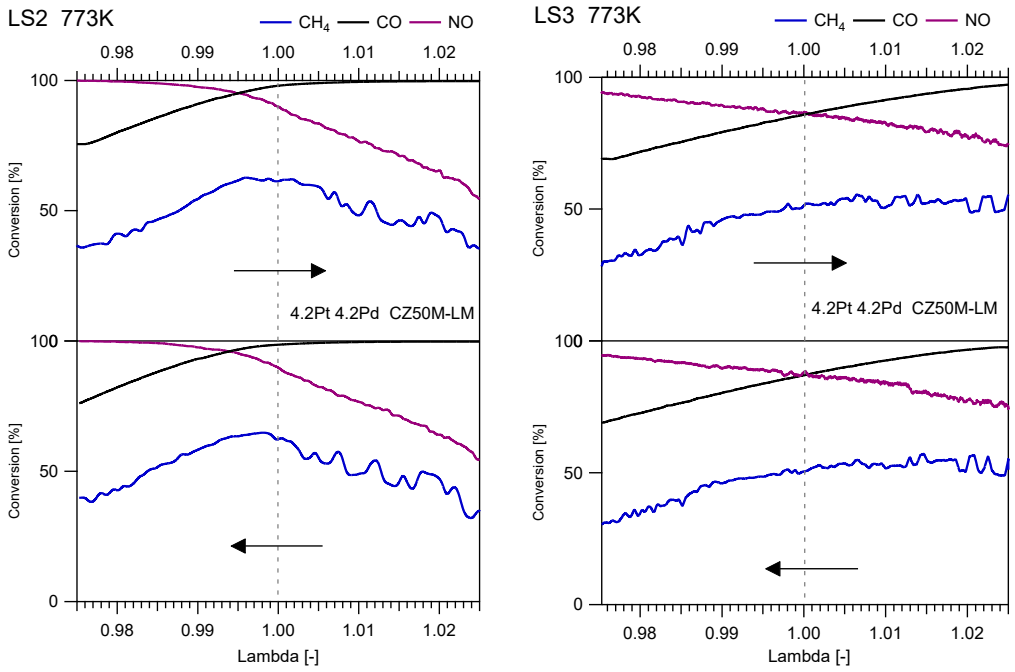

Figure 6-31: lambda sweep test LS2 and LS3 for the sample 4.2Pt4.2Pd CZ50M-LM.

In this case the CO-NO crossover point remains at rich conditions, but again it does not correspond to the maximum CH_4 conversion. In the case of LS3 the conversion of methane seems again smoothed compared to that of LS2, but it has a totally different trend, with a higher conversion in lean conditions than in rich ones. Moreover, this happens even if the conversion of CO considerably decreases. It is difficult to add some considerations only from this picture, but maybe this is due to the contribution of an oxidation path for the conversion of CH_4.

A further lambda sweep test was carried out at 723K, but not reported here, to evaluate the effect of the temperature. The main difference consists in a lower conversion of CH_4 at rich conditions and a higher conversion of CO which again underlines the competition between the two species observed in the light off test.

6.3.3.2 Lambda Sweep Results - Comparison with Umicore reference (fresh samples)

In Figure 6-32 it is reported the lambda sweep test LS2 for the Umicore reference catalyst. The results are similar to the ones of the monometallic catalyst. It shows however very high methane conversion in reducing conditions that does not decrease significantly going to richer values of lambda as the one observed with the milled catalyst. The conversion on lean conditions is comparable with the one of the monometallic milled catalyst, confirming the potential of application of mechanically prepared catalysts for NGV aftertreatment.

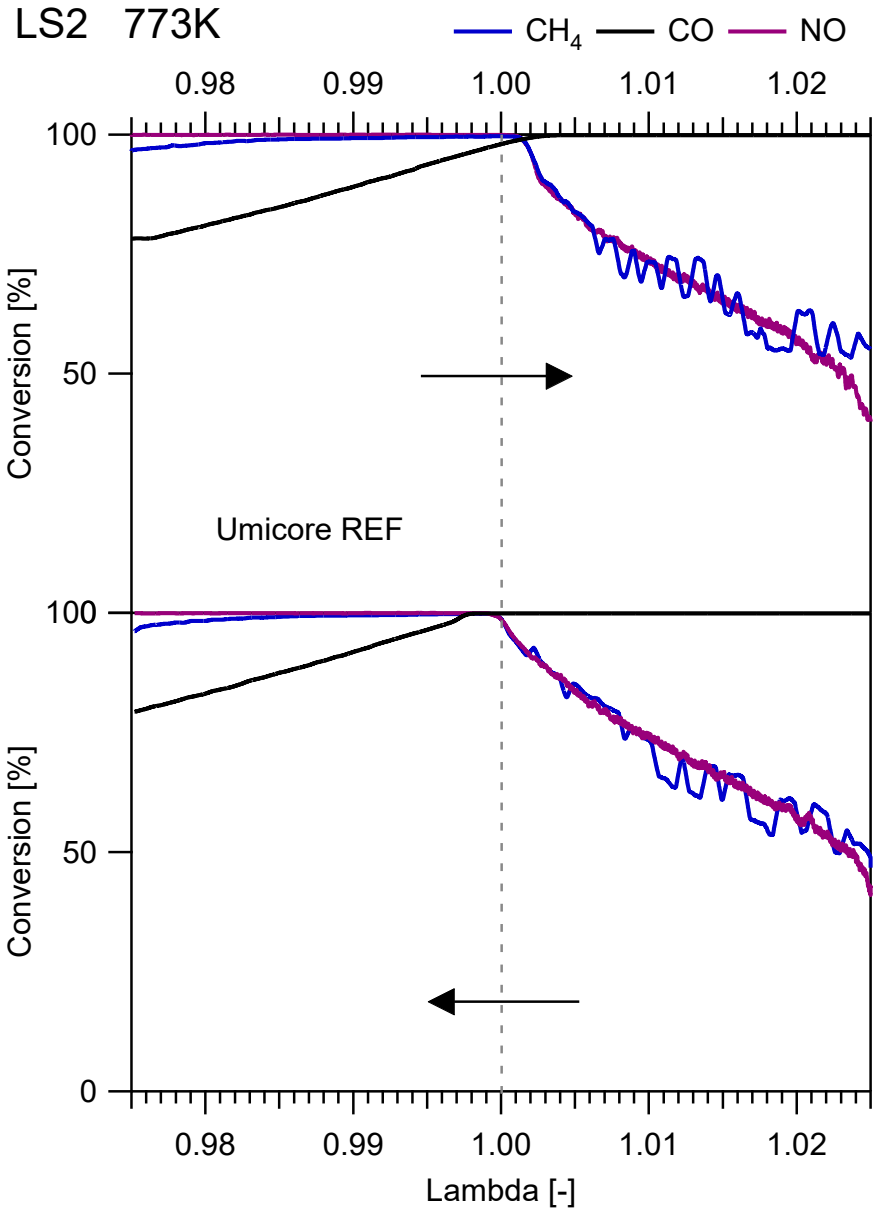

Figure 6-32: lambda sweep test LS2 for Umicore Reference.

6.3.4 Aged Samples

Figure 6-33 displays the conversion of methane and the conversion of carbon monoxide in light off test LO6 for the fresh sample 8.4Pd(ac) CZ50 M-LM, compared to the same sample after the *wet-ageing*, 8h in 10% water and air, or after the *pulsed-ageing*, 16h in oscillating 10%CO-10%O_2.

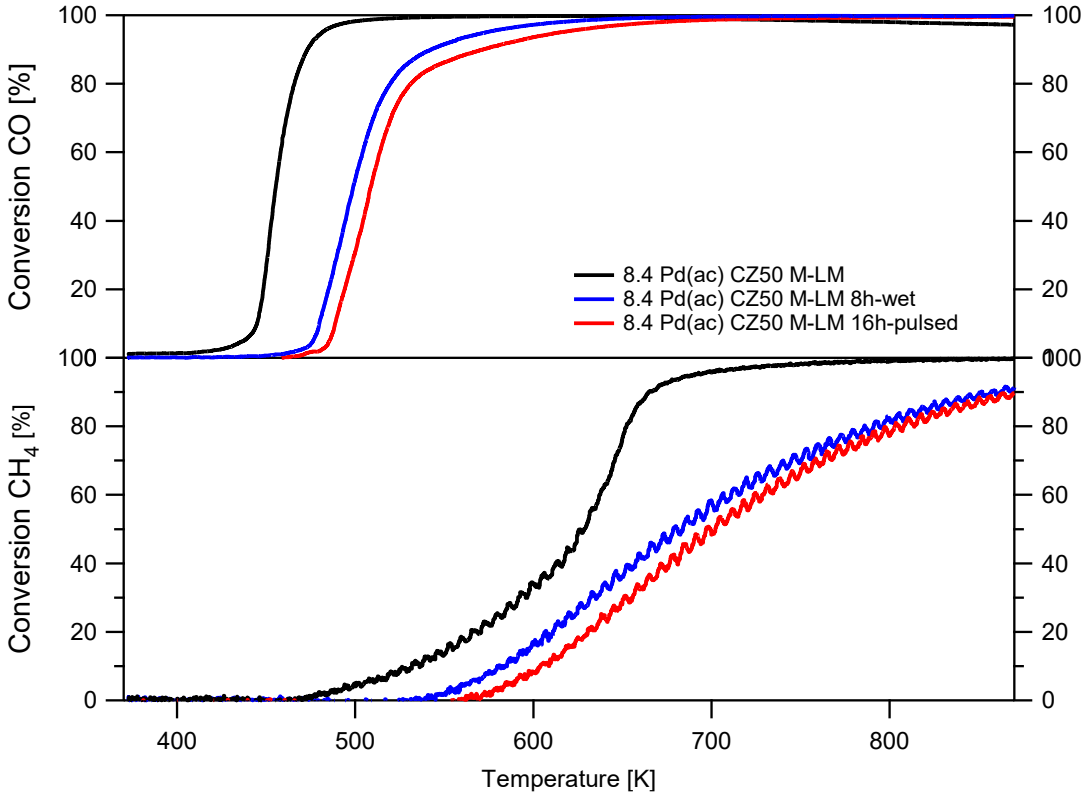

Figure 6-33: comparison between CO conversion (above) and CH_4 conversion (below) on LO6 for 8.4Pd(ac) CZ50 M-LM, fresh and after 8 hours of wet ageing (8h-wet) or 16 hours of pulsed ageing (16h-pulsed).

The catalytic activity for CH_4 is reduced in both cases, with a deeper effect for the longest ageing even if in absence of water.

Similar trend is observed for the activity towards CO, i.e. the longer the ageing the higher the deactivation. Comparing the two set of conversions it can be observed again that there is a connection between the temperature at which CO oxidation is almost completed and CH_4 conversion starts.

Figure 6-34 reports the CH_4 conversions and the CO conversions for fresh and aged samples in the case of 4.2Pt 4.2Pd CZ50 M-LM.

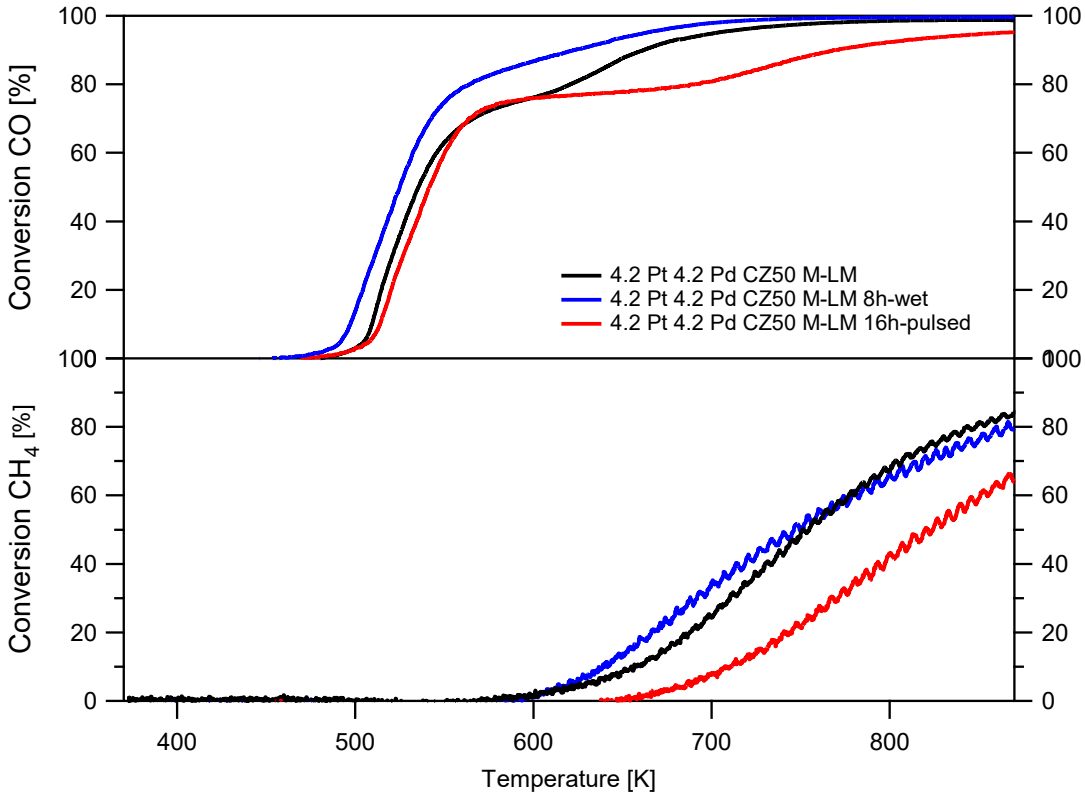

Figure 6-34: comparison between CH_4 conversion on LO6 for 4.2 Pt 4.2 Pd CZ50 M-LM, fresh and after 8 hours of wet ageing (8h-wet) or 16 hours of pulsed ageing (16h-pulsed).

In this case the worst sample is still the one after 16h of ageing, but the one after the 8h ageing in presence of water displays even better conversion at low temperature than the fresh one. Methane starts to convert here when the conversion of CO changes its slope. Again, this behavior was related to the end of the oxidation pathway, favoring the WGS reaction. This improvement on the conversion after ageing in presence of water was observed already for a bimetallic sample prepared by mechanochemical synthesis for CH_4 conversion in lean conditions (Chapter 3). The experiments carried out on the structured catalyst then confirm the positive effect of the aging in presence of water for the bimetallic samples.

Water is known to deactivate Pd-based catalysts also by the sintering of Pd nanoparticles[54]. Pt is known to have a protective effect on this kind of systems[66]. However, when Pt and Pd are mechanically mixed with the OSC material, the catalyst shows a considerable improvement in conversion after being treated in water as already explained in Chapter 3. The comparison between the two treatments clearly shows that water is fundamental for this improvement since the same result is not achieved in the pulsed treatment.

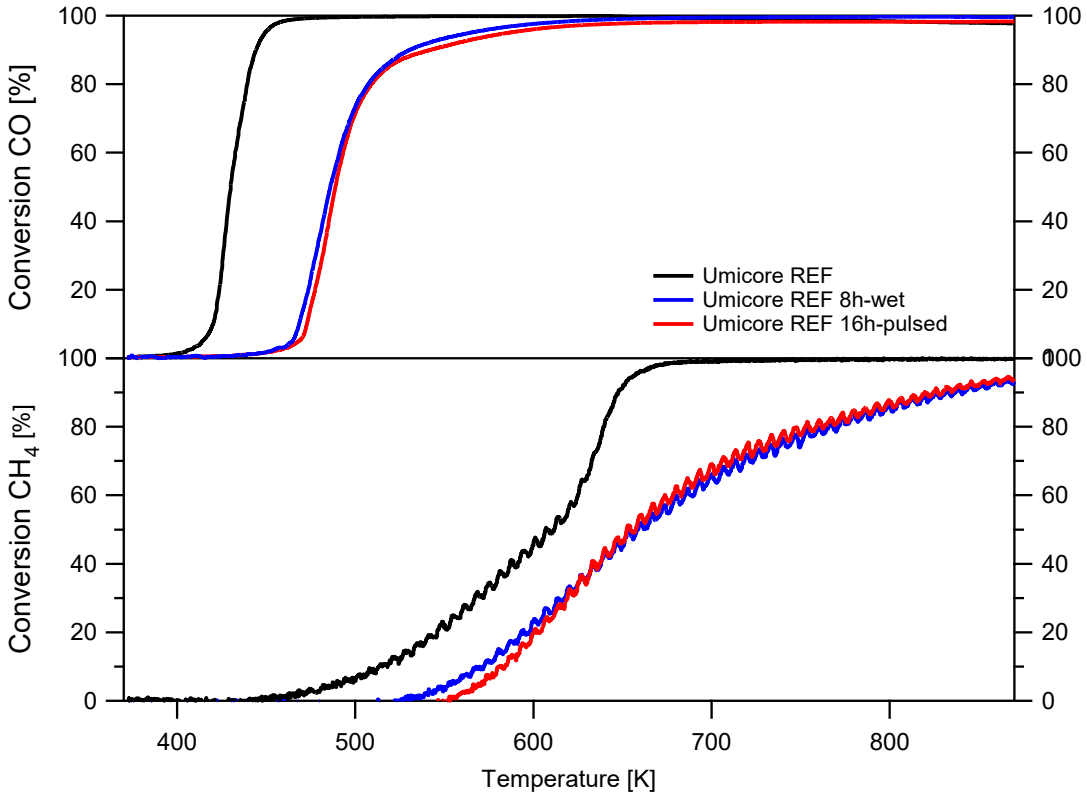

Figure 6-35: comparison between CH_4 conversion and CO conversion on LO6 for Umicore REF, fresh and after 8 hours of wet ageing (8h-wet) or 16 hours of pulsed ageing (16h-pulsed)

The last comparison is carried out with Umicore REF, in Figure 6-35. Of the three samples, indeed this is the one which suffers the most the effect of the ageing. This can be better appreciated by looking at Figure 6-36 reporting the ΔT_{50} between the fresh and aged samples for all the three pollutant conversions. ΔT_{50} is defined as the difference in the temperature to achieve 50% conversion between the fresh and the aged samples.

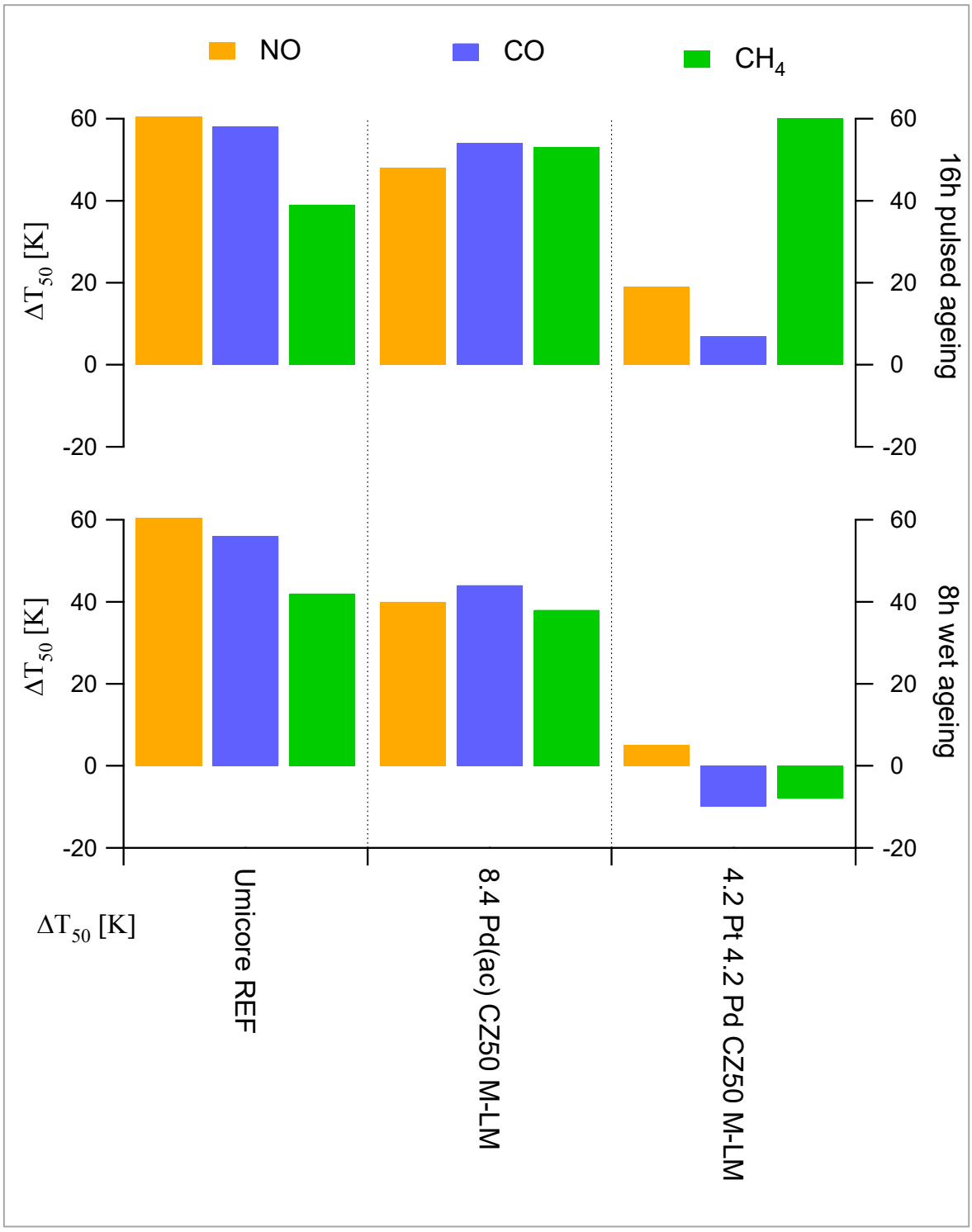

Figure 6-36: ΔT_{50} for the samples Umicore REF, 8.4 Pd(ac) CZ50 M-LM and 4.2 Pt 4.2 Pd CZ50 M-LM after the two ageing treatments.

The lower deactivation of 4.2Pt4.2Pd CZ50 M-LM for NO and CO conversion during the 16h pulsed ageing has to be ascribed to the presence of Pt in the formulation. It is noticeable, anyway, that also the monometallic milled sample shows some stability improvement compared to the Umicore reference. This is much more evident when the

ageing is carried out in presence of water (8h wet ageing). In this case there is a benefit for 4.2 Pd(ac) CZ50 M-LM, which becomes significantly more evident in the bimetallic formulation, especially for methane and CO (the negative ΔT_{50} indicates an improvement in conversion after ageing). This once more indicates the beneficial effect of mechanochemical preparation especially on stabilizing the catalytic active sites in presence of water for the conversion of typical C-containing compounds on TWC systems, as already observed in the powder bench tests, and also for NO and CO.

6.4 Conclusions

Despite the need of further optimization of the catalysts in light of the coating process, the results obtained in a series of lab-scale industrial tests clearly show the potential of these materials for real applications, as inferred from the comparison with the industrial reference. In particular, the monometallic sample had comparable performances with the reference provided by Umicore in the fresh state, while the bimetallic one suffered presumably from the lower amount of palladium.

On the other side, the addition of platinum stabilized the catalyst after ageing carried out in the presence of water, confirming the results already obtained in powder tests.

For both milled samples, a lower degree of deactivation after ageing was observed in wet atmosphere.

It must be noticed in the end that there was a non-negligible distance to cover between the milling procedure developed in Udine for powder catalysts and the one developed at the Umicore laboratories for structured catalysts. As already mentioned, the structured configuration adopted here forced some decisions on the materials prepared, which were still not perfectly optimized.

A crucial point in the preparation of the bimetallic catalyst is the choice of the PGM precursors and their compositions. As reported, not all the precursors can be used efficiently to provide the high amount needed in the real application of the coated catalysts[207]. For this reason, a screening of possible PGM precursors is desirable to make a more solid choice. This is true in particular for the bimetallic case, where no combination other than with metallic Pd and Pt powders was investigated before this study. Moreover, it would be interesting to compare a second bimetallic composition with different Pt and Pd loadings to assess more in depth the effect of the platinum addition in the structured configuration, as already done for the powder catalysts (see Chapter 3).

Another important issue to address for material optimization is the support used for the mechanochemical synthesis. This preparation method seems to lead to higher performances thanks to a core-shell structure, exclusively formed when palladium is mechanically mixed with a cerium oxide with low surface area[126]. In this study the standard ceria-zirconia provided by Umicore was used, and the surface area was one order of magnitude higher than the one of the ceria investigated in our previous research. It is possible that the interaction of Pd with this ceria-zirconia support during

the mechanical mixing is not optimal and this might explain why the catalysts prepared were not better than the reference. This suggests that also a screening on different ceria-zirconia supports can help to improve the material.

The complexity of the feed adopted in this study was very different from the net lean conditions of the static gas mixture used in powder tests (see Chapter 2), that represented our term of comparison. It is evident in fact from this study that the steam reforming is the preferred methane conversion path both in rich and oscillating conditions, and this is strongly limited by the presence of CO. This should be taken into account when evaluating a proper catalyst formulation for a natural gas vehicle TWC system. For example, the static test LO5, even if not specifically close to real conditions (for which oscillating lambda is needed), gave the same results of the more realistic LO6 for the comparison among the catalyst. This test is reproducible in a simple set up and can give important and faster feedbacks in the trial-and-error approach of mechanical synthesis and can be used to substitute the simple lean methane oxidation.

A final observation after all the catalytic tests carried out at Umicore involves the need to integrate them with a proper material characterization, in particular to understand the mechanisms involving Pd in the conversion of CO and CH_4 and their mutual connection shown in this work.

At the end, this study confirmed the validity and the potential of the mechanical milling as a cheaper and ecofriendly method suitable also for industrial scale, and it tracked some indications to efficiently improve this procedure for the real application.

7. Investigation of CO oxidation over dry milled catalysts

Abstract

The dry mechanochemical synthesis developed and explained in the previous chapters was used to prepare ceria-based catalysts for the oxidation of CO. Results show that the dry milling is not as effective as in the case of CH_4 oxidation, and in this reaction the milled catalysts do not outperform the homologous samples prepared by the traditional impregnation method. Among the tested catalysts, the bimetallic Pt-Pd formulation leads to the highest activity, tentatively assigned to the presence of an alloy between the two metals.

7.1 Introduction

In natural gas fueled vehicles aftertreatment, the role of palladium and platinum catalysts is not only to reduce methane content in the exhaust, but also carbon monoxide[209]. The supported metal should promote the simultaneous oxidation of the two C-containing species below the exhaust gas temperature. However, the catalyst can have a different role in the two reactions, due to different mechanisms, structure sensitivity[210,211] or to the nature of active sites[43].

CO oxidation is a well-studied reaction, often used as a model to test novel materials including monometallic Pd and Pt catalysts as well as various bimetallic PtPd compositions.[212,213] CO is more reactive than CH_4 and its total oxidation occurs at much lower temperatures. The following mechanism is generally proposed (Mars van-Krevelen model): CO reacts directly with surface oxygen forming CO_2, leaving surface vacancies that are subsequently filled by gas-phase oxygen[214,215]. The mechanism is similar to that for CH_4 in the sense that a clear contribution is given by adsorption and activation of oxygen for both reactions. One might speculate that there should be a good correlation between the oxidation reactions of the two C-containing compounds. However, in the case of methane, the rate limiting step is the breakage of C-H bond (i.e.

the activation of the methane molecule), and this fundamental step prevents a systematic design of a catalyst highly active for both reactions.

An important role for CO and CH_4 oxidation is played by the metal-support interaction. In this respect, ceria is a well-known promoter for CO oxidation, even without noble metals.[216] Moreover, thanks to its high reducibility it can create strong interaction with the metals supported on the surface, which depends also on CeO_2 crystallites shapes and intrinsic surface exposure.[217,218] For example, an active site for CO oxidation is found to be the interfacial Pt-O-Ce.[219] CO adsorbs on Pt and CeO_2 actively supplies oxygen, with dynamics depending on the metal particle size[220,221] and on oxidative or reductive treatments[222–224]. A similar situation has been proposed also for Pd-based catalysts[225,226,]. Nonetheless, there is uncertainty regarding the active phase of Pd on CeO_2 in CO oxidation. Pd can be found either in metallic phase Pd^0, PdO phase or in solid solution with Ce and these phases are often present simultaneously, making difficult to determine the real active phase. For example, Pd^0 was reported as the active phase for CO oxidation,[227] but some recent studies affirm that single atoms in Pd^{2+} valence show the highest activity.[228,229] Moreover, the size and dispersion of Pd play a major role in this reaction.[167] Oxidizing treatments at high temperature, such as atom trapping, followed by CO or H_2 reducing treatments in2crease the dispersion of both Pt and Pd catalysts on CeO_2, being effective for CO low-temperature oxidation. However, it appears easier to tune Pt dispersion with respect to Pd exploiting the PtO_2 volatility, due to the different stability of the oxidized phases.[229] In the case of Pd-based catalysts instead, hydrogen pretreatment can result in an increase of the metallic Pd phase,[230] and also in the formation of oxygen vacancies in the solid solution Ce-Pd-O.[231] Finally, it should be recalled that CO itself may have a non-negligible impact on the degree of oxidation of the metal phase, changing in-situ the catalytic activity for the abatement of other pollutants.[164] A competitive dynamic may occur when other pollutants are present in the feed, with a great inhibiting effect by CO.[232]

The variables increase further when a bimetallic PdPt formulation is chosen. Many studies deal with bimetallic PdPt catalysts for CO oxidation, which are the state-of-the-art for diesel oxidation catalysts[163]. The activity has been reported to improve for high Pd content, but optimal formulations are usually close to 1:1 molar ratio, considering also durability[233]. The alloying of Pd with platinum can improve the oxidation activity, but at the same time the control of dispersion becomes more difficult.[234]

There is a large number of studies on CO oxidation trying to elucidate all the parameters dependencies and mechanisms involved in the reaction, and strong simplifications are assumed with a rich panel of conditions. Thus it is difficult to systematically compare results in this massive database, especially when trying to mimic close-to-real conditions. This appeared evidently also in this work, when comparing CH_4-CO-NO conversion in full exhaust feed (Chapter 6). However, it is evident from the results reported in Chapter 6 that CH_4 activation is delayed by the presence of CO. Trying to elucidate this aspect, it was thendecided to carry out a qualitative study for three catalyst formulations (Pd monometallic, Pt monometallic, PtPd bimetallic) prepared by ball milling and by incipient wetness impregnation. The investigation was carried out in a simple setup for lean CO oxidation with the aim of studying the effect of the mechanochemical synthesis on this model reaction. The effect of reducing pretreatment and of wet aging was also investigated.

7.2 Materials and methods

Pure cerium oxide (CeO_2, Umicore) previously calcined at 1473 K for 3 hours was used as support for the catalysts. Metallic palladium (Pd black, Sigma Aldrich, surface area 40-60 m^2/g) and metallic platinum (Pt black, Sigma Aldrich, ≤20μm) nanopowders were mechanically mixed with CeO_2 in a Mini-mill Pulverisette 23 (Fritsch) to obtain the samples defined as milled (M), according to the procedure already reported in Chapter 2.

The total PGM amount was fixed again at 1%, with the bimetallic catalyst containing 0.5wt% Pd and 0.5wt% Pt and prepared by milling first Pd with ceria, then adding Pt. The samples were named (1-x)PtxPdCe-M, where x is the wt% of Pd. Three homologous samples were prepared by incipient wetness impregnation with the same procedure and precursors reported in Chapter 3.2. The catalytic activity for CO oxidation was investigated according to the procedure reported in Chapter 2.3.3.

All samples, with relative names and composition, are summarized in Table 7-1.

Table 7-1: Composition, mass and molar ratios, and names of samples considered in this work.

Sample NAME	Nominal Pt wt%	Nominal Pd wt%	m^{Pd}/m^{Pt}	Pd/Pt molar ratio
1PdCe M	/	1	/	/
1PtCe M	1	/	/	/
0.5Pt0.5PdCe M	0.5	0.5	1	1.83
1PdCe IW	/	1	/	/
1PtCe IW	1	/	/	/
0.5Pt0.5PdCe IW	0.5	0.5	1	1.83

7.3 Results and discussion

In Table 7-2 the surface area values of the samples studied, together with that of the support oxide, are reported. All values are comparable with that of the support.

Table 7-2: BET surface area of catalysts and support oxide used in this study.

Sample	BET surface area (m^2/g)
CeO_2(1473K)	4.2
1PdCe M	4.3
1PtCe M	4.3
0.5Pt0.5 PdCe M	4.3
1PdCe IW	4.6
1PtCe IW	4.5
0.5Pt0.5 PdCe IW	4.5

Figure 7-1 shows the XRD spectra of the samples in the 38-42° 2θ range. The characteristic peaks of cubic CeO_2 are located at 33.1° and 47.3° and present on all samples (not shown). A peak at 39.8° corresponding to metallic Pt is observed on both1PtCeM and 1PtCeIW, whereas on 1PdCeM a peak at 40.1° belonging to metallic Pd is detected. On 1PdCeIW Pd and PdO are not observed. On this sample the presence of PdO would be expected due to calcination, but it is likely that high dispersion and/or low loading prevent its appearance in the x-ray diffraction analysis. The bimetallic samples show a peak centered in between metallic Pd and Pt features, which is broader on the milled catalyst and attributed to the formation of a PdPt alloy.

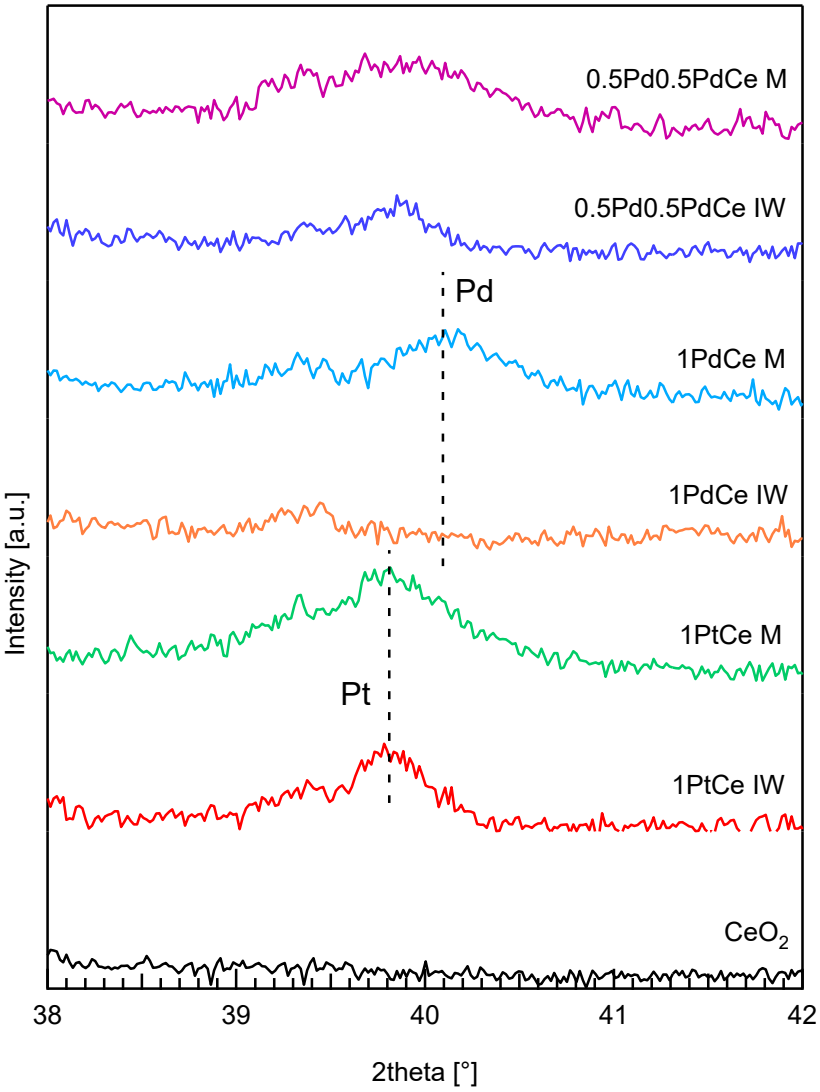

Figure 7-1: XRD spectra of fresh catalysts in the 38-42° 2ϑ range.

Catalytic activity for CO oxidation is shown in Figure 7-2 for the monometallic samples 1PtCeM and 1PtCeIW, with and without reducing pretreatments (for experimental details see Chapter 2.3.3).

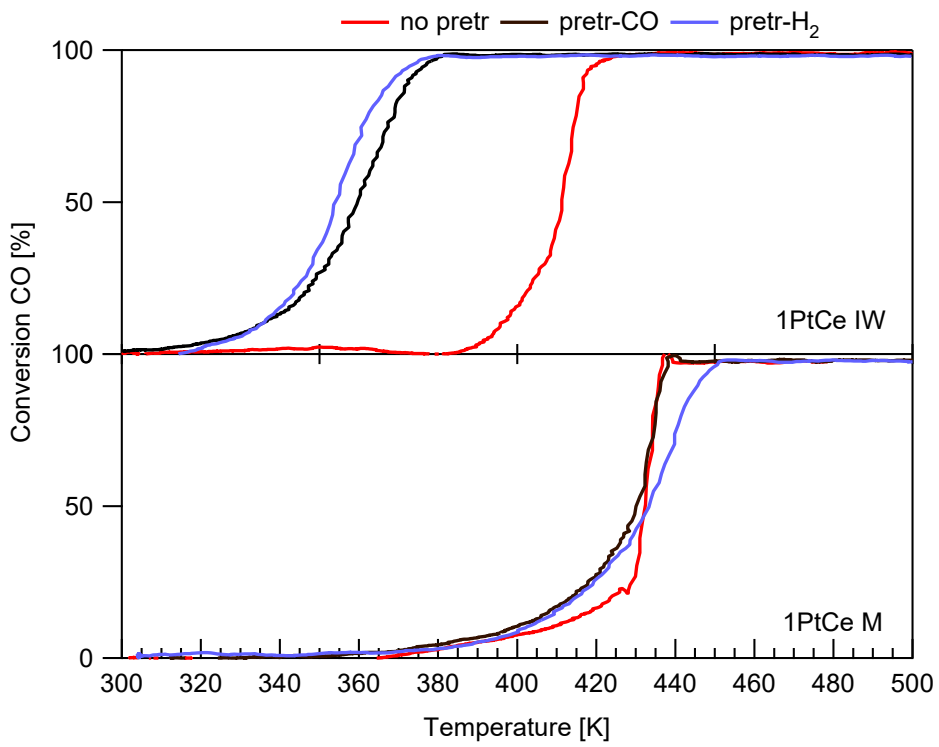

Figure 7-2: LO tests for samples 1PtCeM (below) and 1PtCeIW (above). Sample not pretreated (red); pretreated in CO (black); pretreated in H_2 (blue).

In the absence of any pretreatment (red line), there is a slight difference between the Pt-based impregnated and milled sample, the T_{10} and T_{50} (temperatures at which 10% and 50% CO conversion are achieved) being 396K and 411K for the former and 409K and 432K for the latter, respectively. The situation changes drastically after the reducing pretreatments. Table 7-3 lists the ΔT_{10} and ΔT_{50}, defined as the differences of T_{10} and T_{50} of the pretreated samples with respect to the non-treated ones. The negative values indicate the improvement, which is clearly observable also by the light-off curves in Figure 7-3. The more negative they are, the higher the improvement obtained after the pretreatment. In the case of the impregnated sample, both pretreatments have a strong impact on the activation temperature. It is not the case for the milled sample, where the improvement is negligible and only slightly better with CO.

Table 7-3: ΔT_{10}(K) and ΔT_{50}(K) for the samples 1PtCeM and 1PtCeIW.

Sample	ΔT_{10}(K)	ΔT_{50}(K)
1PtCe M – CO	-10	-2
1PtCe M – H_2	-7	+1
1PtCe IW – CO	-61	-52
1PtCe IW – H_2	-60	-57

Different results are obtained for palladium-based samples, as it can be observed from Figure 7-3. First of all, the effect of the pretreatment is negligible for both catalysts (see also Figure 7-4). Moreover, in the case of CO oxidation the impregnated sample is the best performing one and it has even better performances than the homologous platinum sample. This is opposite to what observed for methane oxidation: Figure 7-3 (right) shows also the conversion of CH_4 during transient lean oxidation on the same samples, where the milled catalyst is better than the impregnated one.

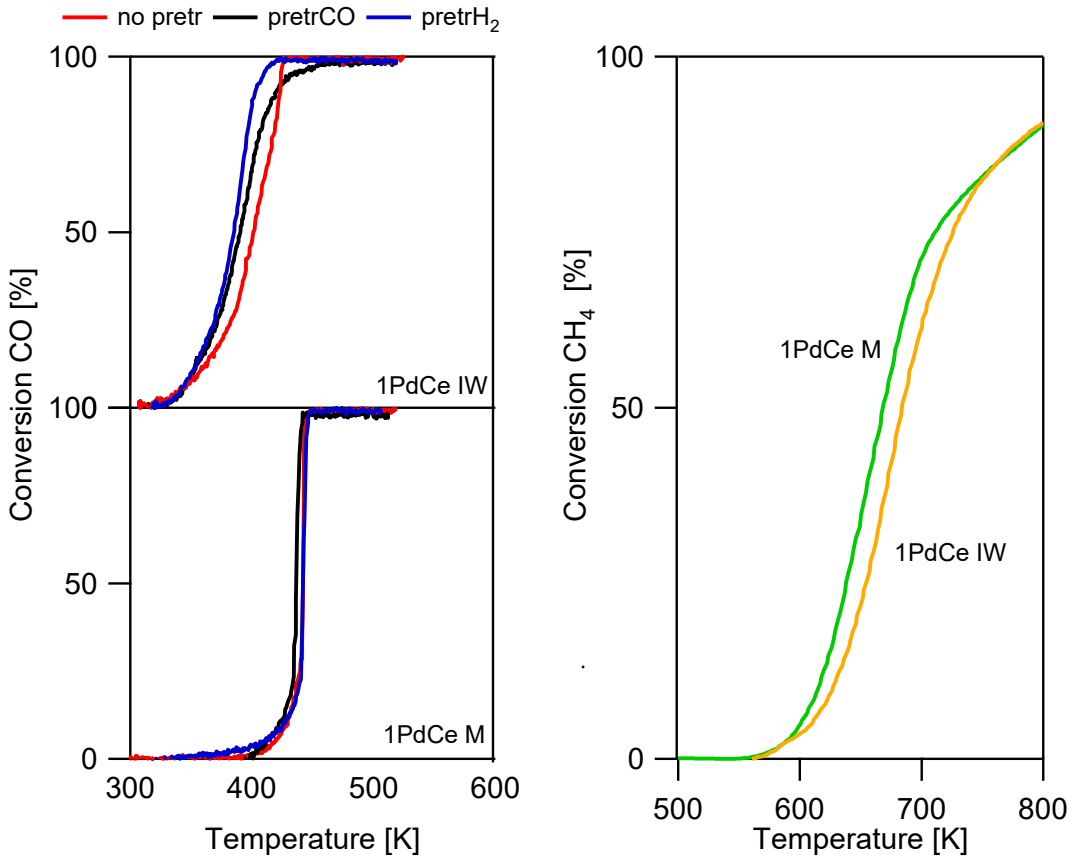

Figure 7-3: left: CO conversion for samples 1PdCeM (below) and 1PdCeIW (above). Sample non pretreated (red); pretreated in CO (black); pretreated in H_2 (blue). Right: CH_4 conversion for the samples 1PdCeM and 1PdCeIW (0.5%CH_4; 2%O_2).

It should be observed, though, that this difference is not so marked as it was observed in our previous works[126], and this might be ascribed to some morphological differences in the ceria support which we could not investigate in depth due to lack of time.

Table 7-4: ΔT_{10}(K) and ΔT_{50}(K) for the samples 1PdCeM and 1PdCeIW

Sample	ΔT_{10}(K)	ΔT_{50}(K)
1PdCe M – CO	-3	-7
1PdCe M – H_2	-4	0
1PdCe IW – CO	-5	-11
1PdCe IW – H_2	-6	-16

The behavior of the monometallic catalysts can be discussed in light of literature reports. For Pt/CeO_2 it is not surprising that the reducing pretreatment has such a strong effect on the impregnated sample. As it is known, thermal treatments can promote Pt redispersion, eventually to atomic level, on the surface of the support.[223,235,236] The impregnated sample, differently from the milled ones, is calcined for 3h in air at 1173K and thus a good dispersion might be expected after this process. Usually, after reducing treatments the formation of well-sized particles with much higher activity is observed.[222] This is likely to happen also for 1PtCe IW. In the case of milled sample, Pt is expected to be mainly in the metallic form since the precursor is metallic platinum. Thus, the effect of the pretreatment is reasonably negligible, also considering the low temperature of the reducing treatment.

The behavior of Pd/CeO_2 samples is more difficult to discuss. As for Pt it is reported that a high dispersion can be achieved after oxidation treatments.[229, 237] This is associated with an improvement in the catalytic activity, which can further increase by treating furtherly the samples in a reducing environment which allows to modify the size of the particles.[238–240] Recently it was reported that Pd, existing initially as relatively large PdO clusters on the surface, can penetrate into CeO_2 lattice during oxidation treatments forming Pd-Ce-O structures reaching a certain level of Pd substitution. If the treatment is continued, the process is inverted and Pd starts to migrate from ceria lattice to the surface, now forming very small particles of PdO with adsorbed oxygen. Thus, depending on how long the treatment lasts, the sample can have different amount of Pd-Ce-O phase rather than surface PdO in the form of big or small particles.[241] Different catalytic activity is obtained by the different morphologies, and the best performances are achieved by the sample with small PdO particles. In the mentioned study the authors also consider the effect of a further pretreatment in H_2, highlighting the advantage of increasing the Pd^0 phase. All the samples are indeed improved, but not the already active one with small PdO particles. The authors conclude that the small nanoparticles can be reduced already during CO oxidation, so that the reducing treatment has almost the same effect. At the same time CO is not able to

modify the morphology of the other samples with bigger particles, where instead a H_2 treatment appears effective.

The impregnated catalyst tested here should be formed by similar small PdO nanoparticles, in agreement with HRTEM analysis carried out on analogous samples [126]. Thus, during CO oxidation it is efficiently reduced obtaining the same result as with a reducing pretreatment. In the case of 1PdCe M, palladium is present already in metallic form and something similar to what was proposed for 1PtCe M can be supposed, observing its lower activity compared to the impregnated sample and no benefits from the reducing pretreatments.

After considering the monometallic catalysts, also the bimetallic ones have been tested for CO oxidation. In this case, due to the improvement observed for PtPdCe M after wet TOS treatment for methane oxidation, it was tested also the milled sample after wet time on stream at 623K (wet TOS, see Chapter 2). In Figure 7-4 it is reported the normalized conversion of CH_4 during wet TOS experiment, which resembles the result already obtained for the bimetallic sample prepared on a different ceria support (Chapter 3).

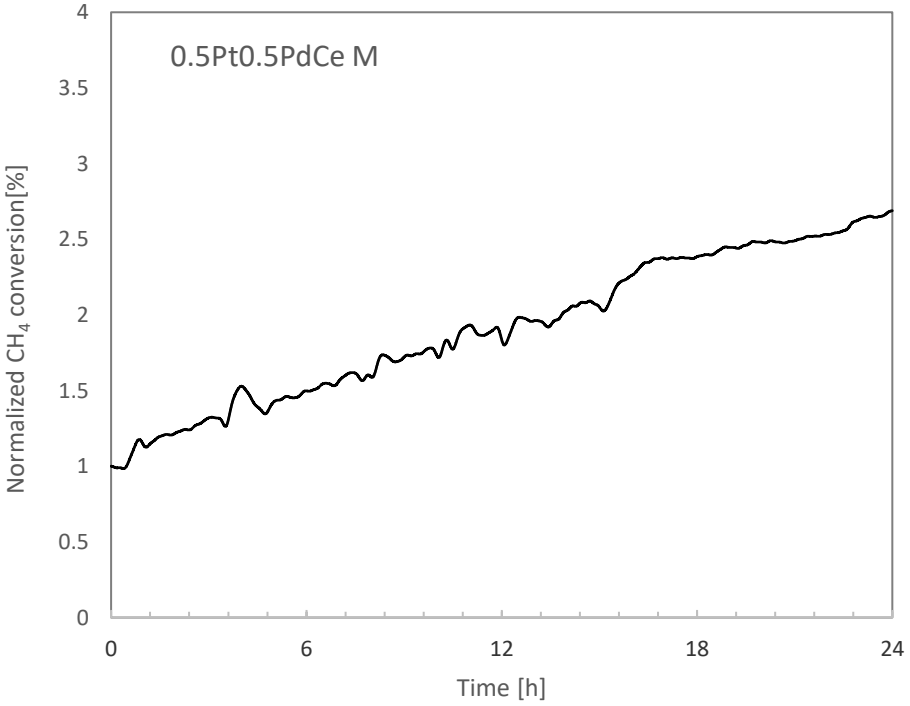

Figure 7-4: normalized CH_4 conversion for the sample 0.5Pt0.5PdCe M during the 24h isothermal treatment at 723K (0.5% CH_4; 2% O_2).

Figure 7-5 shows the XRD spectra of the bimetallic sample after the wet TOS, together with the untreated sample as reference. The peak visible at 40° is now sharper and it is

thus excluded the possibility of a superimposition of Pd and Pt single peaks, as supposed for the untreated sample. A new peak at 33.9° appears and it can be referred to PdO.

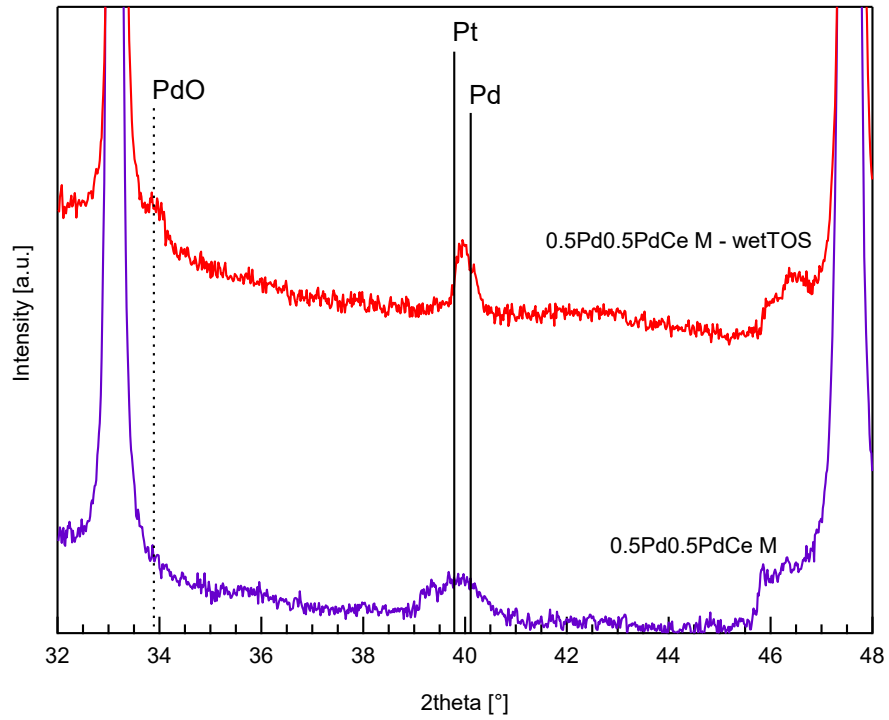

Figure 7-5: XRD spectra for the sample 0.5Pt0.5PdCe M after wetTOS in lean CH_4 oxidation (above) compared to 0.5Pt0.5PdCe M (below).

Figure 7-6 shows the comparison between PtPdCe IW and PtPdCe M for CO oxidation, with or without pretreatments. The results are similar to the behavior of monometallic PdCe samples. As for the monometallic palladium catalyst, also the comparison for dry lean CH_4 oxidation is reported. For CO oxidation PtPdCe IW still shows better performances than the milled counterpart, the opposite happening for CH_4 oxidation.

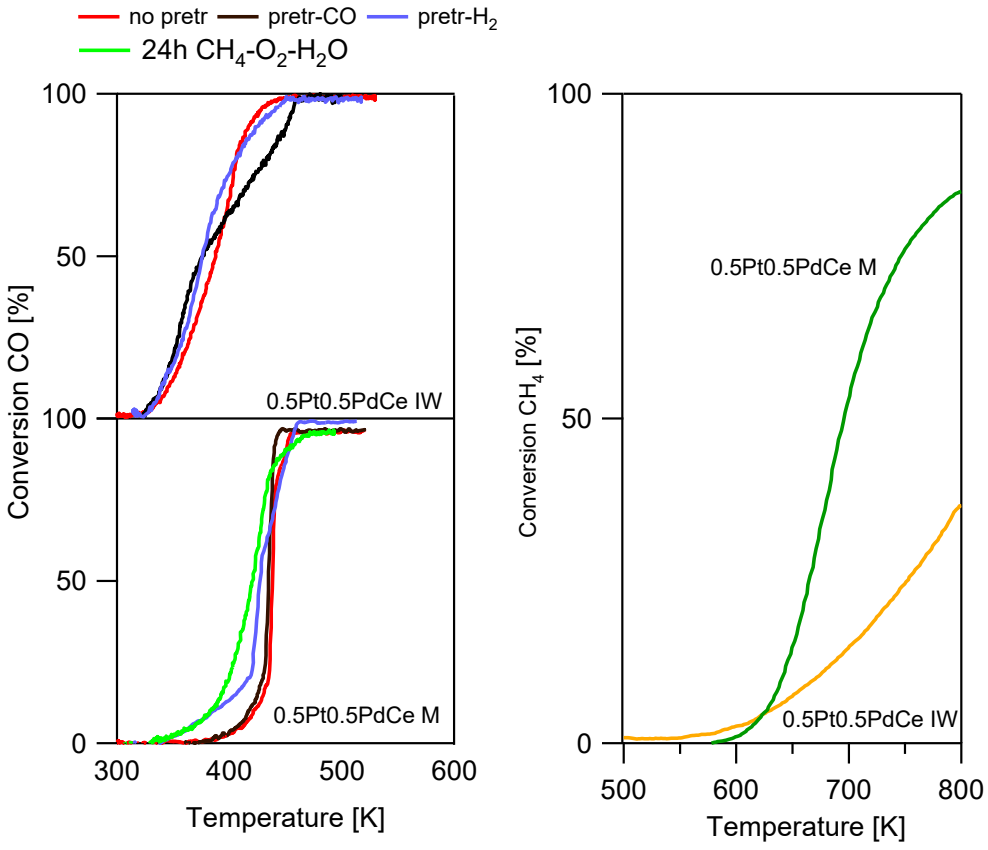

Figure 7-6: CO conversion for the samples 0.5Pt0.5PdCeM (below) and 0.5Pt0.5PdCeIW (above). Sample non-pretreated (red); pretreated in CO (black); pretreated in H_2 (blue). For the milled sample a further treatment was analyzed: pretreated in wet lean CH_4 oxidation (green).

In absence of pretreatments, the T_{10} and T_{50} were 420K and 438K for PtPdCe M, 346K and 387K for PtPdCe IW. These are the lowest values recorded in this study for as prepared samples. The effect of the pretreatment also resembles that observed for monometallic Pd catalyst, but with a higher influence for the milled sample after being treated in H_2 and especially after the wet TOS. This is also visible by the differences in T_{10} and T_{50} after the pretreatment, reported in Table 7-5.

Table 7-5: ΔT_{10}(K) and ΔT_{50}(K) for the samples 1PdCeM and 1PdCeIW, pretreated in CO or H_2 or in a 24 hours in wet lean CH_2 oxidation at 623K.

Sample	ΔT_{10}(K)	ΔT_{50}(K)
0.5Pt0.5PdCe M – CO	-4	-4
0.5Pt0.5Pd Ce M – H_2	-35	-12
0.5Pt0.5Pd Ce IW – CO	-6	-11
0.5Pt0.5Pd Ce IW – H_2	-7	-12
0.5Pt0.5Pd Ce M – H_2O	-37	-18

The effect of the pretreatment discussed for the two monometallic impregnated samples is no more valid, as now also the reciprocal interaction between the two metals should be taken into account. The high mobility of Pt due to the formation of volatile PtO_2 species is in fact limited by a trapping effect of PdO particles and by the formation of an alloy on the surface of the support.[242] Moreover, the alloying of Pt and Pd occurs already during calcination (as observed in Chapter 3 on the analogous sample) likely preventing Pt oxidation, thus explaining the similar performances of the fresh and pretreated bimetallic impregnated catalysts and their difference with 1PtCe IW.

As for the milled samples, it is worth noting that 1PtPdCe M after wet TOS treatment is the best performing among all milled samples for CO oxidation. Similarly to what was hypothesized for CH_4, it is likely that the formation of a PtPd alloy is the reason of the improvement observed after wet TOS pretreatment. It is reported in fact that PtPd alloy has high activity for CO oxidation.[234]

7.4 Conclusions

A systematic comparison was carried out between Pt, Pd and bimetallic PtPd catalysts prepared by mechanochemical synthesis and incipient wetness impregnation for CO oxidation. The results obtained show that IW samples achieve better performances, differently from what observed for methane oxidation. The behavior of PtCe IW is further improved by reducing treatments, which reduce the oxide phase likely formed during calcination. These treatments seem to not affect Pd-based samples, which however show conversions higher than Pt catalysts. This point needs further investigation, as also in the literature there are some discrepancies on Pd active phases for CO oxidation. For the bimetallic sample, the formation of the alloy seems to have a key role for the catalytic activity, in line with literature findings. The alloy has been detected for the as-prepared PtPdCe IW, as well as for PtPdCe M after wet-TOS treatment, which are indeed the best performing samples with higher CO conversion.

The opposite results obtained in the two reactions, CO and CH_4 oxidation, for milled and impregnated Pd-based catalysts deserve further investigation, as in light of the evidences presented in this chapter it is not possible to draw definitive conclusions. One hypothesis, also based on previous literature findings, is that different Pd phases are active for the two reactions, and clearly the strong Pd-Ce interaction found beneficial for methane oxidation has not the same effect on the oxidation of CO. This would imply that the results observed in Chapter 6 for a fully formulated feed cannot be explained straightforwardly by the competition of the two species for a similar active site. However, it is worth noting once more that treating the bimetallic sample during wet TOS methane oxidation improves its catalytic activity, irrespective of the reaction considered. This result might provide an effective strategy for the preparation of an economical and efficient catalyst in the optic of close-to-real full gas composition.

8. Future perspectives

The positive results obtained by ball milling for the preparation of monometallic Pd/Ce catalysts were extended to bimetallic formulations. The aim was to obtain more stable methane oxidation catalysts, as well as to cover as much as possible the compositions most applied in NGVs aftertreatment, which involve not only palladium but also platinum. From an economical point of view this is itself a convenient alternative in view of the future trends of platinum and palladium prices that may force to shift to the combination of the two metals or to the choice of other bimetallic systems. The effectiveness of mechanochemical synthesis rely on the realization of a strong interaction between Pd and CeO_2, which has been found unaltered when Pt is added and has a strong and beneficial impact on the rearrangement of Pt and Pd during catalytic tests.

A large characterization effort was spent in the identification of the morphology and oxidation states of these bimetallic catalysts and this allowed a preliminary scale-up of the synthesis. It was then possible to extend the application of the milled catalysts to the preparation of an industrial coating with which structured catalysts were prepared and tested in close-to-real conditions, thanks to the collaboration with the automotive catalyst industry Umicore. The passage from the lab scale to the pilot scale was well managed thanks to the versatility of the mechanical milling, that allowed to prepare many different samples in a relatively short time by varying in a fast and smooth way the synthesis parameters. This partially compensated the initial uncertainty around optimal formulations and created the base for solid future developments. A step in this direction was already added through specific preliminary studies of different bimetallic compositions and of CO oxidation. These attempts demonstrate that it is possible to use the mechanochemical synthesis to prepare various catalyst for different applications, allowing a fast and effective material screening without too much effort, and that the same synthesis might be scaled up relatively easily for an extension to industrial level.

9. References

1. Arrhenius S. On the influence of carbonic acid un the air upon the temperature of the ground. *Philos Mag J Sci*. 1896;41(5):237-276. doi:10.1002/cta.4490080404

2. Williams J, Austin SE. Construction of environmental problems. *Sociological*. 1998;68(4):476-497.

3. Al-Ghussain L. Global warming: review on driving forces and mitigation. *Environ Prog Sustain Energy*. 2019;38(1):13-21. doi:10.1002/ep.13041

4. UNFCCC. *Kyoto Protocol*.; 1997.

5. IPCC. Special Report on Global Warming of 1.5 °C (SR15). 2018.

6. UN Department of Economic Social Affairs. *World Population Prospects 2019*.; 2019. http://www.ncbi.nlm.nih.gov/pubmed/12283219.

7. Friedlingstein P, Jones MW, O'Sullivan M, et al. Global carbon budget 2019. *Earth Syst Sci Data*. 2019;11(4):1783-1838. doi:10.5194/essd-11-1783-2019

8. Agency IE. Global Energy & CO2 Status Report- The latest trends in energy and emissions in 2018. 2019. doi:10.4324/9781315252056

9. Brockway PE, Owen A, Brand-Correa LI, Hardt L. Estimation of global final-stage energy-return-on-investment for fossil fuels with comparison to renewable energy sources. *Nat Energy*. 2019;4(7):612-621. doi:10.1038/s41560-019-0425-z

10. Eurostat. *Energy, Transport and Environment Statistics. 2019 Edition*.; 2019. doi:10.2785/660147

11. Chen H, Geng HP, Ling HT, et al. Modeling the coal-to-gas switch potentials in the power sector: A case study of China. *Energy*. 2020;192:116629. doi:10.1016/j.energy.2019.116629

12. Scarlat N, Dallemand JF, Fahl F. Biogas: Developments and perspectives in Europe. *Renew Energy*. 2018;129:457-472. doi:10.1016/j.renene.2018.03.006

13. Ferella F, Cucchiella F, D'Adamo I, Gallucci K. A techno-economic assessment of biogas upgrading in a developed market. *J Clean Prod*. 2019;210:945-957.

doi:10.1016/j.jclepro.2018.11.073

14. Winquist E, Rikkonen P, Pyysiäinen J, Varho V. Is biogas an energy or a sustainability product? - Business opportunities in the Finnish biogas branch. *J Clean Prod*. 2019;233:1344-1354. doi:10.1016/j.jclepro.2019.06.181

15. Ardolino F, Arena U. Biowaste-to-Biomethane: An LCA study on biogas and syngas roads. *Waste Manag*. 2019;87:441-453. doi:10.1016/j.wasman.2019.02.030

16. Meng B, Gu C, Zhang L, et al. Hydrogen effects on X80 pipeline steel in high-pressure natural gas/hydrogen mixtures. *Int J Hydrogen Energy*. 2017;42(11):7404-7412. doi:10.1016/j.ijhydene.2016.05.145

17. Timmerberg S, Kaltschmitt M. Hydrogen from renewables: Supply from North Africa to Central Europe as blend in existing pipelines – Potentials and costs. *Appl Energy*. 2019;237(July 2018):795-809. doi:10.1016/j.apenergy.2019.01.030

18. Wang J, Huang Z, Fang Y, et al. Combustion behaviors of a direct-injection engine operating on various fractions of natural gas-hydrogen blends. *Int J Hydrogen Energy*. 2007;32(15 SPEC. ISS.):3555-3564. doi:10.1016/j.ijhydene.2007.03.011

19. Speirs J, Balcombe P, Johnson E, Martin J, Brandon N, Hawkes A. A greener gas grid: What are the options. *Energy Policy*. 2018;118(April):291-297. doi:10.1016/j.enpol.2018.03.069

20. Traub-merz R. *The Automotive Sector in Emerging Economies : Industrial Policies , Market Dynamics and Trade Unions, Trend & Perspectives in Brazil, China, India, Mexico and Russia*.; 2017.

21. Sangvikar B, Pawar A, Kolte A, Mainkar A, Sawant P. How Does Green Marketing Influence Consumers? The Market Trend Examination towards Environmentally Sustainable Products in Emerging Indian Cities. *Int J Recent Technol Eng*. 2019;8(3S):561-571. doi:10.35940/ijrte.c1114.1083s19

22. Yu H, Stuart AL. Impacts of compact growth and electric vehicles on future air quality and urban exposures may be mixed. *Sci Total Environ*. 2017;576:148-158. doi:10.1016/j.scitotenv.2016.10.079

23. Bicer Y, Dincer I. Comparative life cycle assessment of hydrogen, methanol and electric vehicles from well to wheel. *Int J Hydrogen Energy*. 2017;42(6):3767-3777. doi:10.1016/j.ijhydene.2016.07.252

24. Yazdanie M, Noembrini F, Heinen S, Espinel A, Boulouchos K. Well-to-wheel costs, primary energy demand, and greenhouse gas emissions for the production and operation of conventional and alternative vehicles. *Transp Res Part D Transp Environ*. 2016;48:63-84. doi:10.1016/j.trd.2016.08.002

25. Çabukoglu E, Georges G, Küng L, Pareschi G, Boulouchos K. Battery electric propulsion: an option for heavy-duty vehicles? Results from a Swiss case-study. *Transp Res Part C Emerg Technol*. 2018;88(February):107-123. doi:10.1016/j.trc.2018.01.013

26. Mulholland E, Teter J, Cazzola P, McDonald Z, Ó Gallachóir BP. The long haul towards decarbonising road freight – A global assessment to 2050. *Appl Energy*. 2018;216(February):678-693. doi:10.1016/j.apenergy.2018.01.058

27. Brand C. Beyond 'Dieselgate': Implications of unaccounted and future air pollutant emissions and energy use for cars in the United Kingdom. *Energy Policy*. 2016;97(X):1-12. doi:10.1016/j.enpol.2016.06.036

28. Shammut M, Cao M, Zhang Y, Papaix C, Liu Y, Gao X. Banning diesel vehicles in London: Is 2040 too late? *Energies*. 2019;12(18). doi:10.3390/en12183495

29. Karagöz Y. Analysis of the impact of gasoline, biogas and biogas + hydrogen fuels on emissions and vehicle performance in the WLTC and NEDC. *Int J Hydrogen Energy*. 2019;44(59):31621-31632. doi:10.1016/j.ijhydene.2019.10.019

30. He L, Fan Y, Bellettre J, Yue J, Luo L. A review on catalytic methane combustion at low temperatures: Catalysts, mechanisms, reaction conditions and reactor designs. *Renew Sustain Energy Rev*. 2020;119(November 2019). doi:10.1016/j.rser.2019.109589

31. Kalam MA, Masjuki HH, Amalina MA, Abdesselam H, Mahlia TMI. CO, HC and NOx Emissions Characteristics of a Retrofitted Bi-Fuel Natural Gas Engine. *HKIE Trans Hong Kong Inst Eng*. 2005;12(3):25-30.

doi:10.1080/1023697X.2005.10668009

32. Boucher O, Friedlingstein P, Collins B, Shine KP. The indirect global warming potential and global temperature change potential due to methane oxidation. *Environ Res Lett*. 2009;4(4). doi:10.1088/1748-9326/4/4/044007

33. Agency IE. The Contribution of Natural Gas Vehicles to Sustainable Transport. *Contrib Nat Gas Veh to Sustain Transp*. 2010. doi:10.1787/5km4rm5c0pzp-en

34. Wadud Z, Khan T. Air quality and climate impacts due to CNG conversion of motor vehicles in Dhaka, Bangladesh. *Environ Sci Technol*. 2013;47(24):13907-13916. doi:10.1021/es402338b

35. Camuzeaux JR, Alvarez RA, Brooks SA, Browne JB, Sterner T. Influence of methane emissions and vehicle efficiency on the climate implications of heavy-duty natural gas trucks. *Environ Sci Technol*. 2015;49(11):6402-6410. doi:10.1021/acs.est.5b00412

36. Raj A. Methane emission control. *Johnson Matthey Technol Rev*. 2016;60(4):228-235. doi:10.1595/205651316X692554

37. Korakianitis T, Namasivayam AM, Crookes RJ. Natural-gas fueled spark-ignition (SI) and compression-ignition (CI) engine performance and emissions. *Prog Energy Combust Sci*. 2011;37(1):89-112. doi:10.1016/j.pecs.2010.04.002

38. Zeng F, Hohn KL. Applied Catalysis B : Environmental Modeling of three-way catalytic converter performance with exhaust mixture from natural gas-fueled engines. *"Applied Catal B, Environ*. 2016;182:570-579. doi:10.1016/j.apcatb.2015.10.004

39. Lampert JK, Kazi MS, Farrauto RJ. Palladium catalyst performance for methane emissions abatement from lean bum natural gas vehicles. *Appl Catal B Environ*. 1997;14(3-4):211-223. doi:10.1016/S0926-3373(97)00024-6

40. Gélin P, Primet M. Complete oxidation of methane at low temperature over noble metal based catalysts: A review. *Appl Catal B Environ*. 2002;39(1):1-37. doi:10.1016/S0926-3373(02)00076-0

41. Farrauto RJ. Low-Temperature Oxidation of Methane. *Science (80-)*. 2012;337(August):659-660. doi:10.1007/s12239

42. Monai M, Montini T, Gorte RJ, Fornasiero P. Catalytic Oxidation of Methane: Pd and Beyond. *Eur J Inorg Chem*. 2018;2018(25):2884-2893. doi:10.1002/ejic.201800326

43. Meng L, Lin JJ, Pu ZY, et al. Identification of active sites for CO and CH 4 oxidation over PdO/Ce 1-xPd xO 2-δ catalysts. *Appl Catal B Environ*. 2012;119-120:117-122. doi:10.1016/j.apcatb.2012.02.036

44. Oh SH, Mitchell PJ, Siewert RM. Methane Oxidation over Noble Metal Catalysts as Related to Controlling Natural Gas Vehicle Exhaust Emissions. 1992:12-25. doi:10.1021/bk-1992-0495.ch002

45. Jørgensen M, Grönbeck H. First-Principles Microkinetic Modeling of Methane Oxidation over Pd(100) and Pd(111). *ACS Catal*. 2016;6(10):6730-6738. doi:10.1021/acscatal.6b01752

46. Huang F, Chen J, Hu W, et al. Pd or PdO: Catalytic active site of methane oxidation operated close to stoichiometric air-to-fuel for natural gas vehicles. *Appl Catal B Environ*. 2017;219:73-81. doi:10.1016/j.apcatb.2017.07.037

47. Colussi S, Gayen A, Camellone MF, et al. Nanofaceted Pd-O sites in Pd-Ce surface superstructures: Enhanced activity in catalytic combustion of methane. *Angew Chemie - Int Ed*. 2009;48(45):8481-8484. doi:10.1002/anie.200903581

48. Farrauto RJ, Hobson MC, Kennelly T, Waterman EM. Catalytic chemistry of supported palladium for combustion of methane. *Appl Catal A, Gen*. 1992;81(2):227-237. doi:10.1016/0926-860X(92)80095-T

49. Mayernick AD, Janik MJ. Methane oxidation on Pd-Ceria: A DFT study of the mechanism over Pd xCe1-xO2, Pd, and PdO. *J Catal*. 2011;278(1):16-25. doi:10.1016/j.jcat.2010.11.006

50. Senftle TP, Van Duin ACT, Janik MJ. Methane Activation at the Pd/CeO2 Interface. *ACS Catal*. 2017;7(1):327-332. doi:10.1021/acscatal.6b02447

51. Xiong H, Lester K, Ressler T, Schlögl R, Allard LF, Datye AK. Metastable Pd ⇔ PdO Structures During High Temperature Methane Oxidation. *Catal Letters*. 2017;147(5):1095-1103. doi:10.1007/s10562-017-2023-7

52. Felici R, Rijn R Van, Frenken JWM, Andersen JN, Lundgren E, Gro H. The Active Phase of Palladium during Methane Oxidation. *J Phys Chem Lett*. 2012.

53. McCarty JG. Kinetics of PdO combustion catalysis. *Catal Today*. 1995;26(3-4):283-293. doi:10.1016/0920-5861(95)00150-7

54. Gholami R, Alyani M, Smith KJ. *Deactivation of Pd Catalysts by Water during Low Temperature Methane Oxidation Relevant to Natural Gas Vehicle Converters*. Vol 5.; 2015. doi:10.3390/catal5020561

55. Salaün M, Kouakou A, Da Costa S, Da Costa P. Synthetic gas bench study of a natural gas vehicle commercial catalyst in monolithic form: On the effect of gas composition. *Appl Catal B Environ*. 2009;88(3-4):386-397. doi:10.1016/j.apcatb.2008.10.026

56. Geng H, Yang Z, Zhang L, Ran J, Yan Y. Methane oxidation with low O 2 / CH 4 ratios in the present of water : Combustion or reforming. *Energy Convers Manag*. 2017;132:339-346. doi:10.1016/j.enconman.2016.11.033

57. Geng H, Yang Z, Zhang L, Ran J, Chen Y. Experimental and kinetic study of methane combustion with water over copper catalyst at low-temperature. *Energy Convers Manag*. 2015;103:244-250. doi:10.1016/j.enconman.2015.06.076

58. Schwartz WR, Ciuparu D, Pfefferle LD. Combustion of methane over palladium-based catalysts: Catalytic deactivation and role of the support. *J Phys Chem C*. 2012;116(15):8587-8593. doi:10.1021/jp212236e

59. Kang SB, Han SJ, Nam SB, et al. Effect of aging atmosphere on thermal sintering of modern commercial TWCs. *Top Catal*. 2013;56(1-8):298-305. doi:10.1007/s11244-013-9970-z

60. Bartholomew CH. Mechanisms of catalyst deactivation. *Appl Catal A Gen*. 2001;212(1-2):17-60. doi:10.1016/S0926-860X(00)00843-7

61. Shinjoh H. Noble metal sintering suppression technology in three-way catalyst: Automotive three-way catalysts with the noble metal sintering suppression technology based on the support anchoring effect. *Catal Surv from Asia*. 2009;13(3):184-190. doi:10.1007/s10563-009-9076-6

62. Pecchi G, Reyes P, López T, Gómez R. Pd-CeO2 and Pd-La2O3/alumina-

supported catalysts: Their effect on the catalytic combustion of methane. *J Non Cryst Solids*. 2004;345-346:624-627. doi:10.1016/j.jnoncrysol.2004.08.110

63. Trovarelli A, Fornasiero P. Catalysis by ceria and related materials, 2nd Edition. *Catal Sci Ser*. 2013;12:888. doi:10.1142/p870

64. Colussi S, Trovarelli A, Vesselli E, et al. Structure and morphology of Pd/Al2O3 and Pd/CeO 2/Al2O3 combustion catalysts in Pd-PdO transformation hysteresis. *Appl Catal A Gen*. 2010;390(1-2):1-10. doi:10.1016/j.apcata.2010.09.033

65. Goodman ED, Dai S, Yang AC, et al. Uniform Pt/Pd Bimetallic Nanocrystals Demonstrate Platinum Effect on Palladium Methane Combustion Activity and Stability. *ACS Catal*. 2017;7(7):4372-4380. doi:10.1021/acscatal.7b00393

66. Nassiri H, Hayes RE, Semagina N. Stability of Pd-Pt catalysts in low-temperature wet methane combustion: Metal ratio and particle reconstruction. *Chem Eng Sci*. 2018;186:44-51. doi:10.1016/j.ces.2018.04.028

67. Maione A, André F, Ruiz P. Structured bimetallic Pd-Pt/γ-Al2O3 catalysts on FeCrAlloy fibers for total combustion of methane. *Appl Catal B Environ*. 2007;75(1-2):59-70. doi:10.1016/j.apcatb.2007.03.011

68. Geng H, Zhang L, Yang Z, Yan Y, Ran J. Effect of Pd/Pt ratio on the reactivity of methane catalytic combustion in bimetallic Pd-Pt catalyst. *Int J Hydrogen Energy*. 2018;43(24):11069-11078. doi:10.1016/j.ijhydene.2018.05.029

69. Qu P, Wang S, Hu W, et al. A novel strategy to design PtPd bimetallic catalysts for efficient methane combustion. *Catal Commun*. 2020;135(December 2019):105900. doi:10.1016/j.catcom.2019.105900

70. Nassiri H, Lee KE, Hu Y, Hayes RE, Scott RWJ, Semagina N. Water shifts PdO-catalyzed lean methane combustion to Pt-catalyzed rich combustion in Pd–Pt catalysts: In situ X-ray absorption spectroscopy. *J Catal*. 2017;352:649-656. doi:10.1016/j.jcat.2017.06.008

71. Nassiri H, Lee K-E, Hu Y, Hayes RE, Scott RWJ, Semagina N. Platinum Inhibits Low-Temperature Dry Lean Methane Combustion through Palladium Reduction in Pd−Pt/Al $_2$ O $_3$: An In Situ X-ray Absorption Study. *ChemPhysChem*. 2017;18(2):238-244. doi:10.1002/cphc.201600993

72. Johns TR, Gaudet JR, Peterson EJ, et al. Microstructure of bimetallic Pt-Pd catalysts under oxidizing conditions. *ChemCatChem*. 2013;5(9):2636-2645. doi:10.1002/cctc.201300181

73. Xu P, Wu Z, Deng J, et al. Catalytic performance enhancement by alloying Pd with Pt on ordered mesoporous manganese oxide for methane combustion. *Cuihua Xuebao/Chinese J Catal*. 2017;38(1):92-105. doi:10.1016/S1872-2067(16)62567-6

74. Goodman ED, Ye AA, Aitbekova A, et al. Palladium oxidation leads to methane combustion activity: Effects of particle size and alloying with platinum. *J Chem Phys*. 2019;151(15). doi:10.1063/1.5126219

75. Dianat A, Seriani N, Ciacchi LC, Pompe W, Cuniberti G, Bobeth M. Dissociative adsorption of methane on surface oxide structures of pd-pt alloys. *J Phys Chem C*. 2009;113(50):21097-21105. doi:10.1021/jp905689t

76. Habibi AH, Semagina N, Hayes RE. Kinetics of Low-Temperature Methane Oxidation over SiO2-Encapsulated Bimetallic Pd-Pt Nanoparticles. *Ind Eng Chem Res*. 2018;57(24):8160-8171. doi:10.1021/acs.iecr.8b01338

77. Karinshak KA, Lott P, Harold MP, Deutschmann O. In situ Activation of Bimetallic Pd−Pt Methane Oxidation Catalysts. *ChemCatChem*. 2020;12(14):3712-3720. doi:10.1002/cctc.202000603

78. Hou M, Zhang X, Fu C, Cen W, Chen J. Effects of a Pd/Pt bimetal supported by a γ-Al2O3 surface on methane activation. *Phys Chem Chem Phys*. 2020;22(8):4692-4698. doi:10.1039/c9cp05920b

79. Chetyrin IA, Bukhtiyarov A V., Prosvirin IP, Khudorozhkov AK, Bukhtiyarov VI. In Situ XPS and MS Study of Methane Oxidation on the Pd–Pt/Al2O3 Catalysts. *Top Catal*. 2020;63(1-2):66-74. doi:10.1007/s11244-019-01217-7

80. Zhang J, Everson MP, Wallington TJ, Field FR, Roth R, Kirchain RE. Assessing economic modulation of future critical materials use: The case of automotive-related platinum group metals. *Environ Sci Technol*. 2016;50(14):7687-7695. doi:10.1021/acs.est.5b04654

81. Alonso E, Field FR, Kirchain RE. Platinum availability for future automotive

technologies. *Environ Sci Technol*. 2012;46(23):12986-12993. doi:10.1021/es301110e

82. Ores U, Economy C. Platinum Group Elements in Geosphere and Anthroposphere : Interplay among the Global. 2020.

83. Kumsung W, Chareonpanich M, Kongkachuichay P, Senkan S. Single and bimetallic catalyst screenings of noble metals for methane combustion. *Catal Commun*. 2018;110(December 2017):83-87. doi:10.1016/j.catcom.2018.03.022

84. Hou Z, Liu Y, Deng J, et al. Highly Active and Stable Pd−GaOx/Al2O3 Catalysts Derived from Intermetallic Pd5Ga3 Nanocrystals for Methane Combustion. *ChemCatChem*. 2018;10(24):5637-5648. doi:10.1002/cctc.201801684

85. Guo X, Brault P, Zhi G, et al. Synergistic combination of plasma sputtered Pd-Au bimetallic nanoparticles for catalytic methane combustion. *J Phys Chem C*. 2011;115(22):11240-11246. doi:10.1021/jp203351p

86. Lin J, Chen Y, Liu X, et al. Microstructural property regulation and performance in methane combustion reaction of ordered mesoporous alumina supported palladium-cobalt bimetallic catalysts. *Appl Catal B Environ*. 2020;263(October 2019):118269. doi:10.1016/j.apcatb.2019.118269

87. Stefanov P, Todorova S, Naydenov A, et al. On the development of active and stable Pd-Co/γ-Al2O3 catalyst for complete oxidation of methane. *Chem Eng J*. 2015;266:329-338. doi:10.1016/j.cej.2014.12.099

88. Nassiri H, Hayes RE, Semagina N. Tin Dioxide as an Alternative to Platinum Promoter in Palladium- Catalyzed Wet Lean Methane Combustion. *Top Catal*. 2019;62(1):386-390. doi:10.1007/s11244-018-1084-1

89. Hao L, Lu Y, Sato H, Asanuma H, Guo J. Analysis on energy transfer during mechanical coating and ball milling - Supported by electric power measurement in planetary ball mill. *Int J Miner Process*. 2013;121:51-58. doi:10.1016/j.minpro.2013.03.003

90. Broseghini M, D'Incau M, Gelisio L, Pugno NM, Scardi P. Homogeneity of ball milled ceramic powders: Effect of jar shape and milling conditions. *Data Br*. 2017;10:186-191. doi:10.1016/j.dib.2016.11.070

91. M. Broseghinia, L. Gelisioa, M. D'Incaua, C.L. Azanza Ricardoa, N.M. Pugnob, c, d PS. Modellazione del processo di macinazione ad alta energia tramite mulino a biglie planetario. *Analisi&Calcolo*. 2016;102.

92. Broseghini M, Gelisio L, D'Incau M, Azanza Ricardo CL, Pugno NM, Scardi P. Modeling of the planetary ball-milling process: The case study of ceramic powders. *J Eur Ceram Soc*. 2016;36(9):2205-2212. doi:10.1016/j.jeurceramsoc.2015.09.032

93. Rosenkranz S, Breitung-Faes S, Kwade A. Experimental investigations and modelling of the ball motion in planetary ball mills. *Powder Technol*. 2011;212(1):224-230. doi:10.1016/j.powtec.2011.05.021

94. Burmeister CF, Kwade A. Process engineering with planetary ball mills. *Chem Soc Rev*. 2013;42(18):7660-7667. doi:10.1039/c3cs35455e

95. Schreyer H, Eckert R, Immohr S, de Bellis J, Felderhoff M, Schüth F. Milling Down to Nanometers: A General Process for the Direct Dry Synthesis of Supported Metal Catalysts. *Angew Chemie - Int Ed*. 2019;58(33):11262-11265. doi:10.1002/anie.201903545

96. R.M. Davis BMCCK. Mechanical Alloying of Brittle Materials. *Metall Trans*. 1988;19A(December):2867-2874.

97. Enayati MH, Mohamed FA. Application of mechanical alloying/milling for synthesis of nanocrystalline and amorphous materials. *Int Mater Rev*. 2014;59(7):394-416. doi:10.1179/1743280414Y.0000000036

98. Bolm C, Hernández JG. Mechanochemistry of Gaseous Reactants. *Angew Chemie - Int Ed*. 2019;58(11):3285-3299. doi:10.1002/anie.201810902

99. Takacs L. The historical development of mechanochemistry. *Chem Soc Rev*. 2013;42(18):7649-7659. doi:10.1039/c2cs35442j

100. Baláž P, Achimovicová M, Baláž M, et al. Hallmarks of mechanochemistry: From nanoparticles to technology. *Chem Soc Rev*. 2013;42(18):7571-7637. doi:10.1039/c3cs35468g

101. Trovarelli A, Zamar F, Llorca J, Leitenburg C de, Dolcetti G, Kiss JT. Nanophase Fluorite-Structured CeO2–ZrO2Catalysts Prepared by High-Energy

Mechanical Milling. *J Catal*. 1997;169(2):490-502. doi:10.1006/jcat.1997.1705

102. Šepelák V, Bégin-Colin S, Le Caër G. Transformations in oxides induced by high-energy ball-milling. *Dalt Trans*. 2012;41(39):11927-11948. doi:10.1039/c2dt30349c

103. Šepelák V, Düvel A, Wilkening M, Becker KD, Heitjans P. Mechanochemical reactions and syntheses of oxides. *Chem Soc Rev*. 2013;42(18):7507-7520. doi:10.1039/c2cs35462d

104. Furlani E, Aneggi E, de Leitenburg C, Maschio S. High energy ball milling of titania and titania-ceria powder mixtures. *Powder Technol*. 2014;254:591-596. doi:10.1016/j.powtec.2014.01.075

105. Do JL, Friščić T. Mechanochemistry: A Force of Synthesis. *ACS Cent Sci*. 2017;3(1):13-19. doi:10.1021/acscentsci.6b00277

106. James SL, Adams CJ, Bolm C, et al. Mechanochemistry: opportunities for new and cleaner synthesis. *Chem Soc Rev*. 2012;41(1):413-447. doi:10.1039/c1cs15171a

107. Ralphs K, Hardacre C, James SL. Application of heterogeneous catalysts prepared by mechanochemical synthesis. *Chem Soc Rev*. 2013;42(18):7701-7718. doi:10.1039/c3cs60066a

108. Barbara Szczęśniak, Sylwia Borysiuk, Jerzy Choma MJ. Mechanochemical synthesis of highly porous materials. *Mater Horizons*. 2020. doi:10.1039/D0MH00081G

109. Mario J. Muñoz Batista, Daily Rodríguez-Padrón, Alain Rafael Puente Santiago and RL. Mechanochemistry : towards sustainable design of advanced nanomaterials for electrochemical energy storage and catalytic applications. *ACS Sustain Chem Eng*. 2018. doi:10.1021/acssuschemeng.8b01716

110. Chunping X, Sudipta D, Alina M. B, Manuel O, Rafael L. Mechanochemical synthesis of advanced nanomaterials for catalytic applications. *Chem Commun*. 2015;51:6698-6713. doi:10.1039/C4CC09876E

111. Dong H, Moys MH. Assessment of discrete element method for one ball bouncing in a grinding mill. *Int J Miner Process*. 2002;65(3-4):213-226.

doi:10.1016/S0301-7516(01)00083-7

112. Gilardi G, Sharf I. Literature survey of contact dynamics modelling. *Mech Mach Theory*. 2002;37(10):1213-1239. doi:10.1016/S0094-114X(02)00045-9

113. Feng YT, Han K, Owen DRJ. Discrete element simulation of the dynamics of high energy planetary ball milling processes. *Mater Sci Eng A*. 2004;375-377(1-2 SPEC. ISS.):815-819. doi:10.1016/j.msea.2003.10.162

114. Chen W, Schoenitz M, Ward TS, Dave RN, Dreizin EL. Numerical simulation of mechanical alloying in a shaker mill by discrete element method. *KONA Powder Part J*. 2005;23(March):152-162. doi:10.14356/kona.2005018

115. Da Silva KL, Menzel D, Feldhoff A, et al. Mechanosynthesized BiFeO3 nanoparticles with highly reactive surface and enhanced magnetization. *J Phys Chem C*. 2011;115(15):7209-7217. doi:10.1021/jp110128t

116. Enayati MH. Formation of nanoscale layered structures and subsequent transformations during mechanical alloying of Ni60Nb40 powder mixture in a low energy ball mill. *KONA Powder Part J*. 2015;32(32):196-206. doi:10.14356/kona.2015010

117. Borchers C, Martin ML, Vorobjeva GA, et al. Cu–CeO2 nanocomposites: mechanochemical synthesis, physico-chemical properties, CO-PROX activity. *J Nanoparticle Res*. 2016;18(11). doi:10.1007/s11051-016-3640-6

118. Maeda Y, Akita T, Kohyama M. High activity of gold/tin-dioxide catalysts for low-temperature Co oxidation: Application of a reducible metal oxide to a catalyst support. *Catal Letters*. 2014;144(12):2086-2090. doi:10.1007/s10562-014-1376-4

119. Tang C, Sun B, Sun J, et al. Solid state preparation of NiO-CeO2 catalyst for NO reduction. *Catal Today*. 2017;281:575-582. doi:10.1016/j.cattod.2016.05.026

120. Zhou M, Zhao J, Zhang P, Chen N, Yang S. Solvent-free and rapid synthesis of mesoporous Pt-iron oxide catalysts: Via mechanochemical assembly. *Catal Sci Technol*. 2019;9(15):3907-3913. doi:10.1039/c9cy00970a

121. Kondrat SA, Shaw G, Freakley SJ, et al. Physical mixing of metal acetates: A simple, scalable method to produce active chloride free bimetallic catalysts.

Chem Sci. 2012;3(10):2965-2971. doi:10.1039/c2sc20450a

122. Kamolphop U, Taylor SFR, Breen JP, et al. Low-temperature selective catalytic reduction (SCR) of NO x with n-octane using solvent-free mechanochemically prepared Ag/Al2O 3 catalysts. *ACS Catal*. 2011;1(10):1257-1262. doi:10.1021/cs200326m

123. European-Commission. Chemicals Strategy for Sustainability Towards a Toxic-Free Environment. 2020;COM(2020).

124. Anastas PT, Kirchhoff MM. Origins, current status, and future challenges of green chemistry. *Acc Chem Res*. 2002;35(9):686-694. doi:10.1021/ar010065m

125. Sheldon RA. Metrics of Green Chemistry and Sustainability: Past, Present, and Future. *ACS Sustain Chem Eng*. 2018;6(1):32-48. doi:10.1021/acssuschemeng.7b03505

126. Danielis M, Colussi S, de Leitenburg C, Soler L, Llorca J, Trovarelli A. Outstanding Methane Oxidation Performance of Palladium-Embedded Ceria Catalysts Prepared by a One-Step Dry Ball-Milling Method. *Angew Chemie - Int Ed*. 2018;57(32):10212-10216. doi:10.1002/anie.201805929

127. Danielis M, Colussi S, De Leitenburg C, Soler L, Llorca J, Trovarelli A. The effect of milling parameters on the mechanochemical synthesis of Pd-CeO2 methane oxidation catalysts. *Catal Sci Technol*. 2019;9(16):4232-4238. doi:10.1039/c9cy01098j

128. Vilé G, Colussi S, Krumeich F, Trovarelli A, Pérez-Ramírez J. Opposite face sensitivity of CeO2 in hydrogenation and oxidation catalysis. *Angew Chemie - Int Ed*. 2014;53(45):12069-12072. doi:10.1002/anie.201406637

129. Lott P, Deutschmann O. Lean-Burn Natural Gas Engines: Challenges and Concepts for an Efficient Exhaust Gas Aftertreatment System. *Emiss Control Sci Technol*. 2020;(x). doi:10.1007/s40825-020-00176-w

130. Burch R, Urbano FJ, Loader PK. Methane combustion over palladium catalysts: The effect of carbon dioxide and water on activity. *Appl Catal A, Gen*. 1995;123(1):173-184. doi:10.1016/0926-860X(94)00251-7

131. Ciuparu D, Pfefferle L. Support and water effects on palladium based methane

combustion catalysts. *Appl Catal A Gen*. 2001;209(1-2):415-428. doi:10.1016/S0926-860X(00)00783-3

132. Monai M, Montini T, Chen C, Fonda E, Gorte RJ, Fornasiero P. Methane Catalytic Combustion over Hierarchical Pd@CeO2/Si-Al2O3: Effect of the Presence of Water. *ChemCatChem*. 2015;7(14):2038-2046. doi:10.1002/cctc.201402717

133. Persson K, Pfefferle LD, Schwartz W, Ersson A, Järås SG. Stability of palladium-based catalysts during catalytic combustion of methane: The influence of water. *Appl Catal B Environ*. 2007;74(3-4):242-250. doi:10.1016/j.apcatb.2007.02.015

134. Wilburn MS, Epling WS. Applied Catalysis B : Environmental Sulfur deactivation and regeneration of mono- and bimetallic Pd-Pt methane oxidation catalysts. *"Applied Catal B, Environ*. 2017;206:589-598. doi:10.1016/j.apcatb.2017.01.050

135. Xiong H, Wiebenga MH, Carrillo C, Gaudet JR, Pham HN. Applied Catalysis B : Environmental Design considerations for low-temperature hydrocarbon oxidation reactions on Pd based catalysts. 2018;236(March):436-444. doi:10.1016/j.apcatb.2018.05.049

136. Nguyen TS, Mckeever P, Arredondo-arechavala M, et al. Catalysis Science & Technology Correlation of the ratio of metallic to oxide species with activity of PdPt catalysts for methane oxidation †. 2020. doi:10.1039/c9cy02371b

137. Chen J, Wu Y, Hu W, et al. Insights into the role of Pt on Pd catalyst stabilized by magnesia-alumina spinel on gama-alumina for lean methane combustion : Enhancement of hydrothermal stability. *Mol Catal*. 2020;496(July):111185. doi:10.1016/j.mcat.2020.111185

138. Persson K, Ersson A, Jansson K, Iverlund N, Järås S. Influence of co-metals on bimetallic palladium catalysts for methane combustion. *J Catal*. 2005;231(1):139-150. doi:10.1016/j.jcat.2005.01.001

139. Castellazzi P, Groppi G, Forzatti P. Effect of Pt/Pd ratio on catalytic activity and redox behavior of bimetallic Pt-Pd/Al2O3 catalysts for CH4 combustion. *Appl*

Catal B Environ. 2010;95(3-4):303-311. doi:10.1016/j.apcatb.2010.01.008

140. Yashnik SA, Chesalov YA, Ishchenko A V., Kaichev V V., Ismagilov ZR. Effect of Pt addition on sulfur dioxide and water vapor tolerance of Pd-Mn-hexaaluminate catalysts for high-temperature oxidation of methane. *Appl Catal B Environ*. 2017;204:89-106. doi:10.1016/j.apcatb.2016.11.018

141. Sadokhina N, Smedler G, Nylén U, Olofsson M, Olsson L. Deceleration of SO2 poisoning on PtPd/Al2O3 catalyst during complete methane oxidation. *Appl Catal B Environ*. 2018;236(April):384-395. doi:10.1016/j.apcatb.2018.05.018

142. Pieck CL, Vera CR, Peirotti EM, Yori JC. Effect of water vapor on the activity of Pt-Pd/Al2O3 catalysts for methane combustion. *Appl Catal A Gen*. 2002;226(1-2):281-291. doi:10.1016/S0926-860X(01)00914-0

143. Lapisardi G, Urfels L, Gélin P, et al. Superior catalytic behaviour of Pt-doped Pd catalysts in the complete oxidation of methane at low temperature. *Catal Today*. 2006;117(4):564-568. doi:10.1016/j.cattod.2006.06.004

144. Amin A, Abedi A. A kinetic model for methane emission oxidation over Pd-Pt bimetallic monolith catalysts. *Int J Energy Res*. 2018;42(15):4642-4653. doi:10.1002/er.4205

145. Qi W, Ran J, Zhien Z, et al. Methane-combustion-reactivity-during-the-metalmetallic-oxide-transformation-of-PdPt. *Appl Surf Sci*. 2018;435:776-785. doi:10.1016/j.apsusc.2017.11.178

146. Kraikul N, Jitkarnka S, Luengnaruemitchai A. Catalytic methane combustion on Pd-Pt-La catalysts and their surface models. *Appl Catal B Environ*. 2005;58(1-2):143-152. doi:10.1016/j.apcatb.2004.12.004

147. Martin NM, Nilsson J, Skoglundh M, et al. Characterization of surface structure and oxidation/reduction behavior of Pd-Pt/Al2O3 model catalysts. *J Phys Chem C*. 2016;120(49):28009-28020. doi:10.1021/acs.jpcc.6b09223

148. Nie H, Howe JY, Lachkov PT, Chin YHC. Chemical and Structural Dynamics of Nanostructures in Bimetallic Pt-Pd Catalysts, Their Inhomogeneity, and Their Roles in Methane Oxidation. *ACS Catal*. 2019;9(6):5445-5461. doi:10.1021/acscatal.9b00485

149. Danielis M, Betancourt LE, Orozco I, et al. Methane oxidation activity and nanoscale characterization of Pd / CeO 2 catalysts prepared by dry milling Pd acetate and ceria. *Appl Catal B Environ*. 2021;282(September 2020):119567. doi:10.1016/j.apcatb.2020.119567

150. Wu J, Shan S, Cronk H, et al. Understanding Composition-Dependent Synergy of PtPd Alloy Nanoparticles in Electrocatalytic Oxygen Reduction Reaction. *J Phys Chem C*. 2017;121:14128-14136. doi:10.1021/acs.jpcc.7b03043

151. Chen G, Chou WT, Yeh C. The sorption of hydrogen on palladium in a flow system. *Appl Catal*. 1983;8:240.

152. Bonarowska M, Karpiński Z. Characterization of supported Pd-Pt catalysts by chemical probes. *Catal Today*. 2008;137(2-4):498-503. doi:10.1016/j.cattod.2007.11.001

153. Ranga Rao G. Influence of metal particles on the reduction properties of ceria-based materials studied by TPR. *Bull Mater Sci*. 1999;22(2):89-94. doi:10.1007/bf02745559

154. Persson K, Ersson A, Jansson K, Fierro JLG, Järås SG. Influence of molar ratio on Pd-Pt catalysts for methane combustion. *J Catal*. 2006;243(1):14-24. doi:10.1016/j.jcat.2006.06.019

155. Persson K, Ersson A, Colussi S, Trovarelli A, Järås SG. Catalytic combustion of methane over bimetallic Pd-Pt catalysts: The influence of support materials. *Appl Catal B Environ*. 2006;66(3-4):175-185. doi:10.1016/j.apcatb.2006.03.010

156. Monai M, Montini T, Fonda E, et al. Nanostructured Pd-Pt nanoparticles: evidences of structure/performance relations in catalytic H2 production reactions. *Appl Catal B Environ*. 2018;236(April):88-98. doi:10.1016/j.apcatb.2018.05.019

157. Vara M, Roling LT, Wang X, et al. Understanding the Thermal Stability of Palladium-Platinum Core-Shell Nanocrystals by in Situ Transmission Electron Microscopy and Density Functional Theory. *ACS Nano*. 2017;11(5):4571-4581. doi:10.1021/acsnano.6b08692

158. Jiang D, Khivantsev K, Wang Y. Low-Temperature Methane Oxidation for E ffi cient Emission Control in Natural Gas Vehicles: Pd and Beyond. 2020;(x).

doi:10.1021/acscatal.0c03338

159. Hu W, Wu Y, Chen J, Qu P, Zhong L, Chen Y. Methane Combustion with a Pd-Pt Catalyst Stabilized by Magnesia-Alumina Spinel in a High-Humidity Feed. *Ind Eng Chem Res*. 2020;59(24):11170-11176. doi:10.1021/acs.iecr.0c01362

160. Petrov AW, Ferri D, Kröcher O, Van Bokhoven JA. Design of Stable Palladium-Based Zeolite Catalysts for Complete Methane Oxidation by Postsynthesis Zeolite Modification. *ACS Catal*. 2019;9(3):2303-2312. doi:10.1021/acscatal.8b04486

161. Murata K, Kosuge D, Ohyama J, et al. Exploiting Metal-Support Interactions to Tune the Redox Properties of Supported Pd Catalysts for Methane Combustion. *ACS Catal*. 2020;10(2):1381-1387. doi:10.1021/acscatal.9b04524

162. Barrett W, Nasr S, Shen J, et al. Strong metal-support interactions in Pd/Co3O4catalyst in wet methane combustion: In situ X-ray absorption study. *Catal Sci Technol*. 2020;10(13):4229-4236. doi:10.1039/d0cy00465k

163. Bergman SL, Granestrand J, Xi S, et al. Probing the Oxidation/Reduction Dynamics of Fresh and P-, Na-, and K-Contaminated Pt/Pd/Al2O3 Diesel Oxidation Catalysts by STEM, TPR, and in Situ XANES. *J Phys Chem C*. 2020;124(5):2945-2952. doi:10.1021/acs.jpcc.9b07655

164. Marchionni V, Nachtegaal M, Ferri D. Influence of CO on Dry CH4 Oxidation on Pd/Al2O3 by Operando Spectroscopy: A Multitechnique Modulated Excitation Study. *ACS Catal*. 2020;10(8):4791-4804. doi:10.1021/acscatal.9b05541

165. Lott P, Eck M, Doronkin DE, et al. Understanding sulfur poisoning of bimetallic Pd-Pt methane oxidation catalysts and their regeneration. *Appl Catal B Environ*. 2020;278(June). doi:10.1016/j.apcatb.2020.119244

166. Lee G, Zheng W, Goulas KA, Lee IC, Vlachos DG. 110th Anniversary: Kinetics and X-ray Absorption Spectroscopy in Methane Total Oxidation over Alumina-Supported Pt, Pd, and Ag-Pd Catalysts. *Ind Eng Chem Res*. 2019;58(38):17718-17726. doi:10.1021/acs.iecr.9b03094

167. Murata K, Eleeda E, Ohyama J, Yamamoto Y, Arai S, Satsuma A. Identification

of active sites in CO oxidation over a Pd/Al2O3 catalyst. *Phys Chem Chem Phys*. 2019;21(33):18128-18137. doi:10.1039/c9cp03943k

168. Lovón-quintana JJ, Santos JBO, Lovón ASP, La-salvia N, Valenc GP. Low-temperature oxidation of methane on Pd-Sn/ZrO2 catalysts. *J od Mol Catal A Chem*. 2016;411:117-127.

169. Willis JJ, Goodman ED, Wu L, et al. Systematic Identification of Promoters for Methane Oxidation Catalysts Using Size- and Composition-Controlled Pd-Based Bimetallic Nanocrystals. *J Am Chem Soc*. 2017;139(34):11989-11997. doi:10.1021/jacs.7b06260

170. Leyssens L, Vinck B, Van Der Straeten C, Wuyts F, Maes L. Cobalt toxicity in humans—A review of the potential sources and systemic health effects. *Toxicology*. 2017;387(March):43-56. doi:10.1016/j.tox.2017.05.015

171. Liu C, Xian H, Jiang Z, et al. Insight into the improvement effect of the Ce doping into the SnO 2 catalyst for the catalytic combustion of methane. *Appl Catal B Environ*. 2015;176-177:542-552. doi:10.1016/j.apcatb.2015.04.042

172. Barrett W, Shen J, Hu Y, Hayes RE, Scott RWJ, Semagina N. Understanding the Role of SnO2 Support in Water-Wolerant Methane Combustion: In situ Observation of Pd(OH)2 and Comparison with Pd/Al2O3. *ChemCatChem*. 2020;12(3):944-952. doi:10.1002/cctc.201901744

173. Zhao Z, Wang B, Ma J, et al. Catalytic combustion of methane over Pd/SnO2 catalysts. *Cuihua Xuebao/Chinese J Catal*. 2017;38(8):1322-1329. doi:10.1016/S1872-2067(17)62864-X

174. Li J, Fu H, Fu L, Hao J. Complete combustion of methane over indium tin oxides catalysts. *Environ Sci Technol*. 2006;40(20):6455-6459. doi:10.1021/es061629q

175. Xue D, Wang Y, Zhang Z, Cao J. Porous In2O3 nanospheres with high methane sensitivity: A combined experimental and first-principle study. *Sensors Actuators, A Phys*. 2020;305:111944. doi:10.1016/j.sna.2020.111944

176. Moalaghi M, Gharesi M, Ranjkesh A, Hossein-Babaei F. Tin oxide gas sensor on tin oxide microheater for high-temperature methane sensing. *Mater Lett*. 2020;263:127196. doi:10.1016/j.matlet.2019.127196

177. Upham DC, Agarwal V, Khechfe A, et al. Catalytic molten metals for the direct conversion of methane to hydrogen and separable carbon. *Science (80-)*. 2017;358(November):917-921.

178. Tajima H, Ogihara H, Yoshida-Hirahara M, Kurokawa H. Methane conversion on cobalt-added liquid-metal indium catalysts. *New J Chem*. 2020;44(40):17198-17202. doi:10.1039/d0nj03808c

179. Zheng Y, Wang C, Li J, Zhong F, Xiao Y, Jiang L. *Enhanced Methane Oxidation over Co3O4-In2O3-x Composite Oxide Nanoparticles via Controllable Substitution of Co3+/Co2+by In3+Ions*. Vol 3.; 2020. doi:10.1021/acsanm.0c02075

180. Aneggi E, Rico-Perez V, De Leitenburg C, et al. Ceria-Zirconia Particles Wrapped in a 2D Carbon Envelope: Improved Low-Temperature Oxygen Transfer and Oxidation Activity. *Angew Chemie - Int Ed*. 2015;54(47):14040-14043. doi:10.1002/anie.201507839

181. Gade SK, Keeling MK, Davidson AP, Hatlevik O, Way JD. Palladium-ruthenium membranes for hydrogen separation fabricated by electroless co-deposition. *Int J Hydrogen Energy*. 2009;34(15):6484-6491. doi:10.1016/j.ijhydene.2009.06.037

182. Roa JJ, Gilioli E, Bissoli F, et al. Study of the mechanical properties of CeO 2 layers with the nanoindentation technique. *Thin Solid Films*. 2009;518(1):227-232. doi:10.1016/j.tsf.2009.07.132

183. Shao BL, Jiang D, Gong J. Nanoindentation Characterization of the Hardness of Zirconia Dental Ceramics. 2013;(8):704-707. doi:10.1002/adem.201200367

184. Deng X, Chawla N, Chawla KK, Koopman M. Deformation behavior of (Cu, Ag)-Sn intermetallics by nanoindentation. *Acta Mater*. 2004;52(14):4291-4303. doi:10.1016/j.actamat.2004.05.046

185. Edalati K, Horita Z. Correlations between hardness and atomic bond parameters of pure metals and semi-metals after processing by high-pressure torsion. *Scr Mater*. 2011;64(2):161-164. doi:10.1016/j.scriptamat.2010.09.034

186. Bardini L, Pappacena A, Llorca J, Boaro M, Trovarelli A. Structural and electrocatalytic properties of molten core Sn@SnOx nanoparticles on ceria.

"*Applied Catal B Environ*. 2016;197:254-261. doi:10.1016/j.apcatb.2016.02.050

187. Skála T, Šutara F, Prince KC, Matolín V. Cerium oxide stoichiometry alteration via Sn deposition: Influence of temperature. *J Electron Spectros Relat Phenomena*. 2009;169:20-25. doi:10.1016/j.elspec.2008.10.003

188. Skála T, Šutara F, Škoda M, Prince KC, Matolín V. Palladium interaction with CeO2, Sn-Ce-O and Ga-Ce-O layers. *J Phys Condens Matter*. 2009;21. doi:10.1088/0953-8984/21/5/055005

189. Luo MF, Zheng XM. Redox behaviour and catalytic properties of Ce0.5Zr0.5O2-supported palladium catalysts. *Appl Catal A Gen*. 1999;189(1):15-21. doi:10.1016/S0926-860X(99)00230-6

190. Blankenbuehler MT, Van Ness B. Staying the Course. *ACS Symp Ser*. 2018;1278:17-25. doi:10.7748/ns2011.09.26.3.64.p6378

191. Gharehghani A, Hosseini R, Mirsalim M, Yusaf TF. A comparative study on the first and second law analysis and performance characteristics of a spark ignition engine using either natural gas or gasoline. *Fuel*. 2015;158:488-493. doi:10.1016/j.fuel.2015.05.067

192. Chen H, He J, Zhong X. Engine combustion and emission fuelled with natural gas: A review. *J Energy Inst*. 2019;92(4):1123-1136. doi:10.1016/j.joei.2018.06.005

193. Farrauto RJ, Deeba M, Alerasool S. Gasoline automobile catalysis and its historical journey to cleaner air. *Nat Catal*. 2019;2(7):603-613. doi:10.1038/s41929-019-0312-9

194. Brinkmeier C. Automotive three way exhaust aftertreatment under transient conditions: measurements, modeling and simulation. *Thesis*. 2006:1-180. http://elib.uni-stuttgart.de/opus/volltexte/2007/2813/.

195. Gandhi HS, Piken AG, Shelef M. of Three-Way Catalysts. 1970.

196. Delosh RG, Heyde ME, Engineering AE, Company FM. H. S. Gandhi, A. G. Tiken, H. K. Stepien and M. Shelef.

197. Lan L, Yan C, Chen S, et al. Designed synthesis of semi-embedded Pd over

CeO2-ZrO2/Al2O3 as advanced three-way catalyst. *J Taiwan Inst Chem Eng*. 2018;85:98-105. doi:10.1016/j.jtice.2017.12.022

198. Möller R, Votsmeier M, Onder C, Guzzella L, Gieshoff J. Is oxygen storage in three-way catalysts an equilibrium controlled process? *Appl Catal B Environ*. 2009;91(1-2):30-38. doi:10.1016/j.apcatb.2009.05.003

199. Xi Y, Ottinger N, Liu ZG. Development of a Lab Reactor System for the Evaluation of Aftertreatment Catalysts for Stoichiometric Natural Gas Engines. 2018. doi:10.4271/2017-01-0999.Copyright

200. Bounechada D, Groppi G, Forzatti P, Kallinen K, Kinnunen T. Applied Catalysis B : Environmental Effect of periodic lean / rich switch on methane conversion over a Ce – Zr promoted Pd-Rh / Al 2 O 3 catalyst in the exhausts of natural gas vehicles. *"Applied Catal B, Environ*. 2012;119-120:91-99. doi:10.1016/j.apcatb.2012.02.025

201. Beulertz G, Votsmeier M, Moos R. Applied Catalysis B : Environmental Effect of propene , propane , and methane on conversion and oxidation state of three-way catalysts : a microwave cavity perturbation study. *"Applied Catal B, Environ*. 2015;165:369-377. doi:10.1016/j.apcatb.2014.09.068

202. Ferri D, Elsener M, Kröcher O. Applied Catalysis B : Environmental Methane oxidation over a honeycomb Pd-only three-way catalyst under static and periodic operation. *"Applied Catal B, Environ*. 2018;220:67-77. doi:10.1016/j.apcatb.2017.07.070

203. Burch R, Ramli A. A comparative investigation of the reduction of No by CH4 on Pt, Pd, and Rh catalysts. *Appl Catal B Environ*. 1998;15(1-2):49-62. doi:10.1016/S0926-3373(97)00036-2

204. Marchionni V, Nachtegaal M, Petrov A, Kröcher O, Ferri D. Operando XAS study of the influence of CO and NO on methane oxidation by Pd/Al2O3. *J Phys Conf Ser*. 2016;712(1):8-12. doi:10.1088/1742-6596/712/1/012051

205. Nilsson J, Carlsson P, Martin NM, et al. Methane oxidation over Pd / Al 2 O 3 under rich / lean cycling followed by operando XAFS and modulation excitation spectroscopy. *J Catal*. 2017;356:237-245. doi:10.1016/j.jcat.2017.10.018

206. Gallagher PK, Gross ME. The thermal decomposition of palladium acetate. *J Therm Anal*. 1986;31(6):1231-1241. doi:10.1007/BF01914636

207. Danielis M, Colussi S, de Leitenburg C, Trovarelli A. The role of palladium salt precursors in Pd-PdO/CeO2 catalysts prepared by dry milling for methane oxidation. *Catal Commun*. 2020;135(December 2019):105899. doi:10.1016/j.catcom.2019.105899

208. Zorn K, Giorgio S, Halwax E, Henry CR, Grönbeck H, Rupprechter G. CO oxidation on technological Pd-Al2O3 catalysts: Oxidation state and activity. *J Phys Chem C*. 2011;115(4):1103-1111. doi:10.1021/jp106235x

209. Huang C, Shan W, Lian Z, Zhang Y, He H. Recent advances in three-way catalysts of natural gas vehicles. *Catal Sci Technol*. 2020. doi:10.1039/d0cy01320j

210. Osaki T. Activity-determining factors for catalytic CO and CH4 oxidation on Pt/CeO2–ZrO2–Al2O3 cryogels. *Res Chem Intermed*. 2020;46(6):3125-3143. doi:10.1007/s11164-020-04141-8

211. Mao X, Foucher A, Stach EA, Gorte RJ. A Study of Support Effects for CH 4 and CO Oxidation over Pd Catalysts on ALD-Modified Al 2 O 3. *Catal Letters*. 2019;149(4):905-915. doi:10.1007/s10562-019-02699-6

212. Soliman NK. Factors affecting CO oxidation reaction over nanosized materials: A review. *J Mater Res Technol*. 2019;8(2):2395-2407. doi:10.1016/j.jmrt.2018.12.012

213. Van Spronsen MA, Frenken JWM, Groot IMN. Surface science under reaction conditions: CO oxidation on Pt and Pd model catalysts. *Chem Soc Rev*. 2017;46(14):4347-4374. doi:10.1039/c7cs00045f

214. Schaube M, Merkle R, Maier J. Interdependence of point defects and reaction kinetics: CO and CH4 oxidation on ceria and zirconia. *J Phys Chem C*. 2020;124(34):18544-18556. doi:10.1021/acs.jpcc.0c03256

215. Kim Y, Lee H, Kwak JH. Mechanism of CO-oxidation on Pd / CeO 2 (100): The unique surface- structure of CeO 2 (100) and the role of peroxide. 2(100):1-29.

216. Kim HJ, Jang MG, Shin D, Han JW. Design of Ceria Catalysts for Low-Temperature CO Oxidation. *ChemCatChem*. 2020;12(1):11-26. doi:10.1002/cctc.201901787

217. Dey S, Dhal GC. Cerium catalysts applications in carbon monoxide oxidations. *Mater Sci Energy Technol*. 2020;3:6-24. doi:10.1016/j.mset.2019.09.003

218. Soler L, Casanovas A, Urrich A, Angurell I, Llorca J. CO oxidation and COPrOx over preformed Au nanoparticles supported over nanoshaped CeO2. *Appl Catal B Environ*. 2016;197:47-55. doi:10.1016/j.apcatb.2016.02.025

219. Liu HH, Wang Y, Jia AP, Wang SY, Luo MF, Lu JQ. Oxygen vacancy promoted CO oxidation over Pt/CeO 2 catalysts: A reaction at Pt-CeO 2 interface. *Appl Surf Sci*. 2014;314:725-734. doi:10.1016/j.apsusc.2014.06.196

220. Lang W, Laing P, Cheng Y, Hubbard C, Harold MP. Co-oxidation of CO and propylene on Pd/CeO2-ZrO2 and Pd/Al2O3 monolith catalysts: A light-off, kinetics, and mechanistic study. *Appl Catal B Environ*. 2017;218:430-442. doi:10.1016/j.apcatb.2017.06.064

221. Soni Y, Pradhan S, Bamnia MK, et al. Spectroscopic Evidences for the Size Dependent Generation of Pd Species Responsible for the Low Temperature CO Oxidation Activity on Pd-SBA-15 Nanocatalyst. *Appl Catal B Environ*. 2020;272(April):118934. doi:10.1016/j.apcatb.2020.118934

222. Gänzler AM, Casapu M, Vernoux P, et al. Tuning the Structure of Platinum Particles on Ceria In Situ for Enhancing the Catalytic Performance of Exhaust Gas Catalysts. *Angew Chemie - Int Ed*. 2017;56(42):13078-13082. doi:10.1002/anie.201707842

223. Nie L, Mei D, Xiong H, et al. Activation of surface lattice oxygen in single-atom Pt/CeO2 for low-temperature CO oxidation. *Science (80-)*. 2017;358(6369):1419-1423. doi:10.1126/science.aao2109

224. Lee J, Ryou Y, Chan X, Kim TJ, Kim DH. How Pt interacts with CeO2 under the reducing and oxidizing environments at elevated temperature: The origin of improved thermal stability of Pt/CeO2 compared to CeO2. *J Phys Chem C*. 2016;120(45):25870-25879. doi:10.1021/acs.jpcc.6b08656

225. Fernandez-Garcia M, Martinez-Arias A, Iglesias-Juez A, et al. New Pd/CexZr1-xO2/Al2O3 three-way catalysts prepared by microemulsion Part 1. Characterization and catalytic behavior for CO oxidation. *Appl Catal B Environ*. 2001;31(1):39-50. doi:10.1016/S0926-3373(00)00265-4

226. Cargnello M, Doan-Nguyen VVT, Gordon TR, et al. Control of metal nanocrystal size reveals metal-support interface role for ceria catalysts. *Science (80-)*. 2013;341(6147):771-773. doi:10.1126/science.1240148

227. Hinokuma S, Fujii H, Katsuhara Y, Ikeue K, Machida M. Effect of thermal ageing on the structure and catalytic activity of Pd/CeO2 prepared using arc-plasma process. *Catal Sci Technol*. 2014;4(9):2990-2996. doi:10.1039/c4cy00291a

228. Gulyaev R V., Stadnichenko AI, Slavinskaya EM, Ivanova AS, Koscheev S V., Boronin AI. In situ preparation and investigation of Pd/CeO 2 catalysts for the low-temperature oxidation of CO. *Appl Catal A Gen*. 2012;439-440:41-50. doi:10.1016/j.apcata.2012.06.045

229. Jiang D, Wan G, García-Vargas CE, et al. Elucidation of the Active Sites in Single-Atom Pd 1 /CeO 2 Catalysts for Low-Temperature CO Oxidation . *ACS Catal*. 2020;10(19):11356-11364. doi:10.1021/acscatal.0c02480

230. Satsuma A, Osaki K, Yanagihara M, Ohyama J, Shimizu K. Low temperature combustion over supported Pd catalysts - Strategy for catalyst design. *Catal Today*. 2015;258:83-89. doi:10.1016/j.cattod.2015.03.047

231. Kurnatowska M, Kepinski L, Mista W. Structure evolution of nanocrystalline Ce 1-xPd xO 2-y mixed oxide in oxidizing and reducing atmosphere: Reduction-induced activity in low-temperature CO oxidation. *Appl Catal B Environ*. 2012;117-118:135-147. doi:10.1016/j.apcatb.2011.12.034

232. Daneshvar K, Krishna Dadi R, Luss D, et al. Experimental and modeling study of CO and hydrocarbons light-off on various Pt-Pd/Γ-Al2O3 diesel oxidation catalysts. *Chem Eng J*. 2017;323:347-360. doi:10.1016/j.cej.2017.04.078

233. Kang SB, Hazlett M, Balakotaiah V, Kalamaras C, Epling W. Effect of Pt:Pd ratio on CO and hydrocarbon oxidation. *Appl Catal B Environ*. 2018;223:67-75.

doi:10.1016/j.apcatb.2017.05.057

234. Dong F, Yamazaki K. The Pt-Pd alloy catalyst and enhanced catalytic activity for diesel oxidation. *Catal Today*. 2020;(April). doi:10.1016/j.cattod.2020.08.019

235. Hatanaka M, Takahashi N, Tanabe T, et al. Ideal Pt loading for a Pt/CeO2-based catalyst stabilized by a Pt-O-Ce bond. *Appl Catal B Environ*. 2010;99(1-2):336-342. doi:10.1016/j.apcatb.2010.07.003

236. Shen M, Lv L, Wang J, Zhu J, Huang Y, Wang J. Study of Pt dispersion on Ce based supports and the influence on the CO oxidation reaction. *Chem Eng J*. 2014;255:40-48. doi:10.1016/j.cej.2014.06.058

237. Spezzati G, Su Y, Hofmann JP, et al. Atomically dispersed Pd-O species on CeO2(111) as highly active sites for low-temperature CO oxidation. *ACS Catal*. 2017;7(10):6887-6891. doi:10.1021/acscatal.7b02001

238. Zhu H, Qin Z, Shan W, Shen W, Wang J. Low-temperature oxidation of CO over Pd/CeO2-TiO2 catalysts with different pretreatments. *J Catal*. 2005;233(1):41-50. doi:10.1016/j.jcat.2005.04.033

239. Tereshchenko A, Polyakov V, Guda A, et al. Ultra-Small Pd Nanoparticles on Ceria as an Advanced Catalyst for CO Oxidation. *Catalysts*. 2019;9(4):385. https://www.mdpi.com/2073-4344/9/4/385.

240. Wen C, Liu Y, Guo Y, Wang Y, Lu G. Influence of pretreatment on the structural and catalytic properties of supported Pd catalysts for CO oxidation. *Surf Rev Lett*. 2013;20(2):3-8. doi:10.1142/S0218625X13500133

241. Ye J, Xia Y, Cheng D guo, Chen F, Zhan X. Promoting effects of pretreatment on Pd/CeO2 catalysts for CO oxidation. *Int J Hydrogen Energy*. 2019;44(33):17985-17994. doi:10.1016/j.ijhydene.2019.05.099

242. Carrillo C, Johns TR, Xiong H, et al. Trapping of Mobile Pt Species by PdO Nanoparticles under Oxidizing Conditions. 2014:5-9. doi:10.1021/jz5009483

10. Table of contents